MICROMECHANICAL BEHAVIOUR OF LEAD-FREE SOLDER JOINTS DEVELOPED FOR 3D-IC PACKAGING APPLICATIONS

SIVA SURI CHANDRA RAO BHESETTI

NATIONAL UNIVERSITY OF SINGAPORE

2012

MICROMECHANICAL BEHAVIOUR OF LEAD-FREE SOLDER JOINTS DEVELOPED FOR 3D-IC PACKAGING APPLICATIONS

SIVA SURI CHANDRA RAO BHESETTI

(Master of Engineering, Indian Institute of Science, Bangalore, India)

(B.Tech, National Institute of technology, Warangal, India)

A THESIS SUBMITTED

FOR THE DEGREE OF DOCTOR OF PHILOSOPHY

DEPARTMENT OF MECHANICAL ENGINEERING

NATIONAL UNIVERSITY OF SINGAPORE

2012

DECLARATION

I hereby declare that the thesis is my original work and it has been written by me in its entirety. I have duly acknowledged all the sources of information which have been used in the thesis.

This thesis has also not been submitted for any degree in any university previously.

20-03-2013

Siva Suri Chandra Rao Bhesetti

20 March 2013

PREFACE

This thesis is submitted for the degree of Doctor of Philosophy in the Department of Mechanical Engineering, National University of Singapore (NUS) under the supervision of Associate Professor, Dr. Zeng Kaiyang and Dr.V.Kripesh, Institute of Microelectronics (IME), Singapore. To the best of my knowledge, all of the results presented in this thesis are original, and references provided to works by other researchers. Fabrication and detailed analysis on diffusion kinetics of lead free solder joints have been discussed in the Appendices. The majority portions of this thesis have been published in international journals/conference proceedings or presented at various international conferences as listed. Conference paper entitled "*Effects of nano-sized molybdenum particles on the low-cycle fatigue behaviour of SnAgCu solder alloy*" has been awarded the best paper at IUMRS-ICEM 2010, Seoul, South Korea.

JOURNAL AND CONFERENCE PUBLICATIONS

1. **B.S.S.Chandra Rao**, K.Mohan Kumar, K.Y Zeng and V. Kripesh, *Tensile deformation behavior of nano-sized Mo Particle reinforced SnAgCu solders, Mater.Sci. Eng. A* 528 (2011) 4166–4172.

2. **B.S.S.Chandra Rao**, K.Y Zeng and V. Kripesh, *Morphology and mechanical properties of intermetallic compounds in SnAgCu solder joints, Microelectron. Eng.*, 87 (2010) 2416-2422.

3. V.L.Niranjani, **B.S.S.Chandra Rao**, V.Singh, S.V.Kamat, *Influence of temperature and strain rate on tensile properties of single walled carbon nanotubes reinforced Sn-Ag-Cu lead free solder alloy composites, Mater.Sci. Eng. A*, 529 (2011) 257–264.

4. V.L. Niranjani, **B.S.S.Chandra Rao**, Rajdeep Sarkar, S.V. Kamat, *The influence of addition of nano-sized molybdenum and nickel particles on creep behaviour of Sn-Ag lead-free Solder, J. Alloys. Compound.*, Accepted Manuscript, Available online 27 July 2012.

5. **B.S.S.Chandra Rao,** K.Y Zeng and V. Kripesh, *Diffusion kinetics and Mechanical Properties of Ultra-fine Pitch Lead-free Microbump Solder Joints*

in 3D-Packaging Applications, The 61st IEEE proceedings, ECTC, (2011) 100-108.

6. **B.S.S.Chandra Rao,** K.Y Zeng and V. Kripesh, *Effects of solder volume on Interfacial IMC morphology and diffusion kinetics of micro-bump solder joints,* 12th IEEE proceedings in EPTC -2010; (2010) 423-428.

7. **B.S.S.Chandra Rao,** K.Y Zeng and V. Kripesh, *Determination of tensile properties of solder materials using Nanoindentation.* 12th IEEE proceedings in EPTC -2010 (2010) 309-314.

8. **B.S.S.Chandra Rao,** K.Y Zeng and V. Kripesh, *Fabrication and characterization of Sn/Cu microbump solder joints for 3D-TSV applications*, 12th International Conference on EMAP-2010. (2010) 297-303.

9. **B.S.S.Chandra Rao**, K.Y Zeng and V. Kripesh, *Development and characterization of composite solder materials,* 12th International Conference on EMAP-2010, (2010) 160-166.

10. **B.S.S.Chandra Rao,** K. Mohan Kumar, K.Y Zeng and V. Kripesh, *Effects of strain rate and temperature on tensile flow behaviour of SnAgCu nanocomposite solders*, EPTC-2010, 11th IEEE Proceedings, (2010) 272-277.

11. V.S. Rao, B.S.S.Chandra Rao, F.M.Daniel, L.P.S.Sharon, C.W.S.Kelvin, M. Kunieda, L. Shiguo, T.Furutani, T.Kariya, *Study on copper pillar flip chip interconnections*, EPTC-2012, 13th Proceedings, (2012), Submitted.

INTERNATIONAL CONFERENCE PRESENTATIONS

1. **B.S.S.Chandra Rao,** L.Y. Choo, V.Kripesh and K.Y.Zeng, *Mechanical Behaviour of Interconnect Materials at Device Scale*, ICMAT-2011, 26th June-1st July 2011, Singapore.

2. **B.S.S.Chandra Rao**, J. C. Tan, V.Kripesh and K.Y.Zeng, *Analysis of Indentation Creep Behaviour of Lead-free Solder Joints*, ICMAT-2011, 26th June-1st July 2011, Singapore.

3. **B.S.S.Chandra Rao,** V.N.Sekhar, V.Kripesh and K.Y.Zeng, *Influence of Solder Volume and Aging Conditions on Diffusion Kinetics and Mechanical Properties of IMCs Sn/Cu Microbump Solder Joints*, ICMAT-2011, 26th June-1st July 2011, Singapore.

4. **B.S.S.Chandra Rao,** K.Y Zeng and V. Kripesh, *Interfacial intermetallic morphology, diffusion kinetics and mechanical properties of Lead-free ultra-fine pitch μ-bump solder joints,* IUMRS-ICEM 2010, 22nd -27th August 2010, KINTEX, Seoul, South Korea.

5. **B.S.S.Chandra Rao,** K. Mohan Kumar, K.Y Zeng and V. Kripesh, *Effects of nano-sized molybdenum particles on the low-cycle fatigue behaviour of*

SnAgCu solder alloy, IUMRS-ICEM 2010, 22nd -27th August 2010, Seoul, South Korea.

6. **B.S.S.Chandra Rao,** K.Y Zeng and V. Kripesh, *Effect of surface-finishes on interfacial intermetallic layer growth kinetics and mechanical properties in lead free solder joints*, ICMAT-2009, 28th June-3rd July 2009, Singapore.

7. **B.S.S.Chandra Rao,** K.Y Zeng and V. Kripesh, *Effect of addition of nano-sized Ni and Mo particles on creep behaviour of SnAgCu composite solders*, ICMAT-2009, 28th June-3rd July 2009, Singapore.

8. V.N.Sekhar, and **B.S.S.Chandra Rao**, *Influence of Ta, and TaN barrier layer on the mechanical behavior of the Low-k thin-film stacks,* ICMAT-2011, 26th June-1st July 2011, Singapore.

9. V.L. Niranjani, **B.S.S. Chandra Rao** and S.V. Kamat, *The influence of addition of nano-sized molybdenum particles on creep behaviour of Sn-Ag solder alloy,* NMD-ATM-2011, Indian institute of metals, IIT Madras, Chennai, India.

ACKNOWLEDGEMENT

This thesis would have not completed without the contributions of many individuals, to whom I am deeply grateful. First I would like to thank my advisor Associate Professor Kaiyang Zeng. He has opened a new door for me to view the world through. His discussions have been enlightening and inspirational for me. His passion for science and technology has always invigorated me with a desire to explore further and fascinating topics. He has guided me throughout my time here at NUS, and I believe that my success directly linked to his guidance. I certainly hope that as I grow in years I will retain that which he has shown me.

I am also grateful to my co-advisor, Dr.Vaidyanathan Kripesh for his patient guidance, constant encouragement and invaluable suggestions for my research work. I have benefited significantly from his knowledge and experience. His confidence in my capabilities has given me tremendous opportunities to stimulate my research potential and improve my professional and communication skills. I highly respect his continual guidance and support.

I wish to express my gratitude to the IME Staff, Mr.Navas Khan, Mr. Vempati Srinivasa Rao, Mr. David Ho, Mr.Daniel Moses, Mr.Justin, Ms. Sandy, Mr.Ranjan and Mr. V.N Sekhar for their kind support for fabrication and metrology. I am grateful to the Material Science lab staff, Mr. Thomas Tan Bah Chee, Mr. Abdul Khalim Bin Abdul, Mr. Ng Hong Wei, Mr. Maung Aye Thein and Mr. Juraimi Bin Madon for their support and assistance for many experiments. I am also grateful for the help provided by the staff in in Applied Mechanics lab for tensile and fatigue testing (Mr. Chiam Tow Jong) and Workshop (Mr. Lam). I would like to thank Ms. Shen Lu of A*-STAR IMRE, Singapore for their help in getting access to Nano Indenter XP and conducting indentation tests. I would like to thank Ms. Nirajani and Dr. S.V.Kamat of Defence Metallurgical Research

Laboratory, Hyderabad, India for his help in getting access to microtensile and indentation testing facility.

I would like to thank all my colleagues in the Materials Science lab for their support and understanding. I would like to thank all my friends Dr.Srinath, Dr.Amit, Dr.Shashi, Dr.Samad, Dr.Satyam, and many others for their help and continuous support.

Finally, I wish to thank my family for their support and encouragement, and most of all, my wife, Reshma, for having courage, endurance and determination to pass through a virtual reality marriage for the first 3 years, and raising one lovely daughter (Hasika) in my virtual presence. No words are sufficient to express my gratitude for her support, without her abundant love, support and understanding, everything I have accomplished would have not possible.

SUMMARY

System-in-package (SiP) technology is commonly used for consumer electronic products because it has enough space efficiency to stack different functional dies in a single package, and lower manufacturing costs that may lead to the development of high-density interconnections with fine-pitch. However, the reduced interconnect size poses some mechanical reliability issues. The microstructural morphology of lead-free solder joints at fine-pitch is different from that of the bulk solders, which significantly influences the mechanical reliability of microelectronic packages. In fine-pitch microbump regime, complete conversion of solder into intermetallic (IMC) is possible due to insufficient amount of solder, and IMC change is also associated with the formation of Kirkendall voids within IMC layers. Therefore, understanding of the microstructure and its impacts on the mechanical behaviour of solder joints at device scale is a significant technological issue in advanced packaging applications.

The objective of this thesis is to understand the micromechanical behaviour of lead-free solders, and to that end the thesis covers everything from the conventional ASTM-standard techniques to the indentation characterization techniques. The tensile properties of SnAgCu and Mo-reinforced SnAgCu composite (hereafter referred to as composites) solders are investigated over a range of temperatures and strain rates, to obtain the multivariable thermo-mechanical models. These models can be used to predict the magnitude of the mechanical properties for given reliability conditions.

This study also extends to understanding the impact of solder specimen size (down to 500 μm) on the mechanical properties, using ultra-low load microtensile testing equipment. It was found that mechanical properties were reduced by 10–15% for pure Sn and Sn-5Pb solders, while for composite solders this variation was within experimental error. Nanoindentation experiments were conducted on these micron-sized tensile specimens at the equivalent strain rates (of the microtensile testing) to predict the tensile properties using analytical models. The yield strength was measured using the Tabor relationship, and microtensile test results were compared with nanoindentation analysis. As a further extension of this work, the nanoindentation technique was used to determine the mechanical properties of solder joints as small as 100μm.

Time-dependent deformation of the solder joints was studied using nanoindentation techniques. Indentation creep analysis based on Garofalo's model was used to obtain the creep parameters and was compared with other analytical models. Different types of indenter geometries (the Berkovich and Cylindrical punch) over a range of indentation loads were investigated to confirm the creep properties measured using the indentation method. The mechanical properties of interfacial IMCs in the solder joints, from the ball grid array to the microbump-joint regime, were determined using the nanoindentation technique. Taper-sectioning methodology effectively demonstrates the determination of interfacial IMC layer thicknesses as low as 500nm. Substrate effects due to underlying metallic/intermetallic layers on the measured elastic modulus, and the hardness of interfacial IMCs, were separated and eliminated using S-h (Stiffness-indentation depth) and S^2-P (Stiffness^2-Load) analysis.

LIST OF TABLES

LIST OF FIGURES

LIST OF SYMBOLS

K	Strain strengthening coefficient
n	Strain hardening exponent
T	Temperature
K_1	Strain strengthening constant
n_1	Strain hardening coefficient
b, c	Constant
σ	Strength
σ_Y	Yield strength
σu	Flow stress at 29%
σ_t	Tensile strength
H	Hardness
$\sigma_{0.02}$	Proof stress
m	Strain rate sensitivity
n	Stress exponent
t	Time
τ_1	Time constant1
τ_2	Time constant2
h	Indentation displacement
ζ	Indentation displacement rate
σ_i	Indentation stress
L_0	Gauge length
σ_{flow}	Flow stress
P	Indentation load
C	Kick’s Constant
v_{i}	Poisson ratio of indenter
E_i	Elastic modulus of indenter
v_m	Poisson ration of the materials
E_m	Elastic modulus of materials
A	Indenter contact area
S	Stiffness

α	Indenter Geometric constant
h_c	True contact indentation depth
θ	Strain hardening parameter
e	Engineering strain
ε	True strain
ε_o	Instantaneous strain
$\dot{\varepsilon}$	Strain rate
m	Mass of the indenter
C_f	Load frame compliance
K_f	Stiffness of indenter
K_s	Leaf spring stiffness
P_{os}	Oscillation load
Φ	Phase angle
$h(w)$	Oscillation displacement
c	Tabor conversion constant
C_1, C_2	Fitting constants in kick’s law
h_o	Perfect plastic depth
ε_p	the plastic strain
σ_i	Indentation stress
σ_t	equivalent tensile stress
BGA	Ball Grid Array
UBM	Under Bump Metallurgy
OSP	Organic Solder Preservative
VSB	Virgin Solder Balls
GND	Geometrically Necessary Dislocations
SSD	Statistically Stored Dislocation
ISE	Indentation Size Effect

Chapter 1: NTRODUCTION

1.1. Overview

Rapid advances in microelectronics challenge the current microelectronic packaging technology, as they increase the input/output (I/O) density while lowering the cost. In a microelectronic packaging system, the interconnects between the integrated circuit (IC) and printed circuit board (PCB) substrate play an increasingly vital role in the functionality and reliability of the system. Reduction in the interconnecting pitch to accommodate high-density interconnects (I/O) using lead-free solders is a challenging task, as the lead-free solders are somewhat inferior in terms of physical, electrical and mechanical performances, compared with the traditional Sn-Pb solder. This is because lead-free solders tend to have a higher interfacial intermetallic compound (IMC) growth rate due to their higher reflow temperatures. On the other hand, low reflow temperature solders reduce the electromigration resistance due to their high atomic diffusivity at normal operating temperatures.

Recent attempts have been made to use composite solder materials to mitigate excessive IMC growth rate with enhanced physical, mechanical, and electrical properties without affecting the baseline reflow characteristics of lead-free solders, to achieve improved reliability of the packages. However, composite solder bumping cannot extend beyond the level-2 (100 to 300 μm) interconnection due to the non-availability of flux materials and technological limitations. Alternatively, pure Sn and SnAg solders are being used for high-density level-1 (microbump) wafer-level interconnections due to their base-line advantages of electroplating and process compatibility with standard semiconductor process technology. In any advanced packaging system, different volumes of solder are inevitable with each level (i.e. level-1 to level 3) of interconnection, which leads to a change in mechanical performance of the same solder materials, from the die to the PCB substrate.

In most of the cases, reliability performance of fine-pitch solder joints is predicted based on the mechanical properties of bulk solder, even though mechanical behaviour of the solder joints is significantly different with the microbump joints [1, 2]. Therefore, determination of mechanical properties of the solder joints with reduction in the joint size is a critical issue for the reliability analysis of the advanced packages.

Elastic modulus and yield strength are the two main mechanical properties which are used to predict the thermo-mechanical reliability of packaging systems from the elastic-plastic deformation models. Hardness conversion into yield strength is widely practised for the solder joints as there is neither enough material for testing, nor standard tools available. When the tensile properties of solder joints are needed for accurate prediction of system-level reliability, the above reasons may not be acceptable because the mechanical properties of solder joints are size-dependent [3–5]. Yield strength and elastic modulus of materials are usually determined from the stress-strain curve if it adequately represents the complete tensile behaviour. This information is required for the defect assessment and finite element-calculations.

There are several techniques available to measure elastic modulus, but there is no standard technique available to measure the yield strength of materials at the device level. Most of the thermo-mechanical reliability properties of the level 3 (300 to 760µm) and level 2 solder interconnections are estimated from the bulk solder mechanical properties [6–12]. In reality, the mechanical properties of solder in the solder joints are significantly different from the bulk solders; therefore a large error may be included in the reliability analysis. This is due to the change in the microstructural morphologies by the processing conditions (e.g. reflow temperature, reflow time, solder volume, cooling rate etc.), which vary with reduction in the solder volume in the interconnection. Microstructural morphology strongly influences the mechanical behaviour of solder interconnects in the packages.

Reduction in the solder amount to accommodate high-density interconnection creates several mechanical-reliability issues. One fundamental issue is the formation of intermetallic joints, especially in the fine-pitch regime. IMCs are inherently brittle, besides its conversion from Sn-rich to Cu-rich IMC associated with *Kirkendall voids* within IMC interfaces. Brittle IMCs with voids lead to poor impact reliability (drop testing). Therefore, understanding the mechanical behaviour of solder in the solder joints and its impact on mechanical behaviour from the level-3 (Ball Grid array) to level-1 (microbump regime) is a serious technological issue with regard to the reliability of 3D packages.

1.2. Motivations

The motivations of this study are therefore summarized below:

1. To study the effects of solder volume on the mechanical behaviour of solder joints from the bulk to device level.
2. To develop new characterization methodologies for studying the mechanical behaviour of ultra-fine pitch solder joints.

1.3. Objectives

The overall objective of this study is to understand the mechanical behaviour of lead-free solder interconnects from the bulk to 5μm thicknesses that cover the bulk-to-device scale interconnection.

The more specific objectives are as follows:

1. Fabrication and mechanical characterization of bulk lead-free SnAgCu and SnAgCu-based composite solders, which include the following:
    1. Macro-mechanical characterization using ASTM standard testing.
    2. Micro-mechanical characterization using microtensile and nanoindentation techniques.
    3. Application of these analyses to the measurements to determine the device-scale property.
2. Mechanical behaviour of solder joints at device scale:
    1. Creep behaviour of solder joints.
    2. Mechanical properties of interfacial intermetallic layers from the BGA to ultra-fine-pitch microbump joints.
3. Morphology and diffusion kinetics of solder joints from the BGA to microbump regime.
    1. Composite solder joints
    2. Effect of Sn volume on diffusion kinetics
    3. Diffusion kinetics of SnAg microbump joints.

1.4. Outline of the Thesis

This thesis consists of nine (9) chapters, mainly focused on the micromechanical behaviour of solder joints. The fabrication, morphology and diffusion kinetics of lead-free solder joints from the BGA to microbump regime are discussed in the Appendix.

Chapter 1 discusses the introduction, motivation, objective and outline of the thesis. Chapter 2 discusses the background and provides a literature review of works relating to electronics packaging and different levels of interconnections and their mechanical reliability.

The tensile behaviour of bulk Sn3.8Ag0.7Cu (SCA387) and SAC387 composites are discussed in Chapter 3. Thermo-mechanical models based on the Hollomon model are developed in terms of flow stress, strain rate and temperatures, to predict the tensile property at given reliability-testing conditions. Chapter 4 discusses the impact of the size reduction (down to 500 μm) on micromechanical properties of bulk composite solder materials. Microtensile experiments with a video extensometer were conducted at 10^{-1} to 10^{-4} s^{-1} at 25, 50 and 75°C. Chapter 5 describes the indentation behaviour of the microtensile test specimens at similar strain-rate regimes (as of the bulk tensile testing) to predict the tensile properties. Tabor correlations were used to compare the yield strengths, which in turn were determined using nanoindentation and microtensile testing methods.

Chapter 6 focuses on the creep behaviour of solders, ranging from the bulk solder to 300 μm solder joints using the nanoindentation technique. Chapters 7 and 8 are totally devoted to the mechanical behaviour of interfacial IMCs in the solder joints from the BGA regime to ultra-fine-pitch microbump joints. The taper-mounting methodology effectively demonstrates the determination of the mechanical properties of interfacial IMC layers with thickness as low as 500nm. Substrate effects on mechanical properties of interfacial IMCs can be reduced using *S-h* (Stiffness-depth) and S^2-*P (Stiffness*^{2}*-Load)* analysis. Chapter 9 concludes with a summary of this thesis, with future recommendations.

The fabrication of wafer-level solder bumping from 300μm to the 20 μm microbump joints is discussed in Appendix A. The morphology and diffusion kinetics of IMC layers in the solder joints for level 2 and level 1interconnects are discussed in Appendix B and Appendix C, respectively.

Chapter 2: LITERATURE REVIEW

The evolution of microprocessors over the past 20 years and the forecast of its future show that microprocessor performance continues to fulfil Moore’s law [13].According to Moore’s law, the number of circuits on a silicon chip doubles every year (later revised to every 1.5 years), as shown in Fig. 2.1 [13]. The reality of this “law” can be observed as the technology has evolved from having 10 transistors per integrated circuit (IC) in the 1960s to 100 million transistors per IC today. If the trend of Moore’s law continues, 1 billion transistors will exist on a single IC within the next 5 years. Similarly, the number of input/output (I/O) interconnects for a given set of ICs will grow at the same rate. Rent’s law (based on observation) dictates this and predicts that I/O counts will reach 9000 by 2014 [13].

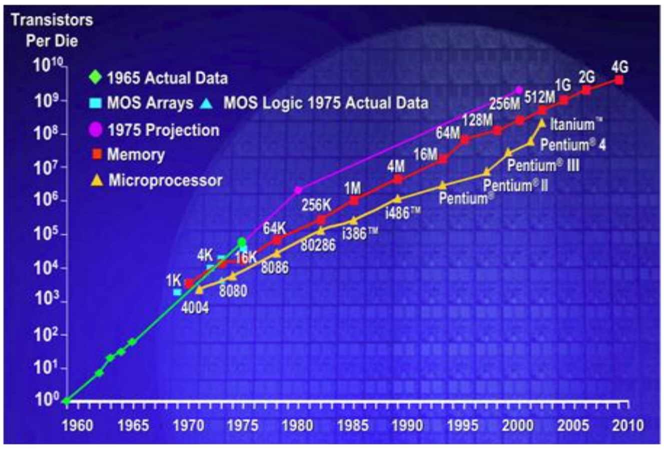

Figure 2-1: The graph shows the increase in the number of transistors in an Intel processor chip over the years, per Moore’s law [13].

2.1. Microelectronic Packaging Overview

Transistors form the “brain” of the ICs, which cannot function without proper packaging. Briefly speaking, the functions of IC packaging can be categorized as follows:

1. To provide an electrical path for off-chip links with high efficiency and signal accuracy.
2. To promote thermal dissipation among the transistors and interconnections.
3. To provide mechanical support to IC dies for safe handling and transfer.
4. To protect functional ICs from external contamination and harsh conditions.

It may be noted from the description above that microelectronic packaging necessitates strong technical knowledge and hybrid technologies in multi-disciplinary fields. Conventional IC packaging can be divided into different hierarchies in terms of its integration level, as shown in Fig. 2.2 [15]. The hierarchy of interconnect levels is shown in Table 2.1. The 0-level interconnects are the metal traces that connect each semiconductor module and make the ICs on the active side of a semiconductor chip. The first level interconnects are the connections between a semiconductor chip and the next-level substrate in a microelectronic package. On this level, the IC die is typically attached to a chip carrier, wire-bonded to a lead frame, and then encapsulated. On the second level, chips are bonded to a printed circuit board (PCB) by either through-hole or surface mount technology. Conductor traces over the PCB act as communication paths between different IC chips and other components. On the third level, many PCBs are mounted on a motherboard through sockets or connectors.

Miniaturization of portable and hand-held electronic devices has stimulated the demand for packages of even smaller size than the usual BGA and chip scale packages (CSP). A wafer-level package (WLP) is a chip-sized package, and it occupies when mounted onto a system-level board is as small as the size of the IC chip itself. Consequently, the WLP can be considered the primary IC-packaging option.

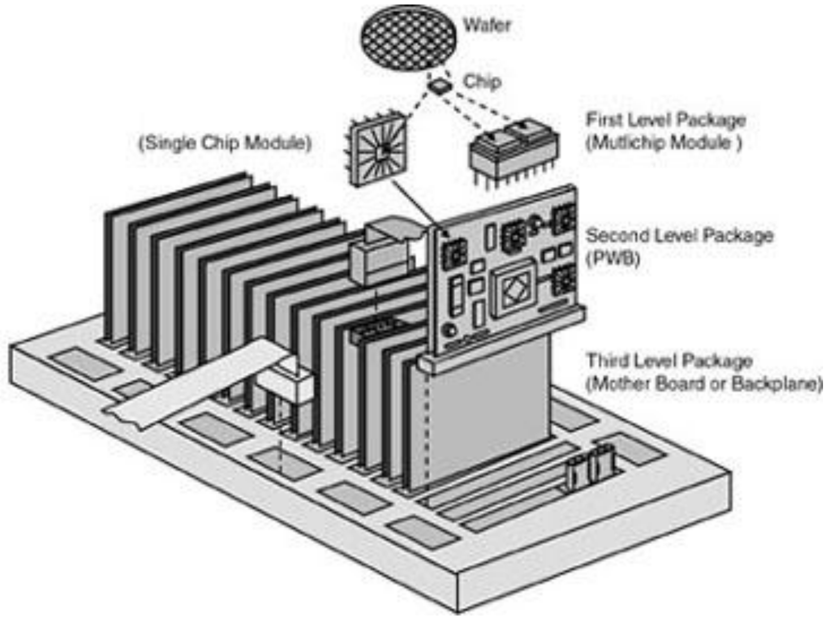

Figure 2-2: Hierarchy of Electronic Packaging [15].

Table 2.1: The Hierarchy of Interconnection Levels.

Level	Application	Interconnect size
Zero	Gate-to-gate interconnect on a monolithic silicon IC chip	<65nm
One	Packaging the IC chips onto chip carrier or next-level Substrate	10 to 50μm (Microbump Regime)
Two	Connecting the IC package to the printed circuit board (PCB)	100 to 300μm (BGA Regime)
Three	Connection between PCB and PCB to motherboard.	300 to 760μm

A good illustration of the size benefits of the WLP is shown in Fig 2.3 [16], which shows the relationship between the chip size and the assembled package for a 10mm square chip. It can be seen that a typical QFP (Quad Flat Pack) occupies an area of 900 mm^2, and a chip directly wire-bonded onto a PWB (Printed wiring board) with Chip-on-Board (COB) technology occupies 225mm^2. In contrast, the WLP occupies the same space as the bare die: 100 mm^2. This clearly offers the minimum size and weight for all products having size and/or weight constraints.

2.2 Wafer-level Packaging Technology

Wafer-level packaging (WLP) is the packaging technology for an IC at wafer-level. WLP is only a chip-scale package technology, because the resulting package is practically of the same size as the die. WLP has the potential to enable true integration of Chip fabrication in terms of packaging, tests, and burn-in at wafer-level in order to streamline the manufacturing process undergone by a device, from silicon to customer shipment.

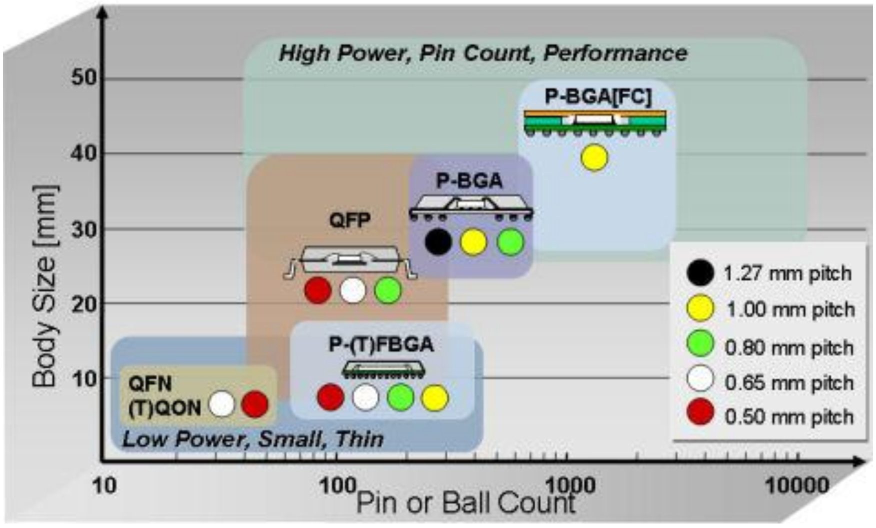

Figure 2-3: Wafer Level packaging as a future trend [16].

WLP consists of extending the wafer-fabrication processes to include device interconnection and device protection processes. Most of the other kinds of packaging techniques performing the wafer dicing first, and then put the original die in a plastic package and attach the solder bumps. On the other hand, WLP attaches the top and bottom outer layers of packaging, and the solder bumps, to the IC while still in the wafer, and only then performs the wafer dicing. The fabrication process of the solder interconnects uses a photolithography and electroplating (UV-LIGA) process, which is compatible with the wafer-level IC fabrication. Therefore, the production cost can be reduced substantially when the I/O number is high.

2.2.1. Conceptual Design

The IC industry demands a high-density I/O interconnection, with better performance coupled with lower cost and superior reliability. However, increased I/O density leads to a reduction in the pitch of interconnection, which creates a plethora of fabrication and reliability issues. One of issue is that the dispensing of underfill with a decreasing of the pitch becomes more and more difficult. Therefore, the adaptation of CTE (coefficient thermal expansion) mismatch materials without underfill would be one of the key challenges for improving the thermo-mechanical reliability. The Cu pillar interconnect, an underfill free off-chip interconnect, is known for superior reliability, which provides reliable electrical and compliant mechanical support between the wafer and die, or between dies [17].

2.2.2. Material Concerns for WLP

Lead-free solders are widely used for the bonding of the off-chip interconnect in WLP applications. The amount of solder in the joint has to be reduced with the increased density of I/O so that the solder bridging can be avoided. This limited amount of solder in the interconnects leads to the formation of an intermetallic solder joint, which severely affects the thermo-mechanical behaviour of the solder joint. To improve the reliability of packages at fine-pitch, the Cu pillar may be identified as the potential interconnect due to its inherently low resistivity and better electro-migration stability at high current densities. Therefore, the Cu pillar can be selected as a potential candidate to meet the above challenges [18]. In addition, the high-density Cu interconnect fabrication is flexible using photolithography and electroplating, which is considered the most cost-effective technology compared with other metal-deposition processes, and is also compatible with standard IC-fabrication technology.

2.2.3. Cu Pillar Interconnect

Cu pillar interconnects result in better reliability because of lower electrical parasitic losses, as the high aspect ratio obtained is due to the increased stand-off height of the copper column. Moreover, the Cu interconnect enjoys better wettability with the entire range of commercial lead-free solders, and the resultant solder-joint system shows better electromigration resistance [19].

2.3 Solder-joint Technology

In a microelectronic system, the solder interconnection between ICs or IC and substrate plays a vital role for functionality and reliability of the device. The layout of footprints in the package has changed gradually from the peripheral array to the area array, with an increase of I/O density keeping the solder the only component material to connect chips to their packaging [12, 20, 21]. Controlled-collapse chip connection (C4) solder joints are one of the solder-joining technologies primarily used at the level 1 and level 2 interconnections of the area-arrayed packages, such as the flip chip. A schematic picture of C4 solder-joint assembly is shown in Fig. 2.4 [22]. Re-distribution layer (RDL) and bond pads are deposited and patterned using sputter deposition and photo lithography. An under bump metallization (UBM) layer is electroplated over the Cu/Ti bond pads prior to solder deposition. The Ti layer serves as a barrier layer to prevent metal diffusion into the IC, and imparts better adherence to the underlying dielectric layers, whereas the Cu layer serves as a seed layer for Cu pillar electroplating.

Solder deposition over the Cu pillar is carried out by either electroplating or screen printing, depending on the pitch of the interconnection. A thermal-reflow process treatment is performed to join the dies (also called chips). Because of the lower stiffness of solders, solder deforms plastically to accommodate the CTE mismatch between the dies, or between the die and substrate. This plastic deformation may be accumulated with each thermal cycle, and eventually leads to failure. An effective way to improve the reliability of the package is to embed the interconnected package system in the under-fill to reduce the stresses/strains. However, the addition of the under-fill step for high-density interconnection in the package is a challenge with existing encapsulates, and is also very expensive.

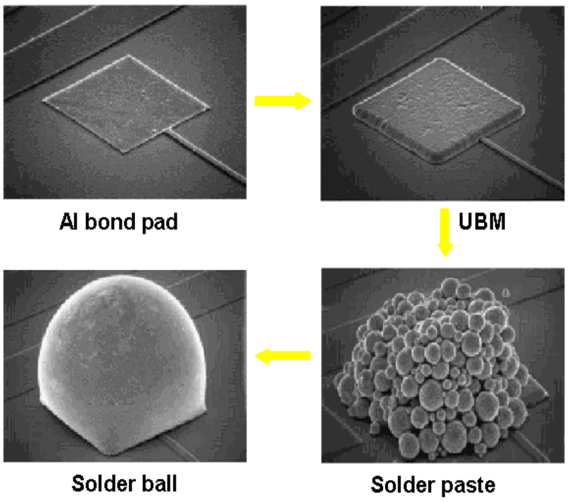

Figure 2-4: C4 solder-joint fabrication [22].

2.3.1 Challenges with Current Lead-free Interconnection.

Sn–Pb solders have long been used due to their advantages of low melting properties and excellent wetting properties. However, from an environmental point of view, lead-containing solders are harmful [24, 25]. In response to the concerns over replacing Pb in the electronic assemblies, numerous investigations have been on-going for the last few years to find an acceptable Pb-free solder for various electronic soldering applications [20, 22, 26–29]. Existing lead-free solders are distinctly inferior in the reliability performance because of their high reflow temperatures, which activate the diffusion process across the solder/UBM interface. This leads to the excessive growth of IMCs. Usually, IMC growth takes place at the expense of solder constituents and UBM; as the interfacial IMC grows, solder composition changes, which leads to serious effects on reliability [27, 30–33].

Moreover, IMC growth in the solder joints is also critical to advanced 3D packaging as solder joints undergo multiple reflows. The dissolution rate of UBM metal can be controlled by selecting an appropriate surface-finish, such as Electroless Nickel Immersion Gold (ENIG). Electroless Ni is widely used as a diffusion barrier layer on the Cu pad for flip-chip and BGA solder bumps [12, 21]. Characteristics of the electroless Ni, such as reduced stress, excellent corrosion resistance, uniform thickness and selective deposition, make the electroless Ni plating more suitable to be a diffusion barrier than that of electrodeposited Ni [34].

2.3.2. Composite Interconnects

To attain better reliability with standard lead-free solder materials, there is a trade-off in electrical and mechanical performance, and possibly cost. A combination of lead-free solder implementation, the constraints of requiring better electrical and thermo-mechanical performance, and the need to lower costs, has driven the development of solder toward a new paradigm. Composite solder can be tailored in such a way that reinforced particles stabilize or refine the microstructure of solder to reduce CTE mismatch. Composite solders reduce the magnitude of elastic-plastic deformation during the thermal cycles, and are therefore expected to increase the dimensional stability and thermo-mechanical reliability without affecting the melting point of the solder matrix. These composite solders can be fabricated by careful addition of reinforcement particles such as oxides, metallic particles, or IMCs, to the traditional solder alloys [35, 36]. Several efforts are made to improve the performance of the lead-bearing solders using the composite approach [37–40].

Mavoori et al. prepared composite solders by mixing 3 vol.% of 10nm sized Al_2O_3 powders and 3 vol.% of 5nm sized TiO_2 powders with 35µm-sized eutectic Sn-37Pb solder powder [37]. Nano-sized, non-reacting, non-coarsening oxide particles distributed uniformly in the solder after repeated plastic deformation. A reduction of three orders of magnitude in the steady-state creep rate was achieved by this method. Lin et al. studied the effects of nano-particles on the solidification kinetics and microstructure – a decrease in both the grain size and the eutectic lamellae spacing in Sn-Pb and Sn-Ag solders was found to improve the strength of composite solder [41]. The effects of particle additions on the microstructure, wettability and other mechanical properties of the composite solder have also been reported in other studies [42, 43]. Kumar et al. extensively studied Sn36Pb and SAC387 solder with the addition of a variety of nano-sized metallic particles, and proved the possible implementation of level 3 interconnection bumping applications [43].

2.3.3. Interfacial Intermetallic Compounds in Microbump Joints

As part of the packaging integration, it is inevitable that microbump joints in each component undergo a number of reflows in order to integrate the components with the die, or one die with another die. Therefore, reflow treatment in the 3D-package fabrication depends on the number of dies to be integrated with the 3D package. The dissolution rate of UBM metal into the solder bump during the reflow processes plays a vital role in the formation and growth of interfacial IMC, as the dissolution rate of UBM metal into the solder increases with the reflow time at a given reflow temperature. This reflow temperature activates the inter-diffusion of Cu and Sn across the interface, which promotes the growth of IMCs in the solder bumps. Figure 2.5 shows the full transformation of solder to the intermetallic after the 3rd reflow in the 3D-integration fabrication process. Figure 2.6 shows the entire conversion of solder to IMC under isothermal aging at 175^{o}C for 2 hours.

Several researches reported that the solder volume plays a vital role in the formation of Cu-Sn IMCs at the Cu/ solder interface. A change in the solder volume would produce different rates of UBM metal dissolution and lead to different intermetallic growth rates upon cooling [44–47]. This dissolved UBM metal in the solder reacts with the Sn and forms the interfacial IMCs. A limited volume of the solder in microbump joints may lead to the complete conversion of solder into IMCs during package integration [48]. Moreover, the non-availability of solder at the interface after the first reflow assists in the conversion of Si-rich IMC (Cu_6Sn_5) into Cu-rich IMC (Cu_3Sn). This Cu-rich IMC change invariably accompanies the changes in volume. This volume change leads to the formation of the Kirkendall voids within the IMCs at the interface (Fig. 2.7).

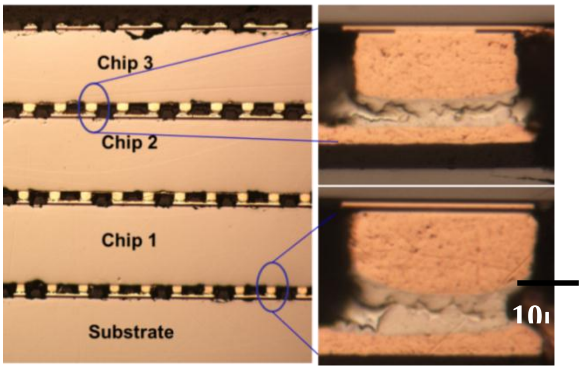

Figure 2-5: 3D integration shows complete conversion of IMC with 10μm Sn layer [48].

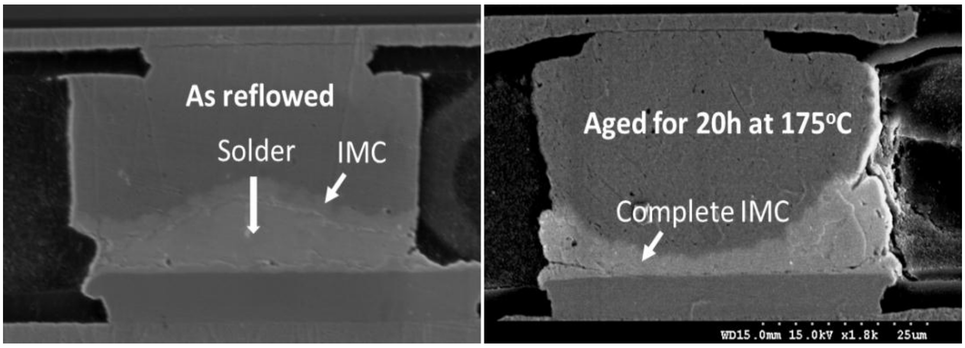

Figure 2-6: Complete conversion of solder into IMC during isothermal aging at normal bonding temperature (175^{o}C).

In general, IMCs are inherently brittle, and voids within IMCs are more susceptible to mechanical failures, which affect the integrity of the 3D packaging system [49]. Therefore, an understanding of the mechanical behaviour of interfacial IMCs in the microbump solder joints becomes a prominent technological issue in advanced 3D packaging applications.

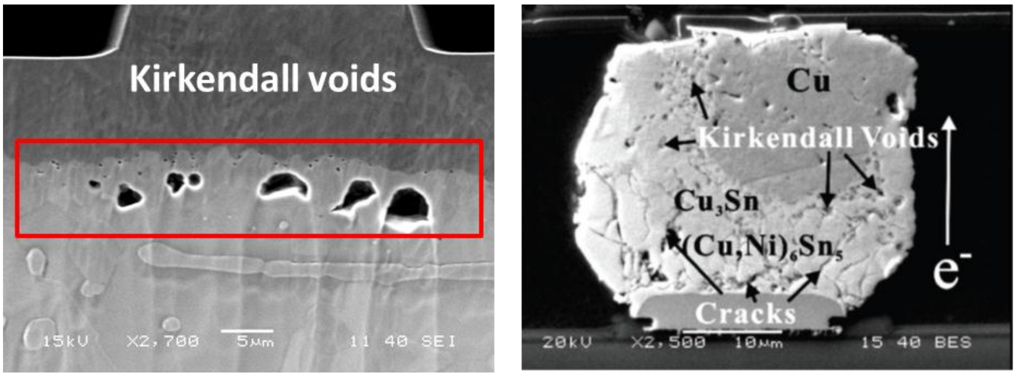

Figure 2-7: Effect of electromigration on IMC growth behaviour of microbump joints.

2.4. Mechanical Properties of Solder Joints

Mechanical properties are strongly influenced by solder-joint size and microstructural morphology, and therefore, knowledge of mechanical properties at the device level must be known prior to the design of the packaging. Wiese et al. suggested that the deformation resistance of Ag_3Sn and Cu_5Sn_6 is much higher than that of *β-Sn* matrix, as the Ag_3Sn and Cu_5Sn_6 phases formed hard particles in the relatively softer *β-Sn* matrix. These particles might slow down or even arrest mobile dislocations.

Chen et al. reported that in the Sn-Ag-Cu system, binary and ternary eutectic phases dispersed at the boundary of *β*-Sn dendrites, including some large Ag_3Sn and Cu_5Sn_6 intermetallic compounds [50]. This multi-phase microstructure of SnAgCu solder might lead to variations in the localized mechanical properties. The mechanical behaviour of solder joints is a complex function of time, temperature, stress, rate of loading and unloading, and distribution of these parameters. Elastic modulus, hardness, and creep parameters of the solder joints play a significant role in the reliability and design issues of microelectronic packages.

2.4.1. Elastic Modulus and Hardness

The reported elastic modulus of SnAgCu solder varies from about 10 to 50 GPa [51]. Huang et al. observed that these variations can be attributed to differences in the specimen microstructure (bulk or solder joint), the specimen geometry (shape, dimension ratio, etc.) and test conditions, [52] as indentation experiments are localized tests, and multiphase components are always subject to large variations in mechanical deformation resistance. When the indentation experiments were conducted on the dendrite (eutectic mixture of Cu_6Sn_5 and β−Sn), the resultant mechanical properties represent the composite properties of two phases. On the other hand, indentation experiments conducted on the β-Sn region were supposed to give lower hardness and modulus than that of the dendritic phase. However, occasionally the hardness of the β-Sn area is greater than that of the dendritic region because of the IMC or dendritic phase underneath the β-Sn phase. This might lead to some magnitude of variation in elastic modulus and hardness of the same solders [51, 52].

2.4.2. Time-dependent Behaviour

Morris et al. reported that solder in the package might eventually fail by creep-fatigue [53]. Creep behaviour is difficult to quantify because it depends on a number of variables. However, for many technological applications it is sufficient to consider the steady-state creep of a material. The steady-state creep rate is a function of temperature, applied stress and time. Creep deformation is usually associated with elevated temperatures for most of the engineering materials; however, creep deformation exists for lead-free solder at room temperature due to lower melting temperature (>0.6Tm). Wiese and Meusel reported that the Sn-37Pb and Sn-3.5Ag solders give almost identical room temperature creep rates at stresses above 15 MPa, while SnAgCu solder attains the same amount of creep at 40 MPa [54].

In general, every microelectronic component invariably experiences some magnitude of mismatch stress because of thermal loading during service. This mismatch stress, coupled with the device’s operating temperature, leads to creep (time-dependent deformation) loading conditions. Englemaier et al. reported that an increase in the holding time at the mismatch stress reduces the number of thermal cycles to failure [55]. It is also mentioned in our earlier report that addition of nano-sized Ni and Mo particles to the SAC387 solder reduces the CTE mismatch [56]. Therefore, composite solder joints are expected to be more resistant to failure during thermal cycling.

McDougall et al. studied the creep behaviour of composite solder joints with 20% (5-8μm) Cu_6Sn_5 reinforcements, using lap-shear testing on solder joints of one square-millimetre dimensions [57]. Villain et al. showed that the creep behaviour of the lead-free solder joints is dependent on the size of the solder joint [58]. Furthermore, indentation techniques were also used to probe the localized creep properties of solder materials [32]. Recently, a constant-load indentation creep method using a sharp indenter tip has attracted attention regarding the exploration of the creep properties of thin film materials. A sharp indenter tip with constant load reduces stresses and strain rates with the increasing contact area during the creep period. Therefore, constant-load creep experiments with a sharp indenter offer full creep deformation characteristics of materials from a single load.

2.4.3. Mechanical Behaviour of Interfacial IMCs

Determination of the mechanical properties of interfacial IMCs in microbump joints using nanoindentation is always a difficult issue, because of the influences of the UBM and solder bump on the indentation-measured properties. Most of the UBMs, such as Ni(V)/Au, Au/Sn, and Ni/Cu/Cu, that form the interfacial IMCs layer thicknesses are less than 2 to 2.5 μm. Therefore, characterization of the ultra-thin IMC layer in a microbump solder-joint system is a non-trivial task because the measured properties of the IMCs are influenced by the adjacent UBM or solder on either side of the interface. The ranges of the elastic modulus values of the Cu-Sn IMCs were reported to be 90~125 GPa and 115~145 GPa for Cu_6Sn_5 and Cu_3Sn, respectively [59–61].

The elastic modulus values of the Cu-Ni-Sn and Ni-Cu-Sn IMCs were reported to be 160~205 and 140~170 GPa respectively [1, 2, 61–65]. Discrepancies in the elastic modulus or hardness are due to the fabrication conditions for test specimens, such as temperature and period of aging, or thermal reflows. These conditions influence the interfacial IMC thickness and hence the morphological structure, which in turn alters the mechanical properties. There has been an attempt to determine the mechanical properties of only the IMC phase (Cu_6Sn_5), using the micro-pillar compression technique [66]. However, the measured properties are strongly affected by the texture and dimensions of the pillar.

Nanoindentation experiments with a continuous stiffness measurement (CSM) technique are commonly used for extraction of mechanical properties of multilayer thin films. This approach is developed primarily for homogeneous materials [67]. The indentation response for the IMC on UBM, or IMC on IMC, is a complex function of the elastic and plastic properties of intermetallic layers and the UBM. In order to determine ‘only-IMC’ properties, a commonly used rule-of-thumb is to limit the indentation depth to less than 10% of the IMC thickness [68]. This rule is experimentally feasible for IMC thicknesses greater than 5 to 10 µm, but this method is not suitable for thinner IMCs with uneven thicknesses. Therefore, an alternative method needs to be considered to separate the substrate effects.

Chapter 3: TENSILE PROPERTIES OF BULK LEAD-FREE SOLDERS

3.1. Introduction

In many of the advanced applications, microelectronic components will experience extreme temperature ranges, such as from −55 to 150^{o}C [55]. This induces severe strains due to the mismatch of the coefficient of thermal expansion (CTE) during the thermal cycles of the electronic device. Moreover, electronic components may also be subjected to impact conditions, such as drop test reliability of the microelectronic packages. Therefore, the mechanical properties of the lead-free solders over a wide range of strain rates must be known prior to the design testing of chips, to ensure better reliability of the device. In order to understand the mechanical behaviour of solder-joint systems, solders are usually tested under mechanical or thermal loading conditions to generate the stress-strain curves from which the mechanical properties, such as elastic modulus, yield strength and strain-hardening properties, can be determined.

There are many research works on the mechanical behaviour of Sn–Pb eutectic solder [56, 67, 69, 70] and lead-free solder alloys [71–73], but there are still many issues to be resolved with composite solder materials, such as those reinforced with nano-sized metal particles, since their mechanical properties strongly depend on the microstructure and reinforcements. It is necessary to examine the mechanical behaviour of newly-developed composite solders at different strain rates and temperatures to predict thermo-mechanical reliability performance.

This chapter therefore focuses on the effects of strain rate and temperature on the tensile and fatigue deformation characteristics of the composite solders (SnAgCu containing Mo nano-sized particles). Tensile testing conditions are represented by a range of strain rates from 10^{-5} to 10^{-1} s^{-1}, and selected testing temperatures range from 25 to 125^{o}C. These results are then analysed using Hollomon constitutive equations to describe the true stress-strain behaviour of the solder materials [74]. Parameters in Hollomon constitutive equations are used to investigate the underlying mechanisms and changes in microstructure that occur during deformation [75]. In general, the plastic-deformation behaviour of several metals and alloys can be described by the Hollomon relationship as follows:

$$\sigma = K\varepsilon_p^n \qquad (3.1)$$

where σ is stress, K and n are fitting constants commonly known as the strain-strengthening coefficient and strain-hardening exponent respectively, and ε_p is the plastic strain. It is well known that the magnitudes of K and n depend on material and deformation conditions. The n value is less than unity, and for metals it usually varies between 0.1 and 0.6, and increases with decreasing strength. K varies between $G/100$ and $G/1000$, where G is the shear modulus [58, 76].

The exponent n is an important parameter for two reasons. It signifies the strain-hardening characteristics of a material, i.e. the higher the value of n, the higher the rate at which the materials gets work harden. Usually, a material with a high value of n is preferred for processes which include the plastic deformation. The second reason is that it is a measure of the uniform strain of a material. In other words, a larger n value indicates more uniform plastic deformation before instability, since n equals the true strain (numerically) at the maximum ultimate tensile strength, which is the limiting value of the strain for uniform deformation. Therefore, accumulated plastic strains in solder joints over a period of time, either due to CTE mismatch or creep/fatigue/impact loads, should not exceed the amount of uniform true-strain, which is equivalent to the strain-hardening exponent. In this study, the empirical expressions for measuring dependence of the tensile parameters with respect to strain rate and temperature are analysed, and parametric constants in these empirical models are determined using linear regression analysis.

Most of the temperature-dependent tensile properties of the Sn-Pb solders have been presented as linear equations [14, 43, 77]. In other works, Shi et al. have investigated the effects of testing temperatures and strain rates on the tensile deformation behaviour of the Sn-Pb solders [70]. In recent years, some researchers have attempted to understand the plastic deformation characteristics of lead-free solder alloys with reference to strain rates and temperatures [19, 56, 67, 71, 73, 78, 79]. However, these studies mainly focused on yield strength and ultimate tensile strength, with a wide range of strain rates. However, there is no study about understanding the plastic deformation behaviour of SAC387 solder in terms of Hollomon parameters. It is not sufficient to use only temperature-dependent properties to understand the thermo-mechanical failures of the solder joints and the reliability of micropackages. Commercially-available solders might appear to have a nearly 50% reduction of tensile strength with increasing testing temperature (up to 120°C), or decreasing strain rate (~ from $10^{-1}s^{-1}$ to $10^{-5}s^{-1}$) [56, 71]. Since plastic deformation characteristics of solder materials are strongly dependent on strain rate and testing temperature, it is necessary to investigate their properties over a range of temperatures and strain rates.

There has been much research about composite solder materials; most of the work has been attempted on bulk solder composites with the addition of either metallic or non-metallic reinforcements. One of the methods is to incorporate the intermetallic (IMC) reinforcements by in-situ or mechanical mixing methods [19, 79]. With this method, the size of the IMC reinforcements was mostly in the range of 10–20μm. However, the size of the reinforcement particles may be coarsened during the manufacturing processes and the service, and this may ultimately reduce the effectiveness of the reinforcement. A different approach is to incorporate inert particulate reinforcements into the solder matrix [80–82]. One of the difficulties with this approach is the agglomeration of the particles and lack of coherency between the particles and solder matrix, which make them very inefficient in enhancing solder reliability. Another approach is the addition of small quantities of Cu or Ni to the lead-free solder to make in-situ composite solders [83, 84]. However, Ni and Cu particles are more tend to form Ni-Sn or Cu-Sn IMCs, and therefore IMC growth is inevitable during long-term thermal exposure in the service.

In this study, nano-sized Mo particle reinforcement is proposed as it is chemically inert with Sn at reflow temperature, and would thus be expected to act as a thermal stabilizer and improve the mechanical strength of the solder-joint system. Solders reinforced with nano-sized particles show an improvement in the service performance, in particular creep and thermo-mechanical fatigue resistance of solder joints. Nano-sized inert metallic reinforcement has been selected for the SAC387 solder, due to its effectiveness in improving the creep resistance by being distributed at the grain boundaries to limit grain-boundary sliding [43].

3.2. Materials and Experimental Methodology

3.2.1. Bulk Composite Solder Fabrication

The SAC387 solder powders were mixed with a selected percentage of nano-sized (15 to 30 nm) Mo particles (1.0 and 2.0 wt.%, respectively). The pre-weighed nano-sized Mo particles and solder powders were blended to achieve homogeneity using a V-cone blender operated at a speed of 50 rpm. The blended composite solder powders were then subjected to ball milling using a planetary mill (*Fristch and Restch*, Germany). The SAC solder powder and milled composite solder powders were consolidated at room temperature into cylindrical rods of 35mm diameter, under compaction pressures of 110 and 120 bars respectively. The size of the compacted samples was 35 mm in diameter and 50 mm in height. These cold-compacted solder bars were sintered at 170°C for three and a half hours in a pure argon atmosphere. These sintered compacts were finally extruded at room temperature with an extrusion ratio of 6:1. The compositions of the composite solders are listed in Table 3.1.

3.2.2. Tensile Testing

Dog-bone shape tensile specimens were fabricated from the 7mm extruded bar as shown in Fig 3.1, with a gauge diameter and length of 5 mm and 25 mm. Prior to the tensile testing, the specimens were annealed for 2h at 75°C to relieve the stresses introduced during the fabrication process. The tensile-testing experiments were conducted using a universal testing machine (INSTRON 8801) with a range of strain rates of 10^{-5} to $10^{-1}s^{-1}$ and temperatures of 25, 75 and 125°C. The temperature during testing was controlled to the accuracy of ± 1°C, and strains were measured via a clip gauge extensometer across the gauge length.

Table 3.1: List of solder materials studied in this work.

Material Code	Composition of the Solder
SAC387	Sn-3.8Ag-0.7Cu
SAC387+1Mo	Sn-3.8Ag-0.7Cu + 1.0 wt.% nano-sized Mo particles
SAC387+2Mo	Sn-3.8Ag-0.7Cu + 2.0 wt.% nano-sized Mo particles

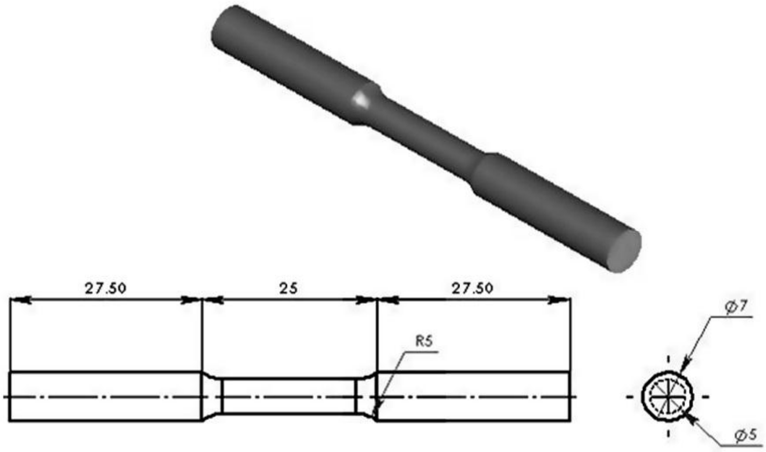

Figure 3-1: Schematic diagram showing the tensile specimen geometry.

3.2.4. Microstructure of Solders

The initial microstructure of all solder materials was studied in the wrought condition. The grain sizes of bulk solder and composite solder were measured using the linear intercept method. Figure 3.2 shows the grain size of the tensile test specimen. The average grain sizes of SAC387 and SAC387+1Mo were determined as 80±11 μm and 65±17μm, respectively. To reveal the morphologies of the fracture surfaces, the failed specimens were examined using a scanning electron microscope (FE-SEM).

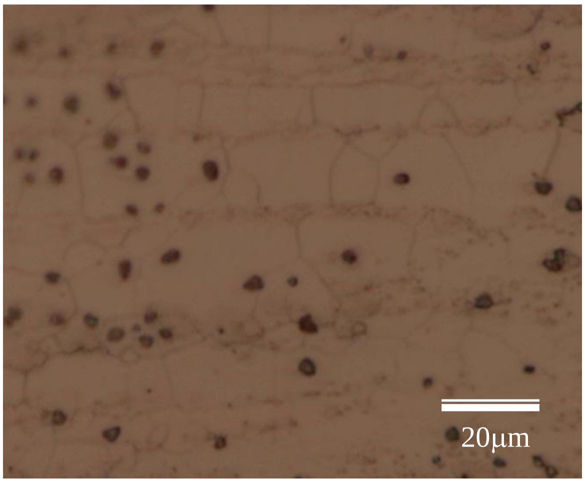

Figure 3-2: Optical Micrograph showing the grain structure of bulk SAC387+1Mo solder.

3.3. Analysis Methodology

The tensile flow properties of material have often been described with a simple state equation [80]:

$$\sigma = \sigma\left(\varepsilon,\ \dot{\varepsilon},\ T,\ E,\ H,\ R\right) \qquad (3.2)$$

where $\boldsymbol{\varepsilon, \dot{\varepsilon}, T, E, H, R}$ are the strain, strain rate, temperature, electric field, magnetic field and radiant field respectively. *E*, *H* and *R* are assumed to be constant at testing conditions. If tensile tests are conducted at a constant temperature and strain rate, the dependence of flow stress with the strain can be approximated as a constitutive equation (Eq. (3.1)) which describes the stress-strain relationship in the plastic region of the curve [74]. In this region, *K* and *n* are the strengthening coefficient and strain-hardening exponent, respectively. In Eq. (3.1) *K* and *n* are usually evaluated by plotting the stress–strain data on a double logarithmic plot and fitting a straight line at the higher strain levels. The slope of the line gives the value of *n* and the intercept at the stress axis gives the value of K. In an ideal case, these flow parameters should describe the shape of the true stress-strain curves completely.

Based on Eq. (3.2), the plastic state equation for tensile deformation carried out at constant temperature can be expressed as follows [85]:

$$\sigma = \sigma\left(\varepsilon,\ \dot{\varepsilon}\right) \qquad (3.3)$$

Differentiate Eq. (3.3)

$$d\ln\sigma = \left.\frac{d\ln\sigma}{d\ln\varepsilon}\right|_{\dot{\varepsilon}} d\ln\varepsilon + \left.\frac{d\ln\sigma}{d\ln\dot{\varepsilon}}\right|_{\varepsilon} d\ln\dot{\varepsilon} \qquad (3.4)$$

Transforming and rearranging terms in Eq. (3.4) gives

$$\frac{d\ln\sigma}{d\ln\varepsilon} = \left.\frac{d\ln\sigma}{d\ln\varepsilon}\right|_{\dot{\varepsilon}} + \left.\frac{d\ln\sigma}{d\ln\dot{\varepsilon}}\right|_{\varepsilon} \frac{d\ln\dot{\varepsilon}}{d\ln\varepsilon} \tag{3.5}$$

$\frac{d\ln\sigma}{d\ln\varepsilon}$ and $\frac{d\ln\sigma}{d\ln\dot{\varepsilon}}$ are generally defined as the strain-hardening exponent (*n*) and strain-rate sensitivity (*m*) of materials, respectively. Therefore, *n* and *m* of the solders can be determined using these equations. In the case of simultaneous variation of strain, strain rate and test temperature, the dependence of strain rate and temperature on tensile parameters can be described using Hollomon Eq. [29]:

$$\sigma = \sigma\left(\varepsilon,\ \dot{\varepsilon}, T\right) \tag{3.6}$$

$$\sigma = K\left(\dot{\varepsilon}, T\right)\varepsilon^{n(\dot{\varepsilon},T)} \tag{3.7}$$

where *K* and *n* are the strengthening coefficient and strain-hardening exponent, respectively. This power law was chosen for the sake of simplicity. For this reason, the strain-rate dependent constitutive equation can be defined by writing the strengthening coefficient (*K*) and strain-hardening exponent (*n*) as a function of temperature [86]:

$$K\left(\dot{\varepsilon}, T\right) = K_1(T)\dot{\varepsilon}^{a(T)} \tag{3.8}$$

Similarly,

$$n(T, \dot{\varepsilon}) = n_1(T)\dot{\varepsilon}^{b(T)} \tag{3.9}$$

The parameters in Eqs (3.8) and (3.9) are determined by fitting the experimental flow curves. In addition, a temperature-dependent constitutive equation can also be obtained by finding the temperature dependency of constants in Eqs (3.8) and (3.9), in accordance with the *Zener-Hollomon* parameter [83]. Using *K* and *n* values with strain rates at different temperatures, the constants of the dependence can be determined using linear regression analysis.

3.4. Results and Discussion

In general, the portion of true stress-strain curve from the onset of yielding to maximum load at a constant strain rate can be described empirically using Holloman’s relationship, as shown in Eq. (3.1). This equation is used to define the Holloman parameters through the linear regression analysis of the double logarithm of true stress-true strain data of the metallic materials [29]. The slope of the double logarithm of the true stress-true strain curve gives *n*, whereas the intercept at the true stress axis gives the strain-strengthening coefficient (*K*). The constants *n* and *K* are called Holloman parameters. In this work, the Holloman parameters of the SAC387 and its composite solders are determined with the method described above, over a range of strain rates (10^{-1} to $10^{-5}s^{-1}$) and with different testing temperatures (25, 75 and 125°C). The results are summarized in Table 3.2.

3.4.1. Yield Strength

The yield strengths of SAC387 and its composite solders are determined as a true-stress at 0.2% true-strain. Figure.3.3 shows the log-log plot of the yield strength versus the strain rates of SAC387 solders at different isothermal temperatures. It was found that the slope of the yield strength versus the strain-rate curve is a constant over a range of strain rates. Hence, it may be concluded that the dependence of the yield strength on the strain rate can be described using Eq. (3.10) at different temperatures, where $\sigma_{Y.S}$ is the yield strength, and *A* and *b* are constants (Table 3.2):

$$\sigma_{Y.S} = A\dot{\varepsilon}^{b} \tag{3.10}$$

It was found that the slopes of the double logarithmic plots of the yield strength versus strain rate increase slightly with an increase in the testing temperature from 25 to 75°C. In general, the parallel lines imply that sensitivity of yield strength to the strain rate is stable over a range of testing temperatures. However, it was found that the strain-rate dependence on the yield strength is stronger at higher temperatures for SAC387 solder. This is because rate-dependent plasticity mechanisms such as dislocation climb are more active at higher temperatures. Since the contribution of creep decreases with increasing strain rate, the yield strength is more or less insensitive to the temperature at higher strain rates.

At a lower strain rate and high temperature regime, the yield strength strongly depends on the strain rate, since the creep contribution increases with an increase in the testing temperature [41]. In addition, a high temperature can result in a recovery process for which the dislocation climb is diffusion-dependent. On the other hand, a low temperature contributes to strain hardening due to dislocation pile-ups. It may also be observed that for the composite solders (Table 3.2), the yield-strength exponent increases with an increasing testing temperature. Figure 3.4 shows the representative plot for yield strength versus testing temperature for SAC387 at different strain rates (10^{-1} to 10^{-5} s^{-1}).

It may also be noted that testing temperature has a crucial effect on the yield strength of solders at constant strain rates. It is understood that the yield strength decreases linearly with increasing temperature at all strain rates (Fig. 3.4). Therefore, linear empirical models can be used to fit the relationship of the yield strength and temperature of SAC387 and composites at constant strain rates. In this work, a statistical method incorporating bi-linear regression analysis is employed to identify the dependence of the yield strength with the temperature and strain rate for SAC387 and composite solders. This method is described below.

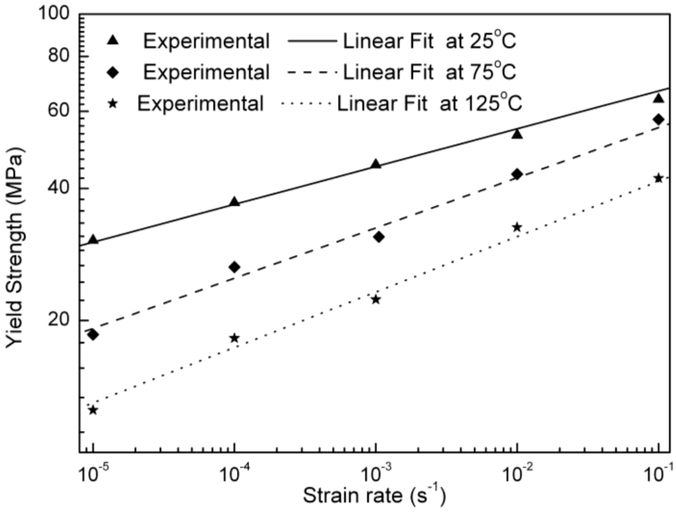

Figure 3-3: Effect of strain rates on yield strength of SAC387 solder at given temperatures.

Based on the experimental results, it can be assumed that yield strength is related to the temperature and strain rate by the following empirical relation [29]:

$$\sigma_{Y.S}(T,\dot{\varepsilon}) = \xi(T)\dot{\varepsilon}^{\psi(T)} \qquad (3.11)$$

where $\xi(T) = b_1T + b_2$, and $\psi(T) = b_3T + b_4$, and b_1, b_2, b_3 and b_4 are constants, T is temperature in ^{o}C, and $\dot{\varepsilon}$ is strain rate. The expressions $\xi(T) = b_1T + b_2$ and $\psi(T) = b_3T + b_4$ represent the temperature dependence of the yield-strength coefficient (*A*) and yield-strength exponent (*b*), respectively. Using linear regression analysis, the constants in Eq. (3.11) can be determined for SAC387 and composite solders, and the results are summarized in Table 3.4.

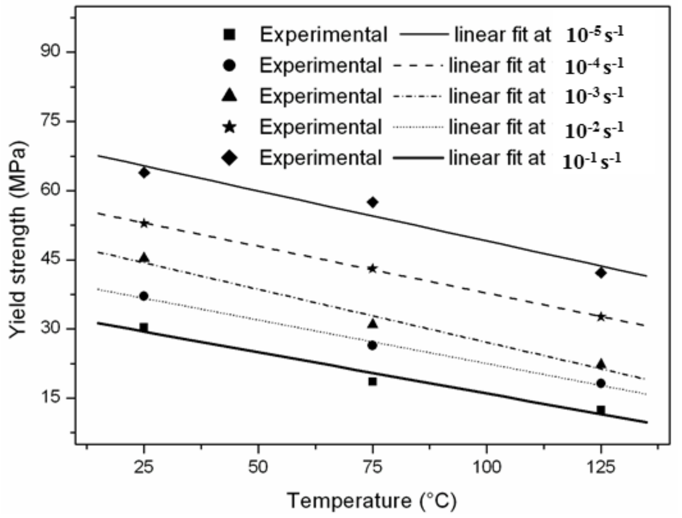

Figure 3-4: Effect of temperatures on yield strength of SAC387 at constant strain rate.

Table 3.2: Empirical equations for yield strength, in terms of strain rates and temperatures of SAC387 and composite solders.

Solders	$\sigma_{Y.S}(T,\dot{\varepsilon}) = (b_1T + b_2)\varepsilon^{(b_3T+b_4)}$			
	b_1	b_2	b_3	b_4
SAC387	-0.11	81	$1.4\text{x}10^{-4}$	0.049
SAC387+1Mo	-0.41	110	0	0.057
SAC387+2Mo	-0.19	124	$4\text{x}10^{-4}$	0.040
SAC387 [71]	-0.32	85.2	$5\text{x}10^{-5}$	0.057
SAC387 [88]	-0.13	67.5	$5.5\text{x}10^{-4}$	0.067

These results (Table 3.4) show that the strengthening coefficient more strongly depends on the testing temperature than on the strengthening exponent function. These findings are in agreement with existing literature [71, 88].

Table 3.3: Yield strength and Hollomon parameters of SAC387 and composite solders with strain rates at isothermal testing temperatures.

Solder	Temp (^oC)	Strain rate (s^{-1})	$\sigma_{Y.S} = A\dot{\varepsilon}^b$		$n = n_1\dot{\varepsilon}^{\phi}$		$K = k_1\dot{\varepsilon}^c$	
			A	b	n_1	ϕ	κ_1	c
SAC387	25	10^{-1} to 10^{-5}	77	0.79	0.14	0.12	164.7	0.14
	75	10^{-1} to 10^{-5}	74	0.11	0.13	0.14	129.3	0.15
	125	10^{-1} to 10^{-5}	57.7	0.13	0.11	0.16	102.9	0.16
SAC387+1Mo	25	10^{-1} to 10^{-5}	93.8	0.059	0.18	0.10	202.4	0.10
	75	10^{-1} to 10^{-5}	75.7	0.066	0.17	0.12	151.6	0.12
	125	10^{-1} to 10^{-5}	70.1	0.086	0.11	0.11	120.7	0.14
SAC387+2Mo	25	10^{-1} to 10^{-5}	102.5	0.044	0.15	0.09	228.5	0.09
	75	10^{-1} to 10^{-5}	88.1	0.060	0.12	0.10	166.9	0.10
	125	10^{-1} to 10^{-5}	75	0.071	0.14	0.12	143.2	0.13
SAC387 [27]	25	0.02 to 22.04	76.5	0.07				
	75	0.02 to 22.04	62.5	0.01				
	125	0.019 to 24.23	44.5	0.012				
Sn-3.5Ag [34]	-10	10^{-1} to 10^{-3}	50.1	0.026				
	22	10^{-1} to 10^{-3}	49.2	0.085				
	75	10^{-1} to 10^{-3}	40.1	0.073				
Sn-Ag3.5-Cu07 [63]	RT	10^{-1} to 10^{-3}	59.5	0.056				
Sn-Ag3.8-Cu07 [64]	RT	$5.6x10^{-2}$ -$5.6x10^{-4}$	63.8	0.081				
	75	$5.6x10^{-2}$ -$5.6x10^{-4}$	53.8	0.019				
	125	$5.6x10^{-2}$ -$5.6x10^{-4}$	51.7	0.014				

Table 3.4: Dependence of yield strength, strain hardening exponent and strain strengthening coefficient on strain rates and temperatures.

Solder materials	Strain rate (s^{-1})	Yield Strength ($\sigma_{Y.S}$) MPa			Strain hardening exponent (*n*)			Strain strengthening coefficient (*K*)		
		25°C	75°C	125°C	25°C	75°C	125°C	25°C	75°C	125°C
SAC387	10^{-5}	30.4	18.6	12.5	0.034	0.025	0.018	34.6	22.9	14.9
	10^{-4}	37.1	26.4	18.2	0.047	0.034	0.024	44.1	33.8	23.8
	10^{-3}	45.3	31.0	22.3	0.061	0.047	0.039	64.6	48.9	33.4
	10^{-2}	52.9	43.1	32.6	0.084	0.066	0.053	82.3	61.6	44.5
	10^{-1}	63.9	57.5	42.2	0.107	0.091	0.078	124.8	90.8	70.7
SAC387+1Mo	10^{-5}	47.1	33.1	24.7	0.056	0.042	0.031	57.1	39.9	23.3
	10^{-4}	58.3	44.5	32.3	0.073	0.056	0.041	82.1	52.1	32.4
	10^{-3}	61.7	48.6	42.3	0.087	0.071	0.052	97.7	64.6	46.6
	10^{-2}	75.3	55.1	43.8	0.119	0.101	0.068	124.5	88.9	62.6
	10^{-1}	79.8	63.8	57.5	0.146	0.128	0.087	164.4	116.1	86.9
SAC387+2Mo	10^{-5}	60.2	43.4	33.1	0.054	0.038	0.034	71.4	47.8	30.5
	10^{-4}	69.7	49.4	38.1	0.066	0.048	0.045	93.9	59.4	44.6
	10^{-3}	73.9	61.8	46.7	0.082	0.061	0.060	117.3	81.7	53.1
	10^{-2}	86.1	68.6	56.1	0.101	0.076	0.079	151.8	101.3	79.8
	10^{-1}	90.7	73.5	62.1	0.124	0.096	0.104	182.9	130.1	106.8
Sn-3.8Ag-0.7Cu [71]	$5.6x10^{-4}$	35.1	26	17.3						
	$5.6x10^{-3}$	40.8	33.5	24.9						
	$5.6x10^{-2}$	51.1	41.5	34						
Sn-3.8Ag-0.7Cu [87]	$4.2x10^{-5}$	30	---	21						
	$8.3x10^{-4}$	---	39	25						
Sn-3.8Ag-0.7Cu [88]	$4.2x10^{-5}$	31	21	13						
	$8.3x10^{-4}$	32	23	17						

--- Data not available for these conditions

3.4.2. Strain-hardening Exponent

Table 3.2 implies that *n* depends on the strain rate and testing temperatures. Log-log plots of *n* over a range of strain rates (10^{-1} to 10^{-5} s^{-1}) at different isothermal testing temperatures (25 to 125^{o}C) show constant slopes for SAC387 and composite solders (Fig. 3.5). Therefore, the variation of *n* versus the strain rates at a constant temperature can be written in an exponential expression, as given below [86]:

$$n = n_1 \dot{\varepsilon}^{\phi} \qquad (3.12)$$

where n_1 and ϕ are constants. The dependence of *n* on the strain rate at a given testing temperature can be determined using the linear curve fitting of Eq. (3.12) for the experimental data presented in Table 3.2 by using Eq. (3.12). The curve-fitting constants n_1 and ϕ are given in Table 3.2. Figure 3.5 shows that the *n* value increases with an increase in the strain rate, but *n* is relatively less sensitive to the changes of the testing temperature at all strain rates used in this work.

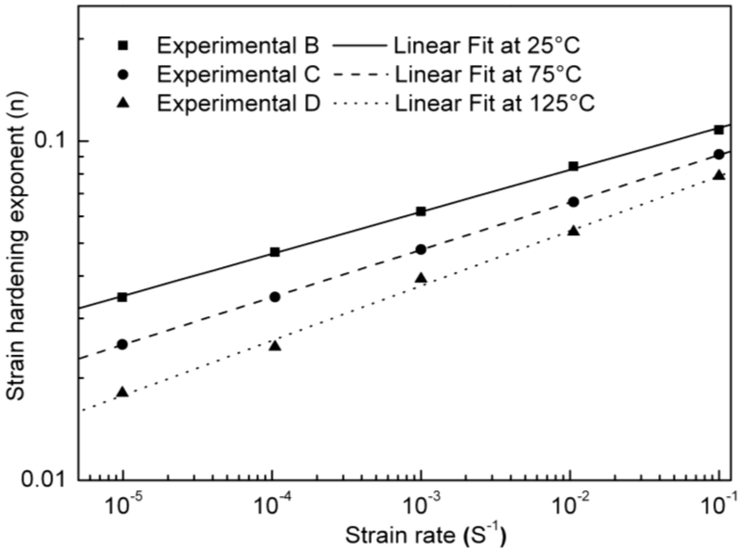

Figure 3-5: Effect of temperatures and strain rates on strain-hardening exponent for SAC387 solder at constant temperatures

The strain-hardening exponent (n) increases from 0.034 to 0.107 when the strain rate increases from 10^{-5} to 10^{-1} s^{-1} at 25°C (Table 3.3). Similar trends have been observed for 75 and 125°C testing temperatures in the same range of strain rates. On the other hand, n values for SAC387 solder decrease from 0.034 to 0.018 with an increase in the testing temperature (25 to 125°C) at a constant strain rate of $10^{-1}s^{-1}$. Similar trends may also be observed for composite solders. The overall dependence of the strain-hardening exponent, n, on both the temperatures and strain rates, can therefore be expressed in the general form of [86]:

$$n(T,\dot{\varepsilon}) = \beta(T)\dot{\varepsilon}^{\phi(T)} \qquad (3.13)$$

where $\beta(T) = a_1T + a_2$ and $\varphi(T) = a_3T + a_4$, where a_1, a_2, a_3 and a_4 are constants, T is temperature in °C, and $\dot{\varepsilon}$ is strain rate. These constants for SAC387 and composite solders are obtained using curve fitting of Eq. (3.13), and are summarized in Table 3.5.

Table 3.5 : Empirical equations for the strain-hardening and strain-strengthening coefficient, in terms of strain rates and temperatures of SAC387 and composite solders.

Solders	$n(T,\dot{\varepsilon}) = (a_1T + a_2)\varepsilon^{(a_3T+a_4)}$				$K(T,\dot{\varepsilon}) = (c_1T + c_2)\varepsilon^{(c_3T+c_4)}$			
	a_1	a_2	a_3	a_4	c_1	c_2	c_3	c_4
SAC387	-0.082	0.11	$4x10^{-4}$	0.09	-0.46	175.8	$2x10^{-5}$	0.12
SAC387+1Mo	-0.062	0.15	$2x10^{-5}$	0.05	-0.38	217.5	$9x10^{-5}$	0.10
SAC387+2Mo	-0.080	0.11	$7x10^{-5}$	0.06	-0.25	243.2	$9x10^{-5}$	0.06
SAC387 [71]	0	0.16	$3x10^{-4}$	0.064	-0.94	220.9	$4x10^{-4}$	0.130

The results in Table 3.5 show that both the strain-hardening coefficient and strain-strengthening coefficient are strongly dependent on the temperature, whereas the exponent functions are insensitive. The study of Long et al. shows that the n and K

functions are insensitive over the testing temperature [71]. This discrepancy might be due to differences between the starting microstructure and wrought microstructure used in this study, while reported literature deals with cast microstructure.

The variation of n with the weight percentage of the nano-sized Mo particle is shown in Fig. 3.6. It shows that the strain-hardening exponent, n, initially increases rapidly with an increase in the addition of nano-sized Mo particles up to 1 wt.%, but thereafter decreases with a further increase in the Mo particles content. The strain-hardening exponent for the SAC387 solder is found to be 0.062, which is in good agreement with its value in other literature [84].

The decreasing strain-hardening exponents of the composite solder at a higher percentage of Mo nano-particles may be due to several factors: (i) Incompatible plasticity between the SAC387 matrix and the Mo particles at more than 1% Mo; (ii) Higher dislocation density in the SAC387 matrix, which makes the matrix stronger; and (iii) The SAC387 matrix gets plastically constrained due to the presence of rigid Mo particles. It was reported that the dislocation density in the metal matrix increases with the weight fraction of nano-particles [89, 90]. The strain-hardening exponent largely depends on the microscopic flow behaviour of the alloy, which is strongly dependent on the dislocation density.

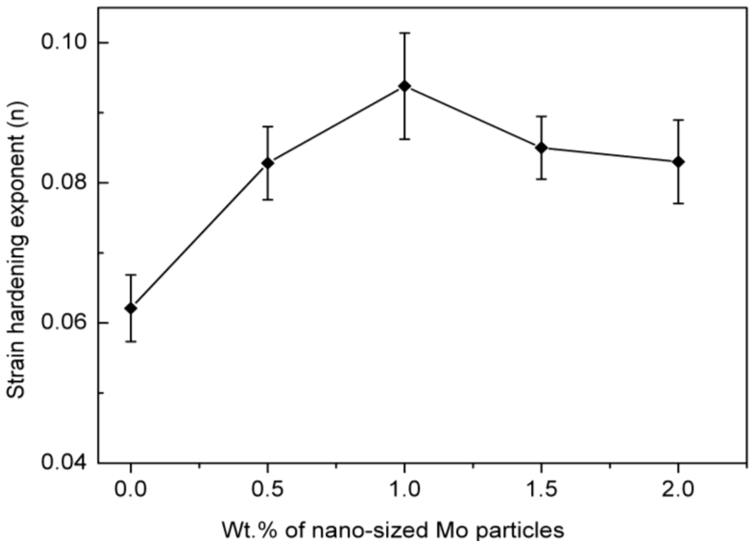

Figure 3-6: Effects of weight percentage of nano-sized Mo particles on strain-hardening exponent of SAC387 solder.

In the case of Mo-reinforced solders, the dislocation density in the matrix increases with the plastic deformation at a lower weight fraction of nano particles, which leads to an increase in the uniform strain before the deformation instability (or critical dislocation density) is reached. This increase in uniform strain may be directly attributed to a rise in the strain-hardening exponent. However, if the addition of Mo particles is more than 1%, dislocation density reaches critical density even at lower uniform strain, and results in a decrease in the strain-hardening exponent.

Franetovic et al. reported that the interactions between dislocations and nano-sized intermetallic particles, such as Cu_6Sn_5, Ni_3Sn_4 and Ag_3Sn, could also contribute to the strain-hardening effects [91]. During the deformation of the composite solder at room temperature, nano-sized Mo particles and grain boundaries often act as dislocation sources, and thus as the deformation progresses, the total dislocation densities in the solder matrix increase due to dislocation interactions with the nano-sized Mo particles. This phenomenon is more intense in composite solders than in the SAC387 solder with micron-sized intermetallic particles. This contributes to the higher strain-hardening exponent in nano-particle-reinforced composite solders. However, an increase in the nano-sized Mo particle content beyond 1 wt.% leads to a reduction in the strain-hardening exponent. The dislocation density at the matrix/particle interfaces may reach its critical value; this may lead to shear localization, and hence a reduction of the uniform true-strain [89].

On the other hand, for SAC387 solder, intermetallic particle size increases with temperature, and this leads to an increase in the inter-particle distance. According to the Orowan theory, the strength of an alloy or composite material is inversely proportional to the inter-particle distance. It is well known that the interfaces between particles act as obstacles for dislocation motion [91–93]. This interface area decreases with increasing particle size, and hence resistance to dislocation motion and dislocation sources will be reduced with increasing particle size. This results in weaker interactions between intermetallic particles and dislocations. In addition to this phenomenon, dislocations may easily surmount the obstacles by the climb mechanism, which is a diffusion-controlled process and is more dominant with an increase in the temperature. Therefore, effective dislocation accumulation in the solder matrix is very minimal, and hence the strain-hardening exponent tends to show a decreasing trend with increasing temperature (Fig. 3.5).

3.4.3. Strain-strengthening Coefficient

The variation of the strain-strengthening coefficient (K) with the strain rate for SAC387 and composite solders at isothermal testing temperatures (i.e. from 25 to 125ºC) can be fitted well with an exponential expression with the form of $K = k_1 \dot{\varepsilon}^c$, where K is the strain-strengthening coefficient and k_1 and c are constants. Figure 3.7 shows a double logarithmic plot of the strengthening coefficient versus the strain rate at different testing temperatures. The parametric curve-fitting values of k_1 and c are summarized in Table 3.5. Figure 3.7 shows that the strain-strengthening coefficient (*K)* increases with an increase in strain rate at a given temperature, but *K* decreases with an increase in the testing temperature for the solder materials at a given strain rate. The value of *K* decreases from 124.8MPa to 70.7MPa with an increase in the testing temperature from 25 to 125^0C at a strain rate of 10^{-1} s^{-1}. Similar reductions in the *K* value with the testing temperature have also been observed for composite solders (Table 3.2). The value of *K* increases from 34.6MPa to 124.8MPa, with the strain rate increments from 10^{-5} to 10^{-1} at 25^oC.

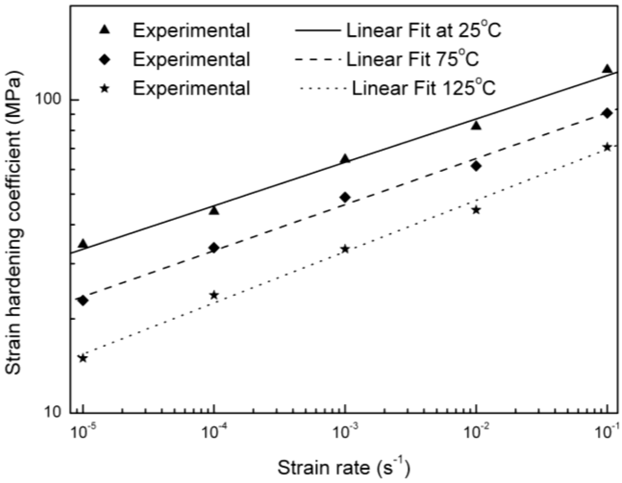

Figure 3-7: Effect of strain rates on strain-strengthening coefficient for SAC387 solder at constant temperatures.

The results in Table 3.3 indicate that the dependence of K on the strain rate is higher for composite solder compared with that of the SAC387 solder. It increases from 71.4MPa to 182.9MPa within the same strain-rate range (10^{-1} *to* 10^{-5} s^{-1}) and the same temperature. At a high temperature, the *K*-value's dependence on the strain rate is stronger for SAC387 solder compared with that for the composite solders. *K* is also less sensitive to the temperature changes at higher strain rates for SAC387 solder. These results are similar to the results obtained from the work by Long et al. on SAC387 solder at somewhat higher strain-rate ranges [71]. Furthermore, the empirical equations for the strain-strengthening coefficient in terms of strain rate and temperature can be expressed in the form:

$$K(T,\dot{\varepsilon}) = \theta(T)\dot{\varepsilon}^{\varphi(T)} \tag{3.14}$$

where $\theta(T) = c_1T + c_2$ and $\varphi(T) = c_3T + c_4$, with c_1, c_2, c_3 and c_4 being constants, T the temperature in ºC, and $\dot{\varepsilon}$ the strain rate. The parameters in Eq. (3.14) are determined using linear regression analysis for SAC387 and the composite solders, and the results are summarized in Table 3.5. It is clear that the K coefficient, $\theta(T)$, strongly depends on the temperature; whereas the K exponent, $\varphi(T)$, is less sensitive with the testing temperature. These results again agree with the results of the studies of Long et al. on the SAC 387 solder [71].

3.4.4. Fracture-surface Analysis

The fractography of SAC387 solder specimens tested at room temperature and a strain rate of 10^{-1} s^{-1} is shown in Fig. 3.8 (a). The fracture surface shows many dimples, which reveals that the fracture mode of the SAC387 solder is ductile at room temperature. At room temperature, work hardening is dominant and therefore results in dimples in the microstructure. Hence, the ductile fracture is a dominant fracture mode for SAC387 solder at room temperature. Higher strain rates during room-temperature tensile tests lead to ductile fracture with a much larger dimple size.

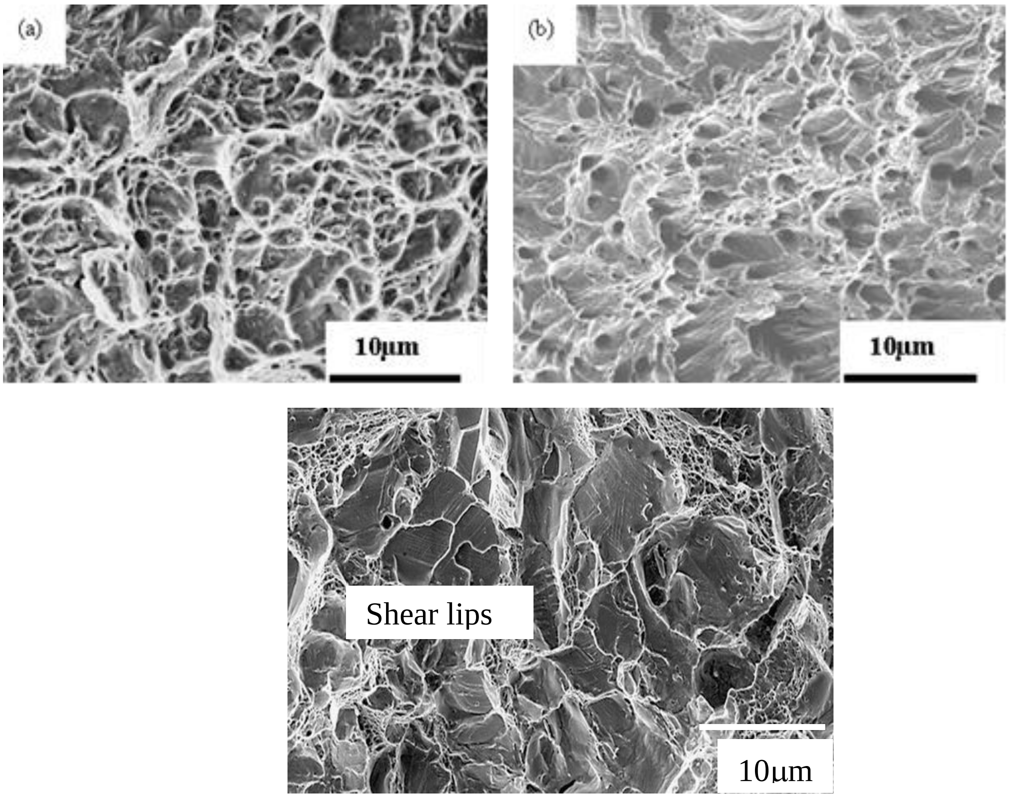

Figure 3-8: Scanning electron micrographs showing the tensile fracture surfaces of solder subjected to uniaxial tensile deformation at: (a) 10^{-1} s^{-1} at 25°C for SAC387, (b) 10^{-1} s^{-1} at 25°C for SAC387+2Mo (c) 10^{-1} s^{-1} at 25°C for SAC387+2Mo.

Overall, SAC387 solder fracture surfaces consist of large populations of macroscopic and microscopic voids; few of the voids undergo considerable growth and their coalescence results in shallow elongated dimples in the tensile load direction. Figure 3.8 (b) shows the fracture surface of the SAC387+1Mo specimen tested at 25^{o}C with a strain rate of 10^{-1} s^{-1}. The fracture surface consists of predominantly ductile fractures with micro-voids in the fracture regions. Figure 3.8 (c) shows the fracture surface of SAC387+2Mo; the fracture surface shows fibrous structure with shear lips. This indicates predominantly shear localization during tensile testing. These results strongly suggest that the addition of *Mo* nano-sized particles also changed the fracture mode during the failure under tensile stresses.

3.5. Summary

In this chapter, the tensile deformation behaviours of Sn3.8Ag0.7Cu and its composite solder materials were investigated with different strain rates ranging from 10^{-5} to $10^{-1}s^{-1}$ and temperatures of 25, 75 and 125°C. The following conclusions can be made based on the results:

1. General empirical expressions can be used to describe the dependence of the strain rates and temperatures on the yield strength (0.2% off set yield stress) and the Hollomon parameters in a wide range of strain rates and temperatures.
2. The yield strength and the Hollomon parameters increase substantially with an increasing strain rate.
3. It may be observed that the strain-hardening exponent increased with an increase in the strain rate for all of the composite solders investigated.
4. The strain-rate dependence on the strain-hardening exponent is stronger at higher temperatures for the base SAC387 solder, while it is weaker for composite solders reinforced with the nano-sized Mo particles.
5. The addition of the Mo nano-sized particles changed the fracture modes of the SAC387 solders.

Chapter 4: MICROTENSILE BEHAVIOUR OF LEAD-FREE SOLDERS

4.1. Introduction

SAC387 solder has been identified as one of the promising candidates for level 3 and level 2 solder-bumping applications [7, 12]. However for these solder joints, most of the thermo-mechanical reliability analyses are predicted using bulk solder mechanical properties. In reality, the mechanical properties of solder joints are most likely different from those of the bulk solders, and so reliability predictions of solder joints based on the bulk solders may not be accurate enough to be used. Possible reasons for this disparity have been discussed in Chapter 1.

The mechanical properties of bulk SAC387 solder have been extensively studied at room temperature and a particular strain rate [94, 95]. However, the effects of strain rates and temperatures on the mechanical properties have received only limited attention [96–98]. In most applications, solder joints simultaneously experience a range of strain rates and temperatures, and therefore it is necessary to understand how the mechanical properties of solders are affected by the strain rate and temperature. Chapter 3 extensively studied the effects of strain rates and temperatures on the tensile properties of SAC387 solder and composites. However, mechanical properties of bulk solders may not be used to predict the reliability analysis at the level 3 solder joints due to possible size effects. To understand the effects of solder volume/specimen gauge thickness on tensile properties, microtensile samples were fabricated using solder volumes of 5 to 10% in the standard size of an ASTM standard test specimen.

This chapter focuses on the microtensile characterization of wrought SAC387 solder and SAC387-based composites at 500μm gauge thickness. The fabrication procedure for nano-sized Mo particle-reinforced SAC387 solder has been described in

Chapter 3. As-cast pure Sn, high-temperature Sn-5Pb solder and SAC387 solders are also selected as a reference solders to compare the thickness effect with their bulk counterpart.

To further understand microtensile behaviour, SWCNT (Single walled carbon nano tubes) reinforced SAC387 has been selected and compared with reinforced Mo-SAC composites over a range of strain rates and temperatures at the same 500μm gauge thickness. The bulk tensile properties of the SWCNT-reinforced SAC387 solder have been investigated at room temperature and up to 1 wt.% of SWCNT [99]. There was a significant improvement in strength for the SWCNT-reinforced SAC alloy up to 0.1 wt.% SWCNT addition, although there was a marginal reduction in % elongation. In this work, SWCNT reinforcement up to 0.1% has been selected to study the tensile behaviour over a range of strain rates and temperatures. The tensile properties of Mo-reinforced SAC387 solder are limited to room temperature due to the limitations of the test facility.

4.2. Experimental Methodology

4.2.1. Materials Preparation

Bulk solder, including Sn, Sn5%Pb and SnAgCu solders, was melted at 300^{o}C for 2h and subsequently cooled to 265^{o}C (typical lead-free reflow temperature) at a rate of 2^{o}C/minute in the rectangular stainless-steel moulds. At 265^{o}C, liquid solder with stainless-steel moulds was allowed to cool in the furnace till it reached room temperature. N_2 was used as cooling medium to control the cooling rate, which was 25^{o}C per minute. Another set of samples of SAC387 solder and nano-sized Mo-particle/CNT-reinforced composite solders was fabricated through the powder metallurgy route (discussed in Section 3.2.1) and subsequently extruded to a 7mm bar. Composite solder strips of 500μm were cold rolled from the 7mm extruded bar of 30mm length in 6 passes [100].

Flat tensile specimens with a gauge length of 3.75mm, width of 1mm and thickness of 0.2, 0.5 and 1mm were EDM-cut from the rolled strips of composite solder (Mo-particle or SWCNT-reinforced SAC387), while the microtensile testing specimens of as-cast Sn, Sn5Pb and SAC387 solder were EDM-cut from the furnace-cooled 6x50x50mm bulk solder blocks. These blocks were pre-shaped, as shown in Fig. 4.1 (a), and subsequently sliced using EDM wire cut to microtensile test specimens. All fabricated test specimens were aged for 1hr at 75^{o}C to stabilize the microstructure and relieve the fabrication-induced stresses.

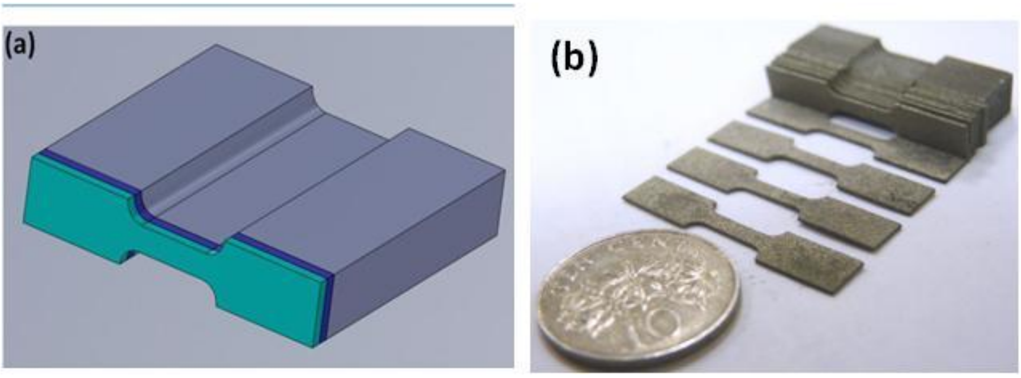

Figure 4-1: (a) Schematic representation of the fabrication process, and (b) fabricated microtensile specimens.

4.2.1. Microtensile Testing

Microtensile experiments were conducted using microtensile testers, such as those for high temperature (*Walter + Bai Ag* make) and room temperature (*MTS Tytron 250*), using a load cell of 500 N. Figure 4.2 shows the typical microtensile experimental set-up for room-temperature solder-tensile characterization. For SWCNT-reinforced SAC387 solder, the microtensile experiments were conducted over a range of temperatures (25 to 75^{o}C) with three different strain rates (5×10^{-2} s^{-1}, 5×10^{-3} s^{-1} and 5×10^{-4} s^{-1}) at each temperature. Mo particle-reinforced SAC387 solder and other as-casted reference solders, the microtensile tests were conducted only at room temperature; all samples were tested to tensile failure. A differential scanning calorimeter (Perkin Elmer DSC 7) was used to study the melting characteristics of the SAC387 and composite solders. These samples were heated to 300ºC at a heating rate of 10ºC/min in an inert atmosphere, and the thermograms were recorded. X-ray diffraction (XRD Philips) was also used to identify the various phases present. The microstructural characterization was done using a scanning electron microscope (SEM).

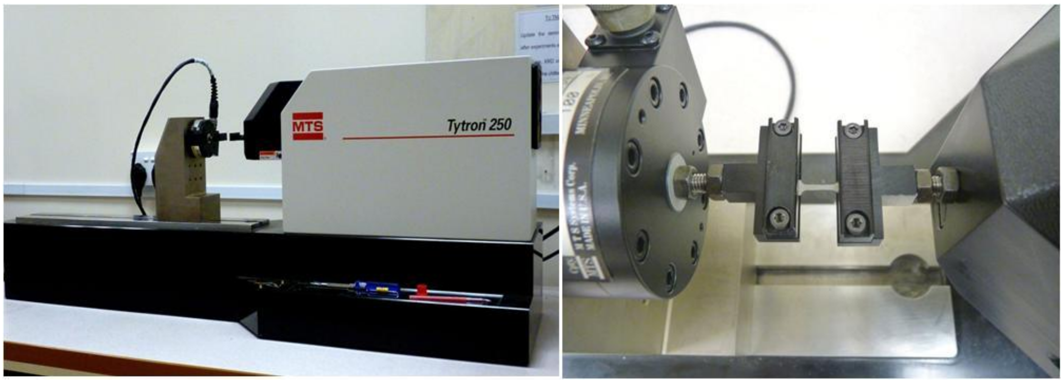

Figure 4-2: Microtensile experimental set up for room-temperature microtensile testing.

4.2.2. Design and Fabrication of the Microtensile Test Specimen

The dimensions of the microtensile test specimen were designed based on the formula by Junghans et al. [97]:

$$L_o = 5.65\sqrt{A_o} \tag{4.1}$$

where L_o = gauge Length and A_o = cross-sectional area of gauge length portion. The microtensile test specimens were fabricated using EDM wire cutting, since this process offers freedom of geometry, high accuracy and fast turnaround [101].

Solid Works FE stress analyses were performed to ensure that the elongation mesh was confined within the gauge length. Figure 4.3 (a) shows the schematic microtensile test specimen dimensions, while Fig. 4.3 (b) and (c) shows the stress pattern distributions. Specimens with a uniform gauge thickness of 200 μm, 500 μm and 1000 μm were used for the SAC387 solder, while for the rest of the solders only specimens with a 500 μm gauge thickness were fabricated.

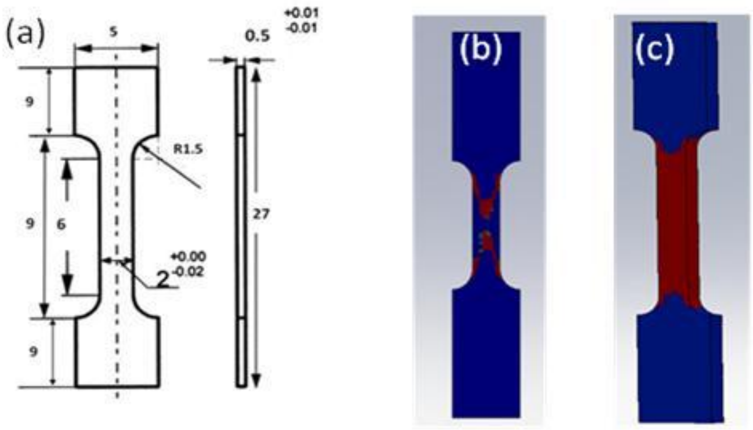

Figure 4-3: (a) Schematic diagram of microtensile test specimen (b & c) stress pattern in the test specimen, with increase in the load.

4.3. Results and Discussion

4.3.1. Microstructure

Fig. 4.4 (a & b) shows the microstructures of the SAC387 solder and the SAC387-0.1wt.% CNT composite, respectively. The SAC387 solder shows the fine Ag_3Sn and Cu_6Sn_5 intermetallic particles interspersed in equiaxed grains of Sn matrix, which was also confirmed by the XRD results shown in Fig. 4.4 (c).

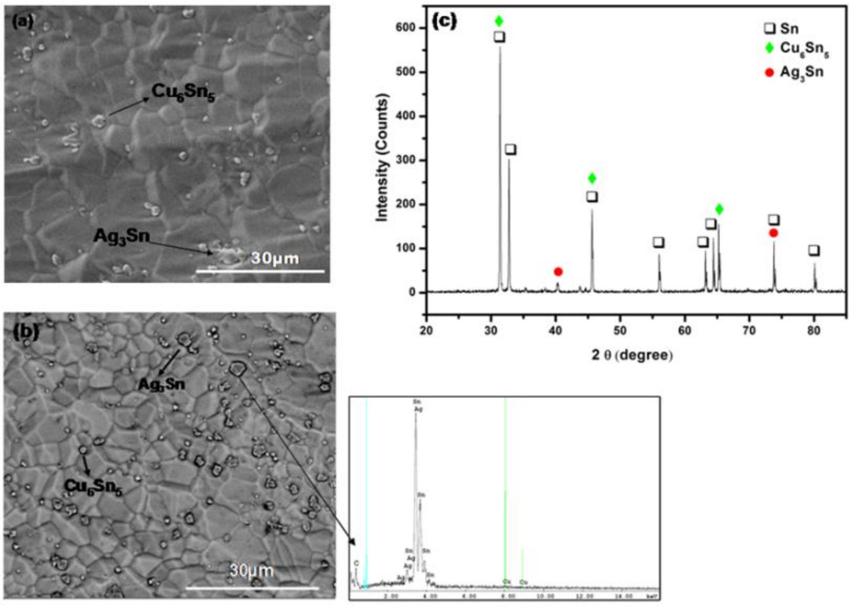

Figure 4-4: SEM micrograph of (a) SAC387 (b) SAC387+0.1%CNT (c) X-Ray diffractogram of SAC387 solder (d) EDS analysis of the layer adjacent to the Ag3Sn Phase.

Figure 4.5 shows the microstructure of as-cast Sn, Sn5Pb and SAC387 solder, while Fig.4.5 (d) shows the wrought structure of Mo-reinforced SAC solder. The grain sizes of furnace-cooled Sn and SAC387 solders are 350 µm and 85 µm, respectively. The SAC387 and Mo-reinforced wrought SAC387 solder are about 10 to 15 µm and 25 µm, respectively (Figure 3.2).

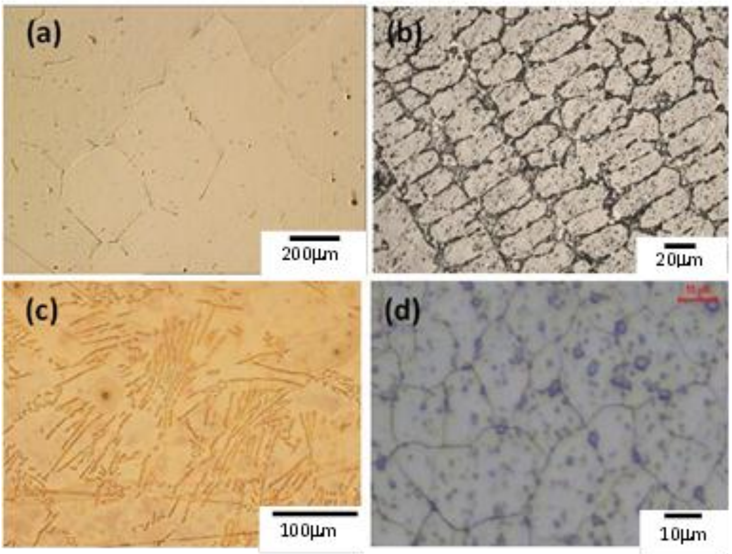

Figure 4-5: Initial microstructure of (a) pure Sn (b) Sn-5%Pb solder (c) furnace-cooled SAC387 (d) SAC387+1%Mo composite solder.

4.3.2. Differential Scanning Calorimetry (DSC)

The DSC trace from the base SAC387 solder is shown in Fig. 4.6 (a). It exhibits a well-defined endothermic peak. Based on this, the onset (solidus) and peak (liquidus) temperatures of melting for the SAC387 solder were determined to be 216.4ºC and 220.0ºC, respectively. Figures 4.6 (b & c) shows the DSC traces for the SAC387+0.05 wt.% SWCNT and SAC+0.1 wt.% SWCNT composites, respectively. It was then determined from these plots that the onset and peak temperatures for the SAC387+0.05 wt.% SWCNT composite were 216.2 and 219.0 ºC, respectively, while for the SAC387+0.1 wt.% SWCNT composite, these temperatures were 215.8 and 218.4ºC, respectively.

The microstructure of the SAC387-0.1 wt.% SWCNT shows the finer grain size and uniformly-distributed fine IMC particles in the composite. SWCNTs are found to be distributed at the edges of the Ag_3Sn particles, which can be seen by the change in contrast in the SEM micrograph and are also confirmed by the EDS analysis shown in the inset of Fig. 4.4 (d). This is similar to the observation of Kumar et al work on bulk SWCNT-reinforced solder [99]. It was also observed that both the onset and peak melting temperatures decreased with an increase in the wt.% of SWCNT, and these results are consistent with what is reported in the literature [99]. This may be attributed to an increase in the surface instability because of the higher surface free energy, due to the addition of SWCNT. Moreover, the presence of SWCNT significantly alters the grain boundary/interfacial characteristics of composites [102–104].

It can be seen (Fig. 4.4) that the addition of SWCNT or Mo particles results in finer grain sizes and also retards the grain growth, and hence the grain boundary free energy and interfacial free energy are not completely consumed for the grain growth. Because of the restricted grain growth, the grain boundary free energy values in the CNT-reinforced solder composites are higher than that in the matrix or base alloy, and this aids the melting process and leads to reduction in both the onset and peak temperatures of the composites.

In the case of Mo-reinforced SAC solder (Fig. 4.7), the melting temperatures increased by 5oC from the equilibrium melting temperature of SAC387 solder. Although there is only a slight increment in the melting temperature, the existing reflow process line for lead-free solder can be used for composite solders without any change in any process configuration. A slight rise in temperature, coupled with reinforcing strengthening of the composite solders, demonstrated the better thermo-mechanical properties , which is about 30 to 40% higher than that of the base alloy [105].

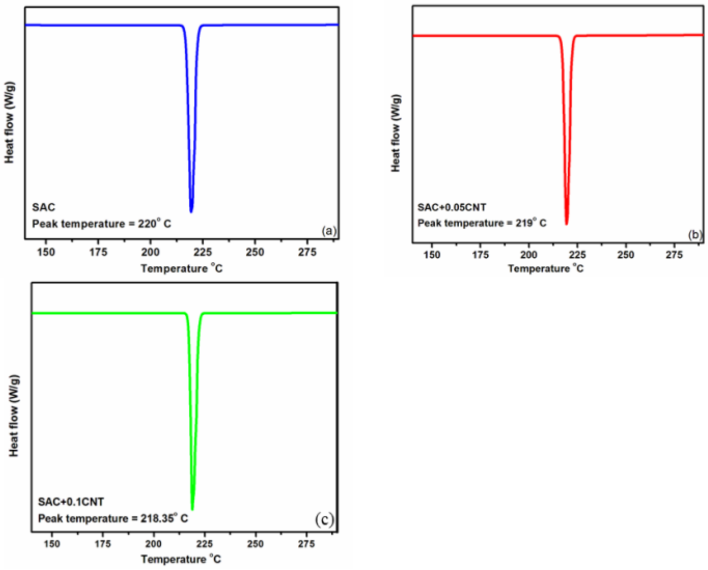

Fig. 2. DSC scans of (a) SAC387 base alloy, (b) SAC387+0.05%CNT and (c) SAC387+0.1%CNT

Figure 4-6: DSC scans of (a) SAC387 solder (b) SAC387+0.05% SWCNT and (c) SAC387+0.1% SWCNT.

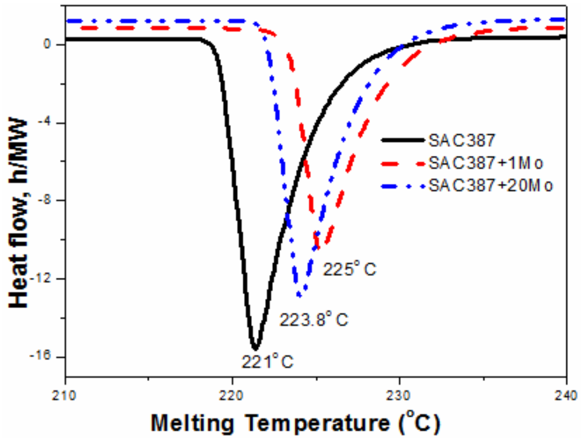

Figure 4-7: DSC scans of (a) SAC387 solder (b) SAC387+1% Mo solder and (c) SAC387+1% Mo solder.

4.3.3. Microtensile Properties of SAC 387 and SWCNT Composites

The representative stress-strain curves at room temperature and at a strain rate of 5×10^{-2} s^{-1} for SAC387 solder and composites containing 0.05 and 0.1 wt.% SWCNT are shown in Fig. 4.8. Similarly, representative stress-strain curves at different temperatures for a given strain rate (5×10^{-4} s^{-1}), and stress-strain curves for different strain rates at a given temperature for SAC387 solder and one of the composites, are shown in Figs 4.9 and 4.10, respectively. The nature of the stress-strain curves reflects the relative dominance of work-hardening and dynamic recovery processes during the deformation. At higher temperatures and lower strain rates the dynamic recovery is more dominant, whereas at lower temperatures and higher strain rates the work-hardening processes are more dominant.

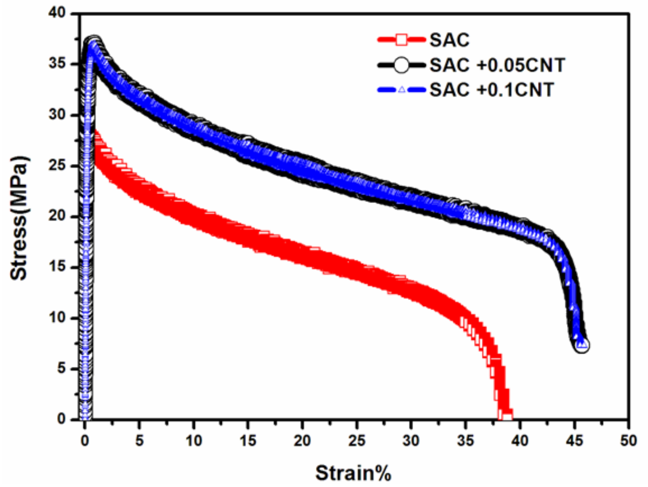

Figure 4-8: Stress-strain plots at room temperature and strain rate of $5x10^{-4}s^{-1}$ for SAC387 solder with 0.05SWCNT variation.

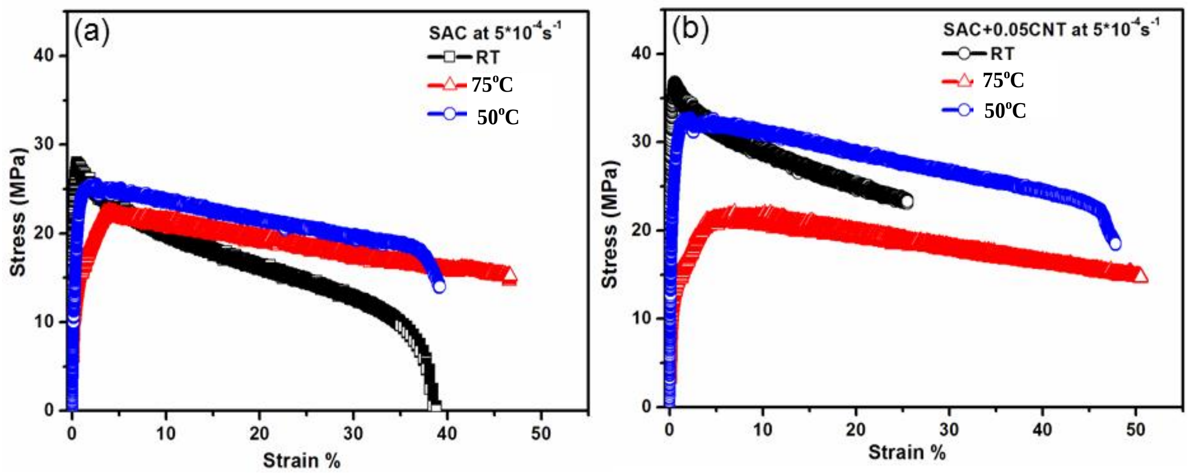

Figure 4-9: Stress strain plots at constant strain rate of $5x10^{-4}s^{-1}$ for different temperatures for (a) SAC387 solder (b) SAC387 with 0.05 wt.% SWCNT.

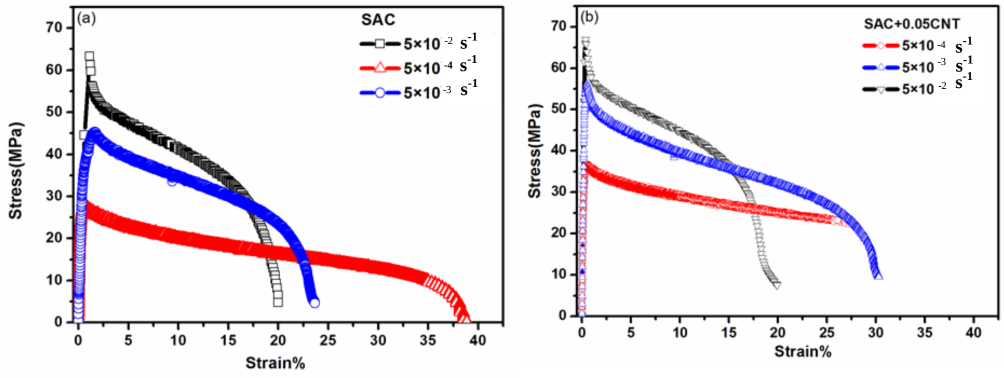

Figure 4-10: Stress strain plots at room temperature for different strain rate for (a) SAC387 solder (b) SAC387 with 0.05 wt.% SWCNT.

The tensile properties (0.2 % yield strength, ultimate tensile strength, uniform elongation and total elongation) at room temperature, 50° and 75°C for the SAC387 solder and SWCNT-based composites are summarized in Tables 4.1 to 4.3. It may be observed that the addition of 0.05 wt.% SWCNT to the SAC387 solder results in an increase in yield and ultimate tensile strengths at all temperatures and strain rates, although the increase in strength values at 75°C is marginal.

Table 4.1: Ultimate tensile strength of SWCNT-based composites at different strain rates and temperatures.

$\dot{\varepsilon}$ (sec^{-1})	Temperature (°C)	SAC	SAC+0.05CNT	SAC+0.1CNT
5×10^{-4}	RT	28.24	36.76	37.13
5×10^{-3}		51.83	55.99	58.01
5×10^{-2}		63.34	66.99	67.16
5×10^{-4}	50	25.55	32.77	36.76
5×10^{-3}		47.03	47.55	50.28
5×10^{-2}		51.00	56.16	56.44
5×10^{-4}	75	22.16	22.18	22.36
5×10^{-3}		37.67	40.18	42.94
5×10^{-2}		55.14	56.05	59.56

This can be attributed to the load transfer to the SWCNTs in the composites and the refinement of the grain size of the matrix, as well as the sizes of the intermetallic particles. Surprisingly, further increase in the SWCNT to 0.1 wt.% does not result in any significant improvements in strength, compared with that of the composite containing 0.05 wt.% SWCNT. Similar results have also been observed by Kumar et al., and all these results can be attributed to agglomeration of SWCNTs with an increase in their volume fraction [99].

The SAC387 alloy, as well as the composites, shows significant total elongation at all temperatures and strain rates although the uniform elongation is limited. The low uniform elongation values are a reflection of the fact that for tests at room temperature, the homologous temperature (T/T_m) is above 0.5, and hence the dynamic recovery processes tend to dominate over the work hardening. The composites also show comparable or even marginally higher total elongation than that of the base alloy.

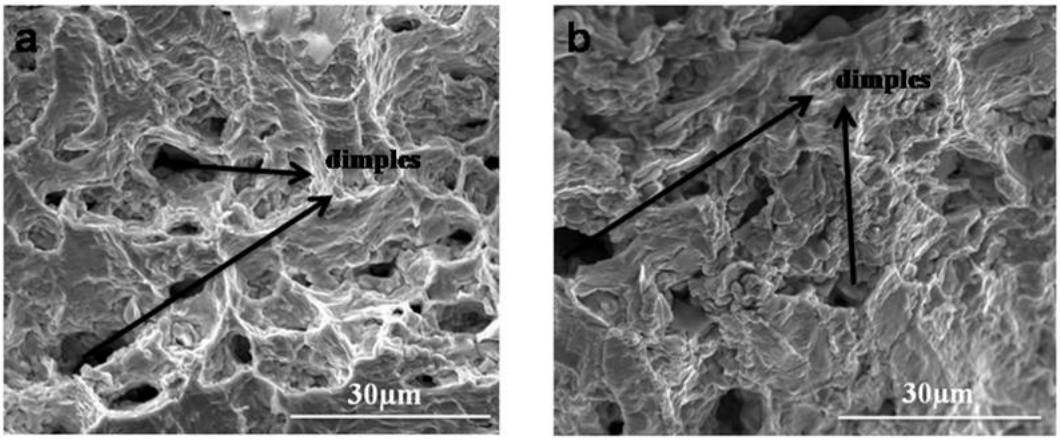

Figure 4-11: SEM fractographs of (a) SAC387 solder (b) SAC387+0.1%CNT at room temperature and strain rate of 5x10^{-3}s^{-1}.

Representative SEM fractographs of the SAC387 base alloy and SAC387 + 0.1 wt.% SWCNT tested at room temperature and strain rate of 5 x 10^{-3} s^{-1} are shown in Fig. 4.11. Dimples can be seen on the fracture surface in the SEM fractographs, which confirms that the fracture mechanism remains ductile in SAC387 solder as well as in the composites. The higher ductility in the composites could be attributed to the fact that the grain sizes, especially of the intermetallic phases, are finer in the composites.

Table 4.2: Yield strength for the SAC387 solder SWCNT-based composites at different strain rates over a range of temperatures.

$\dot{\varepsilon}$ (sec-1)	**Temperature (°C)**	Yield Strength (**MPa)**		
		SAC	SAC+0.05CNT	SAC+0.1CNT
5×10^{-4}	RT	27.97	32.44	34.14
5×10^{-3}		43.58	55.15	56.78
5×10^{-2}		61.33	66.15	67.16
5×10^{-4}	50	21.85	22.69	26.80
5×10^{-3}		31.02	37.51	38.34
5×10^{-2}		40.37	46.43	47.48
5×10^{-4}	75	10.15	12.17	13.26
5×10^{-3}		27.26	27.42	28.26
5×10^{-2}		36.63	44.69	45.30

Figure 4.12 (a & b) shows the variation of yield strength and ultimate tensile strength of SAC387 and composites with a varying percentage of SWCNT as a function of temperature at a constant strain rate of 5×10^{-4} s^{-1}, respectively. It can be observed that both yield strength and ultimate tensile strength decrease with increasing temperature in the SAC387 and the composites, although the decrease seems to be in significant for the composites. This is consistent with the fact that dynamic recovery processes in the matrix alloy become increasingly more important at higher temperatures at a given strain rate. However, the higher softening in the composites suggests that the interface between the SWCNTs and the matrix is also affected at higher temperatures, which then affects the load transfer to the SWCNTs.

Figure 4.12 (c & d) shows the representative variations of yield strength and ultimate tensile strength, with strain rates for SAC387 and composites with a varying percentage of SWCNTs at room temperature, respectively. It can be observed that both yield strength and ultimate tensile strength increase with an increasing strain rate for the base alloy and composites at all temperatures. This is consistent with the fact that work hardening dominates relative to the dynamic recovery processes at higher strain rates and a given temperature. By plotting the logarithm of the ultimate tensile strength as a function of the logarithm of strain rate, one can obtain strain rate sensitivity (m). The values of m for SAC 387 and composites with varying SWCNTs at room temperature, 50ºC and 75 ºC are tabulated in Table 4.4.

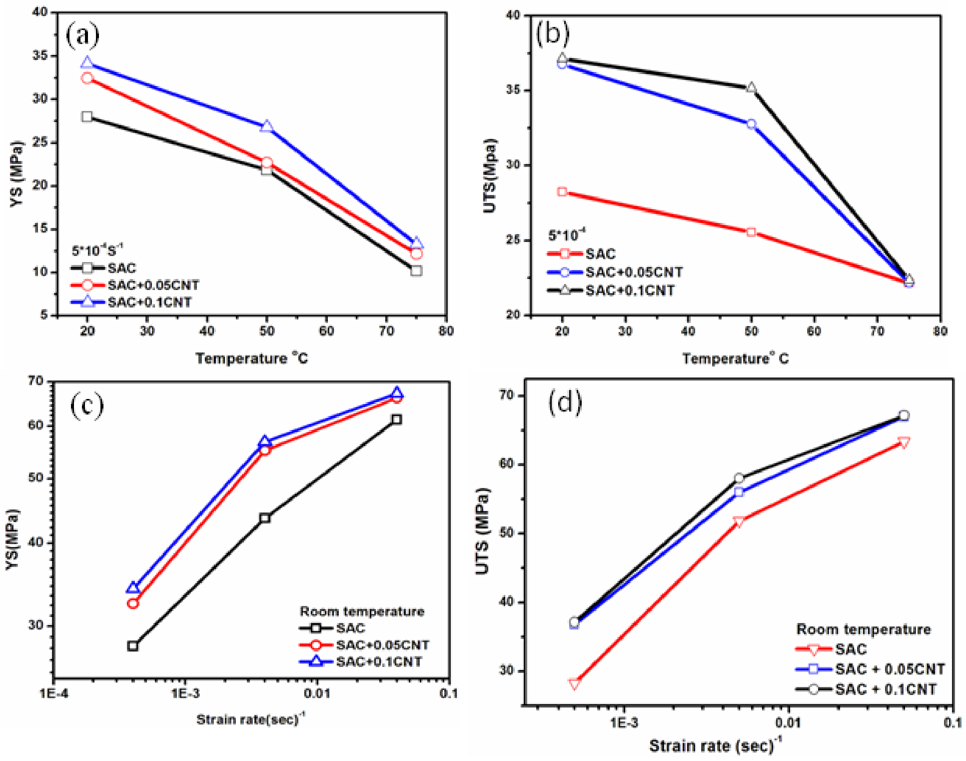

Figure 4-12: Variation of yield strength (YS) and ultimate tensile strength (UTS) with the increasing SWCNT in SAC387 solder (a & b) with temperature (c & d) with strain rate.

Table 4.3: Uniform elongation (UE) and total Elongation (TE) of SAC387 solder and SWCNT-based SAC composites with respect to temperature and strain rates.

$\dot{\varepsilon}$ (sec^{-1})	**Temp. (°C)**	**SAC**		**SAC+0.05CNT**		**SAC+0.1CNT**	
		UE (mm)	TE (mm)	UE(mm)	TE (mm)	UE (mm)	TE (mm)
5×10^{-4}	RT	0.40	38.65	0.80	46.00	0.70	45.00
5×10^{-3}		0.38	23.00	0.44	30.30	0.60	22.20
5×10^{-2}		0.35	20.50	0.36	20.40	0.46	20.20
5×10^{-4}	50	2.37	15.90	2.00	22.50	2.00	25.00
5×10^{-3}		1.80	15.30	1.39	19.50	1.61	17.75
5×10^{-2}		1.70	15.10	1.35	14.30	1.11	9.80
5×10^{-4}	75	3.48	45.30	3.88	52.00	3.52	50.50
5×10^{-3}		2.65	30.20	1.86	32.00	2.98	28.40
5×10^{-2}		1.82	25.40	1.77	16.56	1.73	23.30

The values of *m* determined in this study at room temperature are similar to the values obtained by others with conventional Sn-Pb alloys and other lead-free solder alloys [106]. This indicates that lead-free solders show significant strain-rate sensitivity even at room temperature and medium strain rates [107, 108]. It may be observed that the strain-rate sensitivity does not change much with an increase in temperature from room temperature to 50ºC, but it increases significantly when the temperature increases from 50 to 75ºC for the base alloy and the composites. This is consistent with the fact that dislocation climb-based processes can start contributing to the deformation at higher temperatures. The strain-rate sensitivities for the base alloy and the composites are comparable, which indicates that the deformation mechanisms are similar and the addition of the SWCNTs does not significantly affect the deformation mechanisms.

Table 4.4: Strain-rate sensitivity (*m*) in SAC and SWCNT composites with temperatures.

Solders	**Strain rate sensitivity (*m*)**		
Temperature (ºC)	RT	50	75
SAC	0.17	0.17	0.19
SAC+.05CNT	0.13	0.13	0.20
SAC+0.1CNT	0.12	0.14	0.21

Table 4.3 shows that the uniform strain and total elongations for SAC387 solder and the composites increase with temperature at a given strain rate, whereas both decrease with an increase in the strain rate at a given temperature. Representative SEM fractographs of SAC387 and SAC387 + 0.1 wt.% SWCNT at 75ºC and strain rate of 5×10^{-3} s^{-1}, and at a strain rate of 5×10^{-2} at room temperature, are shown in Fig. 4.13. A comparison with Fig. 4.11 shows that there is no change in the fracture mechanism (which remains ductile) in either SAC387 or the composites at higher temperatures or strain rates, even though the percentage of elongations changes significantly with changes in temperature and strain rate.

The results of this study show that yield strength and ultimate tensile strength of the SAC387 solder alloy can be improved with the addition of 0.05 wt.% SWCNT without compromising the uniform or total elongation, irrespective of the temperature or strain rate. The deformation and fracture mechanism of the SAC387 alloy also remains unaffected by the addition of SWCNT, and hence the effects of strain rate and temperature are similar in both the SAC387 alloy and the SWCNT-reinforced SAC387 solder. It also appears that the mechanical properties of SA387 alloy can be further improved by additions of a higher wt. percentage of SWCNT, if the agglomeration can be avoided or minimized.

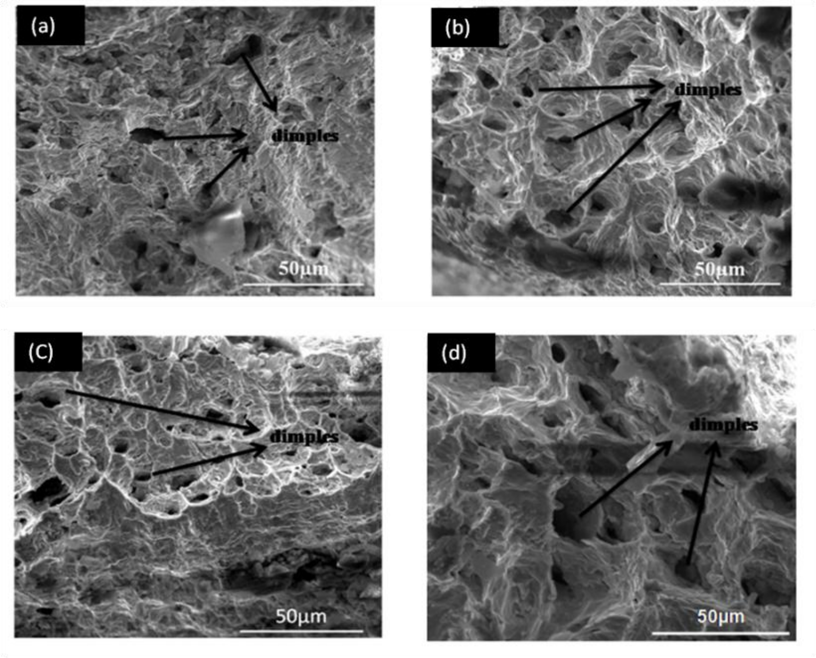

Figure 4-13: SEM fractographs of (a) SAC 387 (b) SAC+0.1% SWCNT at 75°C with strain rate of $5x10^{-3}s^{-1}$ (c) SAC387 (d) SAC+0.1% SWCNT at room temperature and strain rate of $5x10^{-2}s^{-1}$.

4.3.4. Microtensile Properties of β-Sn and Sn5Pb and SAC387 solders

For comparison purposes, the microtensile testing experiments were also conducted on the as-cast pure Sn, Sn5Pb and SAC387 solders. Typical true stress-strain curves for pure Sn and SAC387 solder are shown in Fig. 4.14. The analysis procedure is the same as described in Chapter 3, and a summary of these analyses is presented in Table 4.5. The yield strength and ultimate tensile strength of these solders are in general 10 to 15% lower than those of the respective bulk solders [94]. The cast SAC387 is strongly dependent on the microstructure, and this shows that strain-rate sensitivity of cast SAC387 solder is slightly higher than that of wrought-structured SAC387 solder.

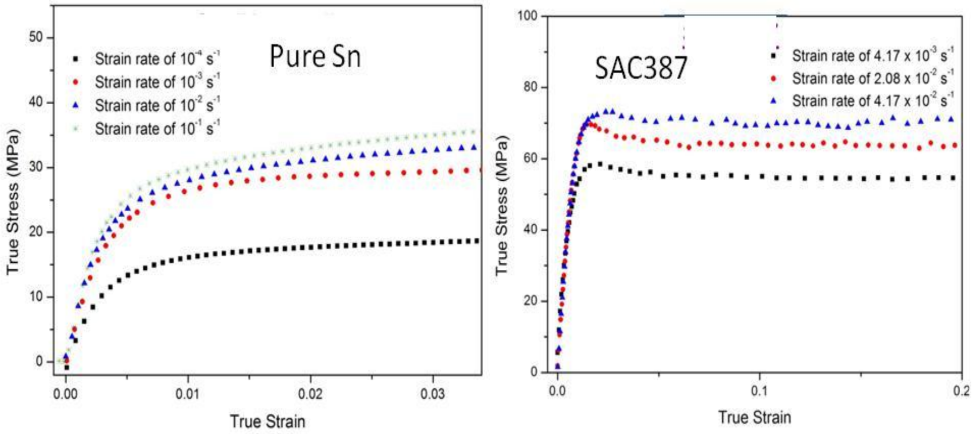

Figure 4-14: Representative true stress-strain curves for pure Sn and SAC387 solders.

Table 4.5: Room-temperature microtensile properties of the traditional solders.

Material	$\dot{\varepsilon}(s^{-1})$	σ_y (*MPa*)	*UTS* (*MPa*)	σ_{flow} (*MPa*)	*m*
Sn-5Pb (High temp. solder)	10^{-4}	13 ± 2	18 ± 3	18 ± 4	0.0903± 0.0001
	10^{-3}	22 ± 4	29± 5	29 ± 5	
	10^{-2}	23 ± 5	33 ± 4	33 ± 2	
Sn	10^{-4}	18 ± 5	29 ± 5	29 ± 3	0.0873 ±0.0051
	10^{-3}	26 ± 2	39± 3	38 ± 5	
	10^{-2}	32 ± 7	45 ±8	44 ± 3	
SAC387	10^{-4}	27 ± 6	28± 4	25 ± 4	0.1101 ± 0.0043
	10^{-3}	43 ± 7	51± 4	49 ± 7	
	10^{-2}	51 ± 5	63± 7	62 ± 6	

4.3.5. Microtensile Properties of Mo Composites

The microtensile properties of Mo-reinforced composite solders were tested at room temperature with variations of the strain rate and percentage of the nano-sized Mo particles. Figure 4.15 shows that the yield strength and ultimate tensile strength increases with addition of the nano-sized Mo particles to the SAC387 solder matrix. The effects of the strain rate on the tensile properties of the SAC387 and SAC387composites are summarized in Table 4.6.

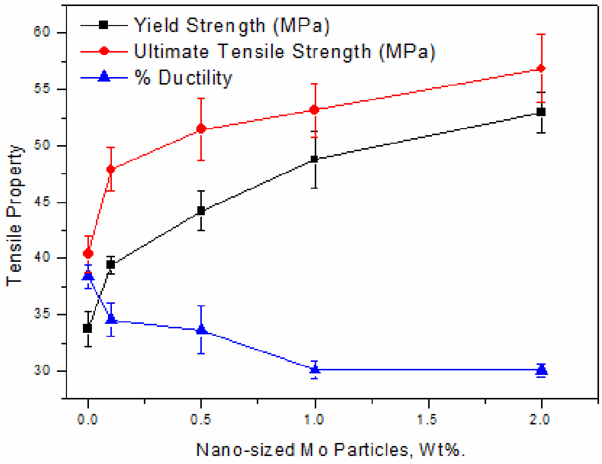

Figure 4-15: Room-temperature microtensile properties of composite SAC387 solders with % wt. fraction of nano-sized Mo-particle addition.

Table 4.6: Room-temperature microtensile properties of Mo-reinforced SAC387 solder.

Material	$\acute{\varepsilon}(s^{-1})$	σ_y (MPa)	UTS (MPa)	σ_{flow} (MPa)	m
SAC387 (Wrought microstructure)	10^{-4}	39 ± 5	43± 4	25 ± 4	0.15 ± 0.004
	10^{-3}	43 ± 7	47± 4	49 ± 7	
	10^{-2}	53 ± 5	56± 7	62 ± 6	
SAC387+1Mo	10^{-4}	51 ± 3	56 ± 8	53 ± 3	0.07±0.003
	10^{-3}	54 ± 5	59 ± 4	57 ± 4	
	10^{-2}	63 ± 4	66 ± 3	62 ± 6	
SAC387+2Mo	10^{-4}	62 ± 3	68 ± 4	66 ± 3	0.06±0.001
	10^{-3}	68 ± 6	71 ± 6	69 ± 5	
	10^{-2}	74 ± 5	76 ± 7	75 ± 4	

It can be seen that both composites showed higher ultimate tensile strength than that of the base alloy. The addition of Mo particles of greater than 1% results in no change in the percentage of the ductility. The strain-rate sensitivity of composite solder is expected to be lower due to its composite strengthening. These nano-sized Mo particles serve as a dislocation source during tensile deformation and reach the critical dislocation density at the minimum deformation, as the concentration of dislocation sources increases with the addition of nano particles. Therefore, strain-rate sensitivity is reduced with the addition of Mo particles.

4.3.6. Effect of the Specimen Thickness on the Mechanical Properties

The effect of the specimen gauge thickness on the yield strength of SAC387 solder is shown in Fig. 4.16. The yield strength of 200µm-thickness SAC387 test specimens was found to be 26MPa, and about 53MPa for a 1000µm sample. Deformation may be less constrained with the lower-thickness specimens because of the larger solder surface area. The effective dislocation density (or pile up) will be lower as dislocation can be annihilated when reach at the free surface, which lowers the resistance for deformation, and hence lowers the yield strength of the solder. In the case of the 1000µm-gauge thickness specimens, the deformation behaviour is similar to that of the bulk materials. Apart from the deformation mechanism, there are several other factors which may affect the measurement of the yield strength of the solder specimen of 200µm-gauge thickness:

(a) Handling of the microtensile test specimens is difficult due to pre-deformation of samples during loading at the grips.

(b) Minimum available load cell is 50N, the maximum load for 200µm specimens during testing is less than 3N (~5% load cell capacity).

(c) Thickness variation in the microtensile test (200μm) specimens.

(d) Surface roughness of specimen in the gauge length due to hard IMC particles shearing when being rolled into the thinner strips (200μm).

To avoid external experimental issues with the measured yield strength of the solders, microtensile testing experiments were conducted on 500μm-gauge thickness specimens for all the solders, in order to understand their microtensile behaviour. Figure 4.17 shows that the yield strengths measured from these microtensile specimens are lower than those from the bulk samples. In general, yield strength should be higher than bulk materials due to finer grain sizes in the microtensile test specimen. This lower yield strength may be attributed to the surface roughness and/or localized stress-concentration area within the gauge length, due to presence of IMC particles in the microtensile specimen. However, in the case of SWCNT-reinforced SAC387 solder (Fig. 4.18), the microtensile test specimens showed higher yield strength.

It was confirmed from the fractured bulk test specimens (with SWCNTs) that there was 5 to 8% porosity in the samples and non-uniform distribution of SWCNTs. On the other hand, for microtensile test specimens, as they rolled from the SWCNT-reinforced bulk SCA387 solder, there was a uniform fine-grained and porous-free microstructure; therefore the yield strength was increased. Monolithic solders such as Sn and Sn-Pb are more sensitive to the thickness than the ternary or composite solders. The yield strength measured from these monolithic solders was less than 30% of the yield strength of the bulk solders. The reason for this behaviour is that the dislocation motion is less restrictive in these solders due to higher β−Sn with no particle reinforcement.

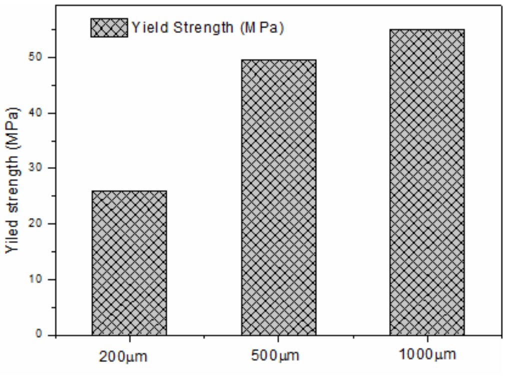

Figure 4-16: Effect of specimen gauge thickness on tensile properties of SAC387 solders.

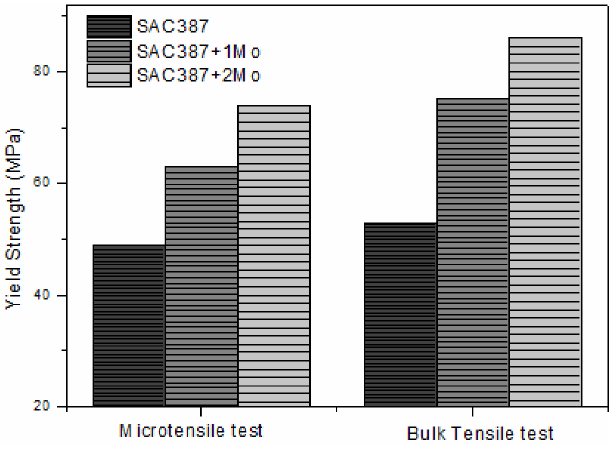

Figure 4-17: Comparison of yield strength, measured using microtensile and bulk-tensile tests for Mo-reinforced SAC387 solder.

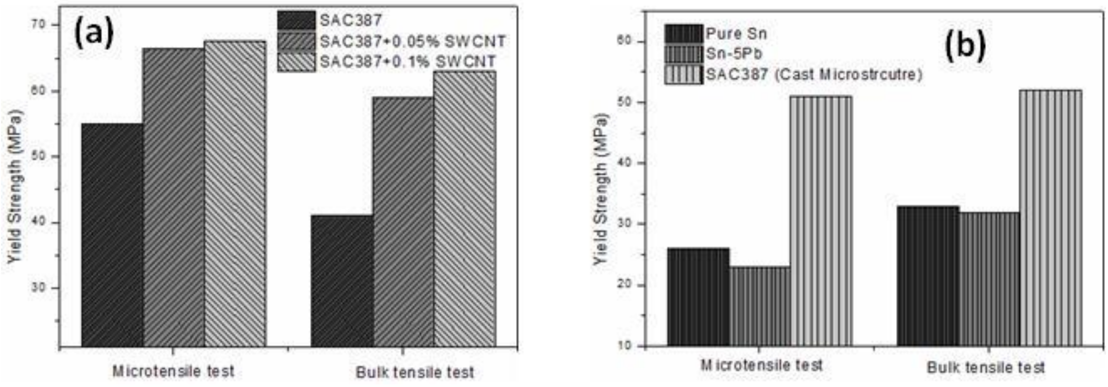

Figure 4-18: Comparison of yield strengths, measured using microtensile and bulk-tensile tests for (a) SWCNT-reinforced SAC387 solder (b) Base-reference solders.

4.5. Summary

The addition of 0.05 wt.% SWCNT to the SAC387 alloy resulted in an increase in yield and ultimate tensile strengths at all temperatures and strain rates. Further increasing the SWCNTs to 0.1 wt.% did not result in any significant improvements in the strengths, compared with those of the composite containing 0.05 wt.% SWCNTs. This may be attributed to the agglomeration of the SWCNTs when their volume fraction is increased.

The SAC387 alloy and the composites exhibited significant total elongation at all temperatures and strain rates, although the uniform elongation was limited. The low uniform elongation values reflect the fact that for tests at room temperature, the homologous temperature (T/T_m) is above 0.5, and hence the dynamic recovery processes are more dominant compared with the work hardening. The composites also showed comparable and, in some cases, even marginally higher total elongation than that of the base alloy. This may be attributed to the fracture being dominated by the failure of the matrix alloy, and the fact that the grain sizes, especially of the intermetallic phases, become finer due to the addition of reinforcements.

Yield and ultimate tensile strengths were found to decrease with an increase in temperature at a given strain rate, and increase with the strain rate at a given temperature, for the SAC387 alloy and the composites. This behaviour may be attributed to the competing effects of the work-hardening and dynamic-recovery processes, and the effects of temperature and strain rates on these processes.

The addition of nano-sized Mo to the SA387 solder improves the room-temperature microtensile tensile properties of the solders; however, there is no significant improvement in tensile properties beyond 1% Mo.

The effects of specimen thickness are more prominent for as-casted monolithic Sn, Sn-5Pb and SAC387 solders. It was found that tensile strength (both yield strength and ultimate tensile strength), determined using a microtensile tester, and is 10 to 15% lower than that derived from the standard ASTM bulk-materials characterization. However, there was little change observed in the composite solders.

Chapter 5: INDENTATION BEHAVIOUR OF LEAD-FREE SOLDERS

5.1. Introduction

The elastic modulus and yield strength are two important tensile properties used for thermo-mechanical modelling, to predict the reliability of the packaging systems. A conversion of hardness to yield strength is widely used as there are insufficient materials and no standard tools available for mechanical characterization at this scale. When the tensile properties of solder joints are needed for better estimation of system-level reliability, these reasons are not acceptable, because the mechanical properties of solder joints are size-dependent. Tensile properties such as yield strength and modulus of elasticity can be estimated from the stress-strain curve, if it adequately represents the complete tensile behaviour. Such information is required for defect assessment and finite element calculations. The elastic modulus of solder joints can be determined more accurately using the indentation technique. However, there is no standard metrology technique available to determine the yield strength of solder with the volume at the device level.

5.1.1. Hardness Conversion and Issues

Most investigators have reported the yield strength of solders and IMCs from the hardness conversion data, with the reason that enough material is not available for tensile testing [11]. However, it is often neglected that the converted hardness provides no information about the dependency of the materials' intrinsic microstructural characteristics. According to testing standards, to obtain an acceptable hardness for pure metals within ± 5 % uncertainty, a minimum of 18 successful indentations need to be performed and evaluated if the testing load equals 1N or more. If the testing load is smaller, indentation size effect is anticipated. In order to obtain a statistically-reliable tensile strength from hardness measurement, an even greater number of indentations would be required. It may be understood that for the case of failure analysis of the in-service structure, materials for standard testing specimens cannot always be extracted. One has to consider that the results of conversions may produce significant errors (more than 20%) in 10 tests. Finding statistical correlations between hardness and “real” tensile strength is not a problem, but generalizing those results is dangerous, especially if evidence is inadequate.

5.1.2. Indentation of the Solder Joints

Nanoindentation is one of the techniques for determining the mechanical properties of materials down to a few tens of micrometres [109–111]. The nanoindentation technique was first introduced in the early 1980s [110], providing the capability to record the load-penetration curves during the loading and unloading processes of the indentation. It was recognized by Doerner and Nix that the slope of the unloading curve at the initial stage of unloading could be adopted to measure the elastic modulus of the materials [111]. This method was later modified by Oliver and Pharr to take into account the large elastic recovery during unloading [109]. More recent development in this direction is focused on determining the contact area at the maximum loading, which is a crucial quantity for deriving Young’s modulus and hardness.

It has been reported that the indentor contact area could be evaluated by a polynomial function of the indentation depths at the maximum load and at the end of unloading [112]. In contrast to the unloading curves, the analyses for the loading behaviour started much earlier, at the time of the introduction of the nano-indentation technique [113]. It is now well-recognized that the loading curves generated using sharp indenters (such as conical, Vickers, and Berkovich) depend on the yielding strength, the strain-hardening property, and the elastic modulus of the materials [113]. These results provide fundamental information to deduce the yielding strength and the strain-hardening parameter. However, because the shapes of these sharp indenters are self-similar, the loading curve can provide only one independent quantity, which is the combination of the elastic and the plastic properties of the materials [114].

In order to realize the potential application of sharp indentation to the measuring of the yield strength, it is necessary to identify the plastic-deformation characteristics in the indentation data. The strain-hardening parameter, which can be related to the unloading penetration depth ratio or the indentation work ratio [112]. This method's validity has been verified extensively using finite element (FEM) calculations, but this method has not widely used for the determination of mechanical properties. Recently, Zeng and Chu proposed a new scheme for using sharp indentation to derive the elastic and plastic properties of materials [115]. The key feature of this method is that the unloading curve in the indentation can be used to determine both the elastic modulus and the strain-hardening parameter. This scheme is an empirical method based on experimental observation as well as on the FEM calculations [116]. The yield strength of materials can be determined by combining the two properties derived from the unloading curve, and adding the loading curve information [117].

In order to examine their empirical method, Zeng and Chu conducted extensive nanoindentation experiments on different materials, whose elastic modulus ranged from 3 (epoxy) to 650GPa (Tungsten carbide), while hardness ranged from 0.1 to 30GPa [115]. The results of Zeng and Chu's study show the consistent with the reported data of other literature. In this work, this empirical scheme is therefore used to extract the yield strength, elastic modulus and strain-hardening parameter of solder materials from the nanoindentation load-penetration data.

5.1.3. Indentation Empirical Models

5.1.3.1. Loading Curve Behaviour

The loading part of an indentation curve can be expressed as follows:

$$P = Ch^2 \tag{5.1}$$

where P is the indentation load, h is the penetration depth measured from the surface, and C is a constant depending on the geometry of the indenter tip and material properties. Many numerical analyses have proved that Eq. (5.1) can be used to extract the yield strength of elastic-perfect plastic and elastic-plastic materials [118]. However, deviations from the loading-curve behaviour have been observed by several authors. It has also been confirmed that this deviation is a distinct characteristic that cannot be attributed to uncertainties or tip-shape defects, suggesting that the single fitting parameter, C, in Eq. (5.1) is not sufficient to make an approximate estimation of the elastic-plastic properties of materials. In addition to this, the quadratic term in Eq. (5.1) implies the supposition of a purely plastic deformation, which is not accepted for elastic-plastic materials.

Kick's law in Eq. (5.1) was originally developed based on the energy aspect of materials, i.e. the energy required for a given size reduction was proportional to the size-reduction ratio. The quadratic relation is obtained by integration of the total energy during reduction. The apparent compatibility of this law with the micromechanical response of indented materials ensured that it was adopted to characterize the load-displacement curve behaviour of materials [112]. The relation (Eq. 5.1) has been demonstrated by numerical simulation for both elastic-perfect plastic and elastic-plastic materials [112, 116, 117]. The constant C is defined for a sharp Berkovich indentation on an elastic material obtained by the finite-element analysis, as shown in Eq. (5.2):

$$P = 2.189(1 - 0.21\nu - 0.01\nu^2 - 0.41\nu^3)\frac{E}{\left(1-\nu^2\right)}h^2 \qquad (5.2)$$

and for the indentation on an elastic-plastic material,

$$P = \frac{1.272}{\left(tan24.7^o\right)^2}\left(1+\frac{\sigma_u}{\sigma_y}\right)\left(1+\ln\left(\frac{E\tan 24.7^0}{3\sigma_y}\right)\right)\sigma_y h^2 \qquad (5.3)$$

where ν is Poisson's ratio, *E* is Young's modulus, σ_{YS} is the yielding stress, σ_u is the stress at 29% strain, and the ratio σ_u / σ_{YS} is used to represent the strain-hardening property of materials. In this work, Eqs (5.2) and (5.3) are applied for extraction of tensile properties from the indentation load versus depth data at larger indentation loads.

5.1.3.2. Unloading Curve Behaviour

The unloading curve is used to derive the elastic modulus of the material by the following formula:

$$\frac{E}{\left(1-\nu^2\right)} = \frac{S}{\alpha\sqrt{A}} \qquad (5.4)$$

where *S* = d*P*/d*h* is the contact stiffness at the initial of unloading process, *A* is the true contact area at the maximum load, and $\alpha = \frac{2}{\sqrt{\pi}}\beta$, β is a geometric constant for the Berkovich indentation [116, 117]. The contact stiffness *S* can be determined by two fitting methods for the unloading curves. The first is the linear-curve fitting method developed by Doerner and Nix, who based it on the Sneddon's flat punch solution, which could be used to describe the unloading curve as follows [111, 119]:

$$P = S\left(h - h_o\right) \tag{5.5}$$

where h_o is the true contact indentation depth. The best-fit results of S and h_o depend on the portion of the unloading curve, and it is suggested that using the top one-third portion of the unloading data gives the best fitting [16]. Eq.uation (5.4) is based on the assumption that the contact area remains unchanged during unloading, which is true for the case of a punch indenting an elastic-perfect plastic material. Doerner and Nix's method can describe the unloading behaviour of soft metals such as Sn and lead-based solders, but often fails to capture that of hard materials such as intermetallics, ceramics etc.

Oliver and Pharr introduced the second method, which is applicable to the nanoindentation of the hard materials, taking into account the large elastic recovery during the unloading process [109]. Earlier indentation studies on solder materials were merely concerned with the evaluation of the elastic modulus from the slope of the unloading curve, and overlooked the shape of the unloading curve and its relationship with the other mechanical properties. Zeng et al. extensively studied the relationship between the shape of the unloading curve and the mechanical properties of materials [115]. Their studies have shown that unloading curves might be adopted to determine the modulus and strain-hardening parameter.

5.2. Experimental Methodology

For this study, indentation experiments were conducted with different strain rates to the maximum-defined indentation depths, in order to eliminate creep effects during the indentation loading and unloading stages. Moreover, the maximum depth (>2.5μm) was defined during the indentation experiments in such a way that deformation under the indentation process represented the global deformation. Extrinsic parameters such as the strain rate and testing temperature, and intrinsic parameters like the microstructure, were kept constant for both the indentation and microtensile methods. CSM measurements were conducted at similar strain rates to those of microtensile test experiments, to the maximum depth of 2500nm. Beyond this depth, the indentation size effect is at its minimum, and hence hardness of the solder is determined at this indentation depth for a given strain rate. CSM experiments were then conducted at different strain rates to predict the correlation coefficient between the hardness and tensile yield strength of the solders.

5.3. Results

Table 5.1 summarizes the elastic modulus (*E)*, derived from Doerner & Nix's and Oliver & Pharr's models. Figure 5.1 shows the typical indentation impressions at a maximum load of 10mN. Indentation experiments were conducted at a strain rate of 10^{-2} s^{-1} with different maximum loads, as shown in Fig. 5.2. The loading and unloading rate of all experiments was fixed at 10^{-2} s^{-1}, to avoid creeping effect during unloading. It may be observed that for pure Sn, the two models predicted similar results because the unloading curves of Sn were straight lines. Indentation loads ranging from 10 mN to 40 mN were used to validate the loading/unloading p-h data for indentation analysis. It may be observed (Table 5.1) that an indentation load beyond 20mN shows that the elastic modulus is reduced, compared with the theoretical elastic modulus of pure Sn. This may be attributed to the creep effect during the indentation process.

Table 5.1: Elastic Modulus of Sn measured using linear and power law models.

Max. Load (mN)	Elastic Modulus (GPa)		
	Doerner & Nix model	Oliver & Pharr model	Theoretical
10	42.6±2.2	41.5±2.2	41.4
20	41.7±0.7	40.9±0.5	
30	40.1±2.2	39.1±1.2	
40	38.2±1.1	38.7±1.7	

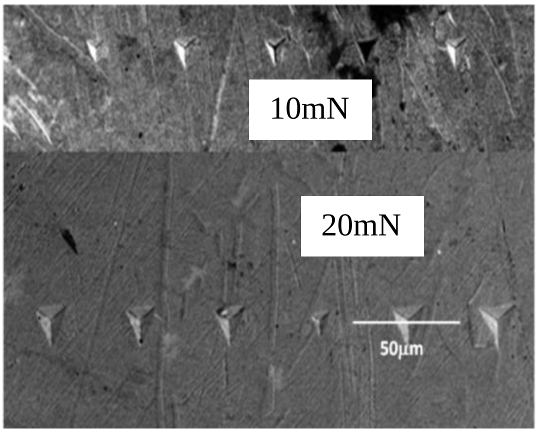

Figure 5-1: The representative indentation impressions at loads of 10mN and 20mN.

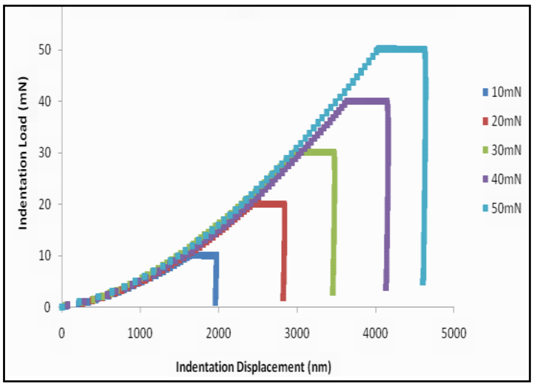

Figure 5-2: Schematic flow diagram showing the analysis sequence of solder joints.

Therefore, the maximum load for the indentation creep experiments for lead-free solder joints is limited to 20mN, to avoid creep during the indentation experiments. Creep deformation during the indentation experiments will affect the indentation depth and, therefore, the elastic modulus and hardness of the solder joints. Figure 5.3 shows the sequence of indentation analysis for determination of the yield strength of the solder joints from the indentation p-h data, at a $10^{-2}s^{-1}$ strain rate.

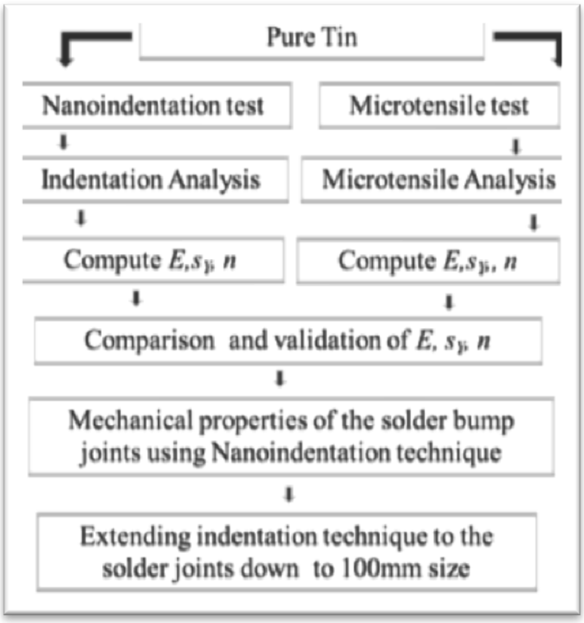

Figure 5-3: Tensile properties analysis flow for indentation and microtensile data.

5.3.1. Indentation-unloading Curve Analysis

For a perfectly elastic material, the indentation-unloading curve will be identical to the loading one as described in Eq. (5.1). The indentation-unloading curve of an elastic perfect-plastic material, on the other hand, can be roughly described as a straight line, as depicted in Doerner & Nix's model. The experimental data presented in Fig. 5.4 clearly shows that the unloading curve for pure Sn is close to the indentation of fully-elastic perfect-plastic cases, i.e. the strain-hardening parameter of solder materials is close to unity. In contrast, for the Cu-Sn intermetallic, the unloading curve will be close to a parabolic curve. This suggests that the unloading curve of elastic-plastic materials can be written as a linear combination of the results of the two extreme cases, as shown below [115]:

$$P=(1-\theta)\,f(\nu)\,Eh^2+\theta S\left(h-h_o\right) \tag{5.6}$$

where

$$S = 2\sqrt{\frac{24.56}{\pi}}\frac{E}{1-\nu^2}h_o \tag{5.7}$$

θ is the fitting parameter. Eq. (5.6) is an empirical equation for analysing the unloading curve of the Berkovich indentation on a general elastic-plastic material.

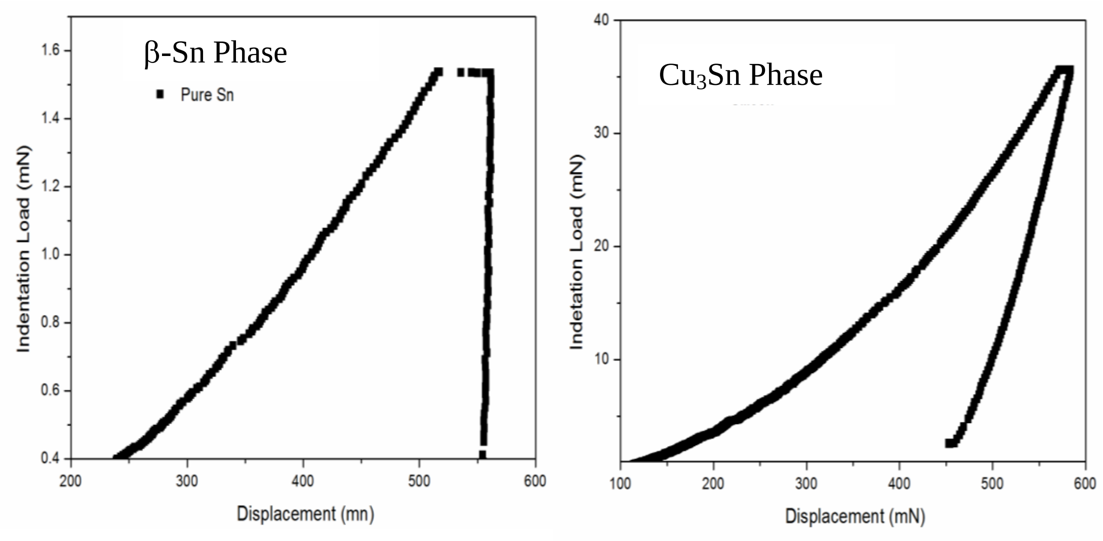

Figure 5-4: Indentation load versus depth curves for different materials.

For solder materials, the effects of the first term in Eq. (5.6) are very minimal, because the unloading curve for the solders is almost a straight line; hence the linear term in Eq. (5.6) gives more weightage to the determination of the elastic modulus and parameter (h_o). This fitting parameter (h_o) has a length (*nm*), which is defined as a perfect plastic depth. The hardness of materials is defined as [115]:

$$PPH = \frac{P}{24.56h_o^2} \tag{5.8}$$

5.3.2. Indentation Loading Curve Analysis

Numerical analyses of sharp indenters (such as those by Cone, Vickers, and Berkovich) indicated that the loading curve follows Eq. (5.1) [112, 116, 117, 119]. Many experimental results, however, have shown that the actual relationship between the indentation load P and penetration depth h deviates from the theoretical prediction. Figure 5.5 shows the curve fitting of the loading curve to a power law relation, $P = Ch^n$, where the derived exponent n is less than 2. However, n = 1.5 perfectly fits the loading data. This discrepancy also has been observed by earlier studies [115]. The discrepancy between the experimental and theoretical results poses a problem with understanding the loading curves obtained in experiments, as well as the material properties derived from interpretation of the curves.

Therefore, it is necessary to have an insight into the discrepancy before adopting Kick's law for the indentation curves. The following comparison scheme is adopted to have a better understanding of the discrepancy between the experimental and theoretical results. In the scheme, the loading curve is contrasted with the two lines, $P = C_1h^{3/2}$ and $P = C_2h^2$, corresponding to the cases of spherical and sharp Berkovich indentation, respectively. The constant C_1 is determined by fitting the first function to the initial part of the loading curve (the first 1/3 of the loading data). On the other hand, the constant C_2 corresponds to the best fit of the second function to the last part of the loading curve (the last 30–50 data points from the maximum load). This comparison scheme has been applied to a number of materials (fused silica, Al_2O_3, and ZrO_2), and the results have been discussed elsewhere [115].

Figure 5.5 shows that the loading curve for pure Sn is described by two different functions, $P = C_1h^{3/2}$ and $P = C_2h^2$, at low and high loads, respectively. The transition of the characteristics of the loading curve suggests that the initial portion of the indentation curve causes the exponent n in the fitting $P = Ch^n$ to deviate from 2. The initial deviation might be due to the shape of the indenter tip, and high stress at the beginning of the indentation tests.

These effects become insignificant as the load increases, and therefore the loading process in the experiments will follow the theoretical prediction closely after the load is sufficiently large. The minimum load required to validate this law depends on the hardness of materials; for solder materials, the load should be larger than 5 mN for nano-indentation to be beyond the transition region. Therefore, the indentation loads have been selected to be 10 mN for the present study.

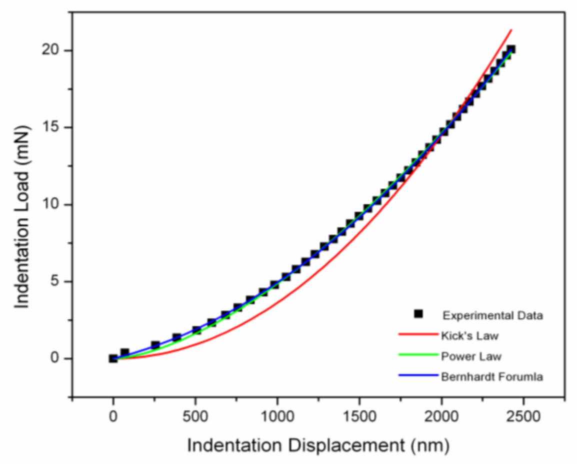

Figure 5-5: Schematic curve-fitting of pure Sn indentation data with a different power law exponent, according to Kick's law.

Table 5.2: Mechanical properties of pure Sn measured from the *P*-*h* data.

P_{max} (mN)	E (GPa)	h_0 (nm)	σ_y(MPa)	H (GPa)
5	43.0±2.2	1564±43	44.6±1.6	0.166 ± 0.003
10	43.0±2.2	1959±23	44.6±1.6	0.106 ± 0.003
20	41.7±0.7	2813±55	41.0±1.6	0.103 ± 0.004
30	39.1±2.2	3546±112	38.8±2.0	0.097 ±0.005
40	38.2±1.1	4123±51	37.3±1.2	0.096±0.002

The maximum load requirement is a key requirement for the solder joints because solders are low melting materials; creep mechanism is dominant during indentation. It may be seen in Table 5.2 that the elastic modulus determined from the slope of unloading data (*p*-*h*) is decreasing with the load increment. This is because creep deformations during indentation are compensating for the recovered elastic strain. In order to avoid the creep effect on the loading and unloading curves, all experiments in this work were limited to a maximum indentation load of 10 mN and strain rate of $10^{-2}s^{-1}$.

This maximum load gives a total indentation depth of approximately 2.5 to 3 μm, which is representative of the global deformation volume. However, this indentation depth brings up another issue, namely that the minimum solder thickness should be at least 10 times more than the depth of indentation to avoid substrate effect during indentation. Therefore, restrictions of maximum indentation load become an issue when the solder thickness is too small. Therefore, the determination of the mechanical properties of solder-joint sizes lower than 100 μm is not possible from this analysis.

5.4. Discussion

In this study, the mechanical properties of various commercial solder joints such as SnAg, SnAgCu, CASTIN and SnZnBiIn lead-free solder joints were determined using present analysis and compared with reported data. Eq. (5.6) was used to perform the indentation analysis of the unloading p-h data, and to determine the values of E, h_o and the strain-hardening parameter (θ). Consequently, using E and θ fitting parameters from the unloading data, σ_Y was determined from the loading data using Eq. (5.3). The range of the indentation load for loading and unloading data analysis was the same for all the materials.

Based on the analysis of the pure Sn, the indentation maximum load was limited to 20mN for all solder joints studied in this work. There were a total of 24 indents (4×6 matrix) conducted for each condition, and four (4) representative indentation results for each solder joint are presented in Table 5.3. It can be observed that the mechanical properties determined using the empirical indentation analysis is consistent for all lead-free solder joints. The average values of the indentation mechanical properties are summarized in Table 5.4. The yield strength of lead-free solder joints measured using these analyses is higher than that reported in the literature in which the traditional techniques (tensile, compression and shear testing) were used. The yield strength of pure Sn was determined to be 44 MPa, which was comparable with the yield strength determined using an ultra-microtensile tester [120].

Table 5.3: Mechanical properties of solder joints at an indentation load of 10mN.

Lead-free Solder	h_o (*nm*)	PPH (*GPa*)	E (GPa)	θ	σ_Y MPa
SnAg	1538	0.172	43	0.963	48
	1575	0.164	53	0.950	41
	1605	0.158	53	0.964	46
	1475	0.187	59	0.992	40
SnAgCu	1149	0.304	53	0.934	67
	1199	0.283	45	0.963	61
	1182	0.291	54	0.964	63
	1147	0.309	52	0.953	57
CASTIN	1288	0.179	48	0.939	40
	1299	0.184	50	0.987	39
	1306	0.211	50	0.978	36
	1264	0.190	46	0.949	47
SnZnBiIn	1322	0.201	53	0.948	54
	1290	0.216	62	0.924	42
	1319	0.198	61	0.920	60
	1190	0.207	63	0.930	46

The yield strength of the SnAgCu bulk solder materials has been reported as 54 MPa at a 10^2 s^{-1} strain rate [96]. However, the yield strength measured using the present analysis scheme is 62 MPa. The yield strengths of the CASTIN and SnZnBiIn solder joints are comparable to the yield strength values determined using standard tensile testing [121]. The strain-hardening parameter (θ) is defined as the ratio of yield strength to ultimate tensile strength, which is lower for the SnAg3.5Cu0.5 compared with other solder joints. This means that the SAC solder shows higher strain-hardening behaviour during deformation before attaining instability.

Table 5.4: Mechanical properties of 500μm solder joints from the indentation data.

Lead-free Solder	h_o (nm)	E GPa)	PPH (GPa)	θ	σy (*MPa)*
Sn	4123	38	0.096	0.981	44
SnAg	1548	51	0.169	0.973	45
SnAgCu	1171	55	0.296	0.933	62
CASTIN	1460	53	0.191	0.963	41
SnZnBiIn	1408	59	0.205	0.953	51

Tabor approximation has been used to compare the measured indentation tensile properties, which is approximately as follows [122]:

$$Yield\ Strength(\sigma_Y) = \frac{Hardness(H)}{Constant(C)} \tag{5.8}$$

The yield strength determined based on the Tabor analysis is higher than the indentation tensile yield strength of the solder joints (Table 5.5). The reported yield strength of all solder joints is lower than that of the yield strength measured using nanoindentation. This discrepancy might be due to microstructure differences (cast or wrought conditions) and processing conditions. In order to compare the mechanical properties measured by various techniques, it is mandatory to ensure that both extrinsic parameters (strain, strain rate, testing temperature) and intrinsic parameters (microstructural morphology, grain size etc.) are comparable, preferably the same.

5.4.1. Tabor Analysis

The hardness (*H*) variation can be significantly reduced with the indentation load selected from the region where the hardness increment approaches a constant with the microindentation load. This change in the hardness with the indentation load is known as the indentation size effect (ISE) [123, 124]. This effect may be attributed to the evolution of the dislocation beneath the indenter, which gives rise to strain gradients.

Material deformation in metals enhances the dislocation formation, motion and pile up, and hence the hardening mechanisms are dependant on the total dislocation density. This is represented by the total coupling between two types of dislocations: statistically stored dislocations (SSDs) and geometrically necessary dislocations (GNDs). SSDs are generated by trapping each other, while GNDs are the stored dislocations that relieve the plastic-deformation incompatibilities within the polycrystal caused by the non-uniform dislocation slip. Therefore, the presence of GNDs would cause an additional storage of defects and increase the deformation resistance by acting as an obstacle to the SSDs [123]. Hence, at a lower mciro-indentation load, there are more GNDs developed to cause an increase in the *H* values.

As the load increases to approximately 1500mN onwards, there are few GNDs present. Hardness completely depends on the SSDs, and hence the consistent *H* values can be reached at higher loads. Therefore, the micro-indentation load of 1961mN was chosen because the indentation size effect is negligible beyond this load for hardness measurement in the present study (Fig. 5.6). It may be observed that the Tabor constant (*C)* decreases with an increase in the strain rate. In order to avoid this discrepancy, nanoindentation experiments were conducted at a similar strain range (of the tensile testing), up to 2500nm depth, in such a way that the representative indentation stress was close to three times the maximum tensile stress during microtensile testing, if verified.

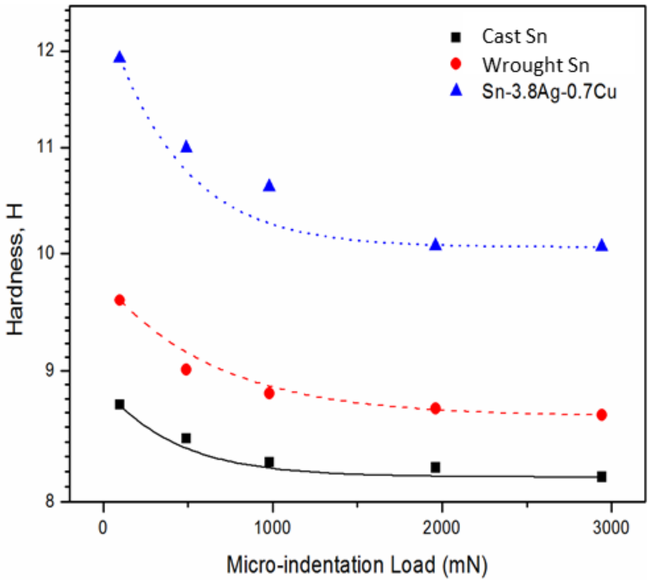

Figure 5-6: Effect of indentation load on micro-hardness (H_V).

5.4.2. Nanoindentation

The yield strengths measured from microtensile and CSM hardness, and measured with the nanoindentation technique over a similar range of strain rates, are summarized in Table 5.5. The Tabor conversion constant changes were from about 3.4 to 3.9, from pure Sn to SnAgCu solder, while there was a 50% reduction with a decrease in the strain rate from the 10^{-2} to 10^{-4} s^{-1}. Table 5.6 shows the conversion of the hardness values of the lead-free solder joints based on Tabor constants determined for the bulk materials with the same composition. Even though the composition of solder was the same for both the bulk and solder joints, the Tabor conversion constant did not give similar yield strengths. This might be due to differences in the microstructural morphology. Therefore, accurate conversion may not be possible without knowledge of the materials' history or fabrication conditions.

Table 5.5: Effect of strain rate on yield strength, hardness of Sn and SnAgCu solder.

Material	Strain rate $(\acute{\varepsilon},s^{-1})$	Yield Strength (MPa)	CSM hardness (GPa)	Tabor constant	Micro-hardness (H_V)	Conversion constant
Sn	10^{-4}	18.81 ± 0.51	0.061 ± 0.01	3.2	8.70	4.54
	10^{-3}	26.53 ± 0.22	0.079 ± 0.02	3.4		3.22
	10^{-2}	32.15 ± 0.79	0.011 ± 0.01	3.42		2.66
SAC387	10^{-4}	27.97 ± 0.62	0.11 ± 0.02	3.9	10.07	3.53
	10^{-3}	43.58 ± 0.79	0.16 ± 0.01	3.68		2.27
	10^{-2}	61.33 ± 0.57	0.24 ± 0.06	3.9		1.61

Table 5.6: Mechanical properties measured using nanoindentation and tensile testing.

Solder Materials	PPH *(GPa)*	σy *(MPa)*	Tabor approximation σy =PPH/3 *(MPa)*	σy
Sn	0.096	44	32	28.5 [121]
SnAg	0.169	45	56	30.3 [121]
SnAgCu	0.296	62	98	44.6 [96]
CASTIN	0.191	41	63	33.3 [121]
SnZnBiIn	0.205	51	68	-----

5.5. Summary

An empirical analysis scheme was used to determine the tensile properties of lead-free solder joints using the nanoindentation technique. A summary of the results is as follows:

1. The yield strength of pure Sn was found to be 44MPa using this analysis scheme, which is close to the value determined using a microtensile tester. However, there was significant variation in the yield strength of ternary alloy solder (SAC387).
2. This variation due to the multi-phase microstructure morphology under the indentation spot (grain boundaries, IMC phases) varied from indent to

indent. These variations largely affected the deformation mechanism during indentation.

3. The Tabor approximation cannot be extended to all materials based on the composition results for one material.
4. The elastic modulus and yield strength measured using the nanoindentation technique is marginally comparable with the measured properties derived from microtensile testing.

Chapter 6: CREEP BEHAVIOUR OF LEAD-FREE SOLDER JOINTS

6.1. Introduction

Creep or time-dependent deformation behaviour of the solder or solder joints plays an important role in the design and reliability performance of microelectronic packages. Creep behaviour is difficult to quantify because it depends on a number of variables. However, for many microelectronic applications it is sufficient to describe the steady-state creep of the solder. The steady-state creep rate is a function of temperature, applied stress and time. Commonly, creep deformation exits in materials only at high temperature, but due to the lower melting points of lead-free solders, creep deformation does exist at room temperature [125]. This mismatch stress arises from the CTE of different materials in the micropackaging, which may act as creep stress during prolonged use and hence lead to the creep deformation, and may also cause the failure of the microelectronic components.

Morris et al. reported that solder joints in microelectronic packaging devices eventually fail by creep-fatigue interactions [126]. Wiese and Meusel reported that at room temperature, conventional solder (Sn-37Pb) and Sn-3.5Ag solders showed almost identical absolute creep rates at stresses above 15MPa, while SnAgCu solder attains the same level of creep at 40MPa [3]. Englemaier et al. showed that the number of cycles to failure may be reduced by increasing the holding time at the mismatch stress during the thermal cycling process [4]. This indicates that creep or fatigue failure of the microelectronic device can be reduced if the solder materials are developed with a lower CTE mismatch for interconnecting applications.

Previous work has proved that the addition of nano-sized particles to the SAC387 solder reduces the CTE mismatch [105]. Therefore, composite solders are expected to have a high resistance to failure during thermal cycling tests. McDougall et al. reported that for a 1mm^2 area, lap-shear SnAgCu solder joints with 20% (5–8μm) Cu_6Sn_5 reinforcements increase the number of cycles to failure because of particle strengthening [5]. On the other hand, Villain et al. reported that the creep deformation of solder joints is size-dependent [127]. There are also several indentation techniques, such as impression creep (constant stress) and indentation creep (constant load), to determine the localized creep properties of metallic materials [128]. Recently, nanoindentation creep experiments with a sharp indenter tip have been developed to probe the creep properties of bulk and thin films. Creep properties such as the stress-exponent can be extracted from a single experiment of the slope of the double logarithm of stresses and strain rates. Therefore, the present study focuses on the analysis of nanoindentation creep data with the Berkovich indenter tip over a wide range of lead-free solder joints, as shown in Table 6.1.

Table 6.1: List of lead-free solder materials studied in this work.

Solder	Process conditions	Microstructure
Virgin Sn3.5Ag balls	Thermal reflow at 260^{o}C for 80s	Cast microstructure
Virgin Sn3.8Ag0.7Cu balls	Thermal reflow at 260^{o}C for 80s	Cast microstructure
Pure Sn Bulk	Furnace cooled from 300^{o}C	>150μm Grain size
Pure Indium Bulk	Furnace cooled from 175^{o}C	>100μm Grain size
SnAgCu Bulk	Furnace cooled from 300^{o}C	>75μm Grain size
SnAgCu solder joint	Reflowed at 265^{o}C for 80s	Cast microstructure
SnAgCu+0.3%Mo joint	Reflowed at 265^{o}C for 80s	Cast microstructure

6.2. Materials and Methods

6.2.1. Indentation Creep Experiments

Nanoindentation experiments were conducted to derive the time-dependent deformation behaviour of the solder balls. Indentation experiments were performed at the maximum loads of 1.5 to 3.0mN, with an interval of 0.5mN for a 10s holding period to define the creep load for solder. This creep period was too short to include any plastic deformation due to creep. As such, any significant plastic deformation may not be attributed to the creep but to the loading. From the preliminary tests, it can be understood that the indentation load of 2.5mN or less does not cause any large plastic deformation in the 10-second holding time. The indentation creep experiments were then performed at the loading 2.5mN and holding for 1000s, and at least eight (8) successful indents were made to generate indentation displacement versus hold-time data for the indentation creep analysis. The stress exponent measured under these conditions is close to diffusion creep.

In order to capture the power-law creep behaviour for the solder joints, indentation loads were increased to 70mN to represent the bulk material behaviour. This 70mN load was limited by instantaneous depth, as a higher load gives a larger indentation depth, which is beyond the detection limit of nanoindentation equipment, i.e. if the total creep deformation is more than 2.5μm in depth, nanoindentation data acquisition cannot be made. Similarly, the maximum loads for cylindrical punch (CP) were limited to 40mN.

In the case of indentation experiments using a cylindrical punch or sharp indenter, the equivalent conventional tensile stress can be approximated from the Tabor relation:

$$\sigma_{indentation\ stress} = c\sigma_{tensile\ stress} \qquad (6.1)$$

where c is a constant, which was reported as 3~4 for β-Tin [127]. The constant c in this study was determined in Section 5.4 as 3.4 for SAC and 3.8 for β-Sn, based on the microindentation and microtensile data of the respective solders.

6.2.2. Data Analysis

A typical indentation load for the indentation creep experiments is plotted against creep time in Fig. 6.1. The total creep period for all experiments was kept constant at 2000s. Instantaneous creep depth at time zero was subtracted from the displacement-hold time data to compare the experiments at different loads. Figure 6.2 shows the effective indentation displacement-holding time data. The average indentation data was calculated by fitting the average function of the eight (8) sets of effective indentation displacement data to a given creep experiment condition. The indentation creep data of the lead-free solders was analysed via non-linear curve fitting, using commercial graphing software (*Origin Lab Pro 8.5*), to determine the properties for time-dependent deformation.

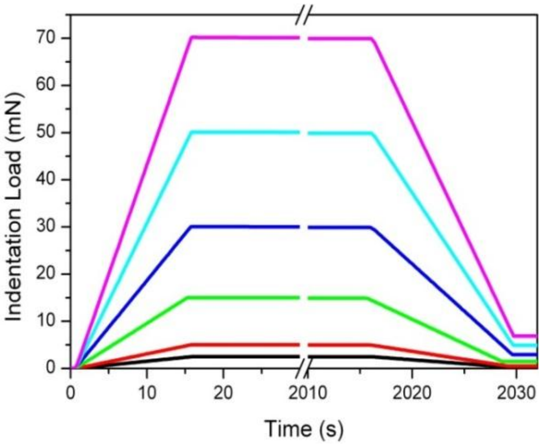

Figure 6-1: Representative indentation load versus holding time curves for pure Sn.

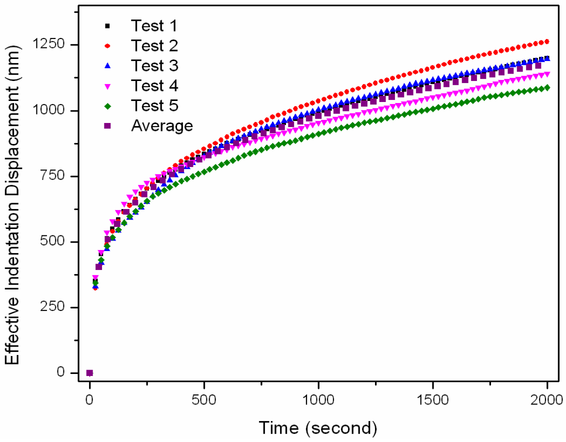

Figure 6-2: Typical indentation load versus holding time (h-t) mean curve generated at 2.5mN load for 1000s of SnAgCu VSB.

6.3. Results

6.3.1. Solder Microstructure

Thermally-treated solder joints are used to understand the creep performance of the solder joints by microstructural morphology and IMC particle (Ag_3Sn, $AuSn_4$ and Cu_6Sn_5) distribution in the solder bump. It is particularly important to compare and correlate the mechanical properties of the solder joints with the reliability performance of devices [129]. In traditional solder, *Sn* and *Pb* solidify in a simple eutectic system with limited miscibility. This leads to a solid solution strengthened by *Sn* and *Pb* phases, which are quite similar in plastic-deformation resistance. However, the binary system of Sn-Ag and Sn-Cu solidifies in a system with more complex intermetallic phases such as Ag3Sn and Cu_5Sn_6 [129].

Wiese et al. suggested that the deformation resistance of the Ag_3Sn and Cu_5Sn_6 phases is higher than that of *β- Sn* matrix, and so these phases might slow down or even prevent the dislocation motion. Chen et al. reported that for the SnAgCu system, binary and ternary eutectic phases are dispersed at the boundary of *β*-Sn dendrites, including some large Ag_3Sn and Cu_5Sn_6 IMCs [130]. The Cu_6Sn_5 IMC particles within the middle of the dendrites possibly behave as a heterogeneous nucleation site for the *β-Sn* dendrites.

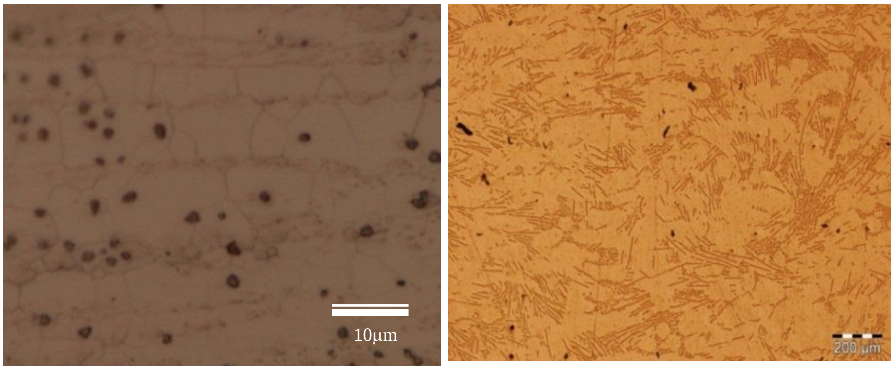

Figure 6-3: Optical microstructure of (a) wrought microstructure of SAC 387 (b) furnace-cooled SnAgCu solder.

Figure 6.3 (a) shows the fine intermetallic particle distribution in the β-Sn matrix, in which dendrites broke into small particles during the extrusion and rolling operation. These particles serve as effective barriers for plastic deformation. Figure 6.3 (b) shows the furnace-cooled SAC387 samples with finer dendritic morphology. Figure 6.4 shows the microstructure of the SAC387 solder bump with electrolytic Ni and ENIG surface-finishes. This multiphase microstructure of the SnAgCu solders leads to variation in the localized mechanical properties. For example, the elastic modulus of SAC387 solder has been reported to be in the range of 10 to 50GPa [131]. Huang et al. observed that this discrepancy could be attributed to specimen microstructure (bulk or solder joint), the specimen geometry (shape, dimension ratio, etc.), and test conditions [132].

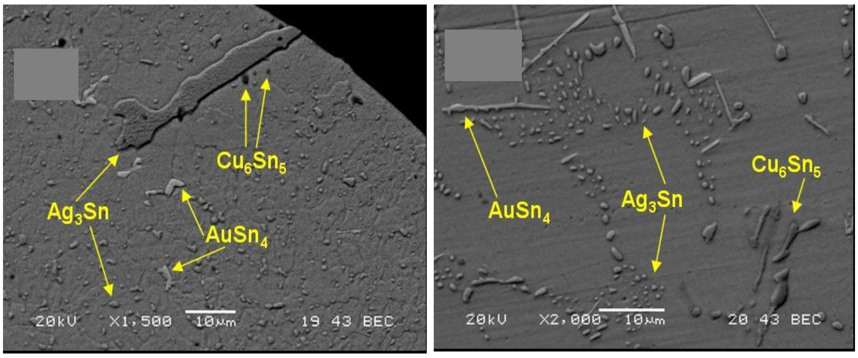

Figure 6-4: Microstructure of solder bump in (a) SAC387/Au/Ni (b) SAC387/Au/Ni (P) joints in as-reflowed condition.

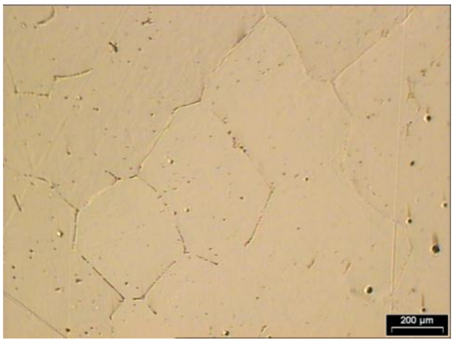

Figure 6-5: Optical microstructure of pure β-Sn (target material for PVD deposition).

Figure 6.5 shows the larger grain size in the as-cast furnace-cooled β-Sn. In this work, pure β-Sn and indium have been selected to understand the creep behaviour of the solders without the influence of the multiphase on the measured properties. Figures 6.6 to 6.8 show the post-indentation impression after the creep experiments. Indentation creep experiments were conducted on the pure Sn using the Berkovich and cylindrical punch at similar indentation stresses, in order to compare the creep parameters.

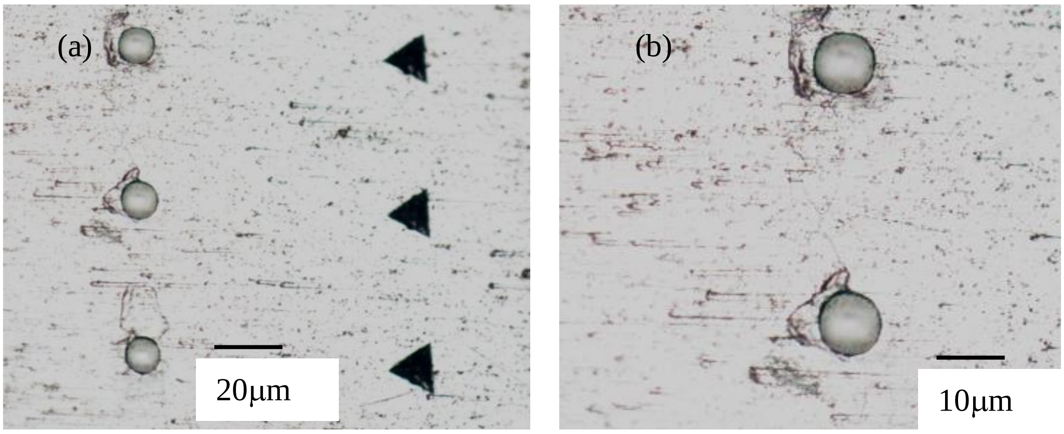

Figure 6-6: Indentation impressions of β-Sn with (a) Berkovich indenter (b) cylindrical punch.

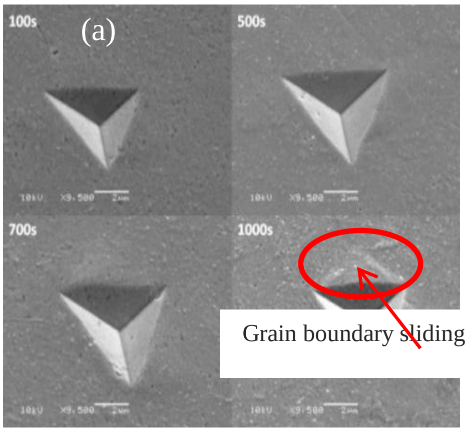

Figure 6-7: Indentation impression during creep process at 2.5mN load for (a) SnAgCu Virgin Solder Balls (VSB)

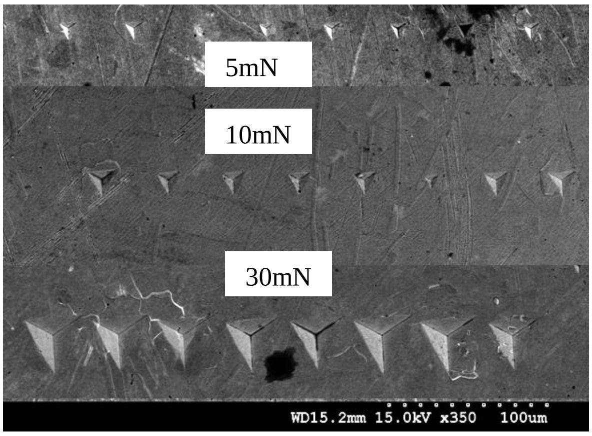

Figure 6-8: Indentation impression on bulk SnAgCu solder after indentation creep.

6.3.2. Indentation Creep models

A number of analytical models have been used to describe the creep behaviour of metallurgical materials since Andrade's pioneering work in 1914. In this study, an attempt has first been made to determine the best model for indentation time-dependent deformation behaviour of the lead-free solders.

The time-dependence of the creep strain in the primary and secondary stages may be described by an equation based on Andrade's law [133]:

$$\varepsilon = \varepsilon_o(1+\beta t^{\frac{1}{3}})\, e^{(\kappa t)} \qquad (6.2)$$

ε is the strain in time while β and κ are time-dependent constants. ε_0 holds the definition of instantaneous strain on loading and *t* is time. This model proposes that creep strain varies with a time exponent factor of 1/3. As discussed by Bernasconi and Piatti, having $t^{1/3}$ will not produce a steady-state creep; the primary creep rate is higher [133].

A modified Andrade's creep model is proposed as follows, to address the large primary creep deformation:

$$\varepsilon = \varepsilon_o(1+\beta t^{\gamma})\, e^{(\kappa t)} \qquad (6.3)$$

The only difference in the modified Andrade model is that the time exponent (γ) is varied instead of fixed at 1/3. Furthermore, considerable success has been achieved in describing the strain, ε_o, obtained through the primary and secondary creep stages by using the Garofalo model. In this model, ε_t is the limit for transient creep, and r is the time-constant for the primary stage:

$$\varepsilon = \varepsilon_0 + \varepsilon_t (1 - e^{(-rt)}) + \frac{d\varepsilon_{ss}}{dt} t \qquad (6.4)$$

ε_o represents instantaneous creep, $\varepsilon_t (1 - e^{(-rt)})$ represents transient creep and $\frac{d\varepsilon_{ss}}{dt}$ represents steady-state creep. Garofalo's model was used successfully to describe the creep deformation behaviour of austenitic stainless steels, cadmium, tungsten, nickel, zinc and iron [134]. However, the primary creep deformation using Garofalo model varies over 10–15%, in such way that the actual creep rates are more than predicted. There is another model called Kraus's model [133, 135, 136]:

$$\varepsilon = A(\sigma)(1 - e^{(-q(\sigma)(t))} + B(\sigma)(1 - e^{(-s(\sigma)(t))}) + \left(\frac{d\varepsilon_{ss}}{dt}\right) t \qquad (6.5)$$

$A(\sigma)$, $B(\sigma)$, $q(\sigma)$ and $s(\sigma)$ etc. are parameters with a function of stress. This model resembles Garofalo's model, which is the basis for further refining of Garofalo's creep model. It can be understood from the experimental data that the individual transient creep term $\varepsilon_t(1-e^{rt})$ in Eq. (6.4) does not capture the behaviour of transient creep. A modified Garofalo model based on Eqs. (6.4) and (6.5) is therefore proposed, and is given as:

$$\varepsilon = \varepsilon_0 + \varepsilon_t (1 - e^{(-rt)}) + \varepsilon_{t_1} (1 - e^{(-r_1 t)}) + \frac{d\varepsilon_{ss}}{dt} t \qquad (6.6)$$

An additional transient creep term was added to Garofalo model, based on Kraus's model as shown in Eq. (6.5). This extra transient creep term in the modified Garofalo's model is expected to capture the creep deformation in metals and alloys.

6.3.3. Adaptation of Creep model

By definition, strain, $\varepsilon = \Delta L / L$, is the ratio of elongation to the original gauge length of the specimen. Applied stress, $\sigma = P/A$, is defined as the ratio of the load to the area exposed to the load. In the case of the indentation, P is the indentation load while contact area (A) is defined as the projected contact area under the indenter tip ($A=24.56h^2$). Analogous to the definition of $\varepsilon = \Delta L/L$, the strain during the nanoindentation creep is defined as $\varepsilon = \Delta h / h_o$, Δh being the creep displacement at constant load, while h is the creep displacement. The modified Garofalo's model is analogous to the Kelvin-Vigot model, and therefore Eq. (6.6) may be adapted to indentation creep in the form:

$$h = h_0 + \alpha\left(1 - e^{-t/\tau_1}\right) + \beta\left(1 - e^{-t/\tau_2}\right) + \zeta t \qquad (6.7)$$

with $\alpha, \beta, \zeta, \tau_1$ *and* τ_2 as unknown constants to be found [137]. The term h_0 is analogous to ε_0 , which is used to characterize instantaneous displacement at time zero. However, this term does not change the shape of the creep curve; hence h_o is subtracted from the data to enable a comparison of the materials studied.

6.3.4. Indentation Creep on Virgin SAC387 Balls

Indentation creep experiments were conducted on virgin solder balls (VSB) in an as-cast microstructure condition. Standard lead-free thermal treatment was performed on the VSB before the creep experiments (Appendix A.4.4). VSB was used for the creep study in order to understand the indentation creep deformation of the solder matrix, without the influence of under bump metallization (UBM). These creep experiments were conducted on the reflowed SAC387 solder joints with Cu and Ni (P) UBMs, in order to study the effects of the UBM on creep performance. Based on the preliminary creep analyses with the existing creep models, the Andrade and Garofalo-based models were selected for analysing the SAC387 data.

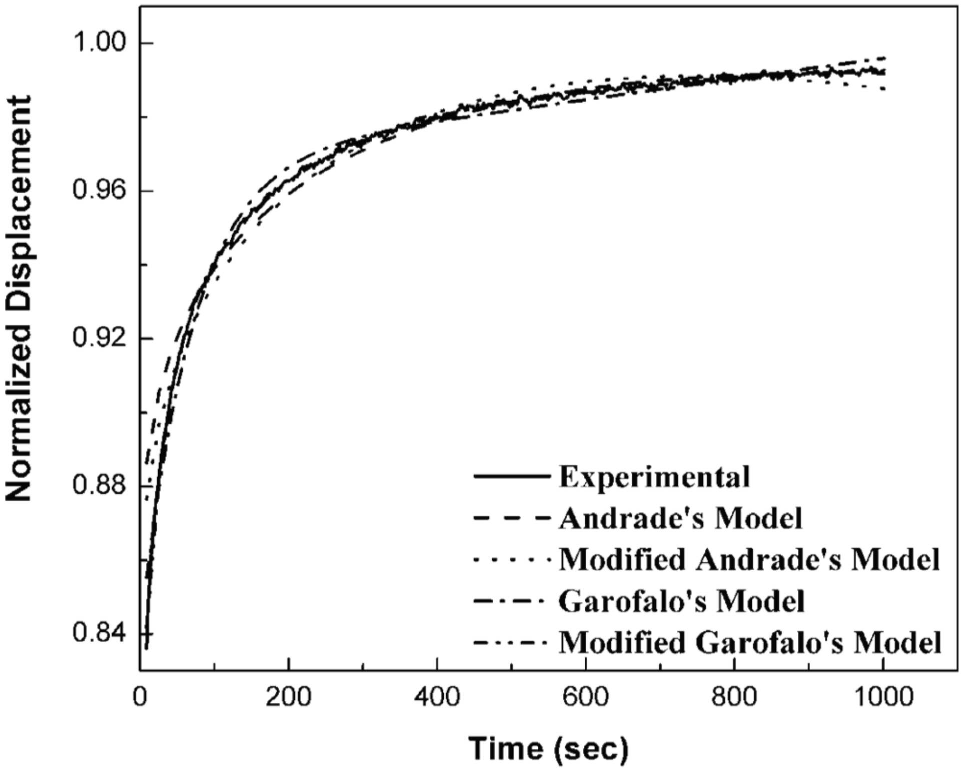

Figure 6-9: Curve-fitting behaviour of SnAgCu VSB using different creep models

Figure 6.9 shows the prediction of the creep behaviour of SnAgCu solders with the Andrade and Garofalo-based models. Table 6.2 shows the fitting parameters of these models. The *Chi*^{2}*/Degree of freedom* values are statistically very close to the ideal value of zero. The R^2 values are also quite close to the ideal value of one (1) for a perfect curve fit when using the modified Garofalo model. It can be observed from Fig. 6.9 (a) that the modified Andrade model gives a better fit for the initial part of the creep curve but a poorer fit as time increases. Figure 6.9 (b) shows the curve-fitting representative of SAC387 VSB with Garofalo's and the Modified Garofalo's Creep (MGC) model. Garofalo's model is not very effective in characterizing transient creep, and slightly over-estimates the creep rate of SAC387 solder.

6.3.5. Graphical Analysis of SnAgCu Solder Balls

Based on the statistics of the MGC model on SnAgCu VSB, the R^2 value and Chi^2/*Degree of freedom* were found to be 0.99655 and 2.26 x10^{-06}, respectively. This model shows better accuracy in creep characterization relative to the other models. It is not surprising that Andrade's creep model ranks the last among the models due to a fixed time-exponent of 1/3. The actual time exponent obtained from analysis for the SnAgCu solder material is 0.42 (Table 6.2). The time-exponent value plays a crucial role in the curve-fitting.

Table 6.2: Curve-fitting analysis of individual creep models for SnAgCu VSBs.

Parameter	**Andrade**	**Modified Andrade**	**Garofalo**	**Modified Garofalo**
h_o	0.84	0.84	0.84	0.84
α	0.02723	0.01773	0.12807	0.0588
τ_1	-0.00007	-0.00013	0.01442	0.0040
β	0.3333	0.42969	------	0.0912
τ_2	------	--------	---------	0.0214
ζ	------	--------	0.00003	3.471x10^{-6}
Chi^2/Degree of Freedom	0.00003	0.00002	6.503 x10^{-6}	2.264x10^{-6}
R^2	0.95411	0.96883	0.99007	0.99655

6.3.5.1. Significance of Modified Garofalo's Model Terms

As the time increases, there is a transition from the primary creep region to the steady-state secondary creep. This is clearly shown when the steady-state viscous term, ζ, in Eq. (6.7) becomes more prominent as time progresses. The parameter ζ in Eq. (6.7) is analogous to the term of $d\varepsilon_{ss}/dt$ in Eq. (6.4). ζ is a displacement rate, which is used for the determination of the indentation strain rate.

6.3.5.2. Analysis of Time Constants, τ_1 and τ_2

Keeping the other parameters constant, the graph of indentation *h-t* data was re-plotted using Eq. (6.7), with a selected time exponent, τ_1 as 16, 48 and 96, to analyse the effects of the time constants on the predicted creep curve. Although the curve with the lowest value of τ_1 =16 shows a steeper gradient at the initial stage of the creep compared with the other curves, all 3 curves eventually merge at 700s with the experimental data. Different time exponent values (τ_1) have no effect on the period of primary creep.

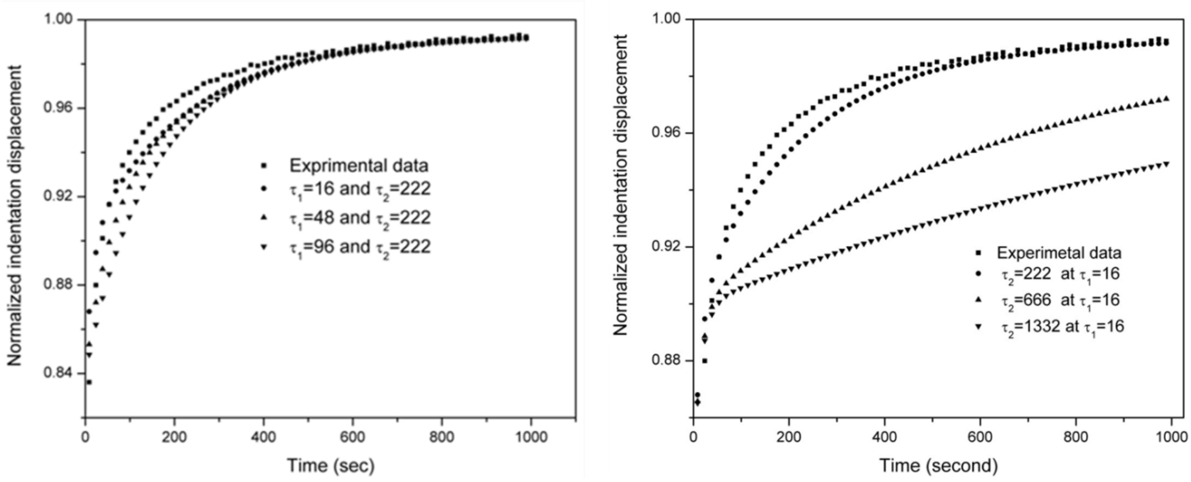

Figure 6-10: Indentation creep data fitted using the modified Garofalo's model with different time constants τ_1 and τ_2

This in turn suggests that the time exponent τ_1 has a larger influence on the initial stages of the primary creep, and in particular determines the gradient of the initial creep curve, or the initial creep rate. A smaller τ_1 will give rise to a steeper gradient on the initial creep curve – in other words, the smaller the time constant, τ_1, higher the initial creep rate. Similarly, an analysis of τ_2 was performed by holding the other parameters constant and re-plotting the indentation creep data with selected time exponents, such as 222, 666 and 1332, to analyse the effects on the predicted creep curve (Fig. 6.10 (b)).

The time exponent (τ_2) shows a distinct effect on the initial stages of the primary creep curve compared with τ_1, as the curves are along the same gradient and subsequently diverge from one another at about 50s. The figure shows a possible trend of the larger time exponent, τ_2 , leading to a longer period of primary creep. The curve with the smallest time exponent, τ_2 , reaches the end of the primary creep at 750s, which is earliest of all the curves. The curves will converge eventually after 1000s during the transient, steady-state stage, and τ_2 has no influence on the initial creep rate. It can also be observed that at a fixed time, for example, 100s, the modified Garofalo model with smaller τ_2 value shows higher deformation.

Table 6.3: Summary of normalized indentation displacement rate of virgin solder balls (VSBs).

Solder	Normalized Indentation rate	Condition
Sn36Pb	2.9×10^{-3}	Virgin solder balls (VSB cast microstructure condition
Sn3.5Ag	1.47×10^{-4}	VSBs- cast microstructure condition
Sn3.8Ag0.7Cu	3.47×10^{-6}	VSBs -cast microstructure condition
Sn3.8Ag0.7Cu	2.47×10^{-5}	As-reflowed SAC387/ENIG

From these analyses, it can be deduced that τ_1 has a stronger influence on the initial creep rate of the primary creep, while τ_2 has a stronger effect on the later stages of the primary creep. Similar analysis was conducted on the creep data of the Sn-36Pb and Sn-3.5Ag VSB, and the results are summarized in Table 6.3. The SAC387 solder shows better creep resistance compared with that of the traditional Sn-36Pb solder (Table 6.3). This analysis methodology is most suitable for a qualitative comparison of the newly-developed solder materials before they are selected for in-depth creep assessment.

6.3.6. Indentation Creep Behaviour

6.3.6.1. Analysis of Time-dependent Deformation

Figure 6.11 shows the average of the indentation displacement (*h*)-holding time (*t*) curves from the eight (8) data sets for pure Sn (β-Sn) at different maximum loads. Figure 6.12 shows the h-t curve generated at a constant creep load (30mN) using the Berkovich indenter. Traditionally, displacement rates are determined using linear regression from the steady-state region of the indentation creep data [138]. However, this method may not be used to differentiate the primary and secondary stages of the creep if the curve-fitting period is short. Usually, the primary creep region also gives a perfect fit with the linear models, provided the period of creep data considered is short.

An empirical creep model recently proposed by Li and Ngan is widely used to determine the indentation creep behaviour of thin and thicker films, as given below [139]:

$$h(t) = h_i + \beta(t - t_i)^{\frac{1}{m}} + kt \qquad (6.8)$$

where β, m, k are fitting parameters. This model fits indentation creep data with $R^2 > 0.99$.

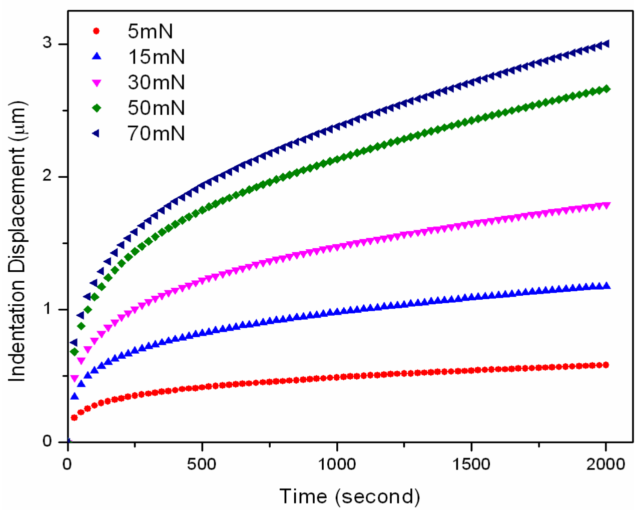

Figure 6-11: Average indentation displacement versus holding time for β-Sn.

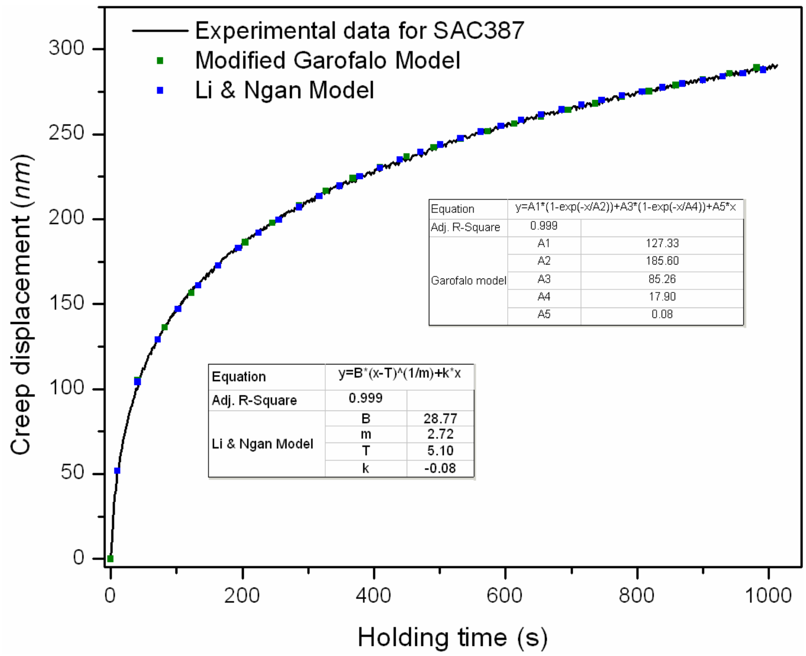

Equation	y=A1*(1-exp(-x/A2))+A3*(1-exp(-x/A4))+A5*x	
Adj. R-Square	0.999	
Garofalo model	A1	127.33
	A2	185.60
	A3	85.26
	A4	17.90
	A5	0.08

Equation	y=B*(x-T)^(1/m)+k*x	
Adj. R-Square	0.999	
Li & Ngan Model	B	28.77
	m	2.72
	T	5.10
	k	-0.08

Figure 6-12: Representative non-linear curve-fitting plots using modified Garofalo and Li & Ngan creep models for creep data for SAC387 solder joints.

However, among the creep rates determined from Eq. (6.8), primary creep and steady-state creep rates cannot be distinguished. Goodall and Clyne critiqued the source of errors associated with the fact that most of the material under stress was likely to be in the primary creep regime [140]. Therefore, the measured strain rates will tend to be higher than those assumed for steady-state creep. The MGC model has been demonstrated to be one of the most suitable creep models for analysis of indentation creep data for the softer materials [141, 142].

The parameters in Eq. (6.7) are defined as a function of applied load and indentation displacements based on the generalized Kelvin model [141]. The physical meanings of the terms and parameters in Eq. (6.7) are discussed elsewhere [142]. This model demonstrates both experimental and FEM simulations on polymeric materials, and could well describe the indentation creep data generated with the Berkovich tip [143, 144]. An attempt being made to apply this model to describe the indentation creep behaviour of composite solder joints.

The indentation creep data was analysed using the *Levenberg-Marquardt* least-square method with the fitting parameters as unknowns. Figure 6.12 describes the representative curve-fitting using the Li and Ngam and MGC models for the SAC387 solder, in an as-reflowed condition at the maximum indentation load of 2.5mN. Both models fit accurately with a correlation coefficient of $R^2 = 0.99$. The indentation displacement rate can be found by differentiating Eqs (6.8) and (6.7):

$$\frac{dh}{dt} = \frac{\beta}{m}\left(t - t_o\right)^{\frac{1}{m}-1} + kt \qquad (6.9)$$

$$\frac{dh}{dt} = \frac{\alpha}{\tau_1} e^{-\frac{t}{\tau_1}} + \frac{\beta}{\tau_2} e^{-\frac{t}{\tau_2}} + \zeta \qquad (6.10)$$

6.3.6.2. Representative Strain Rate and Stress

Mulhearn and Tabor studied the hot-hardness of indium and lead using a spherical indenter, and indicated that the hardness as a function of time correlated closely with the creep characteristics of the materials [145]. They assumed that the strain rate at any stage in the indentation process could be written as $\dot{\varepsilon}_{\mathrm{I}} = \frac{1}{\mathrm{D}}\frac{\mathrm{da}}{\mathrm{dt}}$, where *a* is the radius of contact and *D* is the diameter of the spherical indenter. Atkins and Tabor extended this analysis to the indentation data generated on a range of materials using spherical, conical, and Vickers indenters [122]. They determined that the creep process was not dependent on the indenter shape, and the deformed zone resembled that predicted by the radial compression model for the indentation [146]. The representative strain is defined as $\dot{\varepsilon}_I = \dot{a}/a$, where a is the radius of contact at a given time. Pollack et al. defined the indentation strain rate for conical indentation as follows: $\mathrm{K}\frac{1}{\mathrm{h}}\frac{\mathrm{dh}}{\mathrm{dt}}$, where K is a dimensionless constant [147]. Mayo and Nix proposed a generalized equation for the representative strain rate and stress of a pyramidal indentation, which was [138]:

$$\dot{\varepsilon} = \frac{1}{h}\frac{dh}{dt} \qquad (6.11)$$

and

$$\sigma = \frac{P_{\max}}{24.56h^2} \qquad (6.12)$$

where h is the indentation displacement at a given time.

This proposed representative strain rate and stress was supported by the theoretical calculations of Bower et al. [148], and also by Cheng and Cheng, who used scaling and dimensional analysis [149]. In the present study, representative strain rates and stresses were calculated using Eqs (6.11) and (6.12) for the entire indentation displacement. For the purpose of comparing the creep rates of different solder joints, the representative strain rates were determined at 1000s holding time. Because of a higher indentation displacement (h_o) at time zero ($t = 0$), the representative strain-rate solder was lower than that of composite solder joints. Therefore, an effective creep displacement ($h-h_o$) was used in the calculation of the representative strain rate, in order to compare the representative strain rates of the different solders.

Table 6.4: Representative strain rate (s^{-1}) and stress (GPa) at 1000s holding.

Solder Joint	Representative strain rate (s^{-1}) at 1000s holding	Representative stress (GPa) at 1000s holding
SAC387	1.80×10^{-4}	0.08
SAC387+0.3Ni	1.04×10^{-4}	0.14
SAC387+0.3Mo	7.10×10^{-5}	0.23

Table 6.4 shows a summary of the representative stresses and strains for the composite solder joints at a 1000s hold period. The representative stress for SAC387 solder is 0.08GPa, which is lower than that of the composite solder (0.23GPa) at the 1000s holding time. This shows that composite solders have better creep resistance at room temperature. In order to prove these analyses further, low-melting metals such as pure Tin and Indium were selected as room-temperature indentation creep exponents.

6.3.6.3. Indentation Behaviour of Pure Sn

Figure 6.5 shows the initial grain size of the pure Sn that was studied for the indentation creep experiments. The average grain size of β-Sn is ~300 to 350µm, and therefore the nanoindentation experiments were conducted within the β-Sn grains. Total indentation depths during the nanoindentation experiments exceeded 2.5µm for all of the loads used in this study. These larger depths ensured that the indentation impression covered a considerable volume, so that it represented the global mechanical properties of the specimen during the nanoindentation experiments. Figure 6.8 shows that the size of the indentation impression increases with the maximum holding load. At higher indentation loads, the indentation properties represent the global properties. The effective indentation creep displacements increase from 1µm to 3µm with increase of the maximum load increment from 5mN to 70mN.

The experimental indentation data follows two stages of the transient creep stage, i.e. a faster decay primary creep region followed by a slower decay primary creep region before attaining the steady-state region. This transient creep stage extended to ~300 to ~700 seconds as the load increased from 5mN to 70mN. Most of the indentation creep parameters reported by the data were obtained within 300s creep time. In this study, indentation creep experiments extended up to 2000s, with the effects of the stress exponent studied over a range of indentation depths.

6.3.6.4. Li and Ngan Empirical Model

This model fits accurately the experimental indentation creep data for most of the materials, with a correlation coefficient (R^2) of more than 0.99. The non-linear curve fitting parameters for Eq. (6.8) are summarized in Table 6.5. At lower maximum loads, the parameter (k) is negative and then becomes positive at higher maximum loads. Therefore, individual parameters in Eq. (6.8) do not show any physical significance.

Table 6.5: Curve-fitting parameters of the β-Sn holding segment with Li and Ngan model.

Holding Force (mN)	***B***	t_0	***m***	***k***	R^2
5.0	90.4	4.851	4.075	-0.00196	0.9988
15	164.4	4.287	3.858	-0.00247	0.9991
30	210.3	3.441	3.515	-0.02141	0.9995
50	315.0	4.442	3.680	0.08535	0.9993
70	341.4	3.867	3.658	0.13083	0.9994

The indentation size effect (ISE) is dominant at lower holding periods in the solder materials, which are widely studied using Eq. (6.8). Indentation displacement rates were calculated using Eq. (6.8) for the entire creep data. The representative strain rate and stresses were then calculated using Eqs (6.11) and (6.12), respectively. Figure 6.13 (a) describes the representative strain rate versus holding time for β-Sn. There is a significant change in the creep strain rate at 500 seconds. Similar trends were observed for the indentation stress, which was reduced with the holding time at the maximum creep loads. This is because of the initial high displacement rate, which consists of the ISE. Conversely, the magnitudes of the representative strain rates decrease with an increasing maximum hold load because of higher instantaneous indentation displacement.

Figure 6.14 (a) shows the representative curve-fitting using the Li and Ngan creep model for the indentation creep data generated at 30mN load. Figure. 6.14 (b) shows the representative log (σ)-log ($\dot{\varepsilon}$) plots for different indentation loads. The stress exponents were determined for different periods of creep time, and the results are summarized in Table 6.6. The change in the stress exponent is from 6 to 5 for a 5mN load, and from 3.5 to 2.5 for a 70mN load after a 500s holding period, which is almost insensitive to the indentation creep loads. Representative strain rates and stresses were reduced significantly to a minimum value as the creep time progressed at the maximum load; this phenomenon may be attributed to the ISE. A similar study also reported using this empirical model on the nanoindentation creep data of SAC387 solder [150].

Table 6.6: Stress exponent (n) determined using Li & Ngan Model.

Load (*mN*)	**1500- 2000s**	**1000- 1500s**	**500- 1000s**	**100s - 500s**
2.5	1.029	1.175	1.655	3.367
5	5.068	5.392	6.125	7.046
15	4.412	4.831	5.362	6.402
30	4.080	4.527	4.865	5.590
50	2.797	3.177	3.970	5.049
70	2.565	3.013	3.760	5.120

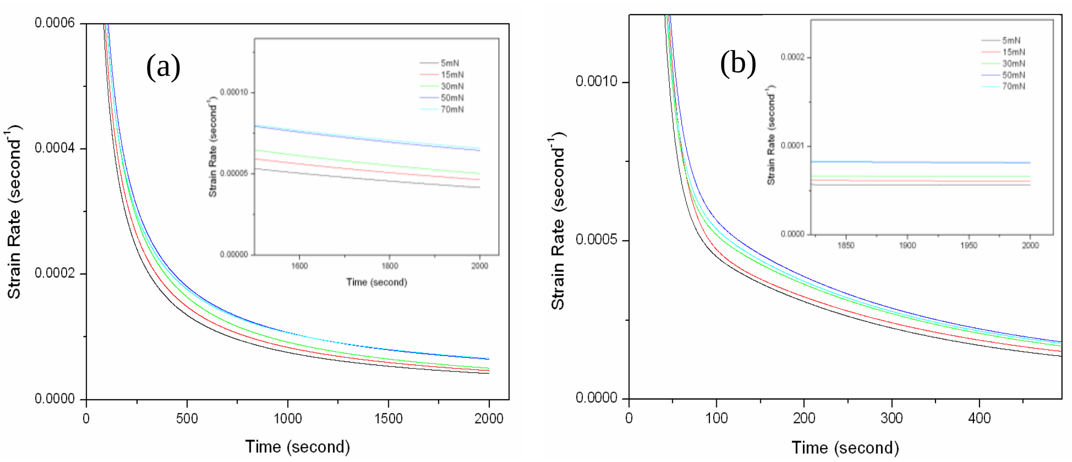

Figure 6-13:(a) Representative strain rate versus holding time data generated using (a) Li and Ngan model (b) Garofalo model.

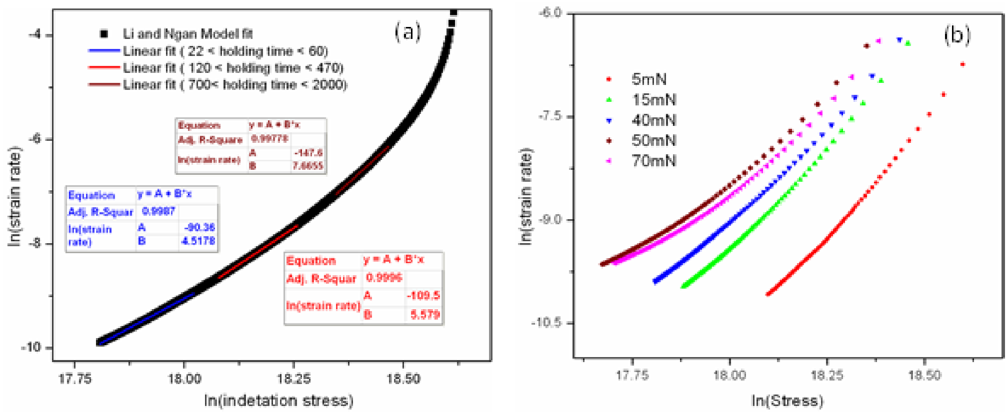

Figure 6-14: (a) Representative stress exponent measurement at 30mN maximum (b) comparison of stress exponent data at all maximum loads fitted with Li and Ngan model.

6.3.6.5. Modified Garofalo Creep (MGC) Model

Similar to the Li and Ngan model, the MGC fits accurately with the experimental indentation creep data for all the maximum holding loads (see Fig. 6.12 and Table 6.7). The representative indentation strain rates and stresses were calculated using Eqs (6.11) and (6.12). The insert of Figure 6.13 (b) shows that the representative strain rate is parallel to the time axis at the later stage of the creep data. Figure. 6.15 (a) shows the log-log plots of representative strain rates versus indentation stress, which give the stress exponent at 30mN maximum indentation load. These logarithmic plots show three distinct stages, which correspond to each term in the MGC model.

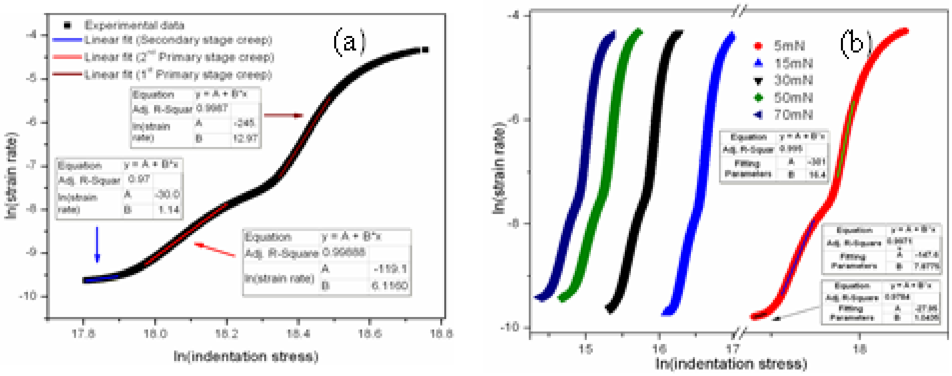

Figure 6-15: (a) Representative stress exponent measurement at 30mN maximum (b) Stress exponent over a range of maximum loads fitted with the MGC.

Table 6.7: Non-linear curve-fitting parameters of β-Sn fitted using the MGC.

Holding Force (*mN*)	α	τ_1	β	τ_2	ζ	R^2
5.0	194.0	14.5	204.0	258.3	0.094	0.99875
15	389.9	16.8	403.7	281.4	0.196	0.99921
30	634.4	15.0	547.5	282.5	0.310	0.99939
50	844.7	16.0	774.2	262.9	0.532	0.99935
70	930.2	15.2	838.2	259.2	0.626	0.99938

Figure 6.16 shows the super-imposition of three models between creep times of 1200 to 2000s. The MGC and linear models have a parallel trend after a creep period of 1500s. However, the Li and Ngan model shows continuous change in the slope of the log strain rate and log stresses. At larger creep displacements (depths), indentation stresses underneath the indenter were reduced to a minimum value, and therefore the slope of this curve is virtually constant. Moreover, at lower stresses, the possible creep mechanism is diffusion creep. But the Li and Ngan model predicts that the stress exponent is equivalent to the power law creep at a lower stress regime. These results suggest that the MGC model predicts the stress exponent values more accurately for the load-free solder materials.

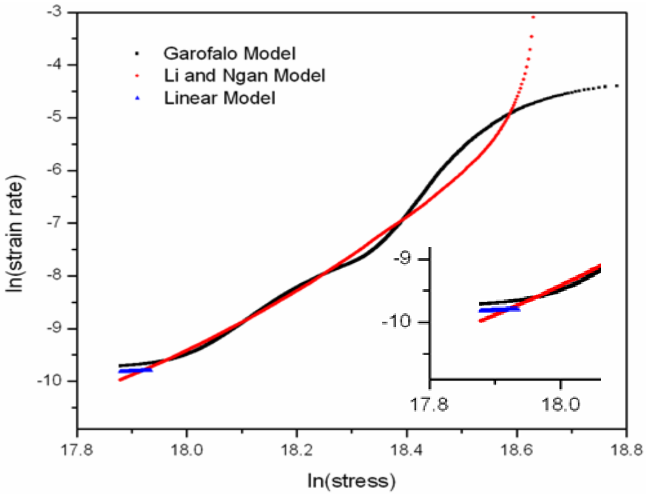

Figure 6-16: Superimposition of different creep models on pure Sn creep data at 30mN.

6.3.6.6. Cylindrical Punch Data

The MGC model was further validated using cylindrical punch indentation creep experiments. Unlike the Berkovich indentor, the cylindrical punch experiences a constant stress during the creep experiments. Figure 6.17 (a) shows the *h-t* curves generated at different maximum hold loads for β-Sn. The steady-state indentation displacement rate was calculated using the MGC and linear models. Both these models yielded the same results. The indentation strain rate and stress are defined for the cylindrical punch as follows [128]:

$$\dot{\varepsilon}=\frac{1}{D}\frac{dh}{dt} \tag{6.13}$$

$$\sigma=\frac{4\times P_{max}}{\pi D^2} \tag{6.14}$$

where D is the diameter of the indenter. Figure 6.17 (b) shows the log (σ)-log ($\dot{\varepsilon}$) plots of data generated using the cylindrical punch; the slope of the log (σ)-log ($\dot{\varepsilon}$) curve is 0.88, which is close to one (1). This indicates that the dominant creep mechanism at larger indentation depths (or lower stress) is a diffusion creep. Based on the cylindrical punch creep data, it can be concluded that the MGC model is more rational for extracting the creep properties of lead-free solder materials.

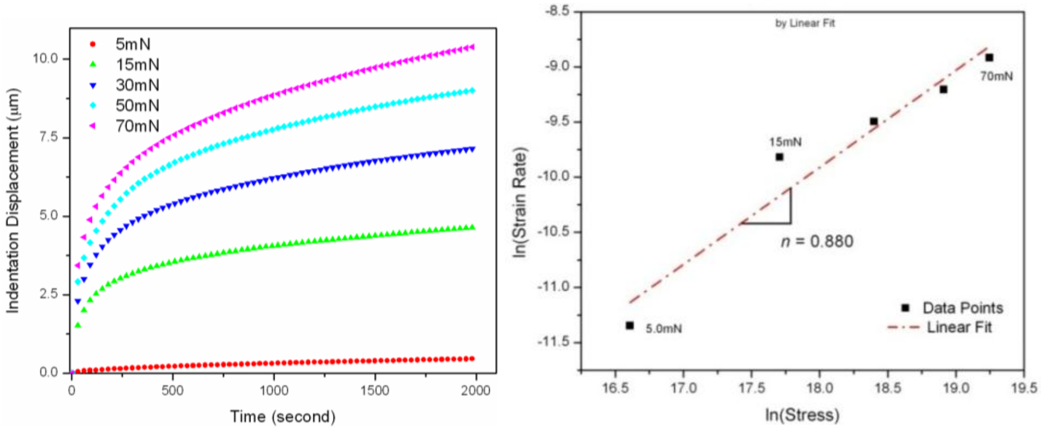

Figure 6-17: (a) Representative Indentation creep (h-t) curves generated under cylindrical punch (b) Stress exponent of pure Sn under cylindrical punch tests.

6.4. Discussion

6.4.1. Stress Exponent

Goodall and Clyne reported that a major source of errors in indentation displacement rates measurements has to do with the fact that much of the material under stress is likely in the primary creep regime [140]. The measured displacement rates or strain rates will tend to be higher than those assumed for steady-state creep. Most of the nanoindentation experiments are conducted over a shorter duration, and the high gradients of stresses and strain rates in the vicinity of the indenter, and the continuously increasing size of the deformation zone, contribute to the ISE. Therefore, indentation displacement rates measured over the short period of creep experiments will affect creep parameters such as the stress exponent and activation energy.

May and Nix determined the stress exponent of coarse-grain β-Sn using the indentation creep method and found that the value was about 11.4, which is higher than that reported by conventional tensile creep tests [138]. Similar studies have also been conducted on polycrystalline Sn at room temperature, and the stress exponent obtained was about 6 to 8. Nai et al. found that the room-temperature tensile stress exponents for SAC387 and SAC-reinforced with 0.04% CNT were 8.8 and 11.3 at a high stress regime, while at a low stress regime it was about 4.5 for both SAC387 and composite solder [151].

Han et al. studied the effects of indentation maximum load on the stress exponent of the SnAgCu solder, and found the stress exponent to be in the range of 6 to 8 [152, 153]. Purisotham et al. determined that the stress exponent for Sn3.5Ag0.5Cu/Cu solder joints using impression creep techniques is about 4.6 [154]. The creep stress-exponent variation might be due to differences in materials preparation, microstructure, data acquisition and analysis methodology.

Table 6.8: Stress exponent obtained from the Li and Ngan Model.

Load (*mN*)	**(1500s < *t* < 2000s)**	**(1000s < *t* < 1500s)**	**(500s < *t* < 1000s)**
5.0	5.068	5.392	6.125
15	4.412	4.831	5.362
30	4.080	4.527	4.865
50	2.797	3.177	3.970
70	2.565	3.013	3.760

Table 6.9: Stress-exponent of β-Sn obtained using Garofalo's model.

Load (*mN*)	**Stage-III**	**Stage-II**	**Stage-I**
5.0	0.982	8.251	16.55
15	0.988	6.842	12.64
30	0.998	6.221	13.03
50	0.997	5.502	11.48
70	0.933	5.518	12.79

Tables 6.8 and 6.9 summarise the stress exponents derived using the Li and Ngan and MGC models, for three time segments. The experimental data shows that the stress exponent decreases with the stress at a longer holding time (see Fig. 6.14). Unlike in the modified Garofalo model, there are no abrupt changes in the gradients (stress-exponents)

in the log-log plots when using the Li and Ngan model. The stress exponent shows the power law creep regime (Table 6.8) that is not supposed to operate at a low stress regime and high temperature. On the contrary, the stress exponent measured using the Garofalo model was close to one (1), which represents the diffusion creep. The representative equivalent tensile stresses determined using Eq. (6.1) under the indenter at a longer holding period (i.e. 1500 to 2000s), are summarized in Table 6.10. The possible creep mechanism at lower stress and 0.65 homologous temperatures is diffusion-controlled. Therefore, the stress exponent measured using the Garofalo creep model is more acceptable than that of any other model, for lead-free solder materials.

Table 6.10: Typical indentation presentation stress with increased maximum load during indentation creep of β-Sn.

Load (mN)	Instantaneous depth (h_o ,nm)	Creep depth (h_c , nm)	Total depth (h_o+h_c , nm)	σ_i (MPa)	σ_t (MPa)
5.0	1095.8	400.0	1495.8	91.0	28.3
15.0	2062.8	600.0	2662.8	86.1	26.8
30.0	2957.2	1200.0	4157.2	70.7	22.0
50.0	3899.9	2400.0	6299.9	51.3	15.9
70.0	4648.9	2950.0	7598.9	49.4	15.3

A similar creep analysis was conducted using the MGC on furnace-cooled SAC387 solder indentation creep data. A summary of the stress exponents at different maximum loads is given in Table 6.11. The ISE is very significant in SAC387 solder within Stage I (Table 6.11).

Table 6.11: Stress exponent over a range of depths for the furnace-cooled SAC387 solder.

Load (*mN*)	Stage-III	Stage-II	Stage-I
2.5	0.635	3.135	12.44
5	0.988	8.272	16.44

15	0.994	6.997	13.38
30	0.998	6.469	13.29
50	0.939	5.636	11.72
70	0.832	5.654	12.90

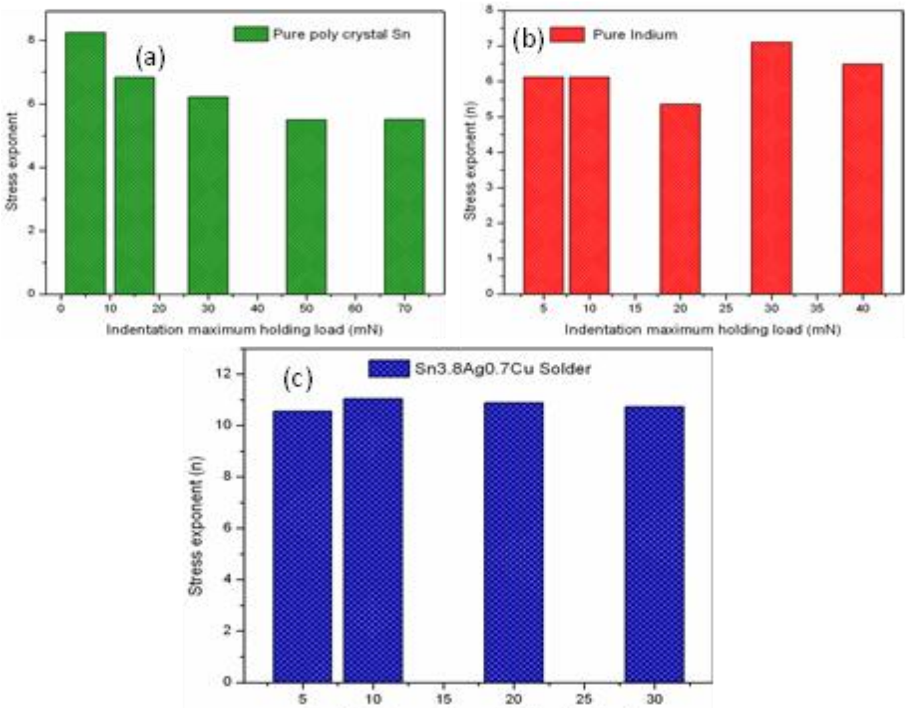

Figure 6-18: Indentation size effect (ISE) on (a) polycrystalline β-Sn (b) indium (c) SAC387

Figure 6.18 shows the ISE on the pure polycrystalline β-Sn, indium and furnace-cooled SAC387 solders. These experiment results show that the ISE is more prevalent in β-Sn compared with indium and SAC387 solder at a creep period of 1000s. This may be because of the anisotropy of β-Sn compared with the SAC387 or indium.

6.4.2. Stress Exponent of Composite Solder Joints

The room-temperature stress exponent for as-reflowed SAC387 solder joints was found to be 7.6, while for SAC387+0.3Ni and SAC387+0.3Mo solder joints, it was 6.2 and 6.7 at a high stress regime, respectively, and 6.0 and 5.5 at a low stress regime, respectively (see Fig. 6.19 and Table 6.12). Therefore, the stress exponent determined from the MGC model (n = 7 to 8) is comparable with that reported by existing literature [151–153].

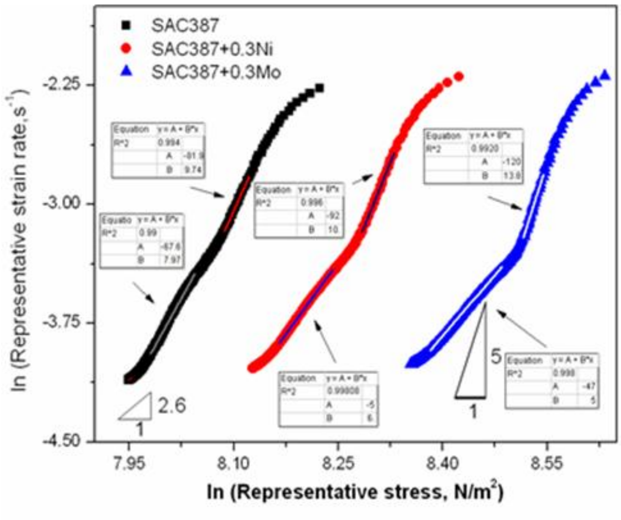

Figure 6-19: Log-log plots of strain rate versus stress for composite solder joints.

6.4.3. Effect of Nano-sized Ni and Mo Particles

Figure 6.20 shows that the additions of nano-sized Ni or Mo particles to the SAC387 solder reduce the indentation displacement rates at a given holding period. The representative strain rates of the SAC387+0.3Ni and SAC387+0.3Mo solder joints were found to be 1.04x10^{-4} s^{-1} and 7.1x10^{-5} s^{-1}, respectively, whereas the representative strain rate was about 1.8 10^{-4} s^{-1}for SAC387 solder, which is almost one order of magnitude higher than that of the SAC387+0.3Mo composite solder.

Table 6.12: Stress exponent of composite solders measured using conventional compression creep experiments at room temperature.

Solder	Low stress range	High stress range
SAC387	4.8	11.5
SAC387+1Mo	7.9	17.2
SAC387+2Mo	8.7	19.8

The addition of nano-sized Mo particles to the SAC387 solder was found to be more effective in terms of improving creep resistance of the SnAgCu solder joints than the addition of nano-sized Ni particles.

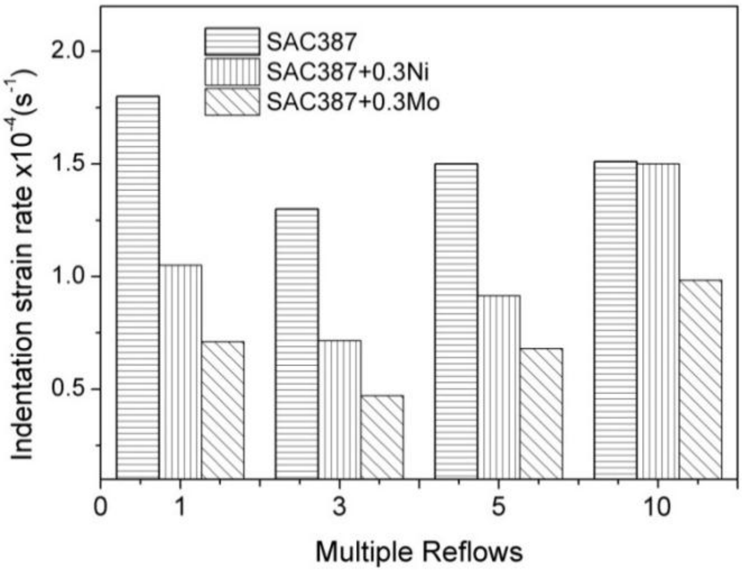

Figure 6-20: Effects of multiple reflows on steady-state representative strain rates at the 1000s hold time of SAC387 composite joints.

6.4.4. Effect of Reflows

During the thermal reflow processes, the solder bump experiences a temperature increase from room temperature to a temperature about 45°C above the melting point of the solder, for about 80 seconds. The fabrication process of the microelectronic packages involves at least two thermal reflows. The first reflow forms an area array of solder bumps on the chip surface, and the second reflow bonds the chip to the substrate. In the multi-chip integration, multiple reflows are needed depending on the number of chips to be integrated in a package.

The primary effect of early reflows is to strengthen the solder by microstructural refinement and formation of fine IMC particles during the cooling of the solder joints [155]. Levis et al. reported that the shear strength of the solder bumps increases in proportion to the reflow times [156]. Figure 6.21 shows that the microstructure changes of the SAC387 solder bumps are up to five (5) times of the reflows. Similar changes in microstructural features with multiple reflows were observed in Sn-3.8Ag [157] and SAC387 solder joints with the ENIG surface-finish [158].

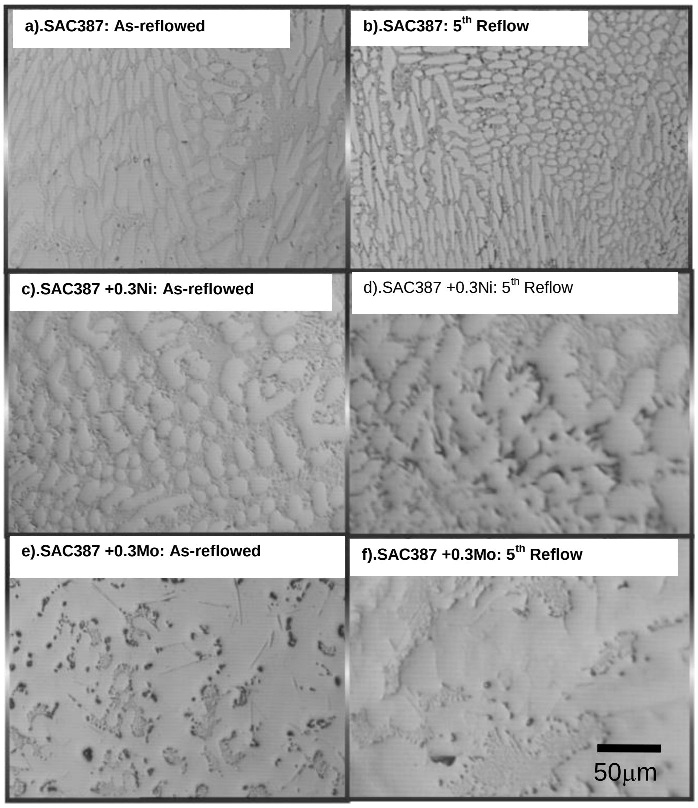

Figure 6-21: Microstructure changes of the SAC387 ((a) and (b)) SAC387+0.3Ni ((c) and (d)) and SAC387+0.3Mo ((e) and (f)) with reference to multiple reflows.

In this work, it was found that the β-Sn dendrites (the white regions in Fig. 6.21) coarsen with the thermal reflows at the same reflow temperature; and the representative strain rate increases from the 3rd reflow onwards. The size of the β-Sn dendrites in the microstructure during thermal reflow may affect the secondary creep behaviour of the SAC387 and SAC387 +0.3Ni solder bumps. The solder bumps are in a molten state during reflow, which helps the individual constituent elements inter-diffuse within the solder bump and form IMCs during solidification. Subsequent multiple reflows further increase the size of the existing IMC particles within the solder bump, as well as at the interfacial intermetallic thickness. This phenomenon is aggravated further by the multiple reflow processes.

Therefore, it can be deduced that the microstructure changes in the SAC387 during reflows may have significant effects on the mechanical behaviour of the solder joints. Figure 6.20 shows the effect of thermal reflows on the representative strain rate at a specified stress for the SAC387 and composite solder joints. The representative strain rate decreased up to three reflows, and then increased with additional reflows. Similar effects were also observed on the SAC387 solder with an addition of nano-sized Ni particles.

During initial reflows, the Ni-Sn IMCs were precipitated from the solder matrix due to the limited solubility of Ni in the Sn. These fine Ni-Sn IMCs improve creep resistance of solder through the particle-strengthening mechanism. However, these precipitates are not stable in the solder matrix, and subsequent reflows facilitate growth of the IMC particles at the expense of other IMC precipitate in the solder. Therefore, after the 10th reflow, the creep resistance of the SAC387+0.3Ni solder was similar to that of the SAC387 solder during the indentation creep experiments.

For the SAC387+0.3Mo solder joints, the magnitude of representative strain rates is about one order lower than for the SAC387 and SAC387+0.3Ni solder joints. Mo nano-particles are thermally stable in the Sn matrix because the self-diffusion coefficient at 25^{o}C is negligible (in the order of 10^{-37}cm/s), and the chemical segregation of Mo in the Sn matrix due to diffusion is rarely possible. Moreover, these nano-sized Mo particles in the solder matrix may serve as effective barriers for dislocation motion during indentation creep testing.

6.4.5. Creep Mechanisms

During an indentation process in very small indents, the deformation zone is very close to the free surface, so the characteristic diffusion lengths from underneath the indenter and the nearby free surface become short. For large indentations, the room-temperature diffusion may become inadequate as diffusion paths are longer and deformation is expected to approach the bulk behaviour. Mavoori et.al. reported that grain-boundary sliding, dislocation glides and climbs are the most active deformation mechanisms in the solders [125]. Figure. 6.6 shows an indented impression for SAC387 VSB solder at 1000s of creep time, and a grain boundary may be observed sliding in the indented impression. It is evident that the solder joint undergoes grain-boundary sliding during the creep process at room temperature. A similar observation was observed in bulk SAC387 solder during room-temperature indentation creep (see Fig. 6.7).

It was found that the stress exponent is close to unity at greater depths. This suggests that the mechanism is likely to be diffusion-controlled. From Table 6.10, representative stress (σ_i) and equivalent tensile stress (σ_t) under the indenter are reduced by three orders of magnitude (i.e. to 20MPa from 2GPa). Moreover, at greater depths, the volume of the plastically-deformed region is relatively high, i.e. there is a high dislocation density structure under the indenter that may cause diffusion flow to occur more easily. This is because dislocation channels may act as effective short-circuiting diffusion paths for the transport of atoms from the highly-stressed indent core to the stress-free specimen surface.

At lower indentation depths, indentation stress was in the order of 1 to 2GPa, and the stress exponent was found to be more than 9, which is the power law break down the regime, this is due to dynamic plastic deformation. Wiese et.al. reported that a high stress regime for SAC387 solders predominantly causes particle shearing and bowing between particles, which does not depend much on temperature [3]. This accounts for the higher stress exponents at a high-stress regime.

As indentation depth progressed, the stress exponent in the β-Sn was reduced from 6 to 1. This indicates that the creep mechanism changed from dislocation creep to diffusion creep. As illustrated in Tables 6.9 and 6.10, the steady-state stress exponent was reduced to 1 as indentation depth increased during the creep process for both the β-Sn and SAC387 solders. For coarse crystalline metals, dislocation is often the dominant creep mechanism, whereas for fine-grain materials, grain-boundary diffusion or grain-boundary sliding dominates [3, 150]. It has also been reported that grain-boundary sliding is predominant at low stress and moderately high temperatures [150].

These results are contrary to the findings of other investigators, which state that the room-temperature stress exponent increases with an increase in P_{max}. There are two reasons for this: (1) A lower indentation creep period, i.e. the ISE is higher during the initial period of creep testing; and (2) The strain-hardening effect of metallic materials. The homologous temperature is more than 0.65 for Sn, where diffusion flow is more prominent. When nanoindentation experiments were conducted on β-Sn with different maximum loads, the stress exponent measured for the entire range of maximum loads after 300s was close to one (1). The equivalent tensile stress (Eq. 6.1) after 300nm depth may be compared to the low-stress regime in conventional tensile creep. Therefore, the MGC model is more capable of characterizing the nanoindentation creep behaviour of solder joints.

6.5. Summary

1. The MGC model is the best model to characterize the indentation creep behaviour of lead-free solders.
2. The MGC model may be used successfully to analyze the time-dependent deformation behaviour during the nanoindentation creep experiments for the SAC387 and composite solders.
3. The addition of the nano-sized Ni particles to the SAC387 solder lowers the indentation creep rate to a minimum at the third reflow, and subsequently increases the indentation creep rate with additional multiple reflows.
4. There are no effects on time-dependent deformation from multiple reflows in the SAC387+0.3Mo solder joints.

Chapter 7: MECHANICAL PROPERTIES OF IMCs IN SOLDER JOINTS

7.1. Introduction

The mechanical characterization of interfacial intermetallic compounds (IMCs) in the lead-free solder joints is a challenging task because of lower IMC thicknesses. The hardness and elastic modulus of these thin IMC layers can be influenced by the adjacent under-bump metallurgy (UBM) and solder bump. Most of the thin-film UBM applications, such as Ni(V)/Au, Au/Sn and Ni/Cu/Cu joints, approximate IMC thicknesses of not more than 2 to 2.5μm. Therefore, characterization of the ultra-thin IMC layer in a micro-sized solder joint system is difficult because the measured properties of the IMCs are influenced by the adjacent UBM or solder on either side of the interface. The ranges of the elastic modulus of the Cu-Sn IMCs have been reported as 90~125GPa and 115~145GPa for Cu_6Sn_5 and Cu_3Sn, respectively [62–64, 161]. The elastic modulus of the Cu-Ni-Sn and Ni-Cu-Sn IMCs have been reported as 160~205 and 140~170GPa respectively [65].

The discrepancy in the elastic modulus and hardness is due to the solder-joint specimen fabrication conditions, such as the time and temperatures during the aging or reflow process. The longer aging period or higher temperatures cause thicker IMC layers for nanoindentation experiments [63–66, 161–163], but also alter the microstructure of the IMC, which strongly influences the mechanical properties. There has been an attempt to determine the mechanical properties of only the IMC phase (Cu_6Sn_5) using a micro-pillar compression technique [66]. However, the measured properties were strongly affected by the texture and dimensions of the pillar. Table 7.1 shows the typical range of mechanical properties for various IMCs in lead-free solder joints [1, 59, 62, 65, 66, 161, 163–169].

Nanoindentation with CSM attachment is used for extraction of the mechanical properties of multilayer thin films. This method was developed especially for homogeneous materials [170]. Nevertheless, the nanoindentation method is usually applied to solder-joint systems to determine the IMC's mechanical properties without explicit consideration of the effects of the UBM or solder bump. The indentation response for IMC on UBM, or IMC on IMC, is a complex function of the elastic and plastic properties of intermetallic layers and the UBM (Fig 7.1).

Table 7.1: Mechanical properties of individual phases in the lead-free solder joints.

Material	Elastic Modulus (GPa)	Hardness (GPa)
Cu	110 ~128	1.5 ~ 2
Ni	185~210	5 ~7
Cu_6Sn_5	85 ~110	4 ~ 6
Cu_3Sn	130 ~150	5 ~ 7
$(CuxNi_{1-x})_6Sn_5$	150 ~210	5 ~ 7
$(NiyCu_{1-y})_3Sn_4$	130 ~150	5 ~ 8
Ni_3Sn_4	130 ~150	3.5 ~ 7

In order to determine 'only IMC' properties, a commonly-used rule-of-thumb is to limit the maximum indentation depth to less than 10% of the total IMC thickness [171]. This rule is experimentally suitable for a uniform IMC with thicknesses between 5 and 10µm, but this method is not suitable for thin IMC layers with irregular thicknesses. Therefore, an alternative method is required to take into consideration the effects of the UBM or solder bump, as well as the thin and irregular thicknesses of the IMCs.

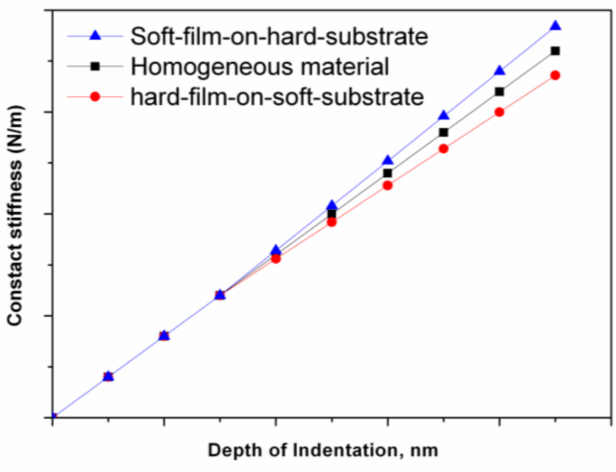

Figure 7-1: Schematic graph showing substrate effects during nanoindentation experiments of multi-layer IMCs in the solder joints.

The objective of this work is to determine the hardness and elastic modulus of the interfacial intermetallic layers from ball grid array (BGA) solder joints and microbump solder joints. Initially, the nanoindentation experiments were conducted on the BGA solder-joint systems with different surface finishes. A 300μm-sized SAC387 solder joint was selected to determine the baseline mechanical properties. Indentation experiments were conducted in different solder joint orientations, such as top, standard and taper cross-section solder joints, in order to verify the dependence of the mechanical properties on the texture of the interfacial IMC layers. Due to the polycrystalline nature of IMCs, the IMCs measured on the standard cross-sectioning (Fig. 7.2), top view sectioning (Fig. 7.3) and taper cross-sectioning (Fig. 7.4) were more or less similar [61].

For the taper samples, solder-bumped dies were first mounted in a taper position using epoxy resin, following which the bumped dies were sectioned and polished horizontally (Fig. 7.4). Söderlund et al. used this approach in their study of the indentations of multilayer structures, and these samples were termed taper samples [172]. Owing to the slanted nature of the IMC layers in the taper position, the thickness of IMC layers usually varies from zero at the UBM side to the actual thickness at the solder side

(Fig. 7.5). Therefore, depending on the locations of the indents on the IMC layer, i.e. whether the indent is close to the solder or UBM side or in the middle of the IMC layer, the materials underneath may or may not affect the indentation properties. At both sides of the IMC layer, the effects of the underlying layer on the measured hardness and elastic modulus need to be separated.

Therefore, the analysis of nanoindentation for thin films can be adopted in such cases [173–180]. If the indents are located in the middle of the layer, the layer may be considered to represent the near-true properties of the IMC. On the other hand, if the indents are made near the sides of the IMC layers, Joslin and Oliver's approach [177], which was developed for extracting the thin-film properties from nanoindentation of film/substrate systems (hard-film-on-soft-substrate or soft-film-on-hard-substrate), can be used to remove the substrate effect caused by the underlying UBM or solder on the measured IMC properties. Depending on the position of the indentations on the IMC layers, substrate can be considered either hard-film-on-soft-substrate, i.e. Sn-Cu IMC layer on Cu UBM substrate, or soft-film-on-hard-substrate, i.e. Ni-Cu-Sn IMC layer on Ni substrate [65, 165].

In particular, two kinds of film configurations in the lead-free solder joints were studied, i.e. Cu_6Sn_5 and Cu_3Sn IMC layers on Cu substrate (hard-film-on-soft-substrate), and Ni-Cu-Sn IMC layers on Ni substrate (UBM) (soft-substrate-on-hard-film). This approach was also extended to the determination of the mechanical properties of ultra-fine-pitch thin-film solder-joint systems, including In/Sn/Cu, Sn/Cu, SnAg/Cu, SnAgCu/Cu,Sn3.5Ag/ENIG, SnAgCu/ENIG and SnAgCu/Ni (V) microbump joints. The test results were compared with the reported values for IMC layers in the lead-free solder joints [1, 62, 65, 161, 164–169, 181–187].

7.2. Experimental Methodology

7.2.1. Standard Cross-sectioning

The standard method of cross-sectioning is suitable for larger solder joints with interfacial IMC thicknesses of more than 5µm. Under standard microelectronic fabrication conditions (Fig. 7.2 (a)), the maximum thickness of the IMC is usually less than 5µm. Figure 7.2 (b) shows multiple reflows (three times) of Sn/Cu microbump solder joints (10µm thickness and 40um diameter). The total thickness of the IMC layers in these solder joints is not more than 4µm. Determination of the mechanical properties over the standard cross-sectioned solder joints is difficult without the influence of adjacent layers. This is because the plastic zone underneath the indenter is usually a spherical shape; the size of the plastic region is proportional to the depth of indentation [188].

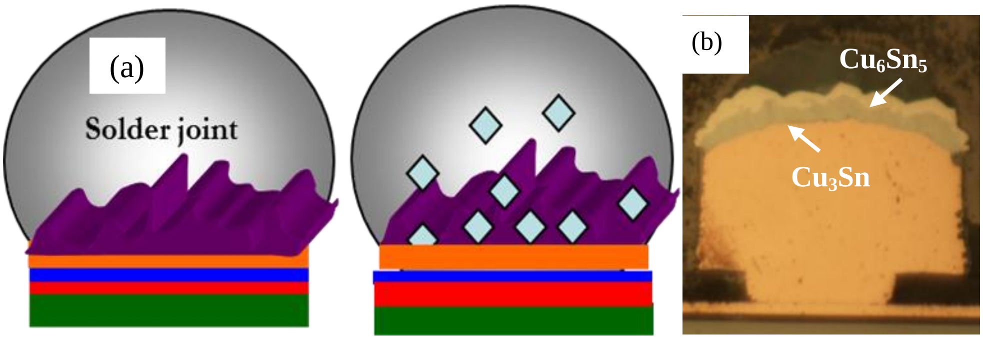

Figure 7-2: Standard cross-sectioning (90^o) of microbump solder joint.

Under the standard indentation testing conditions, the plastic zone volume can be extended to the adjacent UBM or solder layers, which have different elastic-plastic properties. Therefore, the slope of the unloading curve is affected by the elastic recovery of the adjacent layers. To overcome this, a top-sectioned approach is proposed, which allows assessment of the mechanical properties of ultra-thin film IMCs.

7.2.2. Top Sectioning

There have been some attempts to characterize the interfacial IMCs in the top sectioned solder joints using nanoindentation. This approach has its own challenges as IMC layers are usually thin and not consistent. Moreover, sample preparation is tedious and there is a need to prepare different samples for each IMC layer [59, 65]. Figure 7.3 describes the typical top-sectioned joints for indentation experiments.

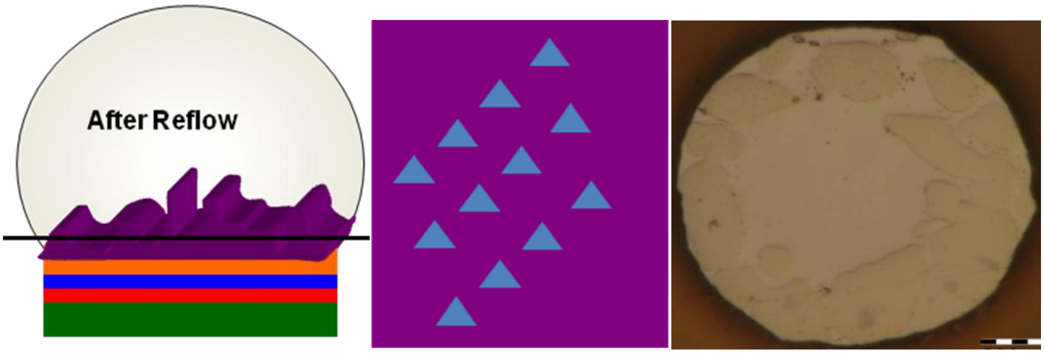

Figure 7-3: Top cross-sectioning (0^o) of microbump solder joint.

7.2.3. Taper Section

Taper cross-sectioning involves mounting the solder die at an angle using epoxy resin cold casting as described schematically in Fig. 7.4. The standard metallographic procedure is used to grind and polish the mounted samples to make a planar view of the surface.

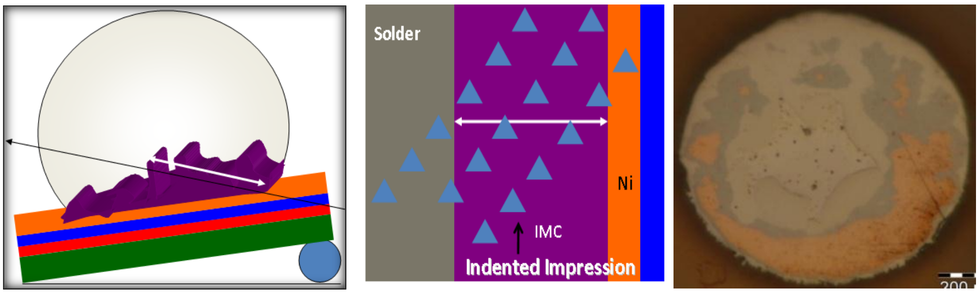

Figure 7-4: Schematic diagram describing the taper sectioning of the solder joint for nanoindentation testing.

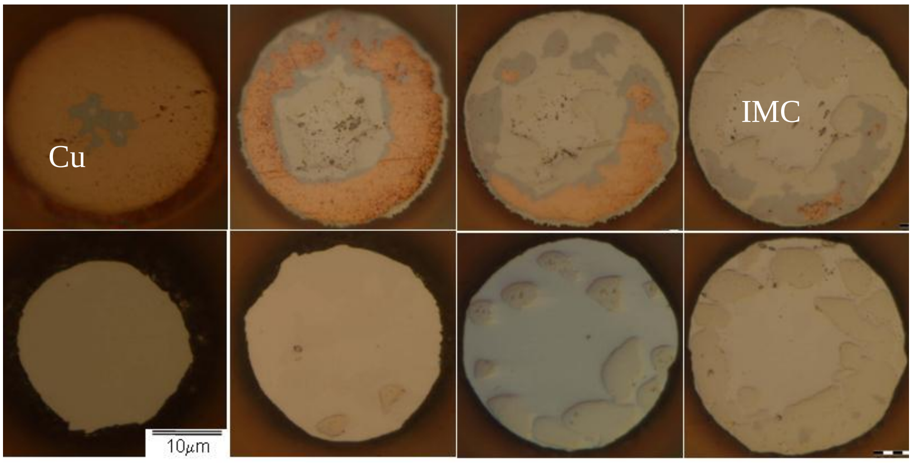

Figure 7-5: Taper-sectioned die shows the Cu UBM, IMCs and solder in a single die.

Since these samples are sectioned at an angle, the exposed IMC layers reveal a wider interfacial IMC area for microbump solder joints (Fig. 7.5), enabling the indentation tests to be conducted at the planar-view surface [61, 172].

7.2.4. Nanoindentation

In this study, the maximum depth of indentation is about 500nm for larger-thickness IMCs (solder joint sizes > 200µm), and with thinner IMCs the depth of indentation is limited to 300nm (solder join size < 100µm). The Poisson ratio of the material being tested is assumed to be 0.32 [189].

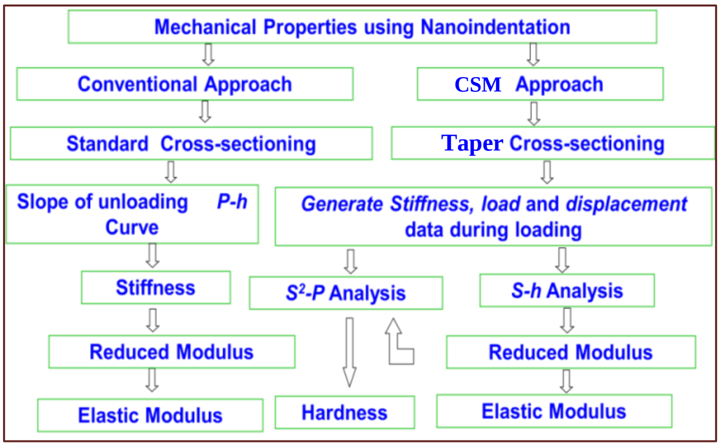

Figure 7-6: Schematic flow describing the differences between the traditional and S-h/S^2-P methodologies for nanoindentation analysis.

The taper-sectioned microbump joints increase the chances of indentation on the right IMC regions. The depth of indentation space between the adjacent indents was fixed at 10 to 30μm, to ensure that these results were not affected by neighbouring indents. The indentation data was analysed using commercial software (Origin Pro 8.0) for determination of the gradients of the S-h (stiffness-displacement) and S^2-P (stiffness^2-load) curves. A typical analysis approach was used to determine the mechanical properties of intermetallic films in the ultra-fine pitch solder joints described in Fig. 7.6.

7.3. Analysis Methodology

7.3.1. CSM Approach

The continuous stiffness measurement (CSM) approach has significantly improved the capabilities of nanoindentation systems. A small sinusoidal signal is imposed on a DC signal to drive the motion of the indenter, and the response of the system is analysed using a frequency-specific amplifier. As a result, a harmonic force is imposed and adds to the normal load which acts on the indenter. The phase angle between the two forces and indentation displacement at corresponding excitation frequency is continuously measured as a function of depth. The contact stiffness can be expressed as a function of depth by solving for the in-phase and out-of-phase segments of the response.

Figure 7.7 shows how the indentation system can be expressed as a simplified dynamic indentation model, and the overall response is dependent on the mass of the indenter (m), the compliance of the load frame (C_f), stiffness of the indenter frame (K_f), the spring constant of the leaf springs supporting the indenter (K_s), the damping coefficient due to the air in the gaps of the capacitor system (C), and the contact system. The imposed driving force can be expressed as

$$P = P_{os} \exp(i\omega t) \qquad (7.1)$$

The displacement response of the indenter is

$$h(w) = h_o \exp(i\omega t + \phi) \tag{7.2}$$

The displacement signal can be expressed as

$$\frac{P_{os}}{h(w)} = \sqrt{\left\{\left(\frac{1}{S}+\frac{1}{K}\right)^{-1} + K_s - m\omega^2\right\}^2 + \omega^2 C^2} \tag{7.3}$$

The phase difference can be expressed as

$$\tan\left(\phi\right) = \frac{\omega C}{\left(\frac{1}{S}+\frac{1}{K}\right)^{-1} + K_s - m\omega^2} \tag{7.4}$$

Therefore, the contact stiffness can be determined from the displacement signal or phase difference as

$$S = \left[\frac{1}{\frac{P_{os}}{h\left(w\right)}\cos\phi - \left(K_s - m\omega^2\right)} - K_f^{-1}\right]^{-1} \tag{7.5}$$

where P_{os} is the magnitude of oscillation load, $h(w)$ is the magnitude of the resulting displacement conciliation, ω is the frequency of the oscillation and φ is the phase angle.

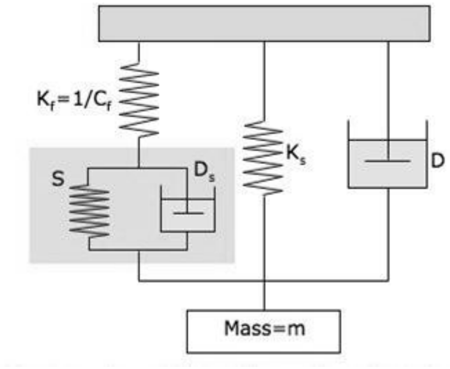

Figure 7-7: Schematic of the dynamic indentation model [190].

The CSM method usually generates contact stiffness (*S*), indentation displacement (*h*) and indentation load (*P*) at a given frequency. Amit and Zeng have developed analysis methodology to determined mechanical properties of multilayer films using CSM data, and their method was successfully demonstrated on several thin-films and multi-layer thin-films [191, 192].

7.3.2. *S*-*h* and S^2-*P* Analysis

Careful attention has to be paid to the analysis of the nanoindentation data obtained from the solder-joint system. The most crucial thing is to ensure the indents are on the correct regions, so these indents can be located after indentation tests. Moreover, due to the slanted nature of the sample, there is a need to ensure sufficient depth of the IMC under the indentation sites. Several researchers have focused on extracting the elastic modulus and hardness directly from the portion of the graphs where the elastic modulus and hardness are independent of depth [59, 65, 166, 169]. Such an approach minimises the contributions from sink-in brittle materials and pile-up from plasticity, which may cause the contact area to be either overestimated or underestimated respectively. This would therefore improve the accuracy of the results. However, the approach fails to take into account the effects of the underlying substrate layer, which may affect the results adversely. As the depth of indentation increases, the effects from the underlying materials may also increase, and thus the measured mechanical properties become composite values of the underlying and top-layer materials.

In this study, the calculation of the elastic modulus and hardness is based on Joslin and Oliver's approach [177], in which the mechanical properties of the IMC layers are analysed using the parameter P/S^2 as a function of the indentation depth to minimise the effects of the underlying materials. For a perfect contact indenter tip, the contact area is

$$A = 24.56 h_c^2 \tag{7.6}$$

and

$$h_c = h - \varepsilon \frac{P}{S} \tag{7.7}$$

where h_c is the contact depth and $\varepsilon = 0.75$ is a constant. For a homogeneous material, the elastic modulus (E) is a constant and S is the linear proportion to the indentation contact depth according to Eq. (5.4). Combining Eq. (5.4) with Eqs. (7.6) and (7.7), and then rearranging the equation gives

$$S = \frac{2}{\sqrt{\pi}} \beta E_r \sqrt{24.56}\, h - \delta \tag{7.8}$$

By plotting the harmonic contact stiffness S against displacement h for each of the indentation tests – namely, the S-h curve – the gradient of the linear portion of the graph can be equated to $2/\sqrt{\pi}\,\beta E_r \sqrt{24.56}$ and the value of E_r can be determined (where $E_r = \frac{E}{1-\vartheta^2}$, is the reduced modulus and $\delta = \frac{2}{\sqrt{\pi}} \frac{\beta\, E}{1-\vartheta^2}\, \epsilon\, \frac{P}{S}$ is the intercept of the S-h

curve). In addition, if the hardness relationship $H = P/A_c$ is substituted into Eq. (5.4) and the terms are rearranged, a new equation is obtained [177]:

$$\frac{S^2}{P} = \frac{4}{\pi}\beta^2 E_r^2 \frac{1}{H} \tag{7.9}$$

This equation suggests that for a homogeneous material with constant elastic modulus and hardness, S^2/P is a constant and independent of indentation depth, *h*. By plotting S^2 against *P* – namely, the S^2-*P* curve – the gradient of the linear portion of the graph can be equated to $4/\pi\,\beta^2 E_r^2\,(1/H)$, and the value of *H* can be determined if E_r is known. It may be observed that the ranges for the linear portion of the *S*-*h* curves and the S^2-*P* curves may not correspond. In this case, the range of *h* for which E_r is a constant should first be determined, and this range would be mirrored onto a range of indentation loads, *P*. Within this range of *P*, the linear segment for which hardness is a constant would then be determined. The “reduced modulus” E_r takes indenter deformation into consideration. To find the elastic modulus of the sample, the following equation is used:

$$\frac{1}{E_r} = \left(\frac{1-\nu_i^2}{E_i}\right) + \left(\frac{1-\nu_m^2}{E_m}\right) \tag{7.10}$$

where *E* and ν are the elastic modulus and Poisson ratio respectively, and the subscripts *i* and *m* refer to the indenter and sample, respectively. For the commonly-used diamond indenter tip, E_i = 1141GPa and ν_i = 0.07.

7.4. Results

7.4.1. Oliver and Pharr Method

Fig. 7.8 shows the typical load (*P*) displacement (*h*) curves of different phases of the SnAg/Cu microbump solder joint. It can be understood from the *P*-*h* curve that the hardness of the Cu_3Sn phase is higher than that of the Cu_6Sn_5 phase, since the former takes a higher load to reach 500nm indentation depths. The stiffness of the IMCs in the solder joint was determined from the slope of the unloading curve using the Oliver and Pharr method. However, elastic recovery of indentation displacement (h_e) during the unloading curve strongly depends on the elastic modulus of the indented materials.

For homogeneous and bulk material, the elastic recovery during unloading is the true representation of the indented material. However, for multilayer material, the elastic recovery is a composite effect of the indented underlying layers, since the indenter passes through the different distinct layers of materials, which gives a composite elastic recovery. Sometimes, cracking of the IMC layer may take place during the indentation. This cracking process releases the elastic energy to create new surfaces in the IMC layer. This phenomenon affects the elastic recovery of materials during the unloading indentation process.

The indentation behaviour of the IMC phases also depends on the rate of loading/unloading during the indentation process. Fig. 7.9 shows the effects of the indentation strain rate on the loading/unloading behaviour of the *P-h* curves. At lower strain rates, elastic recovery is offset by creep deformation, which thus lowers stiffness, while at higher strain rates with no creep effects, the measured stiffness will be higher.

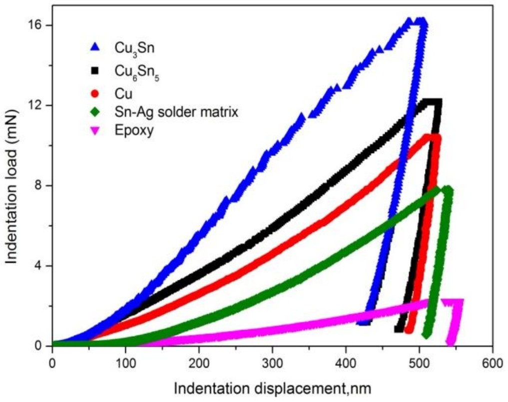

Figure 7-8: Representative P-h curves for SnAg/Cu microbump solder joint.

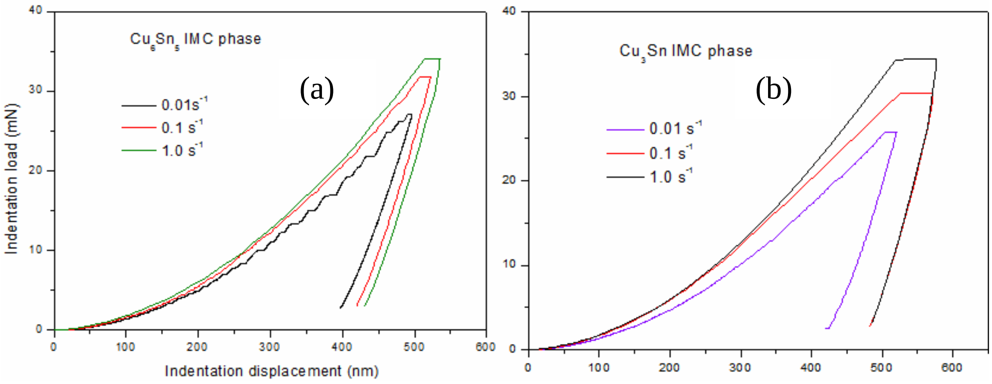

Figure 7-9: Effect of strain rate on indentation of behaviour of (a) Cu_6Sn_5 (b) Cu_3Sn IMC.

7.4.2. Continuous Stiffness Measurement Method

Figure 7.10 depicts the typical indents made on the interfacial IMC layer in a planar view of the SnAgCu/Cu solder joints. After selective etching, the IMCs were slightly polished until a flat IMC surface was obtained. The polishing process was conducted meticulously to ensure that too much IMC was not removed. For the tests on the planar surface, a test array of 2x4μm was conducted with a distance of 5μm between the measurements. Figure 7.11 shows the hardness and elastic modulus variation with indentation depth for indentations made on Cu_6Sn_5 and Cu_3Sn IMCs in the reflowed and 500h-aged solder joints. For Cu_3Sn, the study was conducted on the aged solder joints because the Cu_3Sn IMC layer thickness did not exist in the as-reflowed condition. The elastic modulus as a function of depth is shown in Fig. 7.11(a). The value of the modulus becomes independent of the depth when the displacement increases to 80–100nm.

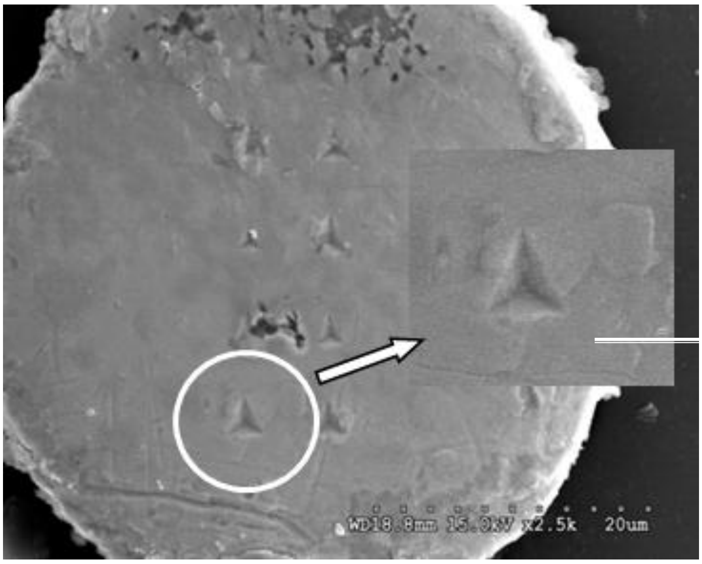

Figure 7-10: Representative indentation impressions at 300nm depth (a) Cu_3Sn (dark phase) and (b) Cu_6Sn_5 (bright phase)

The hardness described in Fig. 7.11 (b) is a function of the applied indentation load on the surface and the corresponding projected contact area. The value of hardness decreases with the increment of the indentation depth. For multilayer structures, where the underlying Cu layer (hardness of the Cu is 1.4GPa) acts as soft substrate, and the indenter tip penetrates the top IMC layer, the elastic-plastic deformation in the underlying Cu substrate generates more elastic deformation, and hence the resultant measured hardness is lower than expected. Moreover, when the indenter penetrates to the underlying layer, the indenter contact area and indentation load are shared between the top and underlying layers. This situation leads to a substrate effect on the measured mechanical properties.

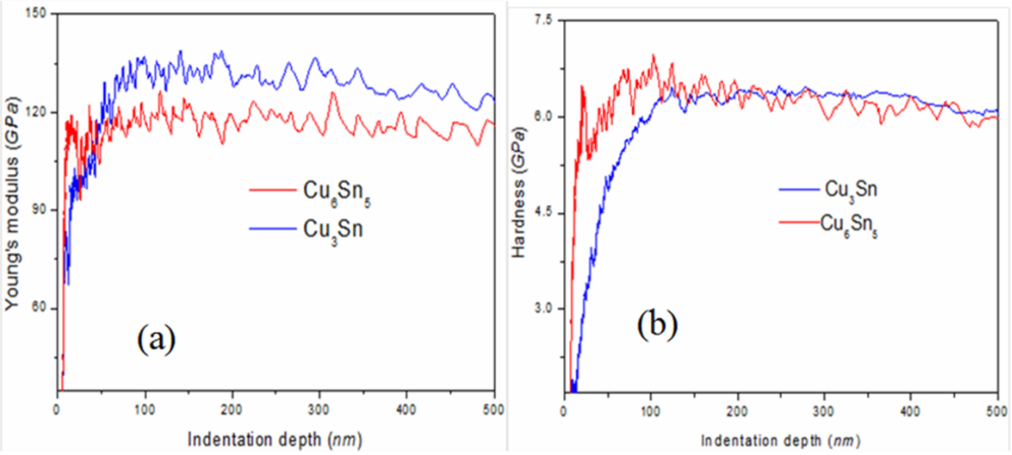

Figure 7-11: (a) CSM modulus and (b) hardness of IMCs in SnAgCu/Cu Solder joints

7.4.3. *S-h and* S^2*-P* Analysis

7.4.3.1. Elastic Modulus

Preliminary studies showed that the taper approach exposed a wide area of IMC phases and ensured an increase in the area available for indentation (Figs 7.4 and 7.5). This method of sectioning increases the overall effective indent area for a given IMC layer and reduces the impact of the neighbouring layers on the indentation results. Indentation experiments can be carried out simultaneously over the different layers in the solder joints from the single specimen. However, as shown in Fig. 7.5, it was still not possible to eliminate the uneven layered structure of the IMC by using taper samples. Therefore, it was crucial to establish the indentation site to ensure that the indents were made on the right region of the IMC phase.

Figure 7.12 shows typical SnAgCu/Au/Ni solder joints fabricated at 260^{o}C and aged at 150^{0}C for 500hrs, which gives an IMC thickness of less than 2.5μm. On the other hand, taper-sectioned solder joints were used to provide a wider area for the mechanical property measurements using the nanoindentation. Figure 7.13 describes the taper cross-sectioned SnAgCu/Cu and SnAgCu/Au/Ni solder joints. The contrast between the Cu-Ni-Sn and Ni-Cu-Sn phases was too low to be distinguished under microscopy (Fig. 7.13 (b)). The thickness and composition of the IMC layers changed from the UBM to the solder side, and therefore the indent location on the solder joints needs to be separated from the post-indentation analysis, because of the significant variations between the hardness and modulus. Therefore, post-indentation analysis was conducted to separate the indentation data of these IMC phases based on their *P-h* curves.

For the Cu/SnAgCu solder joints, two distinct layers can be clearly identified at the solder-joint interface after isothermal aging at 150^{o}C for 500hrs, as shown in Appendix B [Fig. B.2 (a–f)]. However, for the Ni/Au surface (see Fig. 7.12), the contrast between the two intermetallic layers is low, and therefore the assessment of individual IMC layer's hardness and modulus is requiring special attention.

For homogeneous or single-layer materials, the gradient of stiffness versus indentation displacement is a constant. The gradient will be positive for soft-film-on-the-hard-substrate conditions, whereas for hard-film-on-the-soft-substrate, the gradient will be negative. Therefore, using *S-h* or S^2-*P* post-indentation analysis, the actual properties of interfacial IMCs can be determined. The effects of the substrate on the measured *S-h* and S^2-*P* curves are described in Fig. 7.14 and Fig. 7.15, respectively.

Some of the S-h curves deviate from the linearity as the depth of indentation increases, which indicates a change in the elastic modulus (Eq. (7.8), Fig. 7.14). In general, the S-h curves could deviate from linearity for the following reasons:

(a) Substrate effects, i.e. soft substrate or hard substrate in comparison with the film.

(b) Changes of the elastic modulus as a result of strain hardening or softening;

(c) Neighboring layers where an indent has been made at the interface of different layers; and

(d) Free-surface effects – residual stresses at the interface and indenter-tip imperfections.

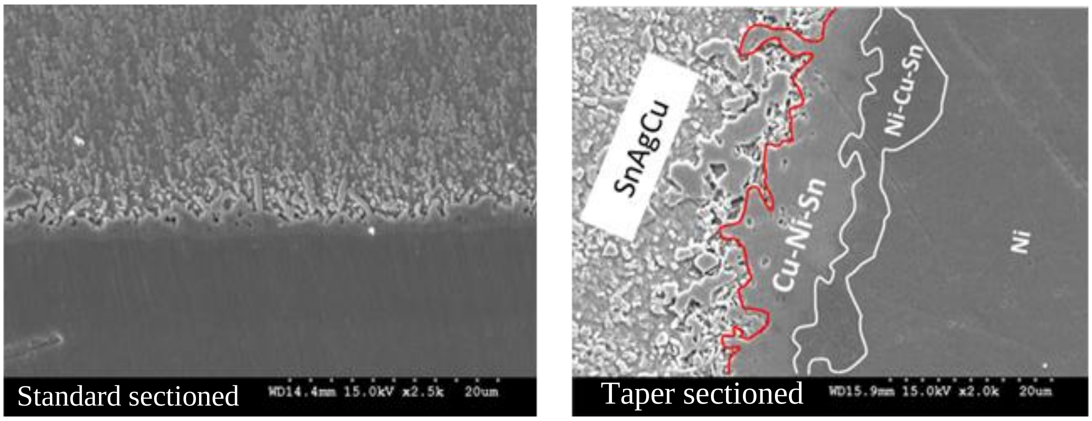

Figure 7-12: Cross-sectional view of taper-sectioned as reflowed SAC387/OSP/Cu joints

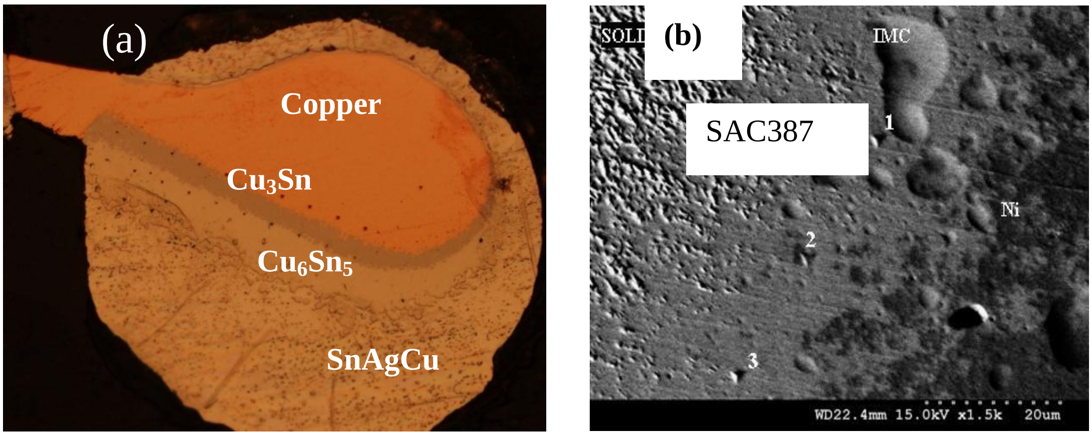

Figure 7-13: Representative micrographs showing the location of indents for (a) SAC387/OSP/Cu (b) SAC387/Au/Ni solder joints.

Upon subsequent examination, it can be concluded that not all the *S-h* curves show the same change as indentation depth increases. Therefore, a second postulation indicates a difference in the elastic modulus of the IMC with depth does not hold. Apropos to the third reason, even for the indents which are solely on a IMC layer, the curves indicate the non-linearity, even the impact from the neighbouring far from their influence. Therefore, the most likely explanation, which affects the linearity of the curves, is that it is due to the substrate effects.

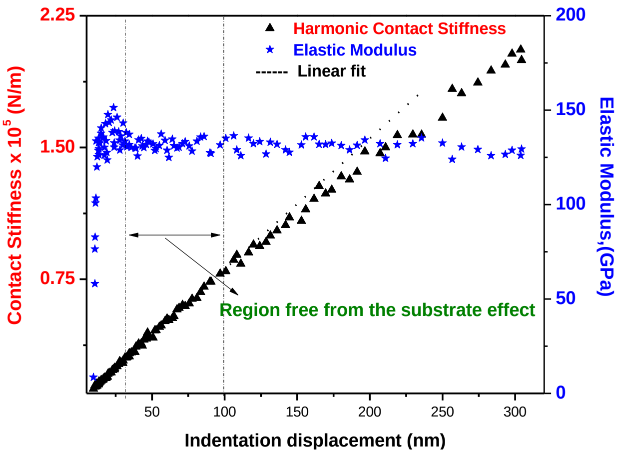

Figure 7-14: Representative S-h curve for nanoindentation on Sn-Cu IMC in SAC387/Cu solder joints in as-reflowed condition.

For the indents made over the intermetallic region, the S-h curve deviates downwards with an increase in depth, as shown in Fig. 7.14. The decrease in gradient can be attributed to the effects of the underlying substrate, since both the modulus and hardness of the Cu substrate beneath the IMC layer are lower than those of the IMC layer [165]. This situation is similar to the case of indentation of hard-film-on-soft-substrate [177].

In fact, some of the *S*-*h* curves also exhibit non-linearity at the beginning. This initial non-linearity cannot be explained by the effects of the substrate alone; some other possible reasons could be indenter shape and size. Table 7.2 summarizes the gradients measured using Eq. (7.8), as well as the corresponding reduced modulus and intermetallic-layer modulus. The changes in the gradients of the *S*-*h* curves in different indentation sites are due to the thickness of the intermetallic layer beneath the indentation site. Figure 7.13 (b) describes indentation site 1, which is closer to the UBM; therefore the underlying IMC thickness will be thinner in the order of a few 10s of nanometres. For indentation site 2, which is closer to the solder side, the IMC thickness will be greater (close to the actual thickness of the IMC layer). In addition to the IMC thickness variation, there is also composition within the intermetallic layer from the UBM side towards the solder.

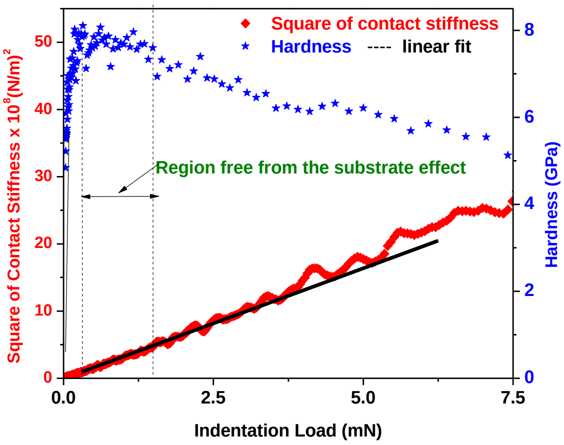

Figure 7-15: Representative S^2-P curve for nanoindentation on Sn-Ni-Cu IMC in SnAgCu/Au/Ni solder joints in as-reflowed condition

7.4.3.2. Hardness

The square of contact stiffness (S^2) is linearly proportional to the indentation load *(P)* for homogeneous material or single layers of constant modulus (E_r) (Eq. (7.9)). Using the smaller range of P corresponding to the linear portion of the S-h curves, the resulting S^2-P curves are mostly not linear throughout the entire S-h segment. The curve can be considered as a case of hard-film-on-soft-substrate (Fig. 7.15). This also can be explained by the underlying UBM layer effect, which causes a deviation in the linearity of the graphs. Table 7.2 summarizes the gradients measured from Eq. (7.9), as well as the corresponding indentation hardness.

7.4.4. Effects of Multiple Reflows and Isothermal Aging

The mechanical properties of interfacial IMC in SAC387 solder joints were studied using a similar analysis. The elastic modulus and hardness of the Cu-Sn IMCs did not change with multiple reflows and isothermal aging. The effects of multiple reflows and isothermal aging on mechanical properties are summarized in Tables 7.3 and 7.4, respectively.

7.5 Discussion

There was little contrast and composition difference between the interfacial IMCs formed in SAC387/Au/Ni solder joints. It was hard to distinguish between the indents on $(Ni_{1-y},Cu_y)_3Sn_4$ or $(Cu_{1-x},Ni_x)_6Sn_5$. Based on the post-indentation analysis, the indentation properties of the $(Ni_{1-y},Cu_y)_3Sn_4$ and $(Cu_{1-x},Ni_x)_6Sn_5$ layers can be separated due to significant differences in the hardness of the IMC phases. Therefore, the mechanical properties of the IMCs reported in this study are of Cu_6Sn_5 and Cu_3Sn from the Cu/OSP surface-finish, and of $(Ni_{1-y},Cu_y)_3Sn_4$ and the $(Cu_{1-x},Ni_x)_6Sn_5$ ternary layer from the Ni/Au surface-finish. The modulus and hardness for $(Ni_{1-y},Cu_y)_3Sn_4$ and $(Cu_{1-x},Ni_x)_6Sn_5$ were highest, followed by Cu_3Sn, and then Cu_6Sn_5.

The results of this work are comparable with reported data from existing literature (Table 7.5). This reported data was obtained from the larger IMC thicknesses of the casted or high-temperature annealed solder joints; thus the reported elastic modulus ranges between 97~123.3 and 114.8~135GPa for Cu_6Sn_5 and Cu_3Sn respectively [1, 59, 62, 65, 161, 163–169, 182, 183, 186, 187]. For the Ni-Cu-Sn ternary layers, an independent analysis was conducted, and the modulus values were 164.9~206GPa for $(Cu_{1-x},Ni_x)_6Sn_5$ and 130~145GPa for $(Ni_{1-y},Cu_y)_3Sn_4$ [59, 65]. For the Cu-Sn IMCs, Cu_6Sn_5 showed a stable trend (no variation) of modulus and hardness with aging time

(Table 7.5). The hardness and modulus of Cu_3Sn are higher than those of Cu_6Sn_5. This could be due to the higher Cu content in Cu_3Sn than in Cu_6Sn_5. However, the Ni-Cu-Sn layer shows a decreasing trend of hardness and modulus with aging time. This may be due to the dynamic changes in the composition of the IMC during the solid-state diffusion process, when the morphology and crystal structure of the Ni-Cu-Sn IMC layers is changing, which results in changes to the mechanical properties. While both $(Cu_x,Ni_{1-x})_6Sn_5$ and $(Ni_y,Cu_{1-y})_3Sn_4$ are ternary IMCs, their moduli are significantly different due to their different crystal structures. Initially, after the reflow process, $(Cu_x,Ni_{1-x})_6Sn_5$ IMC is formed at the expense of Cu atoms from the solder. Therefore, the indents made on these IMCs are likely the properties of $(Cu_x,Ni_{1-x})_6Sn_5$, which has higher modulus and hardness values than those of the $(Ni_y,Cu_{1-y})_3Sn_4$.

After subsequent aging, the Cu from the solder gets depleted, causing a decrease in the amount of Cu diffusing into the interface during the aging, and resulting in the growth of $(Ni_y,Cu_{1-y})_3Sn_4$ between the Ni layer and $(Cu_x,Ni_{1-x})_6Sn_5$ layer. After further aging, there is considerable expansion of the $(Ni_y,Cu_{1-y})_3Sn_4$ layer, caused by the expense of the $(Cu_x,Ni_{1-x})_6Sn_5$ layer from the interface and supply of Ni atoms from the substrate. The indents made on these samples are likely to be the average mechanical properties of both the $(Cu_x,Ni_{1-x})_6Sn_5$ and $(Ni_y,Cu_{1-y})_3Sn_4$. As the percentage of Cu from solder is only 0.5%, $(Cu_x,Ni_{1-x})_6Sn_5$ gets transformed to $(Ni_y,Cu_{1-y})_3Sn_4$ at the interface with consistent teeming of Ni atoms from the substrate. This results after aging for 500h.

Table 7.2: *S-h* and S^2-*P* curve-fitting parameters for 300μm-sized SnAgCu/Cu and SnAgCu/Au/Ni solder joints.

S-h parameters			Elastic Modulus (GPa)		S^2-*P* parameters		Hardness (GPa)		IMC phase
Gradient	E_r (GPa)	E_m (GPa)	CSM	Oliver & Pharr method	Gradient (^{2}), Nm^{-2}	Hardness (GPa)	CSM	Oliver & Pharr method	
769	132.6	134.6	131	129	3.42 x10^{12}	7.0	5.4	5.1	Cu_3Sn
779	134.3	136.6	138	122	3.69 x10^{12}	6.7	5.7	5.3	Cu_3Sn
781	134,7	136.9	147	119	4.78 x10^{12}	5.7	6.1	6.4	Cu_3Sn
781	134.7	136.9	142	131	3.56 x10^{12}	7.0	6.7	5.9	Cu_3Sn
632	109.3	108.1	112	118	2.75 x10^{12}	5.9	4.8	3.8	Cu_6Sn_5
589	101.6	100.0	107	121	2.80 x10^{12}	5.0	5.2	3.9	Cu_6Sn_5
640	110.3	109.6	101	113	2.77 x10^{12}	5.9	5.1	4.8	Cu_6Sn_5
594	102.4	100.9	114	103	2.85 x10^{12}	5.8	4.7	4.2	Cu_6Sn_5
825	142.2	145.8	138	200	3.42 x10^{12}	7.0	6.8	8.4	$(Ni_y,Cu_{1-y})_3Sn_4$
790	136.2	138.7	144	184	3.69 x10^{12}	6.7	7.1	7.7	$(Ni_y,Cu_{1-y})_3Sn_4$
765	131.9	133.8	147	142	4.78 x10^{12}	5.7	6.9	8.8	$(Ni_y,Cu_{1-y})_3Sn_4$
794	136.9	139.5	141	178	3.56 x10^{12}	7.0	6.7	6.9	$(Ni_y,Cu_{1-y})_3Sn_4$
873	150.5	155.5	167	141	2.75 x10^{12}	7.4	7.4	6.3	$(Cu_x,Ni_{1-x})_6Sn_5$
894	154.1	159.8	171	158	2.80 x10^{12}	7.8	7.8	6.8	$(Cu_x,Ni_{1-x})_6Sn_5$
902	155.5	161.5	163	138	2.68 x10^{12}	6.8	8.2	7.1	$(Cu_x,Ni_{1-x})_6Sn_5$
884	152.4	157.8	159	163	2.61 x10^{12}	6.7	8.4	5.9	$(Cu_x,Ni_{1-x})_6Sn_5$

Table 7.3 Elastic modulus and hardness of interfacial IMCs with multiple reflows.

Mechanical property	IMC Type	1st Reflow	3rd Reflow	5th Reflow
Modulus (GPa)	Cu_6Sn_5	112 ± 3	114± 4	109± 5
	Cu_3Sn	---	129 ± 5	134 ± 9
Hardness (GPa)	Cu_6Sn_5	6.1 ± 0.2	5.9 ± 0.3	6.1± 0.6
	Cu_3Sn	---	6.9± 0.4	6.8 ± 0.1

Table 7.4: Elastic modulus and hardness of interfacial IMCs with isothermal aging.

IMC type	Aging time (h)				
	0	100	200	300	500
E of Cu_6Sn_5 (GPa)	110.5	114.7	108.5	112.3	112.8
E of Cu_3Sn (GPa)	-	-	130.9	120.0	135.6
H of Cu_6Sn_5 (GPa)	6.8	6.5	6.2	7.3	5.5
H of Cu_3Sn (GPa)	-	-	7.6	7.7	6.6

A thick layer of $(Ni_y,Cu_{1-y})_3Sn_4$ is formed close to the pad side, with a extremely thin layer of $(Cu_x,Ni_{1-x})_6Sn_5$ close to the solder side. The indentations made on this longer aging sample are likely to be the measurement of the mechanical properties of $(Ni_y,Cu_{1-y})_3Sn_4$, which has a much lower modulus and hardness. These results indicate that there is a gradual reduction of the elastic modulus for the Cu-Ni-Sn IMC to a lower modulus and hardness (Ni-Cu-Sn IMCs) with aging time, as the IMC composition and crystal structure change with aging time.

Table 7.5: Mechanical properties of intermetallic layers measured using nanoindentation.

Lead free Joint	Intermetallic	*S-h* & S^2*-P* Analysis		Condition
		E (GPa)	H GPa)	
Ni/Au/SAC305	$(Cu_x,Ni_{1-x})_6Sn_5$	165±11.6	8.2±1.0	As reflowed at 265°C
	$(Ni_y,Cu_{1-y})_3Sn_4$	137 ±5.9	7.2±0.9	Aging at 150°C for 500h
Cu/OSP/SAC305	Cu_6Sn_5	110 ±2.6	6.8±0.4	As reflowed at 265°C
	Cu_6Sn_5	102 ±5.7	5.5±0.6	Aging at 150°C for 500h
	Cu_3Sn	136 ±4.3	6.6±0.5	Aging at 150°C for 500h
Ni(V)/Au/SAC305	Ni-Cu-Sn	143 ±6	8.2±0.3	Aging at 150°C for 500h
Cu/Sn-Ag-Bi	Cu_6Sn_5	102 ± 7	6.7±0.3	Aging at 150°C for 500h
	Cu_3Sn	138 ± 5	5.7±0.2	As reflowed at 265°C subsequently Aged at 150°C for 500h
Cu/SnAg	Cu_6Sn_5	112 ± 5	6.7±0.5	
	Cu_3Sn	134 ± 5	5.7±0.7	
Cu/Sn	Cu_6Sn_5	109 ± 4	6.7±0.3	
	Cu_3Sn	135 ± 6	5.7±0.5	
Cu/ Sn–3.5Ag	Cu_6Sn_5	112 ± 5	6.7±0.7	Aging at 175°C for 1000 h [186]
	Cu_3Sn	134± 6.7	5.7±0.4	
Cu /Sn-3.5Ag	Cu_6Sn_5	123 ± 6	5.9±0.2	As reflowed at 240°C [166]

Ni/Sn-3.5Ag	Ni_3Sn_4	140 ±7	8.1± .3	As reflowed at 240°C [166]
Cu /Composite solder	Cu_6Sn_5	108	5.9	Indent in Cu_6Sn_5 [168]
	Cu_3Sn	136	6.5	Indent in Cu_3Sn layer [168]
Cu/OSP/SnAgCu	Cu_6Sn_5	97 ±3	----	As reflowed condition [65]
	Cu_3Sn	114 ± 1	----	As reflowed condition [59, 65]
Ni/Au/SnAgCu	$(Cu_{0.78}Ni_{0.22})_6Sn_5$	206± 5	----	As reflowed condition [59, 65]
	$(Ni_{0.51}Cu_{0.49})_3Sn_4$	145 ± 3	----	Aging at 125°C & 500h [59, 65]

However, similar reductions in mechanical properties were not observes in the Cu-Sn IMCs, because the degree of change in composition and structure with aging time was unaltered. Comparing the modulus and hardness values of the Cu_6Sn_5 (hexagonal structure)-based IMCs, the modulus of the $(Cu_{1-x},Ni_x)_6Sn_5$ with Ni substitution was higher than that of the Cu_6Sn_5. Similarly, with the Ni_3Sn_4-based IMCs, the Cu substitution did not show any significant change in the elastic modulus. The elastic modulus of $(Ni_y,Cu_{1-y})_3Sn_4$ is comparable with the reported values of Ni_3Sn_4 (130~140GPa) [166]. Therefore, it may be suggested that $(Cu_x,Ni_{1-x})_6Sn_5$ with Ni substitution is a significant improvement over the elastic modulus of Cu_6Sn_5.

7.6. Summary

1. Nanoindentation measurements were conducted on “taper” sections of actual BGA SAC305 solder joints with OSP and an electrolytic Ni/Au surface finish. The “taper” approach produces consistent results for modulus and hardness for Cu-Sn, and Ni-Cu-Sn IMC layer thicknesses as thin as 2.33μm, and 2.30μm in as-reflowed conditions.
2. UBM layer effects were identified and eliminated by fitting the linear portion of the S^2-P and S-h curves. The elastic moduli of Cu_6Sn_5 and Cu_3Sn after 500h aging were found to be 102 and 136GPa respectively, while hardness values were found to 5.5 and 6.8GPa, respectively.

3. There were no significant changes to the mechanical properties of Cu-Sn IMCs after isothermal aging. Changes in the modulus and hardness of the Ni-Cu-Sn IMC layer were observed with aging at 150°C for 500h.
4. Changes in the elastic modulus and hardness of the Ni-Cu-Sn IMC were observed due to the dynamic changes in composition, morphology and crystal structure of the IMCs during the solid-state diffusion process.

Chapter 8: MECHANICAL PROPERTIES OF IMCs IN MICROBUMP JOINTS

8.1 Introduction

Microbump solder joints with a through silicon via (TSV) interconnection provide electrical connectivity between different functional dies and other potential benefits, such as high density interconnection with fine-pitch, less thermo-mechanical strain due to the coefficient of thermal expansion (CTE) mismatch with silicon chips, and excellent thermal conductivity [159, 160]. However, the reduced interconnect size poses associated mechanical reliability issues. This is because the formation and growth of intermetallics in solder joints increases during 3D IC-package fabrication.

These intermetallics are inherently brittle, and moreover the formation of a Cu-rich intermetallic compound (IMC) invariably accompanies the formation of Kirkendall voids within the IMC layer interface. This lead to a change in the microstructural morphology (grain size, Kirkendall voids, grain boundary orientation etc.) of the IMC layers, from bulk joints to microbump joints. This greatly influences the electrical and mechanical reliability performance of the microelectronic packages. Therefore, knowledge of the mechanical behaviour of microbump solder joints is an important technological issue in advanced 3D-microelectronic packaging applications.

The fabrication, and a detailed study, of diffusion kinetics of the Sn/Cu solder joint is discussed in Appendices A, B and C. Unlike the bulk solder joints, the IMC layers in the microbump joints are extremely irregular and thinner, i.e. 1.5 and 5.5μm for as-reflowed and isothermal aging at 150°C for 500 hours, respectively (see Figs 8.1 and 8.2). It is therefore necessary to separate the effects of underlying layers, which was discussed in Chapter 7. Figure 8.3 shows the representative taper-sectioned Sn/Cu microbump solder joints used in this chapter (Chapter 8).

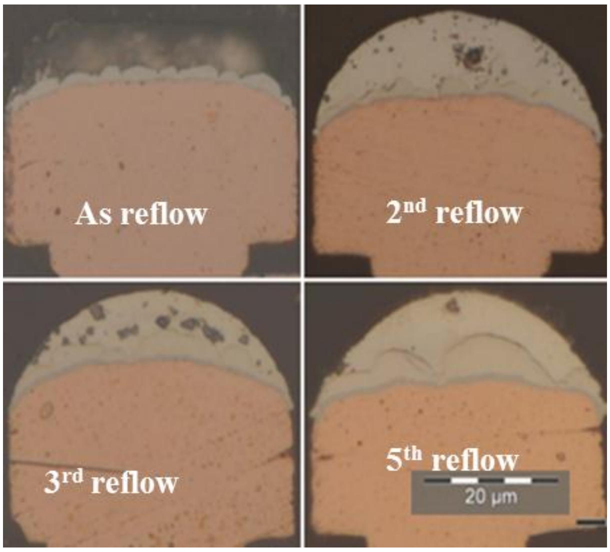

Figure 8-1 Morphology of Sn/Cu joints with reference to multiple reflows at 260°C.

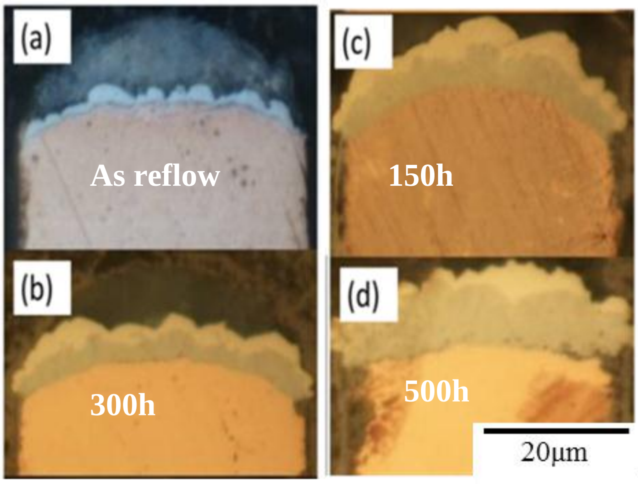

Figure 8-2: Morphology of Sn/Cu joints with isothermal aging at 150°C.

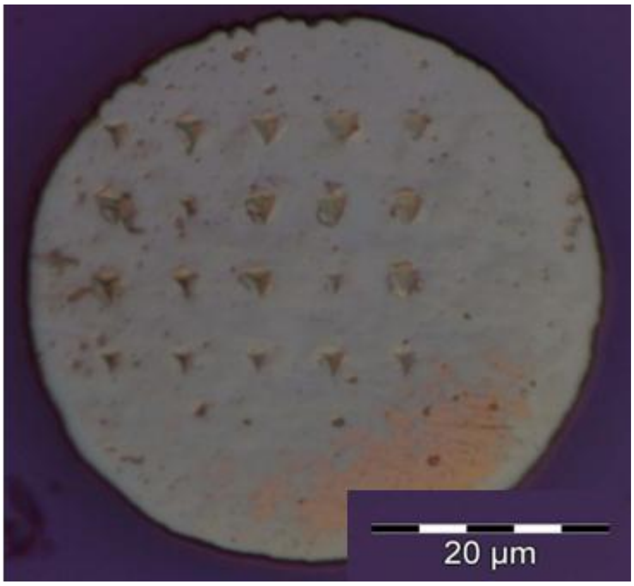

Figure 8-3: Indented impressions on the taper-sectioned Sn/Cu microbump solder joints.

8.1.1. Subtract Effects from *S-h* Analysis

It may be observed that some of the *S-h* curves deviate from the linearity as the depth of indentation increases, and this indicates the change of the elastic modulus with the indentation depth [Eq. (7.8) and Fig. 8.4]. The most likely reason the *S-h* curves' linearity was affected is the substrate effects [172]. For the indents made on the Cu_3Sn IMC, the *S-h* curve deviates downwards with an increase in depth, as shown in Fig. 8.4.

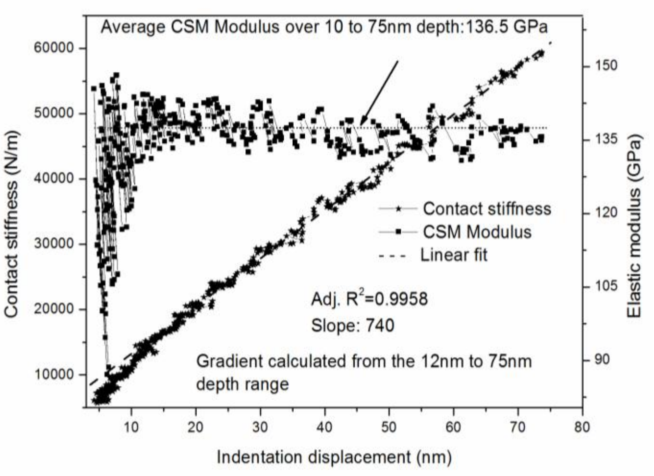

Figure 8-4: Contact stiffness versus indentation displacement of Cu_3Sn.

Table 8.1: *S-h* curve-fitting parameters based on Joslin and Oliver's method.

Gradient	Reduced Modulus (GPa)	Sample Modulus (GPa)	Location of the indent spot
779.29	134.75	133.9	Cu3Sn Layer
781.44	135.12	134.4	Cu3Sn Layer
632.46	109.36	106.08	Cu6Sn5 Layer
588.62	101.78	98.01	Cu6Sn5 Layer

The decrease in gradient is likely to be due to the effects of the underlying Cu under bump metallurgy (UBM), since both the elastic modulus and hardness of the Cu substrate beneath the Cu_3Sn IMC are lower than those of the IMC layer [61]. This phenomenon is similar to the case of hard-film-on-soft-substrate [177]. Table 8.1 summarizes the gradients of the *S*-*h* curve, as well as the corresponding reduced modulus and the elastic modulus of the IMC layers.

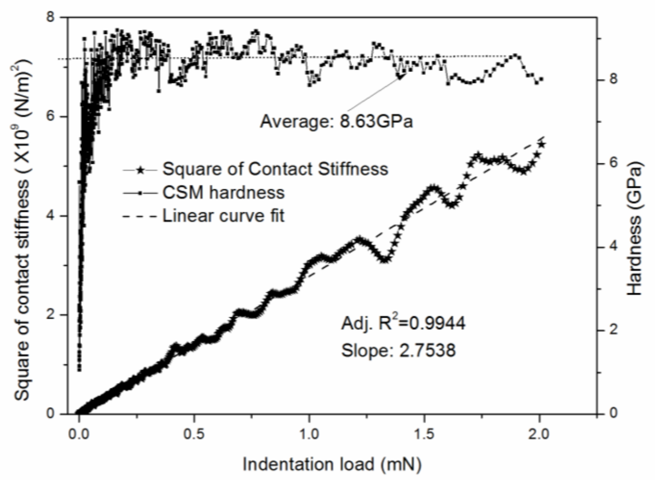

Figure 8-5: Square of Contact stiffness versus indentation load of Cu_3Sn.

From Fig. 8.3, indentation sites located closer to the UBM side experience the effects of UBM, since IMC thickness is extremely superficial. For indentation sites closer to the solder, IMC thickness in the order of microns gives more representative IMC properties.

8.1.2. Subtract Effect from S^2-P Analysis

The S^2-P behaviour of IMC layers can again be understood by the characteristics of the indentation of hard-film-on-soft-substrate (Fig. 8.5), due to the effects of the underlying UBM, which causes the deviation in the linearity of the curves. Table 8.2 also summarizes the average hardness of Cu-Sn IMCs.

Table 8.2: S^2-P curve-fitting parameters based on Joslin and Oliver's method.

Gradient (x10-9)	Hardness (GPa)	Location of the indent spot
3.42	7.0	Cu_3Sn Layer
3.69	6.7	Cu_3Sn Layer
2.75	5.9	Cu_6Sn_5 Layer
2.80	5.0	Cu_6Sn_5 Layer

Figure 8.6 shows the differences in the grain sizes in the interfacial IMCs between the macro-sized and microbump Sn/Cu solder joints. Microbump joints contain at least 3 to 10% Kirkendall voids, depending on the aging conditions and solder volume. Therefore, the hardness and elastic modulus may be expected to show higher scatter for the microbump solder joints than for the bulk solder joints.

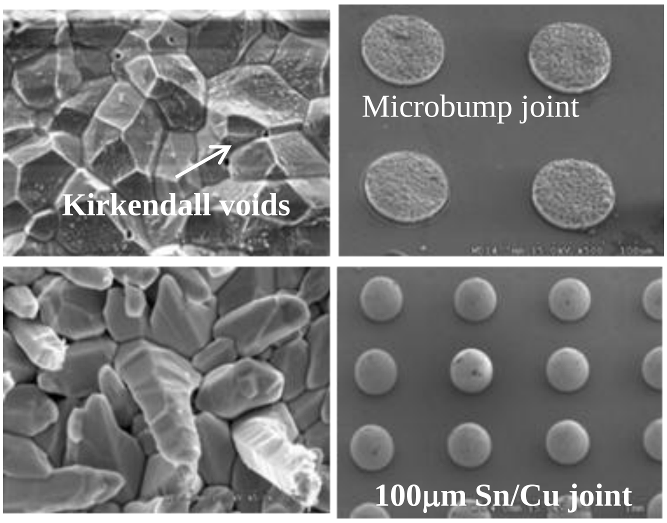

Figure 8-6 : Effects of interfacial IMC grain size with volume of Sn over the Cu substrate.

8.2. Sn 2.7Ag Microbump Solder Joints

The fabrication of electroplated Sn-Ag solder joints is discussed in Appendix A. Figure 8.7 shows the Sn2.7Ag/Cu microbump solder joints used for indentation experiments to study the interfacial Cu-Sn IMC's mechanical properties. Typical taper cross-sectioned SnAg/Cu microbump solder joints were used for the indentation experiments described in Figs 8.3 and 8.8. The gradients of the S-h and S^2-P plots include a depth range of 20 to 100. The initial 20nm depth data was removed from the analysis to avoid the influence of surface roughness and strain hardening (caused by polishing), and to minimize indenter-tip roundness. Besides the IMCs, the mechanical properties of the solder region and UBM were also determined.

Figure 8.9 shows a representative graph for the Cu_3Sn from the SnAg/Cu solder joint. The blue data points were obtained directly from the readings of the continuous stiffness measurement (CSM). It may be observed that the slope of the S/h deviates from the initial linearity as indentation depth increases, illustrating the substrate effects. It was found that the linear portion of the S-h curve coincides with the linear or near-linear portion in the S^2-P plot. Table 8.3 summarizes some of the test results for SnAg/Cu.

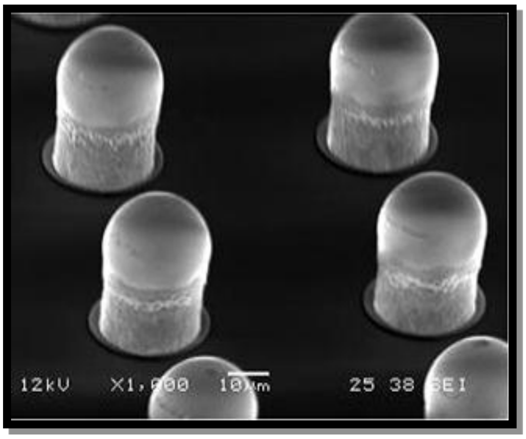

Figure 8-7: Typical SnAg/Cu microbump solder joints used for the measurement of mechanical properties.

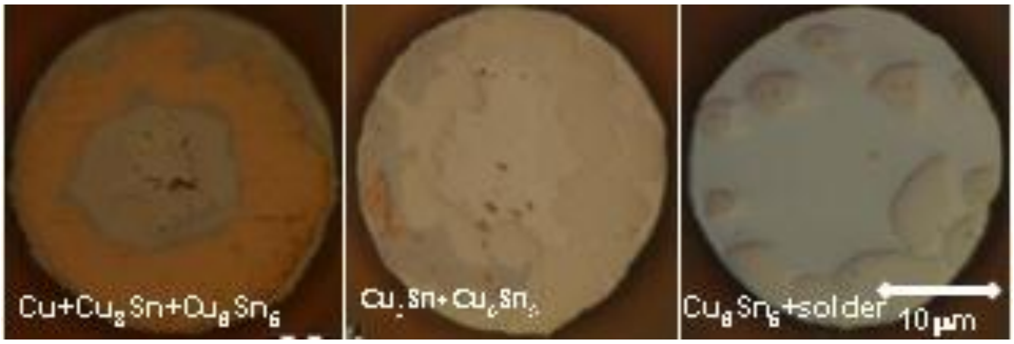

Figure 8-8: Taper cross-sectioned SnAg/Cu solder joint for indentation experiments.

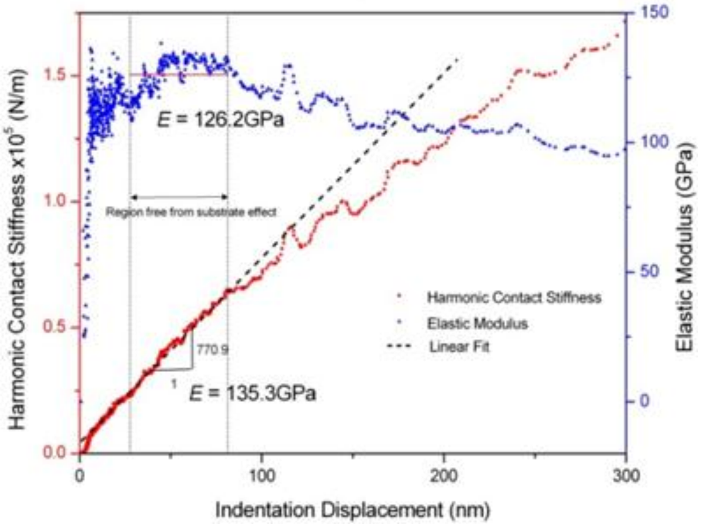

Figure 8-9: Representative *S-h* and S^2-*P* curve for Cu_3Sn IMC phase.

Table 8.3: *S-h* and S^2-*P* analysis of 50µm SnAg/Cu solder Joints.

Test No.	*S-h* analysis		S^2-*P* analysis		CSM		Oliver & Pharr method		Remarks
	Depth Range *(nm)*	*E (GPa)*	Load range *(mN)*	*H (GPa)*	*E (GPa)*	*H (GPa)*	*E (GPa)*	*H (GPa)*	
54	60-140	59.4	0.018-0.13	0.37	39.8	0.17	46.4	0.21	Solder
67	90-140	64.2	0.036-0.10	0.52	27.5	0.13	36.2	0.16	Solder
51	30-70	130.3	0.099-0.69	8.15	83.9	3.60	90.7	1.46	Cu_3Sn
92	25-80	135.3	0.16-1.23	7.67	121.5	6.62	87.9	1.82	Cu_3Sn
11	25-90	113.6	0.16-1.62	6.70	121.7	7.33	89.5	2.98	Cu_6Sn_5
4	30-90	115.7	0.27-1.53	6.74	119.9	7.62	88.1	2.77	Cu_6Sn_5
15	70-240	98.5	0.10-0.87	3.49	24.3	0.30	78.7	1.83	Ag_3Sn
71	40-110	103.9	0.35-1.17	2.40	121.2	4.65	111.6	1.50	Ag_3Sn

It may be noted that results from Table 8.3 were derived using the Oliver & Pharr method, i.e. stiffness calculated from the slope of the unloading curve gives inconsistent results compared with the results from the *S*-*h* and S^2-*P* curve analysis. For the CSM, stiffness was measured continuously at every 2nm, or every cycle of unloading during the loading phase. The final modulus value can be obtained from the linear slope of the stiffness-indentation depth. Therefore, the mechanical properties of interfacial IMCs measured using *S*-*h* and S^2-*P* analysis the CSM method are more precise, with a minimum standard deviation.

8.3. SnAgCu/Au/Ni (V)/Cu Microbump Solder System

SnAgCu/Au/Ni (V) is another microbump joint using chip-level interconnection in advanced packaging applications. A typical 40μm bond pad with Au (100nm)/500nm (Ni (V)/500nm (Cu) surface finish is used for the fabrication of microbump solder joints. The total interfacial IMC layer thickness formed at the interface is less than 1.5μm after the standard fabrication process. The determination of the mechanical properties of these microbump solder joints is a challenging task. A typical taper cross-sectioned SnAgCu/Au/Ni (V) microbump is described in Fig. 8.10, which gives a wider area of Cu-Ni-Sn IMC for indentation testing.

The reported values of the Cu-Ni-Sn IMCs are in the order of 160 to 205GPa [59, 65]. The indentation spot on the Cu-Ni-Sn IMC that is close to the solder side shows no substrate effect because of the higher thickness of the *Cu-Ni-Sn* at the indentation spot. A similar analysis was also applied to the Ni-Cu-Sn IMC phase. A complete analysis for the indentation matrix may be found in Appendix D. The average elastic modulus and hardness of the Cu-Ni-Sn layers were found to be 165±4 and 8±1.0GPa, respectively.

These analyses are in agreement with that of the 300µm-sized SnAgCu/Ni solder joint discussed in Chapter 7 [61].

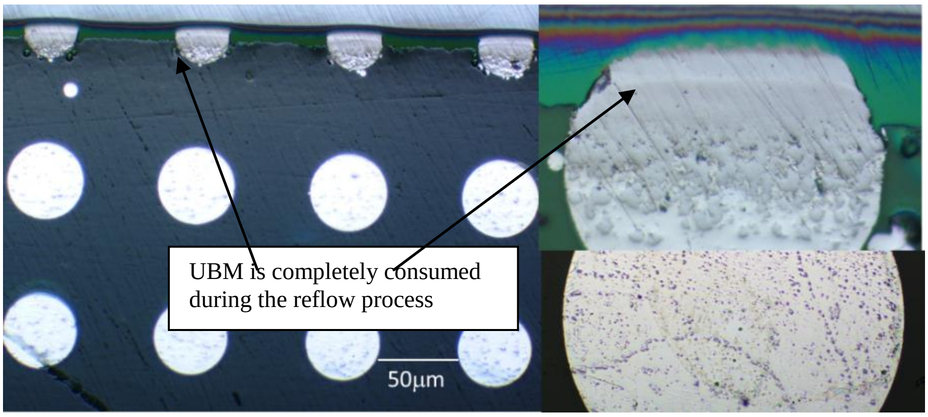

Figure 8-10: Taper-sectioned SAC387/Au /Ni (V)/Cu solder joint.

8.4. SnAgCu/Cu Microbump Solder System

The mechanical properties of the 50µm-sized SnAgCu/Cu solder joints used in wafer-level packaging Fan-Out/Fan-In applications were determined using the nanoindentation technique. The indents close to the solder side, such as test7, test11, test14 and test15, gave a lower elastic modulus due to the underlying soft solder layer. The rest of the locations represent the Cu_6Sn_5 and Cu_3Sn IMC phases. From Table 8-4, it may be understood that the mechanical properties measured using the S^2-P and S-h analysis are more consistent than those derived by the CSM method, which averages over a selected depth indentation data, without considering the substrate effect.

8.5. SnAgCu/ENIG Microbump Solder System

SnAgCu microbump joints with an ENIG surface finish were fabricated using the ball drop method (solder balls dropped over the predefined UBM pad with the help of an automated stencil). Solder balls with a size of about 40±1µm were used to fabricate these solder joints. The mechanical properties of the IMCs in solder joints are tabulated in Table 8.5.

Table 8.4: *S-h* and S^2-*P* analysis of 50µm SnAgCu/Cu solder joints.

S-h Analysis			S^2-*P* analysis		CSM (20 to 150nm depth range)		Annotations
Gradient	Reduced Modulus(GPa)	Modulus (GPa)	Gradient ($\times 10^{12,}$ N/m^2)	Hardness (GPa)	Modulus (GPa)	Hardness (GPa	indent spot (Fig 8.10)
490	85.96	77.16	2.47	4.08	90.653	4.2426	Test 1
764	134.03	120.30	4.54	5.40	95.351	2.6772	test2
681	119.47	107.23	2.01	9.68	96.702	5.8573	test4
560	98.24	88.18	1.70	7.74	98.146	6.7249	test6
555*	97.36	87.39	7.01	1.84	63.312	0.93	test7
550	96.49	86.61	1.74	7.30	96.298	6.7218	test8
660	115.78	103.93	1.95	9.38	107.19	7.0453	test9
524*	91.92	82.51	1.92	6.00	89.888	5.6161	test11
650	114.03	102.35	3.03	5.85	88.966	4.0334	test12
661	117.78	104.13	1.96	9.33	103.9	6.8434	test13
550*	96.49	86.61	8.78	1.45	70.278	0.8319	test14
495*	86.84	76.24	8.87	4.08	61.292	0.7962	test15

Table 8.5: Average *E* and *H* for Ni-Cu-Sn IMC in SnAgCu/ENIG.

IMC Phase	Modulus (GPa)	Hardness (GPa)
$(Ni,Cu)_3Sn_4$	142.9	6.46
$(Cu,Ni)_6Sn_5$	153.4	7.24
Sn–Ni–Cu	168.4	7.85
Ni_3P	145.2	6.04
P rich Ni(P)	192.3	6.93

8.6. Cu/In/Sn Thin-film Solder Joints

The taper cross-sectioning methodology was further extended to the measurement of the mechanical properties of the ultra-thin IMC layers formed in fine-pitch thin-film solder joints. Nanoindentation experiments were conducted on the taper-sectioned solder joints to determine the mechanical properties of *Cu-In-Sn* IMC in *Cu/In/Sn/Cu* film joints (see Fig. 8.11). These thin-film joints were bonded at room temperature and annealed at 200°C for 4h. There were two types of Cu-In-Sn IMCs at the interface, i.e. the $Cu_6(In,Sn)_5$ and $Cu_6(In,Sn)_2$ IMCs [193].

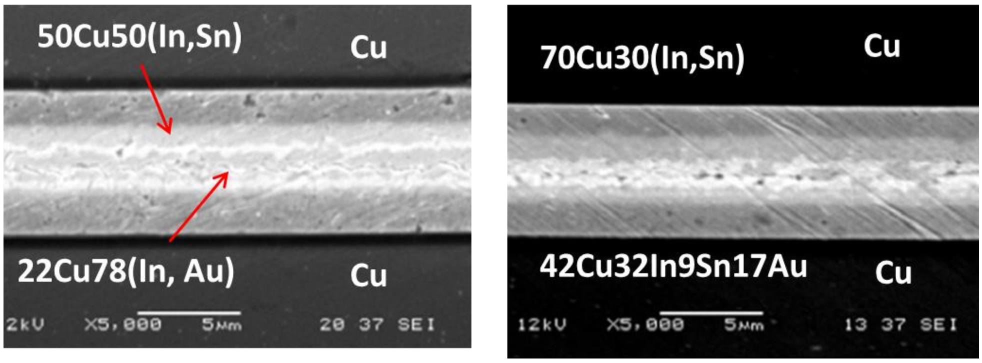

Figure 8-11: Typical In/Cu/Sn thin-film joints used for mechanical properties study

Using the analysis approach as described in Chapter 7, the elastic moduli of the $Cu_6(In,Sn)_5$ and $Cu_6(In,Sn)_2$ IMCs were determined to be 104.0±2.0 and 87.0±3.0GPa, respectively, whereas the hardnesses of the $Cu_6(In,Sn)_5$ and $Cu_6(In,Sn)_2$ IMCs were determined to be 8.0±0.5 and 5.0±0.8GPa, respectively. Typical indentation impressions for In/Cu/Sn thin-film solder joints are described in Fig. 8.12.

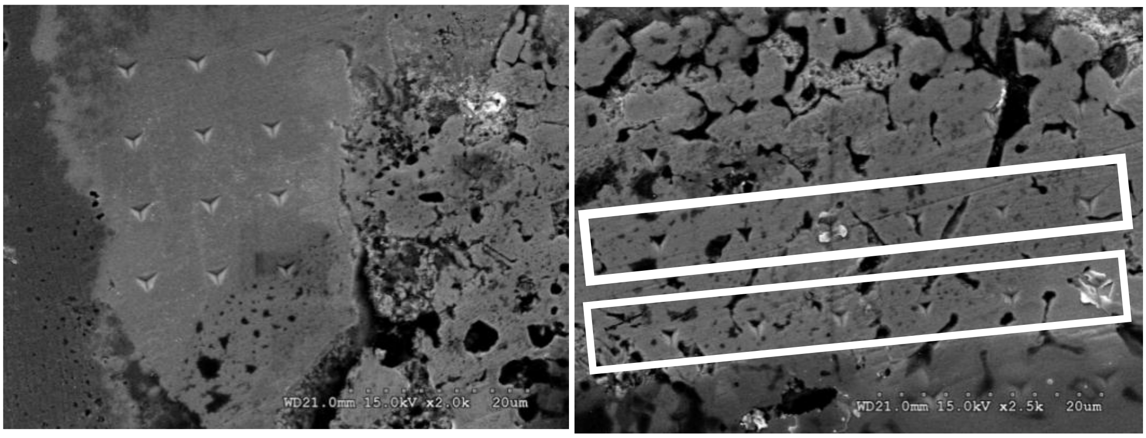

Figure 8-12: Indentation impression on the taper-sectioned In/Sn/Cu thin-film UBM.

8.7. Discussion

Table 7.1 shows the typical discrepancy in the measured elastic modulus and hardness of interfacial IMCs in the lead-free solder joints. These ranges of variation further increased with the reduction in the size of the solder joints due to the substrate effect or influence of adjacent layers. The reported elastic moduli of Cu-Ni-Sn IMCs are in the order of 140 to 205GPa [59, 65].

Table 8.6: Summary of mechanical properties of lead-free microbump solder joints.

Solder Joint	IMC Type	*E (GPa)*	*H (GPa)*	Condition
1.5*μm Cu/In/Sn/Cu*	$Cu_6(In, Sn)_5$	102.0 ± 2.0	8.0±0.5	Bonded at 25°C followed by aging at 200°C for 2h
	$Cu_6(In, Sn)_2$	87.0 ± 3.0	5.0±0.8	
10*μm Sn /Cu*	Cu_6Sn_5	109.0 ± 3.0	5.0±0.8	3rd reflow at 265°C for 80s for each reflow cycle
	Cu_3Sn	135.0 ± 8.0	6.0±1.4	
15*μm Sn-2.7Ag/Cu*	Cu_6Sn_5	113.0 ± 3.0	6.0±0.2	5th reflow @285°C for 80s for each reflow cycle
	Cu_3Sn	134.0 ± 7.0	7.0±0.4	
50*μm SnAgCu/Au/Ni*	$(Cu,Ni)_6Sn_5$	165.0 ± 4.0	8.0±1.0	Reflowed at 255°C and followed by aging

	$(Ni,Cu)_3Sn_4$	137.0 ± 2.0	7.0±0.9	at150°C for 500h
70μm *SnAgCu/Cu*	Cu_6Sn_5	110.0 ± 3.0	7.0±0.4	As reflowed at 265°C for 80s
	Cu_3Sn	135.0 ± 8.0	7.0±0.5	
Ni/SnAgCu	$(Cu_x,Ni_{1-x})_6Sn_5$	165.0 ± 4.1	8.2±1.0	As reflowed at 265°C
	$(Ni_y,Cu_{1-y})_3Sn_4$	136.8 ± 1.8	7.2±0.9	Aging at 150°C & 500h
Cu/SnAgCu	Cu_6Sn_5	110.5 ± 2.6	6.8±0.4	As reflowed at 265°C
	Cu_3Sn	135.6 ± 2.3	6.6±0.5	Aging at 150°C & 500h
Cu/ SnAg	Cu_6Sn_5	112.3 ± 5.0	6.7	Aging at 175°C & 1000 h
	Cu_3Sn	134.2 ± 8.7	5.7	

The taper-approach technique enabled the measurement of the true properties of IMC layers as thin as 500nm without much substrate influence. The elastic modulus and hardness of the Cu-Ni-Sn IMC were found to be 165±4 and 8±1.0GPa, respectively. The elastic modulus and hardness of Ni-Cu-Sn IMC were 137±2 and 7±0.9GPa, respectively. These findings are in agreement with the results presented in Chapter 7 regarding the 300μm-sized SnAgCu/Ni joint [61].

The average mechanical properties of the Sn, SnAg and SnAgCu microbump joints, along with their processing conditions, are summarized in Table 8.6. The hardness and modulus of the Cu_3Sn are higher than those of the Cu_6Sn_5 for the Sn/Cu and SnAg/Cu microbump solder joints. It may also be observed that the hardness and modulus of Cu-Sn intermetallics are consistent with multiple reflows. However, the mechanical properties of Cu_3Sn layers show scatter in the measured quantities. This may be attributed to the microporosity at the Cu/Cu_3Sn interface.

The elastic moduli of the $Cu_6\ (In, Sn)_5$ and $Cu_6\ (In, Sn)_2$ IMCs were found to be 104 and 87GPa, respectively. The hardnesses of the $Cu_6\ (In, Sn)_5$ and $Cu_6\ (In, Sn)_2$ IMCs were determined to be 8±0.5 and 5±0.8GPa, respectively. The elastic modulus and hardness of the Cu-In-Sn IMCs were slightly lower than those of the Cu-Sn IMC. This might be due to the substitution of In for Sn.

8.8. Summary

1. The taper approach for the S-h / S^2-P indentation analysis proved an effective method to probe the mechanical properties of fine-pitch microbump joints.
2. There was no significant variation in the mechanical properties of the Cu-Sn IMCs in the Sn/Cu, SnAg/Cu and SnAgCu/Cu microbump joints.
3. There was a significant variation in the modulus and hardness for the Ni-Cu-Sn IMC layers in the SnAg/Au/Ni, Sn/ENIG and SnAgCu/Au/Ni microbump joints with isothermal aging.
4. The elastic modulus and hardness of the Cu-In-Sn IMCs were slightly lower than those of the Cu-Sn IMC, because of an In substitution for Sn.

Chapter 9: CONCLUSION AND FUTURE RECOMMENDATIONS

9.1. Conclusions

This study focuses on the mechanical behaviour of SnAgCu, SnAg, Sn and other solder systems used in advanced 3D-IC packaging applications. The following general conclusions may be made from this study:

1. The tensile deformation behaviour of Sn3.8Ag0.7Cu and its composite solder materials was investigated with different strain rates ranging from 10^{-5} to $10^{-1}s^{-1}$, and temperatures of 25, 75 and 125°C. The yield strength and Hollomon parameters were found to increase substantially with the strain rate and addition of nano-sized Mo particles. The strain rate's dependence on the strain-hardening exponent is stronger at higher temperatures for the base SAC387 solder, and weaker for composite solders reinforced with the nano-sized Mo particles. Analytical thermo-mechanical models can be used to predict the high temperature tensile performance of the solder.

2. The microtensile behaviour of the composite solder (Mo and SWCNT-reinforced) solders was investigated to understand the deformation behaviour with limited solder volume. The addition of 0.05 wt.% SWCNT to SAC387 alloy resulted in an increase in yield and ultimate tensile strengths at all temperatures and strain rates. This may be attributed to the load transfer to the SWCNTs in the composites, the refinement of the grain size of the matrix, and the sizes of the intermetallic particles (IMCs) as a result of the SWCNT's addition. Further increasing the SWCNT to 0.1 wt.% did not cause an improvement in strength, compared with the

composite containing 0.05 wt.% SWCNT. This may be attributed to the agglomeration of the SWCNTs, with their resultant increase in volume fraction.

3. The SAC387 alloy and its composite solder exhibited significant total elongation at all temperatures and strain rates, although the uniform elongation was limited. The lower uniform elongation is a reflection of the fact that the higher homologous temperature (T/T_m) is above 0.5 at room temperature, and hence the dynamic recovery processes are more dominant compared with work hardening. The composites are also comparable, and in some cases even have a marginally higher total elongation than that of the base alloy. This may be attributed to the fracture being dominated by the failure of the matrix alloy, and the fact that the grain sizes, especially of the intermetallic phases, become finer with the addition of reinforcements.

4. Temperature and strain rates were found to have significant effects on the strengths of both the SAC387 solder and the composites. Both the yield and ultimate tensile strengths were found to decrease with temperature at a given strain rate and increase with strain rate at a given temperature. This behavior may be attributed to the competing effects of the work hardening and dynamic-recovery processes, and the effects of temperature and strain rates on these processes.

5. The addition of nano-sized Mo to the SA387 solder improved the room-temperature tensile properties. The effects of the strain rate on the room-

temperature tensile properties of Mo-reinforced solders are more dominant than with SWCNT-reinforced SAC387solder.

6. The effect of specimen thickness is more prominent for as-cast Sn and SnPb solders. The tensile strength (yield strength and ultimate tensile strength) of these solders was found to be 10 to 15% lower than that of the ASTM bulk materials characterization. However, there was no change observed for the composite solders.

7. An empirical analysis scheme was used to determine the tensile properties of lead-free solder joints using the nanoindentation technique. The elastic modulus and yield strength measured using the nanoindentation technique are comparable with the tensile properties determined using a tensile tester.

8. A modified Garofalo creep model was identified as the best model to characterize the lead-free solder materials. This model was successfully used to analyze the time-dependent deformation behaviour of the SAC387 and its composite, using the nanoindentation creep experiments. The stress exponent of coarse-grained β-Sn was determined by the room-temperature nanoindentation creep experiments conducted over a range of indentation maximum loads. Addition of Ni nano-sized particles to the solder joints caused the creep rate to decline to the minimum at the first few reflows, and subsequently increase with additional multiple reflows. There were no effects on time-dependent deformation from multiple reflows in the SAC387+0.3Mo solder joints.

9. Nanoindentation measurements were conducted on “taper” samples of actual BGA SAC305 solder joints with OSP and an electrolytic Ni/Au surface finish. The “taper” approach produced stable results for the modulus and hardness of the Cu-Sn, and the Ni-Cu-Sn layer thicknesses were as thin as 2.33µm and 2.30µm in as-reflowed conditions. The effects of underlying under ball metallurgy (UBM) layer were identified and eliminated by analysis of the linear portion of the $P\text{-}S^2$ and $S\text{-}h$ curves. The elastic moduli of Cu_6Sn_5 and Cu_3Sn after 500h aging were found to be 102 and 136GPa, and the hardness values to be 6.8 and 7.6GPa respectively.

10. The elastic modulus and hardness for the Ni-Cu-Sn IMC layer were found to change with aging. The change in modulus and hardness of the Ni-Cu-Sn IMC was due to the dynamic changes in composition of the IMCs during the solid-state diffusion process. There were no changes in the mechanical properties of the Cu-Sn IMCs after multiple reflows and isothermal aging.

11. The taper approach and nanoindentation $S\text{-}h\ /\ S^2\text{-}P$ analysis proved to be effective procedures to probe the mechanical properties of fine-pitch solder joints.

9.2. Future Recommendations:

Based on the experimental findings throughout this dissertation, the following recommendations may be made:

1. The tensile properties measured using nanoindentation technique should be verified using modeling and simulation studies.

2. The analytical models should be developed based on the experimental data presented in Appendices B and C of this dissertation. The interfacial intermetallic compound (IMC) thickness as a function of solder volume, reflow time, temperature and bonding force may be used to predict exact process kinetics during 3D-package fabrication. This would be useful in the automation of flip-chip equipment to control the reflow temperature, reflow time, tacking force etc.

3. The validity of Garofalo's creep model in the context of lead-free solder needs to be verified using modeling and simulation studies.

4. The interfacial mechanical properties and Kirkendall void volume need to be statistically correlated for a better understanding of mechanical reliability in the microbump solder joints.

REFERENCES

[1] X.Deng, N.Chawla, K.K.Chawla, M.Koopman, *Acta Materialia*, 52 (2004) 4291.

[2] X. Deng, M. Koopman, N. Chawla, K. K. Chawla, *Mater.Sci. Eng. A*, 364 (2004) 240.

[3] S. Wiese, E. Meusel, *J. Elec. Packag.*, 125 (2000) 531.

[4] W. Englemaier, A.I. Attarwala, *IEEE Trans. Comp. Hybrids, Manufact. Technol.* 12 (1989) 284.

[5] J. McDougall, S. Choi, T. R. Bieler, K. N. Subramanian, J. P. Lucas, *Mater. Sci. Eng. A* 285 (2000) 25.

[6] V. P. Ganesh, S. Lim, D. Witarsa, Y. Hnin Wai, M. Kumar, L. A. Lim, S. W. Yoon, V. Kripesh, *Assembly technology development for 3D silicon stacked module for handheld products* in: *Electronic Components and Technology Conference, 2006. Proceedings. 56th*, (2006) 8.

[7] C. A. Harper, *Electronic packaging and interconnection handbook*, 4th Ed. McGraw Hill Hand Book, (2005).

[8] N. Khan, S.W.Yoon, A. G. K. Viswanath, V. P. Ganesh, R. Nagarajan, D. Witarsa, S. Lim, V.Kripesh, *Advanced Packaging, IEEE Transactions on,* 31 (2008) 44.

[9] Y. Seung Wook, V. P. Ganesh, S. Y. L. Lim, and V. Kripesh, *Advanced Packaging, IEEE Transactions on*, 31 (2008) 519.

[10] S. R. Vempati, N. Su, K. Chee Houe, L. Ying Ying, K. Vaidyanathan, J. H. Lau, B. P. Liew, K. Y. Au, S. Tanary, A. Fenner, R. Erich, and J. Milla, *Development of 3-D silicon die stacked package using flip chip technology with micro bump interconnects in: Electronic Components and Technology Conference, 2009. ECTC 2009. 59th,* (2009) 980.

[11] X.Deng, N.Chawla, K.K.Chawla, M.Koopman, *Acta Mater.,* 52 (2004) 4291.

[12] K. Zeng, Tu, K. N., *Mater. Sci. Engg R*, 38 (2002) 1.

[13] R.Tummala, *Fundamentals of Microsystems Packaging,* 1st edition, Mc Graw-Hill, New York (2001).

[14] J.H.Lau, Y.Pao, *Reliability testing and data analysis In:Solder joint reliability of BGA, CSP, Flip Chip, andFine pitch SMT assemblies.* New York: McGraw-Hill, (1997) 38

[15] W.Nakayama, *Advances in Thermal Modeling of Electronic components and systems,* Hemisphere publishing, New York, 1 (1998) 1.

[16] P. Elenius, *Solid State Technol.,* 1 (1999) 72.

[17] S. Liu, Z. F. Qing, Adv. Electron. Packag. *ASME EEP.*, 19 (1997) 1599.

[18] A.E. Braun, *Aluminium Persists as Copper Age Dawns in : Semiconductor International*, August (1999) 58.

[19] N. Bai, X. Chen, Z. Fang, J.Electron.Mater., 37 (2008) 1012.

[20] S. B. Jung. J.W.Yoon, C.B. Lee, *J.Electron.Mater.,* 32 (2003) 1195.

[21] Y. C. C. M.O.Alam, K.C. Hung,. *J. Elect. Mater*., 31 (2002) 1117.

[22] K. N. K.Suganuma, T.Shoutoku, Y.Nakamura, *J.Mater.Res.,*13 (1998) 2859.

[23] I. Anjo, A. Nishimura, R.Haruta, *Hitachi Review*, 48 (1999) 294.

[24] C.Parameswariah, *IEEE Potentials,* 25 (2006) 29.

[25] C.Shea, *Printed Circuit Des.Manuf.,* 23 (2006) 18.

[26] J. W. Jang, J. K. Lin, D. R. Frear, T. Y. Lee, and K. N. Tu, *J.Appl.Phy,* 88 (2000) 6359.

[27] J.W.Yoon, C.B.Lee, S.B.Jung *Mater.Trans.,* 43 (2002) 1821.

[28] M.Abtew, G. Selvaduray, *Mater.Sci.Eng. R*, 27 (2000) 95.

[29] T. Takemoto, A. Matsunawa, M. Takahashi, *J.Mater.Sci.,* 32 (2003) 4077.

[30] L.Y.Hsiao, S.T.Kao, J.G.Duh, *J.Electron.Mater,* 35 (2006) 81.

[31] P.Liu, P.Yao, J.Liu,, *J.Electron.Mater,* 37 (2008) 874.

[32] J. M. Koo. S.B.Jung, *Microelectron.Eng.,* 82 (2005) 569.

[33] Z.Chen, A.Kumar, M.Mona, *J.Electron.Mater,* 35 (2006) 2126.

[34] Y.D.Jeon, K.W.Paik, K.S.Bok,W.S.Choi,C.L.Cho, *J.Electron.Mater,* 31 (2002) 520.

[35] P.T.Vianco, A.C.Kilgo, R.Grant, *J.Electron.Mater,* 24 (1995) 1493.

[36] S.Choi, T.R.Bieler, J.P. Lucas, and K.N. Subramanian, *J. Electron. Mater.*, 28 (1999) 1209.

[37] M. H. Mavoori, S.Jin , *J. Electron. Mater*., 27 (1998) 1216.

[38] J.L.Marshall, J.Calderon, *Solder. Surf. Mount Technol.*, 9 (1997) 11.

[39] J.L.Marshall, J. Sees, J.Calderon, *Proceedings of Technical Program-Nepcon West Conference,* Anahein, CA, (1992) 1278.

[40] Y.Wu, J.A.Sees, C. Pouraghabragher, L.A.Foster, J.L Marshall, E.G.Jacobs, R.F.Pinizzotto, *J. Electron. Mater.,* 22 (1993) 769.

[41] D.C.Lin, G.X.Wang, T.S.Srivatsan, Meslet Al-Hajri and M.Petraroli, *Mater. Lett.*, 57 (2003) 3193.

[42] C.G.Kuo, S.M.L.Sastry, K.L.Jerina, *Microstructures and Mechanical Properties of Aging Material,* edited by P.K. Liaw, R. Viswanathan, K.L. Murty, E.P. Simonen, and D. Frear, TMS, Warrendale, PA, (1993) 409.

[43] K. M. Kumar, *“Nanoparticle reinforced lead-free composite solders for advanced interconnect application”* Ph.D Thesis, Department of Mechanical Engineering, National University of Singapore, Singapore, 2009.

[44] H.D.Solomon, E.D.Tolksdorf, *ASME: J. Electron.Packag.,*117 (1995)130.

[45] X.Q.Shi, H.L.J.Pang, W. Zhou, and Z.P.Wang, *Int. J. Fatigue*., 22 (2000) 217.

[46] H. A.Ourdjini, M. A. Alam. S.F.J Koh, I S. Aisha, KS. Tan, and Y. T. Chin, in *31st International Conference on Electronic Manufacturing Techniology*, Putrajaya, Malaysia, (2006) 437.

[47] L.Xu, J. H. L. Pang, *Thin solid films,* 504 (2006) 362.

[48] N.Khan, D.H.S.Wee, O.S. Chiew, C. Sharmani, L.S.Lim, H.Y. Li, V.N.Shekar, *Three chips stacking with low volume solder using single re-flow process in* : *Electronic Components and Technology Conference, Proceedings 60th.* (2010) 884.

[49] J.D.Morrow, *Cyclic plastic strain energy and fatigue of metals*. ASTM-STP 378 (1965) 45.

[50] C.M.Chen, S.W.Chen, *J. Appl. Phys.,* 90 (2001) 1208.

[51] A. Syed, *Accumulated Creep Strain and Energy Density Based thermal Fatigue Life Prediction Models for SnAgCu Solder Joints, in: 54th ECTC Conference Proc., (2004) 737*.

[52] M. L. Huang, C. M. L. Wu and L. Wang, *J. Electron. Mater.,* 34 (2005) 1373.

[53] J. W. Morris, Jr. and H.L. Reynolds: *Design and Reliability of Solders and Solder Interconnections,* ed. by R. K. Mahidhara, D. R. Frear, S. M. L. Sastry, K. L. Murty, P. K. Liaw and W. Winterbottom (TMS Soc., Warrendale, PA, (1997) 49.

[54] S. Wiese, E. Muesel, *J. Elec. Packaging.*, 125 (2003) 531.

[55] D. Frear, J. Posthill, J. Morris, *Metall. Mater. Trans. A.* 20 (1989) 1325.

[56] W.J. Plumbridge, C. R. Gagg, *J. Mater. Sci: Mater. Electron.*10 (1999) 461.

[57] Y. Guozheng, Y. Xuexia, S. Xuefeng, *Effects of strain rate and temperature on mechanical behavior of SACB solder alloy In*: *International conference on Electronic Packaging Technology and High Density Packaging*. (2009) 1186.

[58] T. Mattila, J. Kivilahti, *J.Electron.Mater.,* 34 (2005) 969.

[59] L.Xu, J.H.L.Pang, *Thin Solid Films*, 504 (2006) 362.

[60] P.F. Yang, Y.S. Lai, S.R. Jian, J. Chen, and R.S. Chen, *Mater.Sci. Eng.: A*, 485 (2008) 305.

[61] B.S.S.Chandra Rao, J. Weng, L. Shen, T.K. Lee, K.Y. Zeng, *Microelectron.Eng.*, 87 (2010) 2416.

[62] G.Y.Jang, J.W.Lee, J.G. Duh, *J. Electron. Mater.*, 33 (2004) 1103.

[63] J.P. Lucas, H. Rhee, F.Guo, K.N.Subramanan, *J. Electron. Mater.*, 32 (2003)1375.

[64] H.Rhee, J.P.Lucas, K.N. Subramanian, *J. Mater. Sci:Mater. Electron.*, 13 (2002) 477.

[65] L.Xu, J.H.L.Pang, *J.Electron.Mater.*, 35 (2006) 2107.

[66] L.Jiang, N. Chawla, *Scripta Mater.*, 63 (2010) 480.

[67] K. Kawashima, T. Ito, M. Sakuragi, *J. Mater. Sci.*, 27 (1992) 6387.

[68] W.C.Oliver, and G.M.Pharr, *J. Mater. Res.*, 7 (1992) 1564.

[69] M. Cole, T. Caulfield, *Scripta Metall. Mater.*, 27 (1992) 903.

[70] X. Q. Shi, W. Zhou, H. L. J. Pang, Z. P. Wang, *J. Electron.Packag.*, 121 (1999) 179.

[71] X. Long, I. Dutta, V. Sarihan, D.R.Frear, *J.Electron.Mater.*, 37 (2008) 189.

[72] B. Yeung, J.W. Jang, *J.Mater. Sci. Lett.*, 21 (2002) 723.

[73] F. Zhu, H. Zhang, R. Guan, S.Liu, *J. Alloy. Comp.*, 438 (2007) 100.

[74] J.H.Hollomon, Trans. *AMIE.*, 162 (1945) 268.

[75] S. Monteiro, R. Reed-Hill, *Metall. Mater. Trans B.*, 4 (1973) 1011.

[76] R.W.Hertzberg, *Deformation and Fracture Mechanics of Engineering Materials*, USA: John Wiley and Sons, (1996).

[77] W.K. Jones, Y. Q. Liu, M. A. Zampino, G.L.Gonzalez, *Advancing Microelectronics*, (1997) 30.

[78] F. Lang, H. Tanaka, O. Munegata T. Taguchi, T. Narita, *Mater.Character*., 54 (2005) 223.

[79] F. Qin, T. An, N. Chen, *J.Electron Packag.*,131 (2009) 031001.

[80] R. Ninomiya, K. Miyake, *Advances in Electronic Packaging*., 1 (1997) 1329.

[81] S.Choi, J.G.Lee, F.Guo, T.R.Bieler, K. N.Subramanian, J. P.Lucas, JOM: *J. Mineral. Met. Mater. Soc.,* 53 (2001) 22.

[82] J.L.Marshall, J.Calderon, *Solder. Surf. Mount Technol.,* 9 (1997) 11.

[83] M.McCormack, S.Jin, G.W.Kammlott, *IEEE Trans. Compon. Packag. Manuf Technol. Part A*, 17 (1994) 452.

[84] P.Liu, P.Yao, J.Liu, *J. Electron. Mater.,* 37 (2008) 874.

[85] H. J. S.Yuquan, G.Zhiping, *Scinece in China (Series E),* 44 (2001) 647.

[86] E.Bayraktar, C. Levaillant, S.Altintas. *Journal de physique-III,* 3 (1993) 61.

[87] K. S. Kim, S. H. Huh, K. Suganuma, *Mater. Sci. Eng. A.* 333 (2002) 106.

[88] J. H. L. Pang, B. S. Xiong, *IEEE Trans. Comp. Packag. Technol.* 28 (2005) 830.

[89] D. McDanels, *Metall.Mater. Trans. A.,* 16 (1985) 1105.

[90] J. D. B. M.S.Zedalis, P.S.Gilinan, S.K. Das. *J. metal.,* 43 (1991) 29.

[91] V. Franetovic, M. M. Shea, E. F. Ryntz, *Mater. Sci. Eng.* 96 (1987) 231.

[92] I. Dutta, J. D. Sims, D. M. Seigenthaler, *Acta Metall. Mater.,* 41 (1993) 885.

[93] N. J. Sørensen, S.Suresh, V. Tvergaard, A.Needleman, *Mater.Sci.Eng.A.* 197(1995) 1.

[94] J. H. L. Pang, B. S. Xiong, *IEEE Trans. Comp. Packag. Technol*., 28 (2005) 830.

[95] P.T. Vianco, D. Shangguan, *Fatigue and creep of lead-free solder alloys: Fundamental properties, chapter 3 lead free solder interconnect reliability,* ASM International, Materials Park, OH, 2006, p. 67.

[96] B.S.S. Chandra Rao, K. Mohan Kumar, V. Kripesh, K.Y. Zeng, *Mater.Sci.Eng A*, 528 (2011) 4166.

[97] J. Salvetat-Delmotte, A. Rubio, *Carbon* 40 (2002) 1729.

[98] E. Saether, S.J. Frankland, R.B. Pipes, *Compos. Sci. Technol*. 63 (2003) 1543.

[99] K. Mohan Kumar, V. Kripesh, A.O. Taya, *J. Alloy. Compound.* 450 (2008) 229.

[100] D. D. E. Junghans *KOVINE, ZLITINE, TEHNOLOGIJE,* 33 (1999) 451.

[101] E. Uhlmann, S. Piltz, and U. Doll, *J. Mater. Proces. Tech.*. 167 (2005) 488.

[102] F.A. Lindemann, *Phys. Z.* 11 (1910) 609.

[103] P.R. Couchman, C.K. Ryan, *Philos. Mag. A* 37 (1978) 327.

[104] J.M. Ziman, *Principles of the Theory of Solids*, Cambridge University Press, London, (1972).

[105] B.S.S.Chandra Rao, K.Y Zeng and V. Kripesh, Development and characterization of composite solder materials in: *12th International Conference on Electronics Materials and Packaging, Singapore,* (2010) 160.

[106] S. Clyens, J.D. Campbell, Inst. Phys. Conf. Ser., 21 (1974) 62.

[107] Shohji, T. Yohshida, T. Takahashi, S. Hioki, *J. Mat. Sci.*, 15 (2004) 219.

[108] E.H. Wong, S.K.W. Seah, C.S. Selvanayagam, R. Rajoo, W.D. Van Driel, J.F.J.M. Caers, X.J. Zhao, N. Owens, M. Leoni, L.C. Tan, D.R. Frear, Y.S. Lai, C.L. Yeh, *J.Electron. Mater.*, 38 (2008) 6.

[109] W. C.Oliver, G.M. Pharr, *J.Mater. Res.*, 7 (1992) 1564.

[110] J.B.Pethica, R.Hutchings, W.C.Oliver, *Philos. Mag., A* 48 (1983) 593.

[111] M.F.Doerner, W.D.Nix, *J. Mater. Res.,* 1 (1986) 601.

[112] A.E.Giannakopoulos,S.Suresh *Scripta Mater.,* 40 (1999) 1191.

[113] K.L.Johnson, *J. Mech. Physic. Solid.,*18 (1970) 115.

[114] Y.T.Cheng, C.M Cheng, *J. Appl. Phys.,* 84 (1998) 1284.

[115] K.Zeng, C.H.Chiu, *Acta Mater.*, 49 (2001) 3539.

[116] A.E.Giannakopoulos, P.L. Larsson , *Mech. Mater.*, 25 (1997) 1.

[117] P.L.Larsson, A.E.Giannakopoulos, E.SÖderlund, D.J. Rowcliffe, R.Vestergaard, *Int. J. Solid. Struct.*, 3 (1996) 221.

[118] K.Zeng, D.J.Rowcliffe, *Phil. Mag. A*, 74 (1996) 1107.

[119] I.N.Sneddon, *Int. J. Eng. Sci*.,3 (1965) 47.

[120] V. L. Niranjani, B. S. S. C. Rao, V. Singh, and S. V. Kamat, *Mater. Sci. Eng: A,* 529 (2011) 257.

[121] NIST data base, *Database for Solder Properties with Emphasis on New Lead-free Solders,* (2002).

[122] A. G. Atkins and D. Tabor, I. *Mech. Phys. Solid.*, 13 (1965) 149

[123] R. K. Abu Al-Rub, *Mech. Mater.,* 39 (2007) 787.

[124] R. R. Chromik, R. P. Vinci, S. L. Allen, M. R. Notis, *J. Mater. Res., 18 (2003)* 2251.

[125] H Mavoori, *J. Electon. Mater.*, 26 (1997) 783.

[126] J.W. Morris, Jr. and H.L. Reynolds, *Design and Reliability of Solders and Solder Interconnections,* ed. R.K. Madihara, S.M.L. Sanstry, P.L. Liaw, K.L Murty, D.R Frear and W.L. Winterbottem, (Warrendale, PA: TMS), (1997) 49.

[127] J. Villain, O. S. Brueller, T. Qasim, *Sensors and Actuators A: Physical,* 99 (2002) 194.

[128] J. C.M. Li, *Mater. Sci. Eng.,* A 322 (2002) 23.

[129] S. Wiese, K. J. Wolter, *Microelectron. Reliab.,* 44 (2004) 1923.

[130] Z.G Chen, Y.W. Shi, Z.D. Xia, Y.F. Yan, J. Electron. Mater., 31 (2002) 1122.

[131] A. Syed, *Accumulated Creep Strain and Energy Density Based thermal Fatigue Life Prediction Models for SnAgCu Solder Joints, in: 54th ECTC Conference Proc*., (2004) 737.

[132] M.L. Huang , C.M.L Wu and L. Wang, *J. Electron. Mater.*, 34 (2005) 1373.

[133] G.E.Dieter, *Mechanical Metallurgy* 1986: McGraw-Hill Book Co.

[134] G.P.Bernasconi, *Creep of Engineering Materials and Structures,* Applied Science Publishers (1978).

[135] H.E.Evans, *Mechanisms of Creep Fracture,* Elsevier Science Publishing Company (1984).

[136] Harry Kraus, *Creep Analysis*, John Wiley & Sons, (1980) 19.

[137] K.Y.Zeng, *Nanoindentation and Naoindentation creep of ploymers materials,, in Ploymer tribology*, S.K. Shinha and B.J. Briscoe, Editors. 2008, Imperial Collage Press.

[138] M.J. Mayo and W.D. Nix, *Acta Metall*., 36 (1988) 2183.

[139] H.Li, A.H.W.Ngan, *Scripta Mater.*, 52 (2005) 827.

[140] R. Goodall, T.W. Clyne, *Acta Mater*., 54 (2006) 5489.

[141] S.Yang, Y.W Zhang , K.Y.Zeng, *J. Appl. Phys.,* 95 (2004) 3655.

[142] K.Y.Zeng, *Nanoindentation and indentation creep of polymeric materials, in Polymer Tribology*, Eds., S.K. Sinha, B.J. Briscoe, Imperial Collage Press, (2009) 141.

[143] C.Y.Zhang, Y.W.Zhang, K.Y.Zeng, *J. Mater. Res.*, 19 (2004) 3053.

[144] C.Y.Zhang, Y.W.Zhang, K.Y.Zeng and L.Shen, *J. Mater. Res.*, 20 (2005) 1597.

[145] T.O. Mulhearn and D. Tabor, *J. Inst. Metal.*, 89 (1960) 7.

[146] K. L. Johnson, *J. Mech. Phys. Solids* 18 (1970) 115.

[147] H.M.Pollock, D.Maugis, M.Barquins, *Characterisation of submicrometre surface layers by indentation. In: Blau PJ, Lawn BR, editors.Microindentaion techniques in materials science and engineering*. Philadelphia (PA): ASTM, (1986) 47.

[148] A. F. Bower, N. A. Fleck, A. Needleman, and N. Ogbonna, *Proc. R. Soc. London* A441 (1993) 97.

[149] Y.T Cheng, C.M Cheng, *Mater. Sci. Eng: R*, 44 (2004) 91.

[150] Z.H.Cao, P.Y.Li, H.M.Lu,Y.L.Huang, Y.C.Zhou,X.K.Meng, *Scripta Materialia*, 60 (2009) 415.

[151] S. M. L. Nai, J. Wei and M. Gupta, *Mater. Sci. Tech.* 24 (2008) 443.

[152] Y. D. Han, H. Y. Jing, S. M. L. Nai, L. Y. Xu, C. M. Tan and J. Wei, *Int. J. Modern Phys. B*, 24 (2010) 267.

[153] Y.D. Han, H.Y. Jing, S.M.L. Nai, L.Y. Xu, C.M. Tan and J. Wei, *J.Electroc. Mater.* 39 (2010) 223.

[154] P. M. Srinath and P. Aswath, *J.Mater.Sci.* 42 (2007) 7592.

[155] P. Yao, P.Ping, J.Liu, *J. Alloy. Compd.*, 462 (2008) 73.

[156] K. Levis, and A. Mawer, *Assembly and solder joint reliability of plastic ball grid array with lead-free versus lead-tin interconnect. In: Proceedings, Electronic Components and Technology Conference*, (2000) 1198.

[157] B.I.Noh, J.M.Koo, J.W.Kim, D.G.Kim, J.D.Nam, J. Joo, S.B.Jung, *Intermetallics*, 14 (2006) 1375.

[158] L.Y.Hsiao, S.T.Kao, J.G.Duh, *J. Electron. Mater.*, 35 (2006) 81.

[159] K.M. Chen, *J Mater Sci: Mater Electron*., 20 (2009) 484.

[160] S.W.Yoon, V.P. Ganesh, S.Y.L. Lim, V. Kripesh, *IEEE Trans. on Adv. Packag.*, 31 (2008) 519.

[161] P.F. Yang, Y.S.Lai, S.R.Jian, J. Chen, R.S.Chen, *Mater. Sci. Eng.*, A485 (2008) 305.

[162] R.Rhee, J.P.Lucas, K.N.Subramanian, *J. Mater. Sci-Mater.Electron.*, 13 (2002) 477.

[163] P.F.Yang, Y.S.Lai, S.R.Jian, J.Chen, R.S.Chen, *Mater. Sci. Eng A*, 485 (2008) 305.

[164] K.M.Kumar,V.Kripesh, L.Shen, K.Y.Zeng, A.A.O.Tay, *Mater. Sci. Eng. A* 423 (2006) 57.

[165] R.Rhee, J.P.Lucas, K.N.Subramanian, *J. Mater. Sci.-Mater. Electron.,*13 (2002) 477.

[166] G.Y.Jang, J.W.Lee, J.G.Duh, *J.Electron.Mater.*, 33 (2004) 1103.

[167] F.Gao, T.Takemoto, *Mater. Lett.,* 60 (2006) 2315.

[168] J.P.Lucas, H.Rhee, F.Guo, K.N.Subramanian, *J.Electron.Mater.*, 32 (2003) 1375.

[169] K.S.Kim,S.H. Huh,K.Suganuma, *J.Alloys. Compd*., 352 (2003) 226.

[170] W.C.Oliver, G.M.Pharr, *J. Mater. Res.*, 5 (1990) 123.

[171] F.Cleymand, O.Ferry, R.Kouitat, A.Billard, J.Von Stebut, *Surf. Coat.Technol*., 200 (2005) 890.

[172] E.Soderlund, I. Reineck and D.J.Rowcliffe, *J. Mater. Res.*, 9 (1994) 1683.

[173] I.Tsai, E.Wu, S.F.Yen, T.H.Chuang , *J.Electron.Mater.*, 35 (2006) 1059.

[174] A.M.Korsunsky, M.R.McGurk, S.J.Bull, T.F.Page, *Surf.Coat.Technol.*, 99 (1998) 171.

[175] J.Mencik, D.Munz, E.Quandt, E.R.Weppelmann, M.V.Swain, *J. Mater. Res.*, 12 (1997) 2475.

[176] P.J.Burnett, D.S.Richerby, *Thin solid films*, 148 (1987) 51.

[177] D.L.Joslin, W.C.Oliver, *J. Mater. Res.*, 5 (1990) 123.

[178] X.Chen, J.J.Vlassk, *J. Mater. Res.*, 16 (2001) 2974.

[179] Y.Sun, T.Bell, S.Zheng, *Thin solid films*, 258 (1995) 198.

[180] A.K.Bhattacharya, W.D.Nix, *Int. J. Solids Struct.*, 24 (1988) 1287.

[181] B.S.S.Chandra Rao,J.Weng, L.Shen, T.K.Lee, K.Y.Zeng, *Microelectron. Eng.,* 87 (2010) 2416.

[182] M.A.Dudek, N.Chawla, *Intermetallics,* 18 (2010) 1016.

[183] C.Z.Liu,J.Chen, *Mater.Sci.Eng.A*, 448 (2007) 340.

[184] Y.Rosenthal, A.Stern, S.R.Cohen, D.Eliezer, *Mater. Sci. Eng A*, 527 (2010) 4014.

[185] H.Tsukamoto, Z.Dong, H.Huang, T.Nishimura, K.Nogita, *Mater. Sci.Eng. B*, 164 (2009) 44.

[186] X.Deng, M.Koopman,N.Chawla, K.K.Chawla, *Mater.Sci. Eng.A*, 364 (2004) 240.

[187] R.R.Chromik,R.P.Vinci, S.L.Allen,M.R.Notis, *J. Mater.Res.*, 18 (2003) 2251.

[188] K.L.Jhonson, *Wear* 9 (1966) 4.

[189] R.J. Fields, S.R. Low III, G.K. Lucey Jr., *Physical and mechanical properties of intermetallic compounds commonly found in solder joints,* M.J. Cieslak, J.H. Perepezko, S. Kang, M.E. Glicksman (Eds.), *The Metal Science of Joining, TMS*, Warrendale, PA, (1992) 165.

[190] X.Li, B.Bhushan, *Mater. Character*. 48 (2002) 11.

[191] A. Kumar, K.Zeng, *Int. J. Modern Physics* B24 (2010) 256.

[192] A. Kumar, K.Zeng, *Int. J. Appl.Mech.,* 2 (2010) 41.

[193] W.K.Choi; C.S.Premachandran, O.S.Chiew; X. Ling; L.Ebin; A.Khairyanto, B.Ratmin, K.C.W.Sheng, P.P.Thaw; J.H.Lau, *Development of novel intermetallic joints using thin film indium based solder by low temperature bonding technology for 3D IC stacking in: Electronic Components and Technology Conference, 59th*. (2009) 333.

APPENDIX A: FABRICATION OF WAFER-LEVEL BUMPING

A.1. Mask and Test Vehicle Design

A test chip of 10 X 10 mm^2 size designed with area populated I/O off-chip throughout the wafer with a unique pitch for each wafer. The mask design for different pitches described in the Figure A.1 whereas microbump height, diameter and pitches are shown in the schematic diagram (Fig A.2).

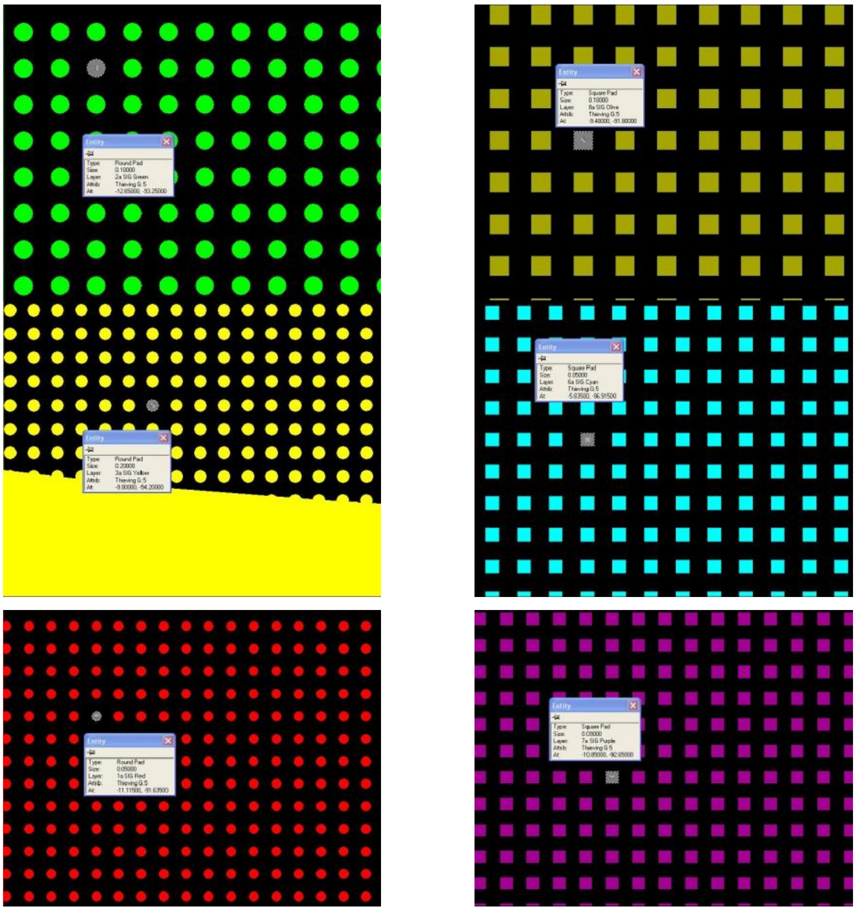

Type: Round Pad
Size: 0.10000
Layer: 2a SIG Green
Attrib: Thieving G.5
At: -12.65000, -93.25000

Type: Round Pad
Size: 0.20000
Layer: 3a SIG Yellow
Attrib: Thieving G.5
At: -9.00000, -94.20000

Type: Square Pad
Size: 0.18000
Layer: 8a SIG Olive
Attrib: Thieving G.5
At: -9.40000, -91.80000

Type: Square Pad
Size: 0.05000
Layer: 6a SIG Cyan
Attrib: Thieving G.5
At: -5.83500, -96.91500

Type: Round Pad
Size: 0.05000
Layer: 1a SIG Red
Attrib: Thieving G.5
At: -11.11500, -91.63500

Type: Square Pad
Size: 0.09000
Layer: 7a SIG Purple
Attrib: Thieving G.5
At: -10.85000, -92.65000

Figure B.1: UBM and solder mask design for different sizes of solder joints fabricated using screen printing (>100μm).

Test vehicle designed for microbump according to the current test chip design as shown in Figure A.1.The Current design consists of 20 daisy chains on Cu/Ti/Si3N4 test chip at RDL layers to assess the level 1 interconnect reliability.

Table A.2: Typical design parameters used in solder bumping by Screen Printing

Diameter of the pad, µm)	Square length of PR via(µm)	B, Pitch(µm)
80	80	200
160	220	300
240	400	600

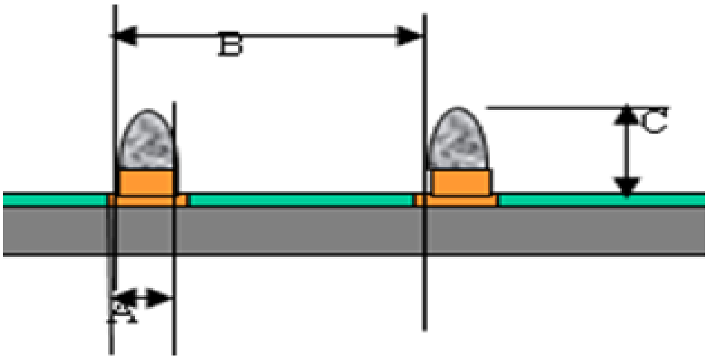

Figure A.3 Typical Test vehicle design used in the wafer-level solder microbumping.

A.2. Materials and Methods

The p-type silicon (100) wafers of 200mm diameter with thin electrical insulating layer of 1000A° SiO_2 used for the fabrication of test chip demonstrator. Sputtered Ti/Ni (v)/Au layers served as pads with daisy chains. The Ni(V) Au layer also acts as the seed layer for electrical contact during the electroplating of copper interconnects. Benzocyclobutene (BCB) dielectric passivates daisy chains and to define the pads for copper interconnects. Dry film photo resist used to make the patterned thick UBM layer for selective plating of copper interconnects. A part from the solder paste screen printing, electroplated Sn and eutectic Sn-Ag also used as a solder bumping materials. Developer and stripper solutions for the above resist materials. Piranha solution (H_2SO_4 + H_2O_2) is for wafer cleaning. Ratio of H_2SO_4 to H_2O_2 was 5:1. Acetone and PI for cleaning of wafers to reclaim the PR coated wafers.

A.3. UBM Fabrication

A.3.1. Thermal Oxide Deposition

SiO_2 is an excellent electrical insulator ($1x10^{20}$ Ω-cm) with high breakdown voltage (10MV/cm). In micro-fabrication process, a thin layer SiO_2 deposited over the bare Si by thermal oxidation process. The procedure involves diffusion of an oxidizing agent into the Si at high temperature and reacts with it. The rate of oxide growth is predicted by the Deal-Grove model. Thermal oxidation of silicon is carried out at a temperature between 1000 and 1200°C, resulting in so called high temperature oxide layer (HTO). Thickness of SiO_2 and nitride layer thicknesses used in this work for all wafers is about 2.4 and 1μm, respectively. KLA SFX200 metrology is used to determine the oxide and low temperature nitride film thicknesses, statistical quantities are shown in the Fig B.4.

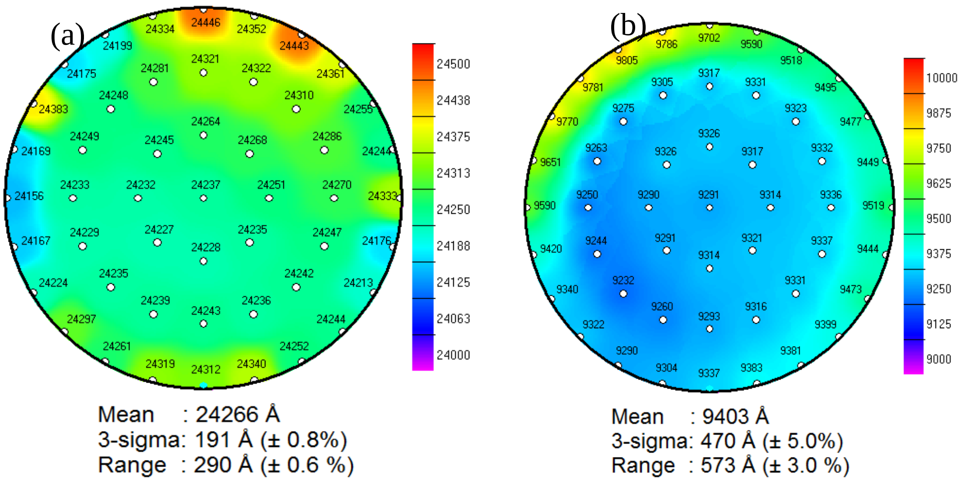

Figure B.4 Typical thicknesses of dielectric films (a) oxide (b) nitride used for wafer-level solder bumping applications.

A.3.2. Seed Layer Deposition

The seed layers for electroplating deposited using sputtering system *(Balzers LLS 502, load lock)*. Ti layer coated on the wafer prior to deposition of Cu seed layer films to promote the adhesion. The 99.9999% purity Cu target used as the cathode for seed layer

Cu deposition. The sputtering conditions such as 4 x 10^{-6} base pressure; 3 x 10^{-1} working pressure; 4KW, 6KW and 1KW sputter power for Ti, Cu and Au respectively. The sputtering chamber seasoned for 20hrs to remove the chamber wall moisture efficiently. High Purity Argon gas used to maintain inert atmosphere. Seed layers deposited by DC magnetron sputtering on the Si (100) substrate. The substrate maintained at a distance of 70mm from the target and the deposition rate of the film estimated to be 2.15nm/s.

A.3.3. RDL patterning

Sputtered Ti/Ni (V)/Au layer used for daisy chains and UBM pads. This also used as a seed layer for electrical contact during the electroplating of copper interconnects.

A.3.4. Dry-Film Lamination and Spin Coating

Dry film laminator (Western Magnum ^{TM} - XRL 240) used for lamination of photo-resist lamination of 20 µm and 50 µm dry films (MX5050 -50 µm thickness DP) over the 8´´ Si –wafer. Top roll temperature of laminator is optimized to 105°C whereas for lower roller is 65°C and speed of both roll is about 0.9rpm. Thicknesses of dry-film other than 20 and 50um, a combination of these thicknesses are being laminated. For positive masks and fine-pitch pattern, a thin layer of dielectric coated to define the mask pattern over the Si-wafer. SVG 90 series spin-coater used to coat, soft bake, post exposure bake and to develop PR material.

A.3.5. Photo Resist Exposure and Development

EVG 640 mask aligner used to expose the photo sensitive layers through plastic masks or chrome masks in the contact mode. Subsequent mask layers aligned using alignment marks in the lithography processes. A UV-light with wave length range 365-405*nm* used to expose the photo-resist films/coat and corresponding optimized exposure energies are summarized in the Table B.2.

Table A.2: Photolithography parameters for wafer-level UBM fabrication process.

Dry-film(DP) thickness (*μm*)	Exposure Energy(*mJcm*$^{-2}$)	Developing time (*Min*)	Targeted feature	Pre-exposure baking (PEB)
200	2500	10~12	> 200 μm via	1 min at 95°C
100	240	7~8	100 ~200μm	1 min at 95°C
50	120	4.5~5	50 ~100μm	1 min at 95°C
40	65	3 min 30s	50μm	30s at 95°C
20	45	2min 20s	25~40μm	30s at 95°C

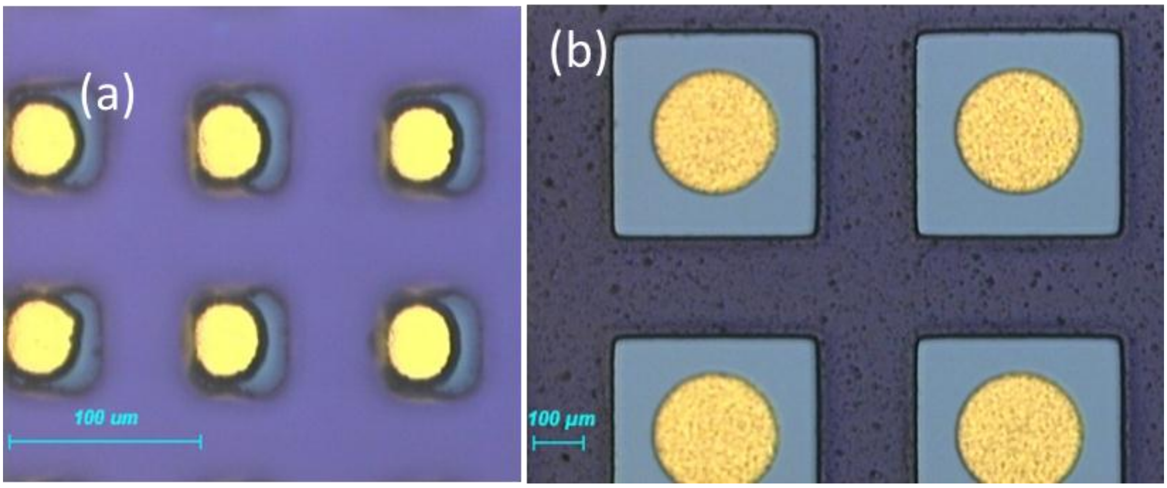

Figure A.5: Typical PR pattern for Cu UBM for Composite solder bumping (a) partial developed UBM pattern (b) developed PR pattern for solder screen printing.

A.3.6. Oxygen Plasma Cleaning

Photo-resist Descum conducted using *Advanced*^{TM} *Vacuum* (*VISION320-RIE*) at 30sccm flow rate O_2 plasma (Descum version1.08 recipe), 400 watts RF power and 50mtorr pressure for 10 minutes. High power selected to remove dry film remains in the deep vias. However, at higher RF power, there is possibility of the dry film etching up to 1 to 1.5um during O_2 plasma. One has to take care of thickness reduction during this process as the thickness of electroplated post is precision. Apart from the cleaning dry film residue, also activates the PR surface to increase the wettability with electrolyte during Cu electroplating.

A.3.7. Electroplating of Copper

Copper electroplating conducted using Moto 8” wafer electroplating tool, which was fountain type (Cup type) in which Sperolyte $CuSO_4$ based solution (Atotech Pte. Ltd) used as electrolyte solution. The principle of plating involves that the wafer loaded in chuck as cathode placed upside down at the top of the plating tool and the soluble copper anode was positioned at the bottom in cup shaped electrolyte chamber. The electrolyte fountainhead from the bottom to the wafer surface through the diffusers. The concentration polarization easily controlled this fountain type electrolyte flow and thereby improved the uniformity and plating efficiency.

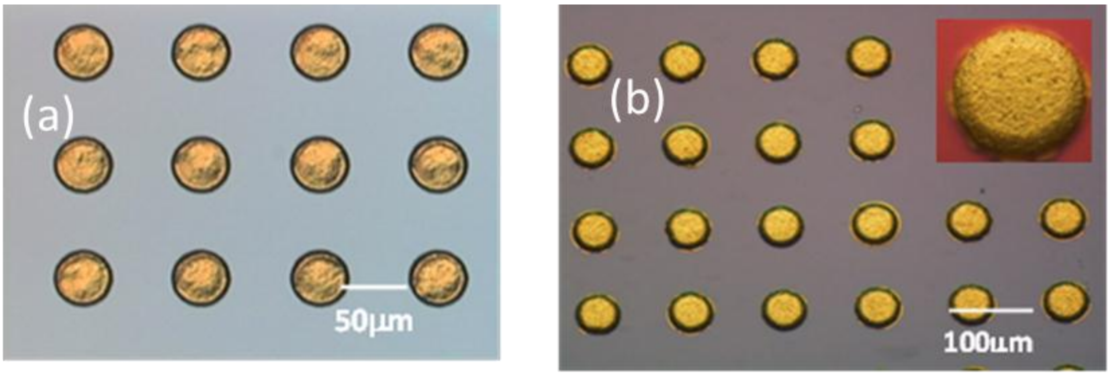

Figure A.6: Typical Electroplated Cu for 50 µm UBM (a) High (b) lower current density.

Table A.3: Typical plating parameters used for Cu plating.

UBM dia. (µm)	Cu pillar hieght (µm)	Current density	Plating time (Min)	Remarks
25	25	0.15A/plated area	60	Planar surface
45	25	0.15A/Plated area	180	Planar surface
100	25	0.45A/plated Area	30	0.5µm roughness
200	15	0.6A/ plated Area	45	1.5µm roughness
400	15	0.6A/ plated Area	120	2 µm roughness

The plating process carried out in two steps, in first step, apply pre-wetting agent (PW-1000) over the pattern wafer for 20 seconds and afterwards rinse with DI water for 40 to 50 seconds. Pre-wetting agent diluted prior to use on the wafer in the ratio of 1:10 for PW-1000: Di H_2O, purpose of Pre-wetting agent is to improve the wettability during plating. In the second step, the flow rate maintained at constant with the rotating speed of the chuck being manipulate to achieve uniform copper plating in the entire wafer. Hence the plating thickness could be controlled by optimizing the current density and platting time and uniformity could be controlled by optimizing the flow rate of electrolyte. The plating process carried out at room temperature. Plating current used for 25um, 50, and 100 via is about 0.15, 0.2 and 2.5A, respectively. Lower current density maintained for all wafers in order to achieve the uniform Cu pillar height. Time of plating for 25umx25um sized Cu pillar optimized about 60 min. Table B.3 shows the summary of optimized Cu platting conditions.

A.4. Solder Bump fabrication

A.4.1. Solder Paste Preparation and Screen Printing

The solder powders (Type 7, supplied by Heraeus Materials Ltd) and nano-sized particles of Mo (30-50*nm* range) weighed according to their weight percentage ratios. The pre-weighed nano-particles and solder powders blended homogeneously using a V-cone blender operated at a rate of 50 rpm. The nano composite solder powder and Customized no-clean halogen-free flux, Supplied by Heraeus Materials Ltd, Singapore) have weighed in the ratio of 88:12 and placed together in the container of a Thinky Mixer (*AR-100 table-top model, Japan*). The Thinky mixer operates on a non-contact mixing system where the material container rotates and revolves at 400G acceleration, resulting in fast and highest-grade mixing without air bubbles. This method offers repeatable and reproducible composite solder paste up to 0.3 wt. % of nano-particle additions.

A.4.2. Electroplating of Tin

The tin deposited at the tip of the copper interconnects using RENA 8 inch wafer electroplating tool, which was a rack type in which spherolyte solution (Atotech Pte. Ltd) electrolyte solution whereas tin pellets serves as anode. Principle of plating involves that the wafer loaded in the chuck and the chuck positioned parallel to the anode as shown in the Fig.B.6. Solder thickness, uniformity and solder shape at the tip of the Cu pillar controlled by optimizing the current density, flow rate of electrolyte and plating time as shown in the table B.4.

Table A.4: Sn plating variable for microbumping.

Sn dia.	Solder thickness	Current density	Plating time	Remarks
25µm	5, 10, 20	0.3A/plated Area	20, 40, 80 min	Fine grain size & uniform plating
45µm	5, 10 20	0.4A/plated Area	15,30, 60 min	Fine grain size & uniform plating
100µm	5, 10, 20	0.7A/Plated Area	12, 24, 40 min	Larger grain size & rough surface

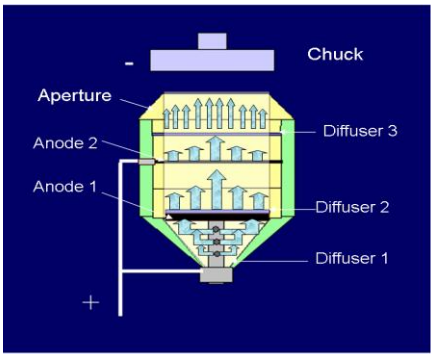

Figure B.7: (a) Schematic diagram of principle of electroplating.

The Surface roughness of plated solder increase with an increase in the plating current density, which described in the Fig B.8 that lower roughness at 03A/plated area comparatively higher current density (0.7A/plated area).

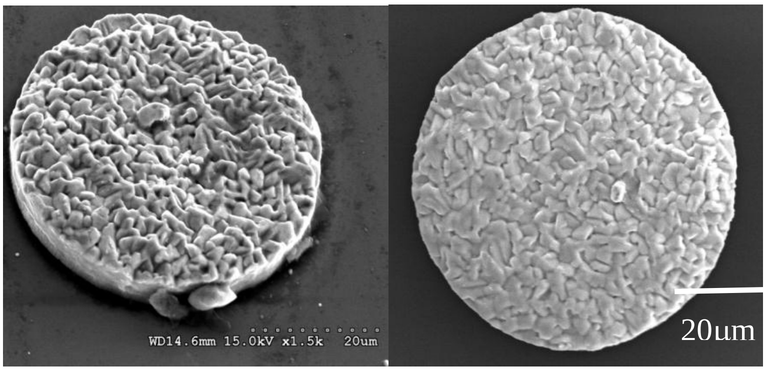

Figure A.8: typical electroplated Sn (a) high current density (0.7A/ plated Area) (b) low current density (0.3A/ plated Area).

A.4.3. Thermal Reflow Process

After stripping the photoresist and seed layer etching, electroplated solder bumps reflowed in 6-zone reflow oven in N_2 atmosphere using reflow profile as described in Fig.A.9. Lead-free solder bumps reflowed at 25 to $50^{o}C$ above it's liquids temperature of Sn and SnAg solder for about 80seconds, to form the solder bump at the tip of Cu UBM. Different reflow times at the peak of the reflow temperature achieved using different conveyer speeds i.e. 10 inch per minute, 15 inch per minute and 21 inch per minute give 60, 80 and 120s, respectively. Figure A.10 shows the planar view of Cu UBM with solder cap before reflow. To obtain a good spherical bump shape, the wafer reflowed twice at the same profile. Reason for the improper bump shape during the first reflow was because the solder was not fully melted. When these solder joints reflowed again with additional flux, this makes the solder bump melt entirely and resulting in spherical bump.

A.4.4. Dry Film Photoresist-Resist Stripping

Dry-film stripper (CST-161) heated to 65°C temperature and wafer gradual development for 10 to 15 minutes depending on DP thickness and subsequently cleaned by DI H_2O Rinse. Dry film thickness 40μm, or less, heating not required to strip the photoresist. Dry fill stripper diluted at the ratio of 1CST-161:10H_2O. However, care need to be taken when stripping the shallow Sn thickness microbump as Sn possibly etched away during stripping. In this case, more diluted CST-161 need to be used to control Sn dissolution in to the stripper.

Table A.5: Typical reflow condition studied Sn/Cu microbump solder joints.

Sn/Cu Joint (μm)	**Reflow Temperature(°C)**	**Multiple Reflows (80 seconds at each reflow)**	**Reflow time at the peak of the reflow , seconds**
10/50*	245, 265 & 285	1st , 2nd ,3rd ,5th ,7th and 10th	80,110 and 170
80/110*	245, 265 & 285	1st , 2nd ,3rd ,5th ,7th and 10th	80,110 and 170
160/200*	245, 265 & 285	1st , 2nd ,3rd ,5th ,7th and 10th	80,110 and 170

Sn→Solder thickness/ bump height; Cu→UBM diameter; Cu thicknesses for all UBM is 14μm

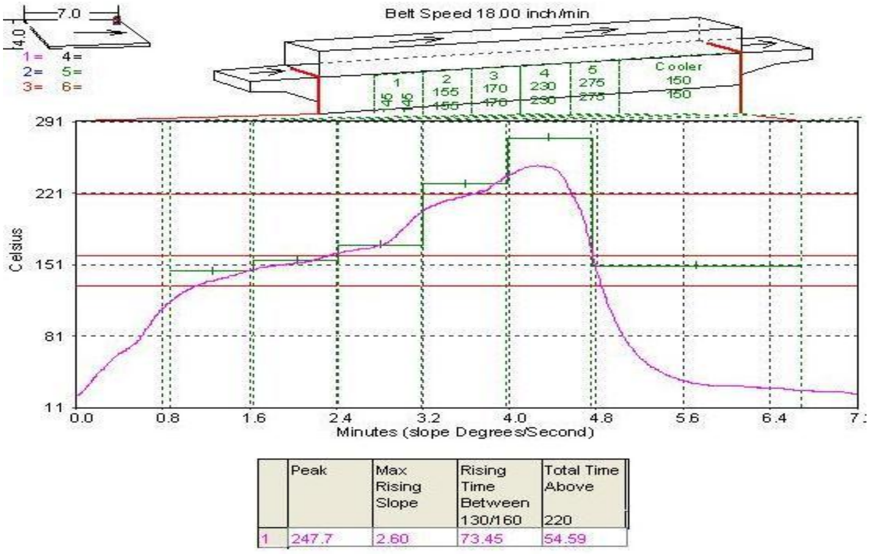

	Peak	Max Rising Slope	Rising Time Between 130/160	Total Time Above 220
1	247.7	2.60	73.45	54.59

Figure A.9: Typical thermal reflow cycle in lead-free solder bumping.

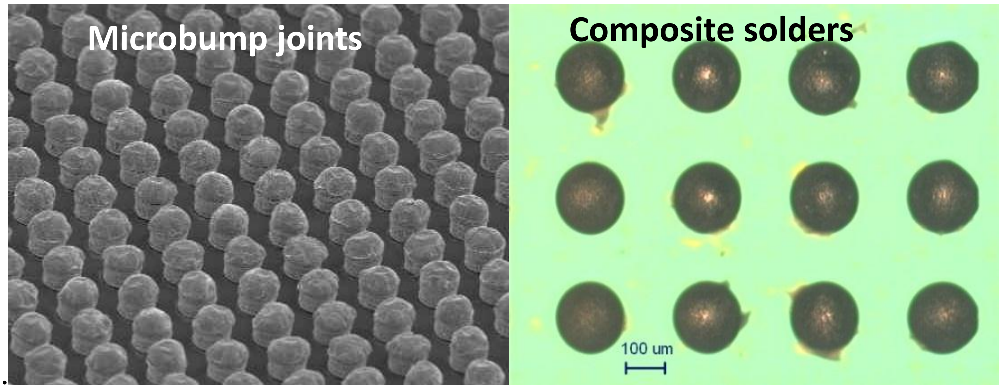

Figure A.10: Shows the solder bump after reflow and PR strip (a) microbump over the Cu pillar (b) SnAgCu/Cu solder joints.

A.4.5. Wafer dicing

After stripping of PR from the fabricated of Cu UBM with solder cap, the wafer diced into individual dies (10X10 mm^2) using dicing machine (DAGE^{TM}). Diamond tip wheel used for cutting. Once the Cu pillars fabricated on the wafer, they were ready for bonding to the next level substrate. Hence, the wafer with Cu pillar diced into individual dies using a dicing machine.

A.6. Characterization of solder bumps

A.6.1. X-ray system

Dage-XD 6500 X-ray system performed on the reflowed bumped dies to examine the voids in the bonded solder and to see whether there any bumps bridged or not. The minimum feature size identification in this system was 2µm. X-ray tube voltage of 30-160KV used. After reflows, solder bumped wafers examined before dicing. If there are any small voids (<2µm) in the solder joints present at this stage, bumped wafer sent back to another reflow.

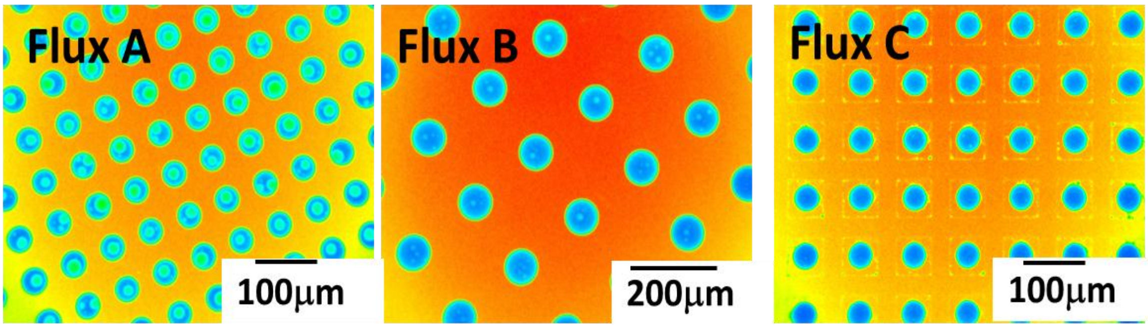

Figure A.11: X-Ray pattern showing voids in the composite solder for different flux A. Flux B and Flux C chemistries used in the solder paste.

A.6.2. Cross-sectioning and Metallography

JEOL 5600LV scanning electron microscope (SEM) used to view the cross-section of the vias in the photo-resist thick layers, electroplated copper interconnects and as well as to analyze the failure mechanisms of the packaged interconnects after thermal cycle testing. The samples mounted on the sample stud by means of double–sided adhesive tapes. The SEM assessment performed at an accelerating voltage of 15kV. Sn/Cu solder joints mounted in the Epoxy resign and subsequently cross-sectioned using mechanical polishing methods down to 0.05µm diamond suspension. For the purpose of revealing grain size of solder joints, these specimens polished with 0.05 µm Silica Gel for 10 minutes with controlled flow of silica gel at 5N holding pressure against the polishing cloth at 50rpm.

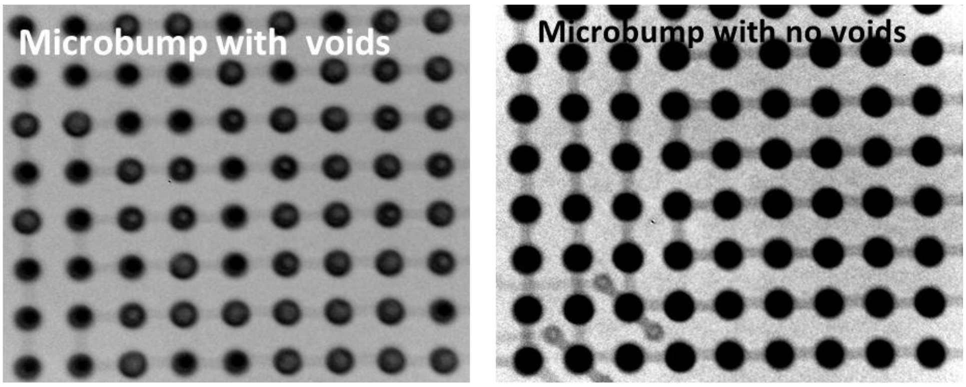

Figure A.12: X-Ray pattern showing (a) voids in microbump joint (b) without voids.

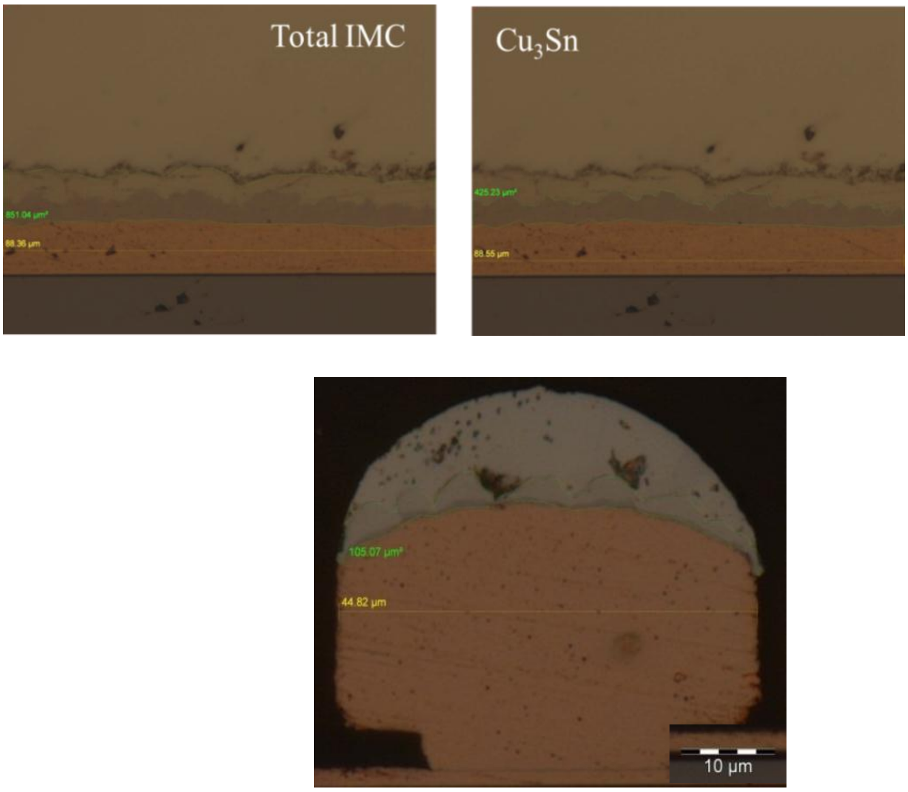

Figure A.13: (a-b) shows the typical IMC assessment technique for BGA solder joints (c) IMC measurements for microbump solder joints.

Grain size and Interfacial intermetallic compound (IMC) film are visible under the optical microscope. However, this approach strongly depends on dexterity of operator. IMC layer imaged using optical microscopy (*OLYMPUS-DD72*) at 500X magnification and elemental analyses of different IMCs determined using SEM-EDAX analysis (JEOL, JAPAN). Thickness of combined intermetallic thickness measured using imaging software (AnalySIS ^{TM}), which based on the total IMC area in solder bump divided by the diameter of the UBM. Figure A.13 shows the approach for total interfacial IMC and Cu_3Sn thickness, whereas Cu_6Sn_5 is difference between the total and Cu_3Sn thickness. IMC measurements conducted three different locations for larger solder joints and average 4 solder bumps reported. In case of microbump joints, IMC data reported average of 9 microbump joints.

A.7. Wafer-level Bumping Fabrication Process

The fabrication process of solder interconnects based on standard photolithography and electroplating (UV-LIGA) process, which is compatible to the wafer-level IC fabrication. The fabrication process of the typical wafer-level single layer Cu pillar interconnects schematically illustrated step-by-step in Fig. B.14. Minimum of two masks required to fabricate the Cu UBM and solder bump using screen printing. In case of microbumping process, only one mask is enough to fabricate Cu pillar and solder electroplating. Different sizes of the solder joints, from the 300 μm size to microbump solder joints fabricated using a different process methods for system level mechanical property characterization.

A.7.1. Fabrication of Different sized Sn/Cu Solder Joints

Different sizes of Sn/Cu solder joints fabricated using solder printing and electroplating technology. Typical process flow described in the Fig A.14. Thermal deposited P-type Si sputtered with Ti/Ni/Au metal layers using magnetron sputtering system (Balzer LLS). Negative toned JSR photoresist materials spin coated and patterned to form bond pads with daisy chains. Ti/Ni/Au layers wet etched one by one and finally photoresist stripped. Secondly, BCB dielectric polyimide spun to passivate the daisy chains and pattern the dielectric layer using UV lithography to open the pads. Negative photo resist thickness of 20µm laminated and patterned. Different sizes of Cu UBM (30, 50, 100, 200µm diameter) with 20µm thickness of Cu pillar electroplated using *Cuprabase 50* electrolyte at a current density of (0.6A / plated area) for 10, 25 and 40 minutes, respectively. Sn thickness (5, 10 and 20µm electroplated over the UBM Cu pillar using *microfabSn-200* electrolyte at a current density of (0.3A/plated area) for 24 min.

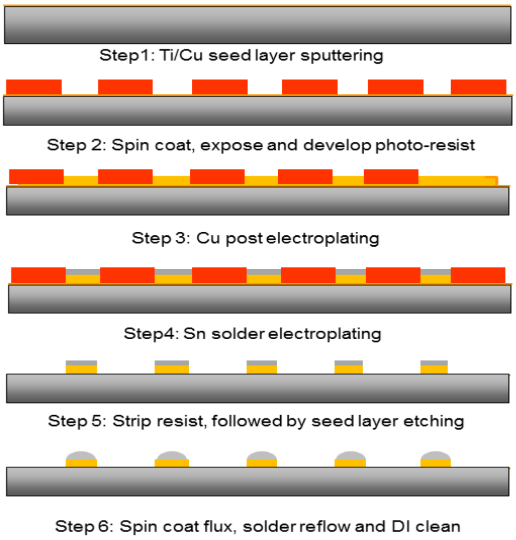

Figure A.14: Typical process flow for the fabrication of wafer-level microbumping.

Larger solder joint sizes such as 80 and 200 µm diameter solder joints are screen printed using tin solder paste (*Spplied by Heraeus Materials Singapore Pte. Ltd, Singapore*). Electrodeposited as well as screen printed wafers subjected to reflow treatments at different peak reflow temperature in N_2 protected reflow oven (*BTU-*

SSA70). After 1st reflow process, the photo resist stripped out using photo resist stripper (RR3 Resist strip) and Ti/Cu film selectively etched out using etchants (A96 and Ti890).

Wafer-level SnAg/Cu (15µm thickness Sn-2.7Ag over the 20x20 µm Cu pillar) microbumping fabricated using standard photo-lithography and electroplating techniques. Wafer-level Cu/Ni/Au/SnAgCu (50µm SnAgCu bump screen printed over the 1 µm Cu/ 0.5µm Ni (V) /100nmAu thin film UBM) microbumping fabricated using Sputtering, photolithography and screen printing techniques. Figure A.14 shows the sequence of the major steps in the wafer-level microbumping process. Process recipe for wafer-level microbumping described in the Table A.6.

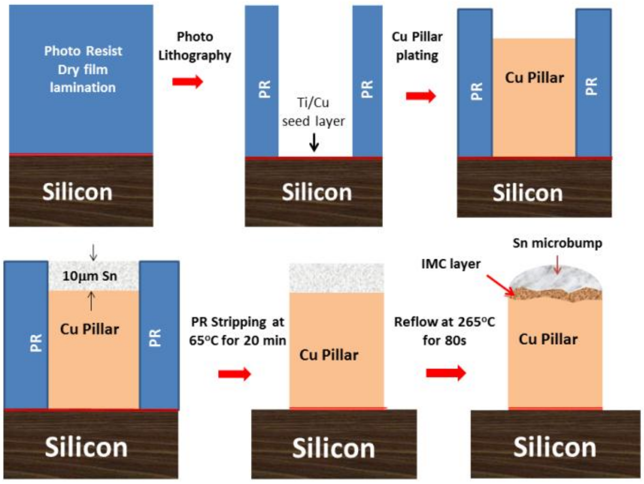

Figure A.15: Schematic representation of typical Sn/Cu microbump fabrication process.

A.7.2. Fabrication of Wafer-level Composite bumping

UBM structures fabricated using conventional lithography methods. The substrate used in this study was an electro-less Cu/Ni (P)/Au substrate with a Ni (P) layer of 5–7µm thickness. The SAC387 and SAC387+0.3Mo solder paste screen printed on the ENIG substrate and then subjected to multiple reflow treatment. Figure A.16 shows the typical solder bumping steps using screen printing methodology for BGA array wafer-level SnAgCu 305 solder bumping. A Typical lead free reflow profile with a peak temperature of 260°C and 60 s used for this work. Composite solder bumping is not successful with available fluxes for SAC305 solder paste. Commercial *TACflux023* is good enough for SAC and Ni reinforced SAC composite solders flux, however, whereas addition of Mo particles severely reduced the wettability of the composite solder with both Cu and ENIG. Different customized fluxes developed at Heraeus Materials Singapore Pte Ltd, which used for composite bumping. Finally grade C flux is perfectly suitable for Mo-reinforced composite solder joints up to 150µm.

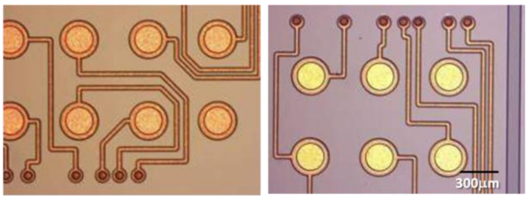

Top view of RDL Patterning

Top view of RDL with UBM

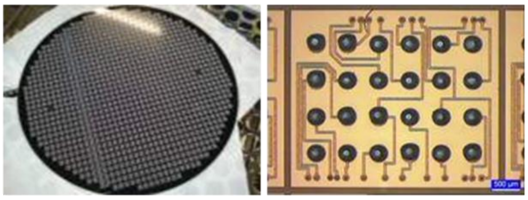

300mm wafer-level Sn3.5Ag0.5Cu solder bumped wafer

300µm solder joint over the UBM

Figure A.16: Typical steps involved during 300µm sized SnAgCu solder bumps.

Composite solder cannot be extended to level 1 interconnection because of process limitations such as screen printing capability and reduced flux quantity in the solder paste with increased amount of fine-particle in the solder paste (Type 7 and above). If apply more squeezing pressure to fill the PR via with type 7 solder paste, there will be a higher chances to flux squeeze out from the PR via, In other words, more squeezing of solder particles with less amount of entrapped flux in the PR via as shown in the figure B.17.

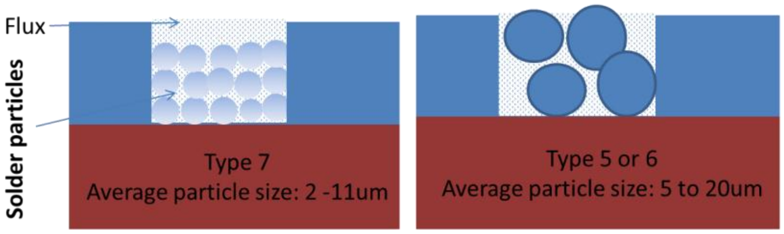

Figure A.17: Schematic representation of via filling with type 7 and type 5 solder pastes.

It is shown clearly that the void space between solder particles is high in the type 6 solder pastes comparatively in type 7 solder pastes. Up on subsequent reflow, insufficient amount of flux leads to inappropriate melting of the solder paste. Figure A.17 describes the effect of different type of fluxes on the bumping quality. Flux C gives sound solder joints without voids in it. Figure A.18 shows the process flow of wafer-level composite bumping.

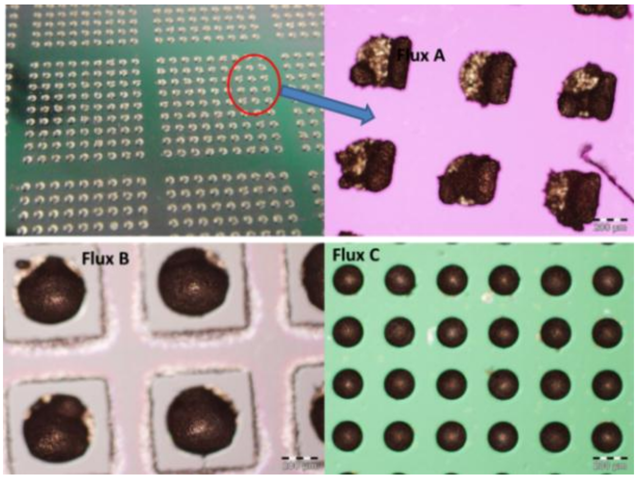

Figure A.18: Mo particle reinforced SnAgCu solder bumping with three fluxes.

A.7.3. Fabrication of Thin-film Interconnects

Indium, Pure Sn, In-Sn and Sn-Au have been identified as alternate lead-free solder materials for ultra-fine-pitch thin-film solder joints for chip side bumping applications because of its baseline advantages of vapor deposited and better wettability at lead-free reflow temperature.

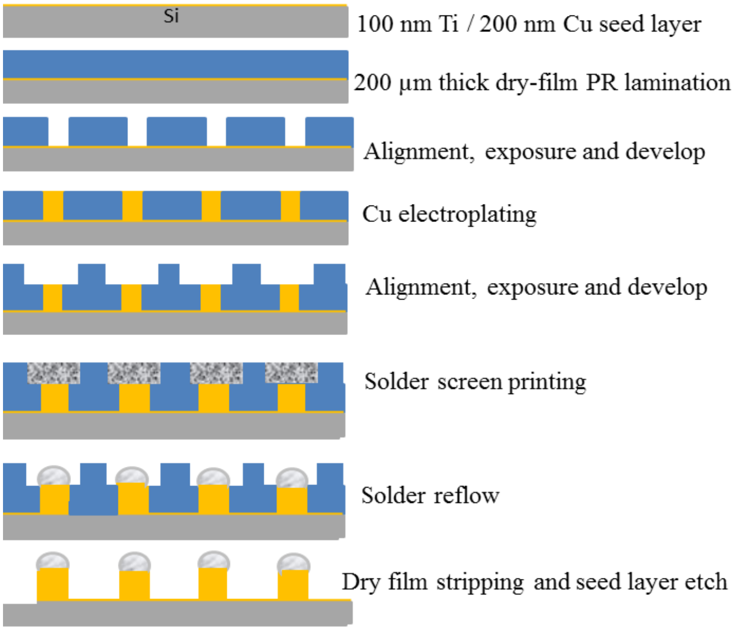

Figure A.19: Typical process flow for the fabrication of thicker Cu UBM and followed by composite solder screen printing.

Figure A.20 shows the typical *lift-off* technique for thin-film solder joints. Cu/In/Sn/Cu (with the thickness of multilayer deposited *In* and *Sn* is about 1.5µm) thin-film microbump joints fabricated using evaporation, lift-off and flip-chip techniques [22]. Process recipe and run-sheet for wafer-level microbumping is given in the Table A.6

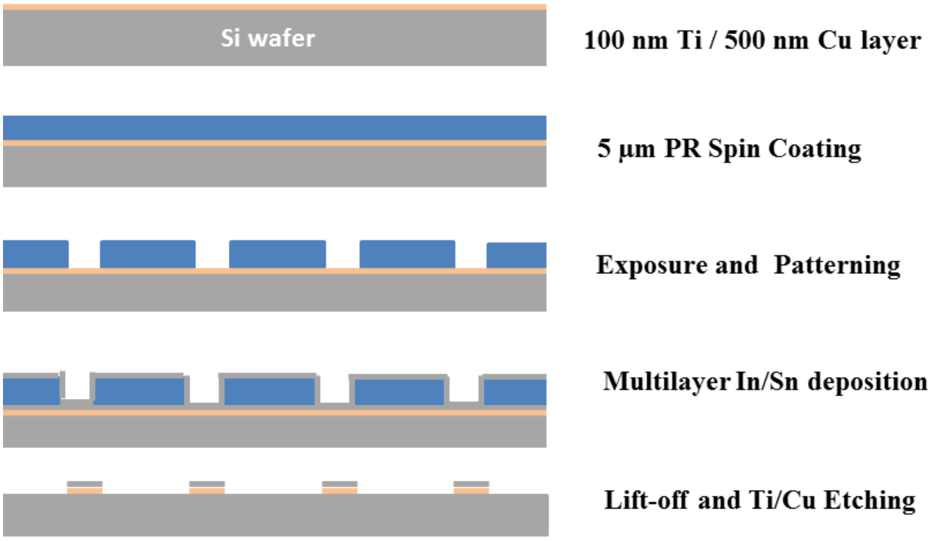

Figure A.20: Typical Lift-off fabrication process for thin film interconnects.

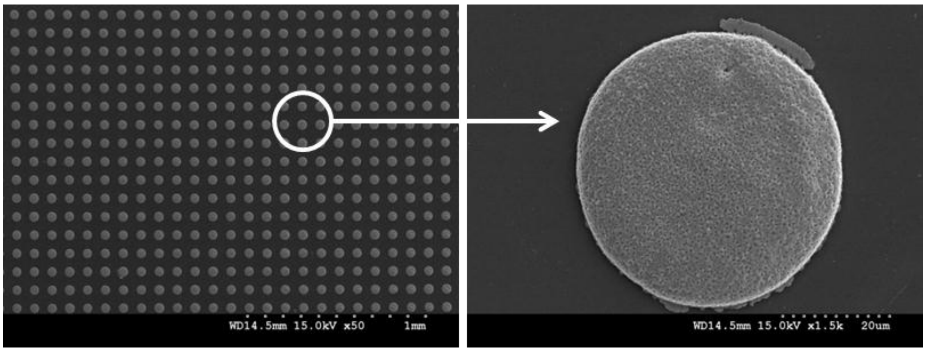

Figure A.21: Cu/Sn thin film microbump developed using lift-off technique.

Table A.6 Process runsheet for the fabrication of wafer-level Cu/In/Sn/Cu thin film joints

Process Step	Materials	Equipment	Parameters
Spin-coat lift-off photoresist	MA-N-1440 negative PR	SVG track	Pre-bake: 150^oC / 5 min; Final spin at 1200 rpm / 30 sec ;Soft bake: 120^oC / 60 sec
UV exposure		EVG aligner	700 *mJ/cm*^{2} ; Contact mode
Developing	MA-D 533/S	Manual	5 min in Developer; Observe for undercut profile under a microscope
O_2 Descum		RIE	O_2 plasma Descum
Acetic acid clean	Acetic acid	Wet bench	Immersion in acetic acid at room temperature for 5 min ; Blow dry in N_2
Ar sputtering		RIE	Argon sputtering for 30 sec
E-beam evaporation		E-beam evaporator	E-beam evaporate metallization in the following order Ti 100 nm / Au 1 μm / Sn 1 μm / In 3 μm / Au 50 nm
Lift-off	MR-Rem 660	Ultrasonic bath	Lift-off in stripper solution in an ultrasonic bath

Table A.7: Process run sheet for wafer-level microbumping fabrication

Process Step	**Materials**	**Equipment**	**Parameters**
Seed layer	Ti/Cu	Balzer	50 nm Ti / 50 nm Cu
Spin-coat photo-resist	SPR220	SVG track	Pre-bake: 150^oC; Final spin at 800 rpm / 60 sec; Soft-bake: 110^oC / 3 min
UV exposure (BB)		EVG aligner	800 mJ/cm^2 Contact mode
Developing	2.38 wt% TMAH	SVG track	Puddle and spin developing ; Developing time depend on feature size and density
PEB		Hot plate / SVG track	110^oC / 1 min
O_2 Descum		RIE	O_2 plasma Descum
Pre-wetting	PW-1000	Manual	Pre-wetting treatment in diluted PW-1000, followed by DI H_2O Rinse; (1 PW-1000 : 10 DI H_2O)
Cu electroplating	$CuSO_4$ bath	RENA / MOT	Low current density, DC plating required to achieve better uniformity; Check set-up wafer for actual plating rate
Sn electroplating	Sn solder bath	RENA	0.30 A DC plating; Check set-up wafer for actual plating rate
Strip PR	PRS3000	Wet bench	Strip in PRS3000, 65 ^oC / 15 min
Etch seed layer	Cu/Ti etchant	Wet bench	A-96 for Cu etching; Ti-890 for Ti etching
Solder thermal reflow (optional)	Water soluble spin coated flux	Reflow oven	Spin-coat water soluble flux prior to reflow. Peak reflow temp at 265^oC. Clean wafer in 70^oC DI H_2O to remove flux.

APPENDIX B: DIFFUSION KINETICS OF INTERRACIAL IMCs

B.1. Introduction

Effect of solder volume on the interfacial IMC formation shows that lower volume solder joints shows thicker interfacial IMC than higher volume solder joint [1]. It is an interesting to note that the dissolution rate of Cu reduced with shrinking solder volume. However, an apparent Cu concentration in the solder joint increasing with thermal reflows. Solder joints undergoes solid-state growth and transformation of interfacial IMC under the influence of temperature, stress and current density. In most of the Sn-based solder alloys, diffusion-driven processes are relatively fast at room temperature since homologous temperature is above $0.5T_m$. In addition to this, microelectronic device undergoes numerous thermal fluctuations during it's service, which promotes the thickening of the interfacial IMC layer. There two types diffusion processes such as volume diffusion and grain boundary diffusion. Grain boundary process is dominant at a lower temperature and fine grain microstructure. However, IMC grain size in the existing solder joints are more than 5μm, and reliability conditions are above 0.7 of homologous temperature. These conditions are most favorable for volume diffusion.

Thickness of interfacial IMC layers in the diffusion couples usually expressed by a simple power-law:

$$\delta = \delta_o + Dt^n \qquad \text{(B.1)}$$

Where, δ is the thickness of the IMC layer, δ_o is the thickness of IMC at a time is zero, D is the growth rate constant, n is the time-exponent and t is the reaction time. The time-exponent evaluated using non-linear regression analysis. The following Arrhenius relationship used to determine activation energies for the total IMCs, Cu_6Sn_5 and Cu_3Sn growth as:

$$D = D_o \exp\left(-\frac{Q}{RT}\right) \qquad \text{(B.2)}$$

where D is the growth rate constant, D_o is the frequency factor, Q the activation energy, R the gas constant (8.314 J/mol K) and T the aging temperature (K). Combining Eq.(B.1) and Eq.(B.2) gives the following model.

$$\delta = \delta_o + D_o t^n \exp\left(-\frac{Q}{RT}\right) \qquad \text{(B.3)}$$

Eq.(B.3) can be used to determine the time exponent, Activation Energy using non-linear curve regression analysis.

B.2. Experimental Methodology

Fabrication and preparation of SnAgCu, SnAg, Sn solder joints for interfacial diffusion study discussed in the Appendix A. A total of nine (9) Sn/Cu bumped wafers subjected to reflow treatment at three different reflow and then diced into 10x10mm. These dies also subjected to multiple reflows as shown in Table A.5. These reflowed dies subjected for isothermal aging, aging condition as the conditions summarized in the Table B-1.

Table B.1: Isothermal aging conditions for Pb-free solder joints from BGA to microbump.

Solder Joint (μm)	Aging Temperature (°C)	Aging Time (h)
SAC387/OSP/Cu	125, 150 and 175	0 - 500
SAC387/Au/Ni	125, 150 and 175	0 - 500
SAC387/ENIG	125, 150 and 175	0 - 1000
Composite/ENIG	125, 150 and 175	0 - 1000
Sn/Cu Joints	150 and 175	0-500
	200	0-25

B.3. Interfacial IMC Diffusion Kinetics in SnAgCu Solder Joints

B.3.1. Effect of Ni/Au Surface-Finish

Figures B.1 (a-c) shows the morphology and growth of the IMC layer for the Ni/Au substrate after aging at 150°C for 500 h aging time. For the Cu substrate with Ni/Au surface-finish, immediately after the reflow process, the thin Au layer dissolves quickly into the solder and precipitated as $AuSn_4$ particles in the solder while exposing the Ni layer to the solder. The Ni layer acts as a diffusion barrier, which prevent the Cu diffusion into the solder. Cu from the solder migrates to the interface and form a ternary phase, $(Cu,Ni)_6Sn_5$ with 24.66%Ni, 29.54% Cu, and 37.42% Sn [Fig B.1(a)]. The growth of the IMC layer is highly irregular, and the average thickness found to be 2.30μm. Upon further aging, another ternary phase $(Ni,Cu)_3Sn_4$ with 34.94% Ni, 10.48% Cu and 48.11% Sn started to form under the $(Cu,Ni)_6Sn_5$ IMC layer [2].

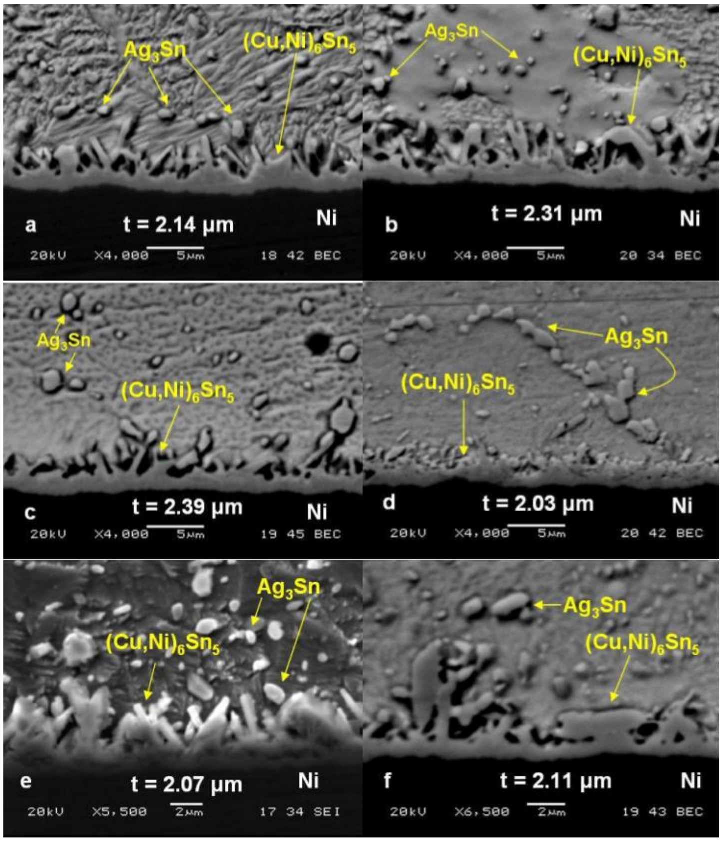

Figure B.1: SEM micrographs of Ni/Au/SAC305 solder aged at 125 and 150°C : (a) 100 h, (b) 300h (c) 500h at 150°C and, (d) 150h (e) 300h (f) 500h at 125°C.

There is a weak contrast between $(Cu,Ni)_6Sn_5$ and $(Ni,Cu)_3Sn_4$ IMC layers and it is hard to distinguish as the Cu3Sn and Cu_6Sn_5 layer. The formation of the $(Ni,Cu)_3Sn_4$ IMC is likely caused by a decrease in the amount of Cu diffusing into the interface during aging. In other words, the upper $(Cu,Ni)_6Sn_5$ IMC grew at the expanse of the available Cu in the solder bump. However, this growth soon limited due to limited Cu in the solder bump. Therefore, during the growth of the $(Cu,Ni)_6Sn_5$ IMC at the interface, the concentration of Cu in the solder bump will gradually reduce. As a result, with an abundance of Ni diffusing from the pad side, the $(Cu,Ni)_6Sn_5$ IMC gradually transformed to $(Ni,Cu)_3Sn_4$. This process lead to a thick $(Ni,Cu)_3Sn_4$ layer closer to the pad side with a thin $(Cu,Ni)_6Sn_5$ layer closer to the solder side after 500h aging. The interfacial microstructure of the Ni-Cu-Sn grows and changes dramatically in morphology as shown in Figures B.1 (a-c). For as-reflowed specimen, the IMC on the solder/ nickel interface was irregular and needle-like in feature. After 300 h of aging, coalescence of the IMC needles leads to lateral thickening and ripening. After 500 h of aging, the IMC layer growth is in a planar or layer-like manner. The change in the morphology or structure of the IMC expected to the change of Gibbs free energy in order to lower the surface energy.

B.3.2. Effect of Cu/OSP Surface-Finish

Figures B.2 describe the morphology and growth of the IMC layer for the Cu-OSP substrate after aging at 150^oC up to 500 hrs. During reflow, OSP passivated film in the Cu/OSP surface-finish removed by the flux, leaving the copper pad exposed to the molten solder. Immediately after the reflow process, scallop-like shaped IMCs formed at the solder joint interface and identified under EDX as Cu_6Sn_5 with 56.67% Cu and 42.94% Sn (η phase). This scallop shaped IMC layers undergoes, to the lateral ripening and thickening at 500 h for 125^oC and 200 h for 150^oC. This also observed that another IMC film formed between the Cu pad and the Cu_6Sn_5 layer by solid-state reaction to satisfying the requirement of local equilibrium, and this layer identified under EDX as Cu_3Sn with 79.60% Cu and 17.60% Sn.

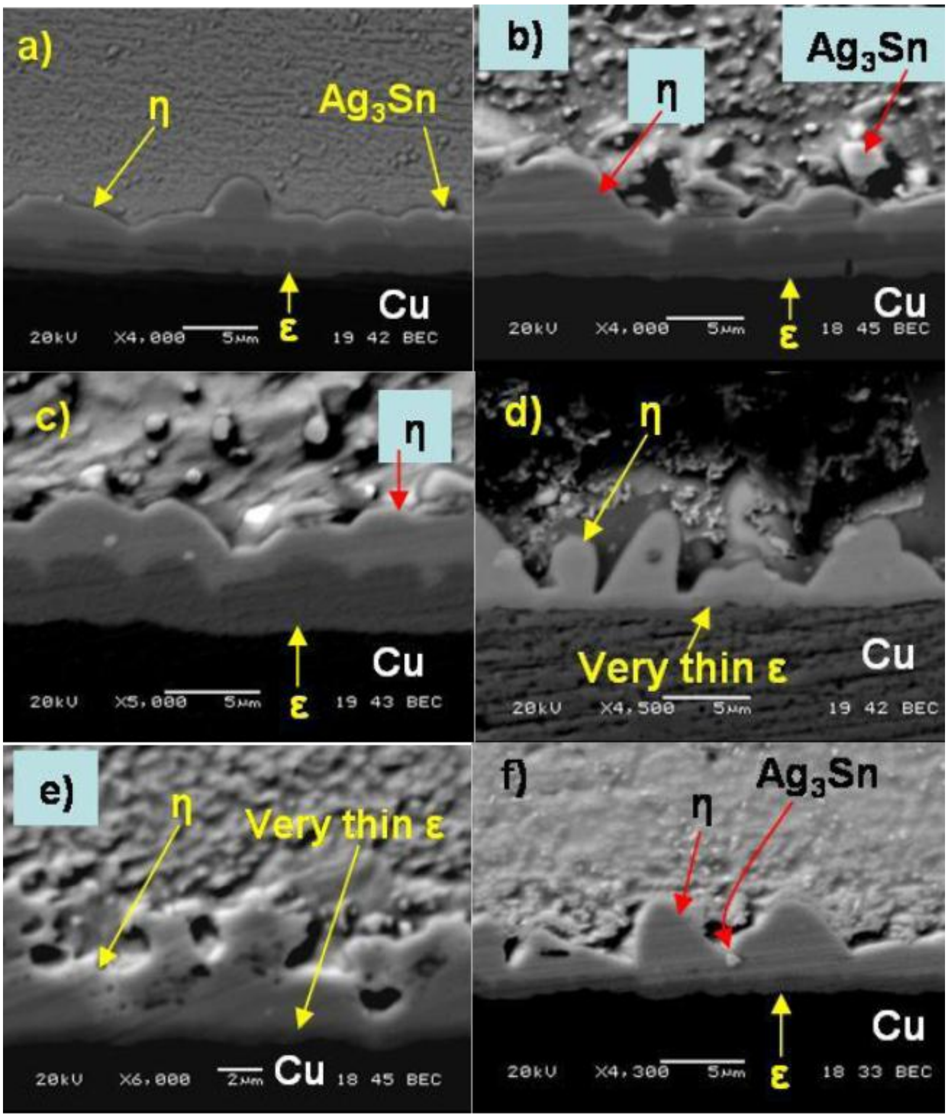

Figure B.2: Cu_6Sn_5 (η) and Cu_3Sn (ε) at the solder/Cu interface for aged: (a) 100h, 150°C, (b) 300h, 150°C, (c) 500h, 150°C, (d) 145h, 125°C, (e) 300h, 125°C, and (f) 500h, 125°C.

The formation of Cu_3Sn is a result of the changing morphology of the Cu_6Sn_5 scallops during aging. As the Cu_6Sn_5 layer evolved during aging to a thicker and more layer-like structure, the inter-scallop diffusion channels closed during aging. Consequently, Sn diffusion to the copper layer restricted, resulting in the formation of the copper-rich Cu_3Sn IMC layer underneath the Cu_6Sn_5 layer, which has a higher Cu to Sn ratio. Upon further aging, both the Cu_6Sn_5 and Cu_3Sn thicken with time as a result of increasing inter-diffusion. The morphology of the layers becomes flatter and more uniform as this lowers the surface energy. It observed from Figure B.2 the Cu_3Sn layer grows much faster than the Cu_6Sn_5 layer upon aging. This is because the Cu_3Sn layer grows in both directions towards the Cu pad and the solder as compared to the Cu_6Sn_5 which grows only in a single direction towards the solder. The Cu_3Sn layer grows towards the Cu pad due to the diffusion of Sn from the solder to the Cu pad side and grows towards the solder due to the conversion of Cu_6Sn_5 at the Cu_3Sn/Cu_6Sn_5 interface. After the Cu atoms arrive at the interface of Cu_3Sn/Cu_6Sn_5 by diffusion through the grain boundaries of the Cu_3Sn layer, the following interfacial reaction happens:

$$Cu_6Sn_5 + 9Cu \rightarrow 5Cu_3Sn$$

By this reaction, Cu_6Sn_5 converted to Cu_3Sn at the interface and hence the amount of Cu atoms that can diffuse to the interface of Cu_6Sn_5/solder significantly reduced. As a result, Cu_3Sn grows rapidly with temperature and time by consuming Cu_6Sn_5 at the interface of Cu_3Sn/Cu_6Sn_5. The growth of Cu_6Sn_5 on the solder side largely depends on the availability of Cu atoms in the solder. Since most of the Cu atoms in the bulk solder used up to create Cu_6Sn_5 particles within the eutectic phase immediately after reflow, the amount of free Cu atoms that can diffuse to the solder/Cu_6Sn_5 interface under aging is very little, greatly limiting the growth of Cu_6Sn_5 on the solder side. Therefore, during isothermal aging, the Cu_3Sn layer appears to grow faster as it expanded on both sides, resulting in the shifting of the Cu/Cu_3Sn interface towards Cu pad and Cu_6Sn_5. This lead to decrease in the thickness of Cu_6Sn_5 after prolonged isothermal aging [3].

B.3.3. Effect of Isothermal Aging Temperature and Time

Effects of aging temperature and time on the intermetallic growth and morphology also studied. It observed that higher aging temperature facilitates the formation of the Cu_3Sn intermetallic layer in a much shorter aging time for Cu-OSP substrate (Fig B.2).

This is because a higher temperature provides the necessary thermal energy to overcome the activation energy to initiate the formation of Cu_3Sn; thus the Cu_3Sn layer formed at a much shorter time at a higher temperature, for example, at 150^{o}C needs 200 hours whereas at 125^{o}C, 500h aging time required. The effective thickness of the intermetallic layer measured for the Cu_3Sn, Cu_6Sn_5 and Ni-Cu-Sn are higher at a higher temperature of 150^{o}C than those at 125^{o}C for the same aging time (Fig B.2). It can be seen that high temperatures will accelerate the growth of the intermetallics as the growth of the intermetallics is diffusion-controlled and temperature-dependent. The effective growth of Ni-Cu-Sn IMC layer thickness after solid-state aging at 150°C for 500h found to be 140nm whereas Cu-Sn IMC layer thickness i.e. 3.37μm at the same aging condition.

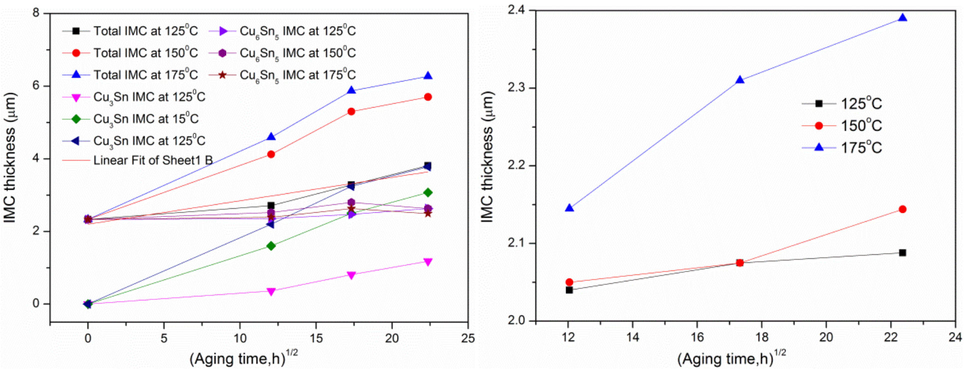

Figure B.3: Effect of aging conditions on IMC growth in 300μm sized SnAgCu joints.

Figure B.3 shows that growth behaviour of Cu_3Sn and Cu_6Sn_5 intermetallic layers is much thicker after aging at the same temperature and time. This implies that the growth of Cu_3Sn is much faster than Cu_6Sn_5 and Ni-Cu-Sn. From Fig B.3, it is also depicting that growth of Cu_6Sn_5 intermetallic layers retarding as time increases at 150°C due to formation Cu_3Sn is at the expense of Cu_6Sn_5 layer. Once formation of Cu_3Sn initiated at Cu/ Cu_6Sn_5 interface, the growth rate of Cu_6Sn_5 entirely controlled by the limited amount of Cu in the solder bump. Therefore, growth rate of Cu_6Sn_5 almost comes to an end. On the other hand, diffusion Cu from the UBM assists the formation of Cu_3Sn at the expense of Cu_6Sn_5. It observed that the Ni-Cu-Sn IMC layer served as a diffusion barrier to prevent the growth of brittle Cu-Ni-Sn IMC layer.

B.4. Interfacial IMC in Composite Solder Joints

Effect of nano-sized Mo particle reinforcement on diffusion kinetics of SAC composite solder joints studied in this section. As-reflowed composite solder joints subjected isothermal aging (High temperature storage) treatment at 125, 150 and 175^{o}C aging temperatures. Figure B.4 shows the cross-sectional SEM images of the interfaces between the SAC and SAC+0.3Mo composite solders with ENIG surface-finish aged at 150°C for 1000h. During reflow, the uppermost Au layer entirely dissolved into the molten solder, leaving the Ni–P layer exposed to the molten solder. At the same time, the Sn, Cu atoms in the solder reacted with the Ni atoms at the interface, to form a Cu-Ni-Sn reaction layer. The thickness of these interfacial intermetallic layers increased with increasing aging time. The needle-like morphology of the $(Cu,Ni)_6Sn_5$ phase gradually evolved into a planar-type after solid-state aging. There are two different intermetallic phases formed, when SAC387 and SAC+0.3%Mo composite solders reflowed on ENIG substrate. The $(Cu,Ni)_6Sn_5$ and $(Ni,Cu)_3Sn_4$ phases identified using EDX analysis. The $(Cu,Ni)_6Sn_5$ formed towards solder side, whereas $(Ni,Cu)_3Sn_4$ formed towards ENIG. However, individual layers cannot measure as the contrast between them is unusually low. The reported IMC is total interfacial IMC for the composite solder joints. There is no traces of Mo within the $(Cu,Ni)_6Sn_5$ phase in the composite solder joints. However, Mo reinforced SAC387 solder shows lower IMC growth than that of SAC387 solder. Therefore, it is an indication that Mo is not involving in diffusion couple and instead creates resistance for IMC growth.

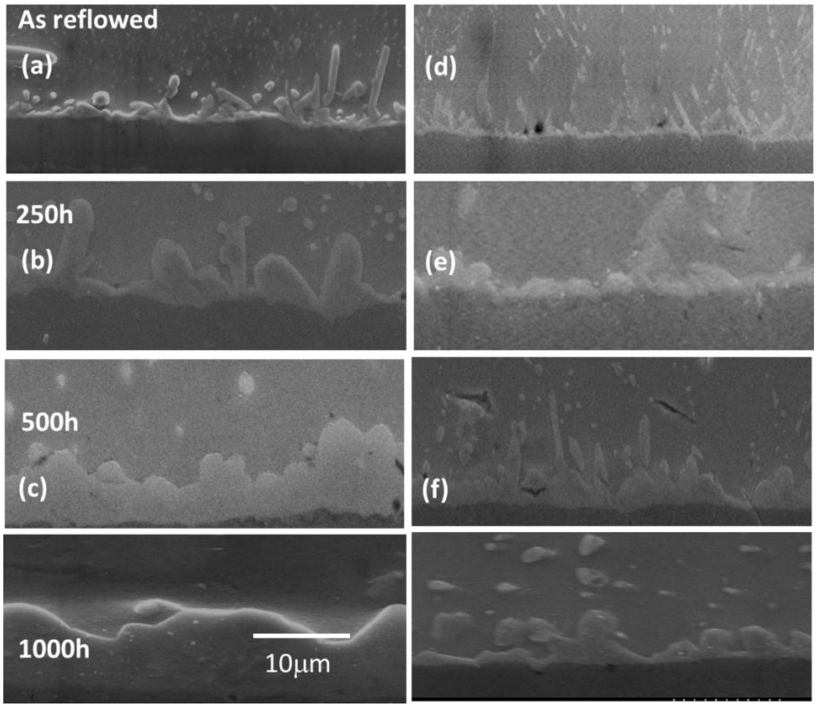

Figure B.4: EM images of cross sections of SAC composite solder joints with different aging times at 150°C for SAC (a, b & c) and SAC+0.3Mo (d, e & f).

B.4.1. IMC Growth Rate and Activation Energy

Figure B.5 (a) shows that the thickness of the $(Cu,Ni)_6Sn_5$ layer as a function of the square root of aging times for different temperatures. The mean thickness of the interfacial IMC layer found to be increasing linearly with the square root of aging time. The thickness of $(Cu,Ni)_6Sn_5$ intermetallic layer was 3µm after aging at 150°C for 1000 hours. However, it can be found from Figure B.5 (b) that the thickness of the $(Cu,Ni)_6Sn_5$ intermetallic layer reached about 2µm after 1000 hours of aging at 150°C. This implies that addition of nano-sized Mo particles can effectively act as a good diffusion barrier for the eutectic SAC387 solder. These slow kinetics is beneficial for the long-term reliability of the solder joint by limiting the formation of potentially brittle interfacial intermetallics and limiting consumption of the substrate by the solder. It can be seen from Fig.B.5 that the growth of the IMCs followed a parabolic law, implying that the growth of the intermetallic layer was diffusion-controlled. Also, several authors reported that the growth of intermetallic layer in the Sn base solder/Cu (or Ni) interface followed the diffusion controlled mechanism [4,5].

Table B.2 : IMC growth rate and activation energies for IME layers formed at the interface between SAC based composite solders and Immersion Au/Ni-P/Cu pad.

Solder Joint	Surface-Finish	Temperature (K)	K^2 (m^2 s^{-1})	Q (kJ/mol)
SAC387	OSP/Cu	398	2.11×10^{-14}	33
		423	3.37×10^{-14}	
		448	5.37×10^{-14}	
SAC387	Au/Ni	398	1.65×10^{-16}	59
		423	4.27×10^{-16}	
		448	12.1×10^{-16}	
SAC387	ENIG	398	1.06×10^{-15}	64
		423	5.64×10^{-15}	
		448	7.05×10^{-15}	
SAC387+0.3Mo	ENIG	398	3.64x 10^{-16}	73
		423	4.4 x 10^{-15}	
		448	1.00 x 10^{-14}	

Thickness of a reaction layer in the diffusion couples expressed by the classic parabolic Eq (B.1). The growth rate constant calculated from a linear regression analysis of d versus $t^{0.5}$, where the slope is k. Growth rate constants calculated for Cu-Ni-Sn intermetallic layers at different aging temperatures as summarized in Table B.2. Arrhenius relationship used to determine the apparent activation energies for intermetallic compound growth at the interface (Eq. (B.2)): The activation energies calculated from the slope of the Arrhenius plot using a linear regression model. Figure C.6 shows the Arrhenius plot for the growth of $(Cu,Ni)_6Sn_5$ IMC layers formed at the interface between SAC387/ENIG solder joint and the apparent activation energy calculated for the growth of the $(Cu,Ni)_6Sn_5$ phase was 64 and 89kJ/mol for SAC and SAC+0.3Mo , respectively.

Although, there is a variation of the solder composition, present results are in good agreement with the results of previous researchers [4,5].

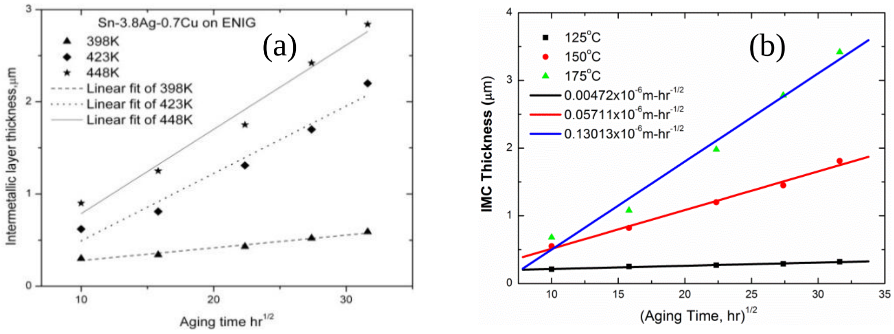

Figure B.5: Plots of IMC thickness as a function of the square root of time t, at aging temperatures of 398, 423, and 448K

B.4.2. Discussion

The effects of nano-particle addition on the intermetallic reactions are significant in the SnAgCu joints. Reinforcing elements influences on the interfacial reactions between the base metals and Sn: Firstly, they can alter the reaction/growth rate; secondly, additives can change the physical properties of the phases formed; and thirdly they can form additional phases or replace the equilibrium phases by forming other reaction phases instead. The change in the reaction layer thickness to be related to changes in the intermetallic composition. It can be proposed that the addition of nano-particle effects on the concentration of structural vacancies existing in the intermetallic [6]. Highly ordered alloys or compounds random motion of vacancy is not possible as it would disrupt the equilibrium ordered arrangement of atoms on lattice sites, all changes in atomic environment expected to influence the diffusion of elements in the interfacial IMC. Kumar has studied the impact of nano-sized Ni particles on IMC growth of SAC387 solder and observed that nano-sized Ni particles within the solder bump converts to fine sized intermetallic particles and acts has barrier for solid state diffusion flow. Belova and Murch have developed several theoretical models for diffusion in stoichiometric and nonstoichiometric intermetallic compounds that predict strong composition dependence on diffusion [7,8]. This explanation clearly accounts for the decrease in the growth rate after the addition of nano-particles to the solder. A recent study carried out by Takemoto and Yamamoto [10] indicated that metallic elements (Ti, Cr, Fe, Mg, Cu and Ni) effectively suppress the formation of Cu_3Sn and Cu_6Sn_5 during isothermal annealing at temperatures between 110 and 150 °C.

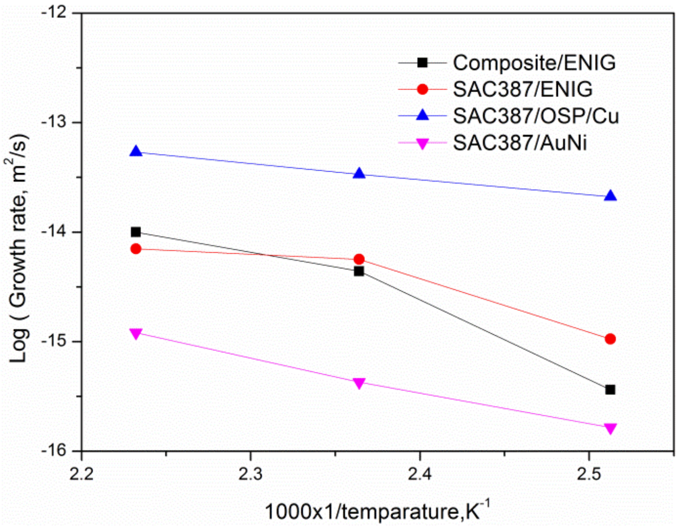

Figure B.6 Arrhenius plot for the formation of IMC layers formed at the interface between SAC, and different surface-finishes.

Table B.3 Activation energies of SAC387 joints with different surface-finishes

Solder joint	Aging temp. range	Aging time	Activation energy	Reference
SAC387/OSP/Cu	125-175	0-500h	33	Present study
SAC387/Au/Ni	125-175	0-500h	59	Present study
SAC387/ENIG	125-175	0-1000h	64	Present study
Composite/ENIG	125-175	0-1000h	73	Present study
SAC387/OSP/Cu	80-175	0-300h	42	228.
SAC387/ENIG	80-175	0-1080h	57	229
SAC387/Au/Ni	100-150	0-300h	73	228

B.4.3. Summary of Bulk Solder Joints

1. The interfacial microstructure of the Ni-Cu-Sn intermetallic thickness grows and changes its morphology from irregular and needle-like to lateral thickening and ripening and composition of intermetallic changes from $(Cu,Ni)_6Sn_5$ to $(Ni,Cu)_3Sn_4$ up on isothermal aging for 500hrs.
2. Aging temperature has an effect on the growth of the Cu-Sn IMCs layers but does not alter the structure of IMCs formed. For the Cu/OSP substrate, Cu_3Sn intermetallic layer formed in solder joint after aging isothermally at 125^{o}C for 300hrs where as it is forming in solder joints in 100hrs at 150°.
3. The growth of Cu_3Sn is much faster than Cu_6Sn_5 and Ni-Cu-Sn at 150°C.
4. Linear relationship between the growth of the IMC thickness and the square root of the aging time indicates that the formation IMC is a diffusion-controlled process.
5. Two kinds of intermetallic compounds, $(Cu,Ni)_6Sn_5$ and $(Cu,Ni)_3Sn_4$ for SAC387 and SAC387+0.3Mo solder with ENIG substrate.
6. Apparent activation energy for the growth of the Cu-Ni-Sn in SAC387 and SAC387+0.3Mo solders found to be 64, and 89 kJ/mol
7. Nano-sized Mo reinforced composite solders can effectively suppress the IMC growth

APPENDIX C: DIFFUSION KINETICS of IMCs IN μ–BUMP JOINTS

Effects of Sn volume on morphology, IMC growth and diffusion kinetics of interfacial Cu-Sn intermetallic compounds (IMC) with reference to the reflow and isothermal conditions studied in this chapter.

C.1. Effect of Multiple Reflows on IMC Morphology

Figure C.1 (a-d) describe the morphology of the interfacial IMC layer of 50 μm Sn/Cu solder joints reflowed for 60s holding period at the peak of 265^{0}C reflow temperature. During reflow process, copper substrate (UBM) exposed to the molten solder. Immediately, after the reflow process, scallop-like shaped IMCs formed at the solder joint interface (Fig.(C.1.(a)) and identified under EDX as Cu_6Sn_5 with 56.67% Cu and 42.94% Sn (η phase). As the number of reflows increases, the morphology of Cu_6Sn_5 changing from scallop to planar shape. Multiple reflows helps mutual inter-diffusion of Cu and Sn atoms across the interface during reflow process, which reduces interfacial free energy of IMC by changing scallop shape to more stable planar shape. There is another Cu rich IMC phase i.e. Cu_3Sn appears underneath Cu_6Sn_5 IMC during multiple reflows.

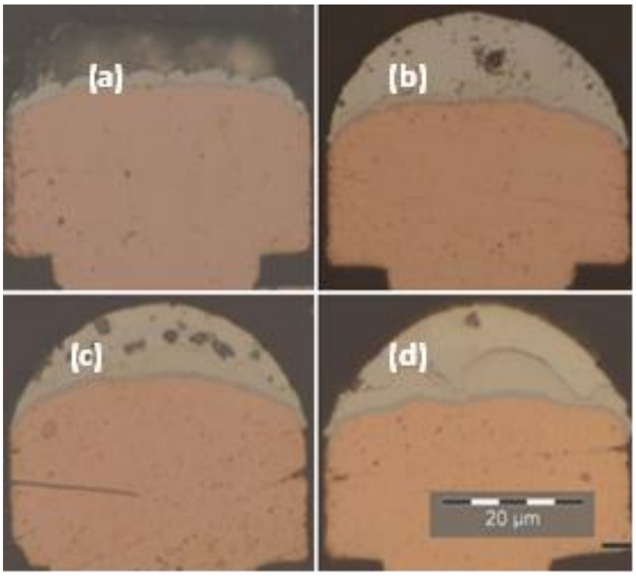

Figure C.1: Morphology of Sn/Cu joints with reference to multiple reflows at 265^{o}C

C.1.2. Effect of Multiple Reflows on IMC Growth

Figure C.1 shows the optical images of the interfacial IMC between the Sn solder bump and Cu UBM of 50μm solder joints during multiple reflows at 265°C. After one, reflow, the interfacial reactions between the Sn and Cu UBM formed Cu_6Sn_5 phase. During reflow, the Cu and Sn atoms inter-diffuse at the solder/Cu interface, causing the formation Cu_6Sn_5 phase. After three reflows, two different IMC layers, consisting of a scallop-shaped Cu_6Sn_5 phase (solder side) and a planar Cu_3Sn phase, as shown in Fig. C.1 (b). It observed from Fig. C.1 (d), nearly 6μm of the total deposited Sn (12 μm) thickness consumed during multiple reflows (10 times). There is no Cu_3Sn IMC observed for the first two reflows. However, it also observed after 3rd reflow onwards small layer 500nm thickness of Cu_3Sn along with thick Cu_6Sn_5 layer observed. The Cu_3Sn layer thickness increased to 1.7 μm at the 10th reflow. Solder joints reflowed at 245°C reflow temperature, only after 7th reflow the Cu_3Sn layer is seen underneath the Cu_6Sn_5.

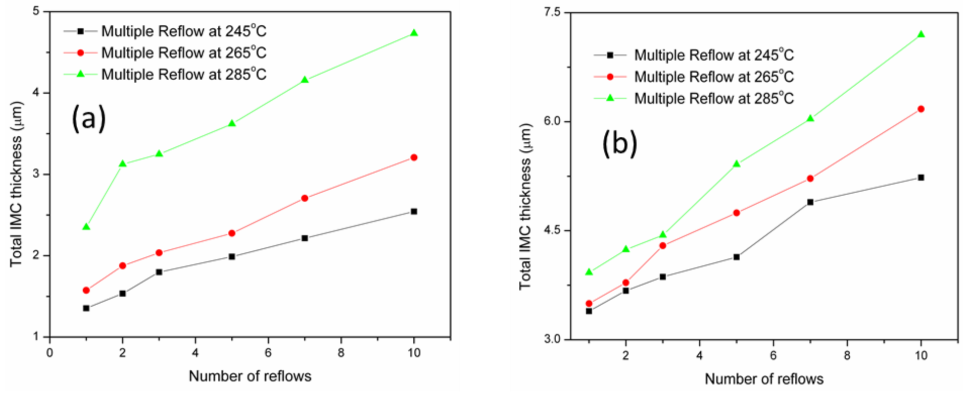

Figure C.2: Effect of multiple reflows on the total IMC thickness in (a) 10/50μmSn/Cu (b) 160/200 μm Sn/Cu solder joints

In case of microbump solder joints reflowed at 285°C, Cu_3Sn layer found right from the 1st reflow onwards. Similar observation also observed in other sizes of solder joints. Fig.C.2 shows the effect of solder volume (or size) on total effective IMC growth behaviour in solder joints with reference to multiple reflow at 265°C temperature.

Formation of early thickness of Cu_6Sn_5 plays an important role in the subsequent growth of interfacial total IMC during multiple reflows.

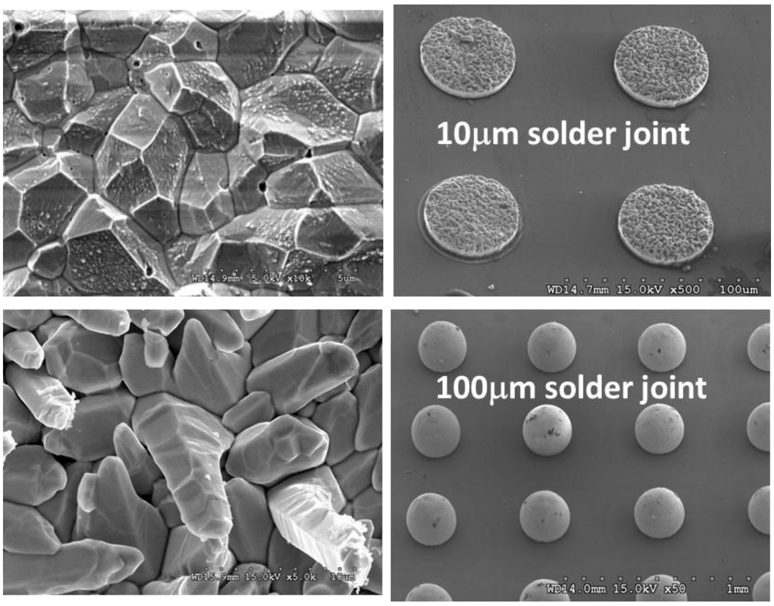

Figure C.3: Effect of solder volume on interfacial IMC in the Sn/Cu joints

In the case of 240μm solder joints reflowed at 265 and 285°C, Initial IMC thickness after 1st reflow is about 3.4 and 3.8 μm, whereas IMC thicknesses is about 6.1 and 7.4 μm respectively. IMC thickness in 50μm solder joints increases from 0.8μm to 4.98 μm from the first reflow to the 10th reflow at 285°C. The effective IMC growth thickness is 4.19μm that is higher than the effective increase in IMC for 240 μm solder joint undergone similar reflowed conditions. In other words, effective growth of IMC thickness during multiple reflows (10 times) is higher for 50 μm solder joints (4.18 μm) than 240 μm solder joint (3.6μm). Based on the experimental observation, it might be concluded that the early thicker IMC acts as a barrier for inter-diffusion of Cu and Sn atoms across the interface during reflow process than the thinner IMC. Therefore, first thinner IMC solder joints shows higher IMC growth during multiple reflows. In other words, smaller solder joints show higher growth rate of IMC during multiple reflows.

Figure C.2 shows IMC growth behaviour of different sizes of solder joints at 245 and 285°C reflow temperatures. Growth of individual IMC layers such as Cu_6Sn_5 and Cu_3Sn studied with multiple reflows at 265°C reflow temperature. The thickness of the Cu_3Sn layer is much smaller than that of the Cu_6Sn_5 layer after 2nd reflow at 265°C. Thickness of Cu_6Sn_5 and Cu_3Sn increasing with multiple reflows, after 7th reflow onwards the Cu_3Sn is more rapid than growth of Cu_6Sn_5. The retardation of Cu_6Sn_5 growth is due to diffusion of Cu in to the solder region limited due to increased IMC layer thickness since IMC layer acts as a barrier for Cu diffusion across the interface. UBM Cu, which migrate towards the interface reacts with Cu_6Sn_5 and form stable Cu_3Sn phase. This leads to increase in thickness of Cu_3Sn. The total IMC thickness of the 50µm Sn/Cu joint increased from about 0.9 µm after one reflow to about 5.2µm after 10 reflows.

Table C.4: Interfacial IMC growth kinetics parameter during multiple reflows

Reflow temperature,(°C)	Sn/Cu joint (µm)	Time-exponent	Growth rate Constant (m^2s^{-1})	Correlation Coefficient
245	10/50	0.28	0.39	0.96
	80/110	0.22	0.31	0.93
	160/200	0.18	1.18	0.93
265	10/50	0.31	0.36	0.95
	80/110	0.26	1.04	0.99
	160/200	0.28	1.01	0.99
285	10/50	0.29	0.68	0.98
	80/110	0.29	0.97	0.91
	160/200	0.41	0.61	0.97

The thickness of the Cu_3Sn IMCs layers increased to 1.7µm linearly with reflow numbers. The Cu_3Sn growth is about 1.1 µm 3.4µm after 10th reflow for solder joints reflowed at 245 and 285°C respectively. Summary of growth rate fitting parameters tabulated in Table C-4. It is shown that time-exponent is close to the 0.3, indicates that diffusion mechanism dominated by bulk grain boundary diffusion. Tables C.5 describe the summary of average growth rates and activation energy of interfacial IMC in different sized Sn/Co solder joints. It is observed that the activation energy of total IMC layer decreases with the reduction in the solder volume in the solder joints.

C.1.3. Effect of Reflow Dwell Time on IMC Growth

Figure C.4 shows that effect of reflow dwell time at the peak of the different reflow temperatures. It observed that microbump solder joint shows higher growth of IMC in 90s continuous reflow comparatively 110 and 240 μm solder joints. Reason for this discrepancy is due to the formation of early Cu_6Sn_5 layer during reflow. In the case of 240 μm pad diameter, more Cu will go into the solder bump due to the high volume of solder.

Table C.5: Growth rate constants and activation energy of different size of Sn/Cu solder joints with continuous reflow

Solder joint (μm)	**Reflow Temperature(K)**	**Growth rate Constant(m^2s^{-1})**	**Activation Energy($kJmol^{-1}$)**
10/50	518	3.61×10^{-15}	25±4
	538	5.32×10^{-15}	
	558	9.63×10^{-15}	
80/110	518	6.56×10^{-15}	37±9
	538	1.82×10^{-14}	
	558	2.68×10^{-14}	
160/200	518	1.29×10^{-14}	44±2
	538	2.92×10^{-14}	
	558	6.9×10^{-14}	

However, this dissolved Cu rapidly forming Cu_6Sn_5 phase during reflow process itself. This phase also acts as a barrier for further dissolution. It observed from the experimental data that total IMC growth rate constants are in the order of 10^{-13} m^2s^{-1} for all solder joints at 285°C reflow temperature whereas for 245°C, in the order of 10^{-14} to $10^{-15} m^2s^{-1}$ depending on the size of solder joint. Increase in the growth rate constant indicates that IMC growth is accelerates with an increase in reflow temperature. In the case of microbump solder joints, total IMC growth rate constant increase two orders from the 10^{-15} to 10^{-13} m^2s^{-1}, when the reflow temperature rises from 245 to 285°C.

However, for 240μm joints, it increases only one order of magnitude with similar reflow temperature range. This means microbump solder joints more sensitive to the reflow temperature and peak reflow time than bulk solder joints.

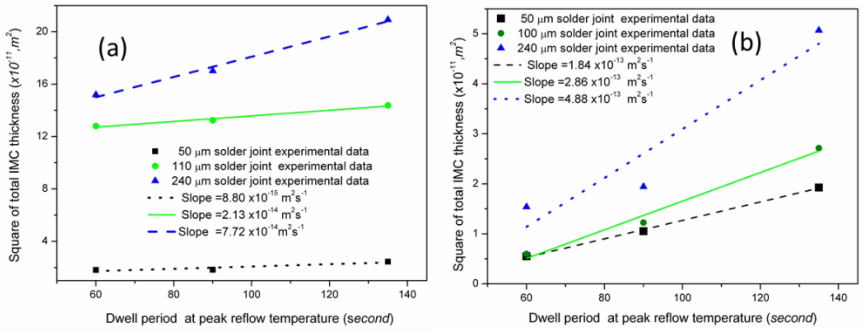

Figure C.4: IMC growth behaviour of different sizes of solder joint at reflow temperature of (a) 245°C (b) 285°C.

Table C.6: Growth rate constants and activation energy of different size of Sn/Cu solder joints with continuous reflow time.

Reflow temperature, (°C)	Sn/Cu joint(μm)	Time exponent	Growth rate Constant	Correlation Coefficient
245	10/50	0.21	5.1 $x10^{-7}$	0.95
	80/110	0.07	2.51 $x10^{-6}$	0.93
	160/200	0.218	1.48 $x10^{-6}$	0.97
265	10/50	0.31	0.44 $x10^{-7}$	0.95
	80/110	0.26	2.48 $x10^{-7}$	0.97
	160/200	0.28	1.22 $x10^{-7}$	0.98
285	10/50	0.29	6.65 $x10^{-8}$	0.99
	80/110	0.29	2.97 $x10^{-8}$	0.99
	160/200	0.41	7.13 $x10^{-8}$	0.89

C.1.4. Effects of Solder Volume on Activation Energy of IMCs

Activation energy for total interfacial IMC calculated from the slope of Log (growth rate constant) versus 1/t reflow temperature using Eq. (B.2) as shown in Fig. C.5. Total IMC growth constants and their activation energies for different sizes of Sn/Cu solder joints summarized in table C-6. It understood that the activation energy is higher for microbump (50μm) solder joints comparatively 240 μm solder joints.

Table C.7: Interfacial IMC growth kinetics parameters during continuous peak reflow.

Sn/Cu joint size (*μm*)	**Reflow Temperature (*K*)**	**Growth rate constant (m^2s^{-1})**	**Activation energy ($kJmol^{-1}$)**
10/50	518	7.5×10^{-15}	79±18
	538	2.11×10^{-14}	
	558	1.57×10^{-13}	
80/110	518	1.83×10^{-14}	68±23
	538	1.53×10^{-13}	
	558	2.43×10^{-13}	
160/200	518	6.56×10^{-14}	48±13
	538	2.65×10^{-13}	
	558	4.14×10^{-13}	

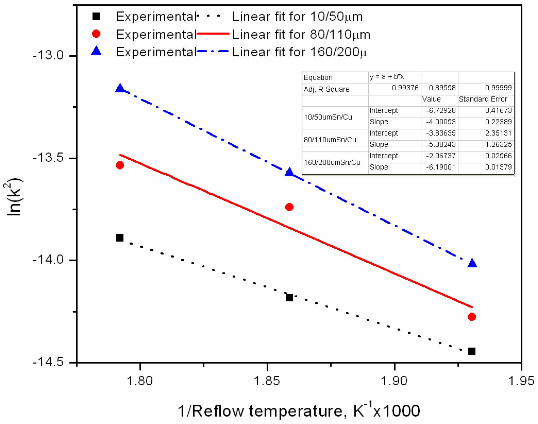

Figure C.6: IMC growth rate versus inverse reflow temperature (T^{-1}, K^{-1})

C.2. Effects of Isothermal Aging on IMC Morphology

Solder joints reflowed at 265°C, subjected to isothermal aging with different temperatures and aging periods. Figure C.6 (a-d) shows interfacial IMC growth of 10/50*μm Sn/Cu* solder joint (reflowed at 265°C) with aging period at 150°C aging. It is evident from the experimental data; a higher isothermal aging temperature facilitates the formation of thicker total IMC ($Cu_3Sn+Cu_6Sn_5$) layer in a much shorter aging time.

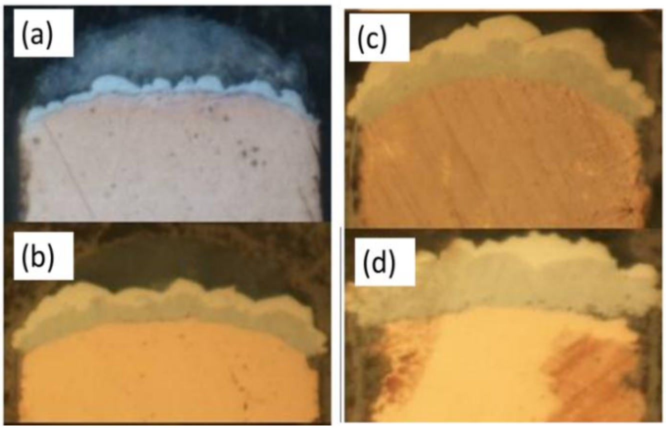

Figure C.6: Morphology of Sn/Cu joints with aging time at 150^0C

Higher aging temperature provides the necessary thermal energy to overcome the activation energy for inter-diffusion of constituent elements. Therefore, Cu_3Sn phase formed at a much shorter time at a higher temperature (for example, at 150^oC, it needs 100 hours and at 200^oC, 3 h needed). The change in the morphology of the Cu_6Sn_5 phase expected to decrease in the Gibbs free energy of the interfacial layer. However, morphology of Cu_3Sn layer is planar right from its formation. This might be abundant availability of Cu at Cu/Cu_6Sn_5. Fig.C.6 (d) shows that Cu_3Sn layer is much thicker than Cu_6Sn_5 after aging at longer periods.

This implies that the growth of Cu_3Sn is much faster than that of Cu_6Sn_5. Figure C.7 shows the relative growth rates of total IMC, Cu_6Sn_5 and Cu_3Sn layers. Growth rate of Cu_6Sn_5 retards as time increases, because of formation Cu_3Sn phase is at the expense of Cu_6Sn_5. Once formation of Cu_3Sn initiates at Cu/Cu_6Sn_5 interface, the growth rate of Cu_6Sn_5 only controlled by the diffusion of Cu through the interfacial IMC grain boundaries. This is evident from the data in the table C.8, the time-exponent is close to 0.3. Therefore, during isothermal aging, Cu_3Sn layer appears to grow faster as it expanded on both sides, resulting in shifting of Cu/Cu_3Sn interface towards Cu pad and Cu_6Sn_5. This leads to a reduction in thickness of Cu_6Sn_5 after prolonged isothermal aging.

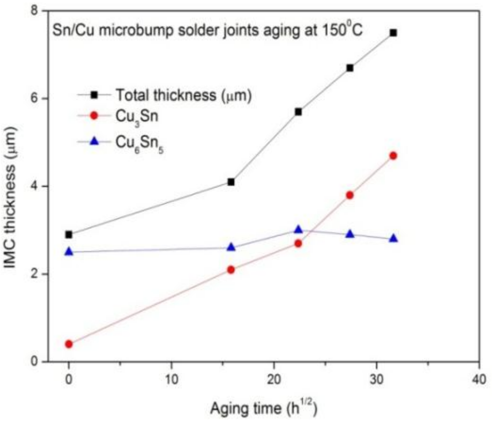

Figure C.6: Relative Cu_6Sn_5 and Cu_3Sn IMC growth behaviour during isothermal aging at 150^0C in microbump joints

Table C.8: Interfacial IMC growth kinetics parameters during isothermal aging

Aging temperature	**Solder joint Size (µm)**	**Time exponent**		
		Total IMC	*Cu_3Sn*	***Cu_6Sn_5***
150	10/50	0.28	0.42	**0.12**
	80/110	0.34	0.29	**0.38**
	160/200	0.44	0.31	**0.15**
175	10/50	0.34	0.43	**0.09**
	80/110	0.56	0.39	**0.72**
	160/200	0.72	0.72	**0.71**
200	10/50	0.28	0.50	**0.06**
	80/110	0.22	0.23	**0.22**
	160/200	0.18	0.08	**0.12**

C.2.1. Growth Rates and Activation Energy of *Sn/Cu* Joints

Thickness of interfacial IMC layers in the diffusion couples usually expressed by using Eq. (B.1) where δ is the thickness of the IMC layer δ_o is the thickness of IMC after first reflow or at aging time zero, *D* is the growth rate constant, *n* is the time-exponent and *t* is the aging time. The time-exponent evaluated using non-linear regression analysis. Figure B-14 shows the typical non-linear curve fitting analysis-using Eq. (B.1) for 10/50µm Sn/Cu joint aged at 150°C up to 450h. The observed linear correlation coefficient is more than 0.97 for IMC thickness-aging time data. Time exponents for total IMC, *Cu_6Sn_5 and Cu_3Sn* for all sizes of *Sn/Cu* joints summarized in the table D-8.

Arrhenius relationship (Eq.B.2) used for calculation of activation energies for the total IMCs, Cu_6Sn_5 and Cu_3Sn intermetallic growth. Activation energy for total interfacial IMC calculated from the slope of *ln* (growth rate constant) versus 1/ reflow temperature as shown in Fig.C.8.

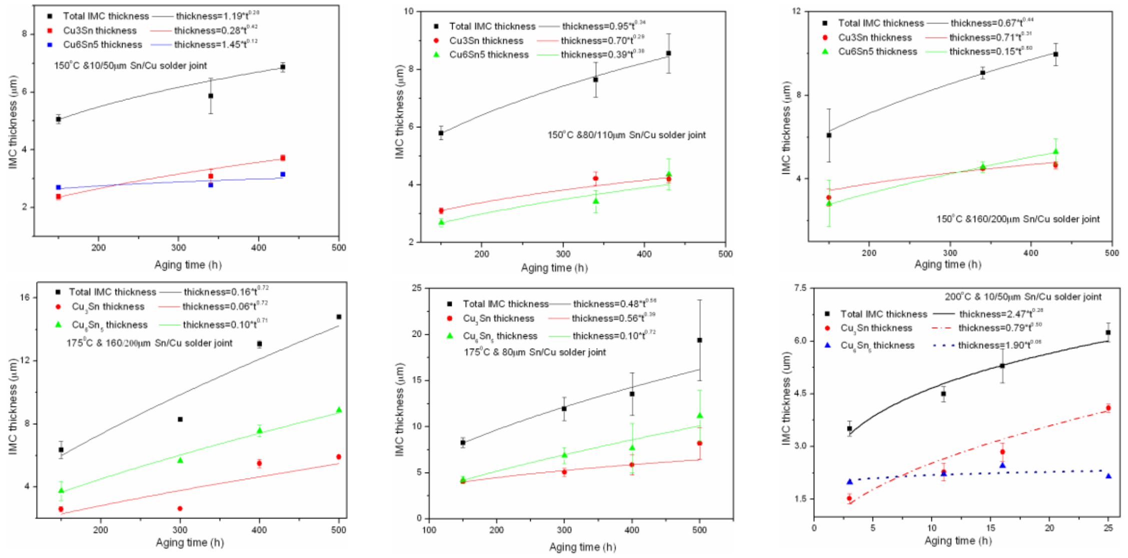

Figure C.14: IMC growth behaviour of different sizes of Sn/Cu joints during aging

The Total IMC growth constants and their activation energies for different sizes of Sn/Cu solder joints summarized in Table C.9. Activation energy found to be higher for microbump (10/50μm) *Sn/Cu* joints comparatively 160/200μm *Sn/Cu* solder joints during aging. Activation energy of Cu_3Sn found to be lower than Cu_6Sn_5 irrespective of size of the solder joint.

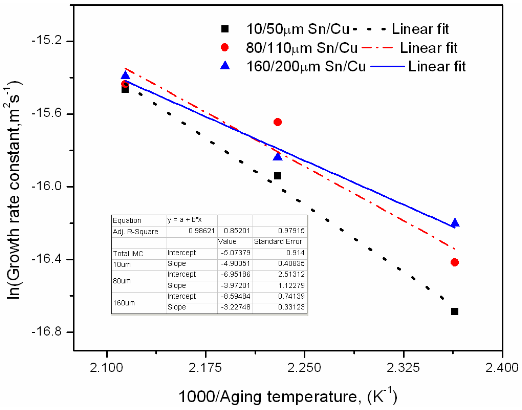

Equation	y = a + b*x		
Adj. R-Square	0.98621	0.85201	0.97915
		Value	Standard Error
Total IMC	Intercept	-5.07379	0.914
10um	Slope	-4.90051	0.40835
80um	Intercept	-6.95186	2.51312
	Slope	-3.97201	1.12279
160um	Intercept	-8.59484	0.74139
	Slope	-3.22748	0.33123

Figure C:15 Log (growth rate) versus inverse isothermal aging temperature for different sized Sn/Cu solder joint during isothermal aging conditions

Table C.9: Interfacial IMC growth kinetics parameters during isothermal aging

Aging temperature	**Solder joint Size (μm)**	**Time-exponent**		
		Total IMC	Cu_3Sn	Cu_6Sn_5
150	10/50	0.28	0.42	**0.12**
	80/110	0.34	0.29	**0.38**
	160/200	0.44	0.31	**0.15**
175	10/50	0.34	0.43	**0.09**
	80/110	0.56	0.39	**0.72**
	160/200	0.72	0.72	**0.71**
200	10/50	0.28	0.50	**0.06**
	80/110	0.22	0.23	**0.22**
	160/200	**0.18**	**0.08**	**0.12**

Table C.10: Growth rate constants and activation energy of different size of Sn/Cu solder joints with isothermal aging conditions

temp. (°C)	**Sn/Cu (μm)**	**Total IMC k^2, (m^2s^{-1})**	**Q, KJ/mol**	**Cu_3Sn k^2,(m^2s^{-1})**	**Q, KJ/mol**	**Cu_6Sn_5 k^2,(m^2s^{-1})**	**Q, KJ/mol**
150	10/50	2.06×10^{-17}	41	7.78×10^{-18}	45	2.35×10^{-18}	----
175		7.17×10^{-16}		1.57×10^{-17}		(-) growth	
200		3.42×10^{-16}		1.82×10^{-16}		1.04×10^{-17}	
150	80/110	3.83×10^{-16}	33	8.51×10^{-18}	24	1.09×10^{-17}	38
175		2.26×10^{-16}		3.76×10^{-17}		7.84×10^{-17}	
200		3.66×10^{-16}		4.43×10^{-17}		1.55×10^{-16}	
150	160/200	6.27×10^{-17}	26	1.24×10^{-17}	20	1.97×10^{-17}	25
175		1.45×10^{-16}		2.54×10^{-17}		5.21×10^{-17}	
200		4.05×10^{-16}		4.94×10^{-17}		1.22×10^{-16}	

C.3. Summary of Microbump Joints

1. Effects of solder volume on Morphology and interfacial IMC diffusion kinetics have been studied.
2. Growth rate constants decrease with reduction in the size of solder joint during multiple reflows for a given reflow temperature.
3. Activation energy of solder joints during reflow process increases with a decrease in solder joint size.

APPENDIX D: MECHANICAL PROPERTIES OF IMCS

TABLE D.1: Mechanical properties of SAC/Ni(V)/Cu solder joints

Test No.	S-h analysis					S^2-P analysis			CSM		Oliver & Pharr		Remarks
	Depth Range (nm)	Gradient	E_r (Gpa)	ν	**E (GPa)**	Load range (mN)	Gradient	**H (GPa)**	E (GPa)	H (GPa)	E (GPa)	H (GPa)	
1	80-185	327.66	56.614	0.32	**53.5**	0.12-1.38	1.65E+09	**2.64**	33.9	1.13	74.7	1.48	ND
2	50-110	534.38	92.33	0.32	**90.1**	0.58-2.05	2.48E+09	**4.67**	118.3	7.09	130.7	6.57	Ni3Sn4
3	25-140	656.70	113.46	0.32	**113.0**	0.09-3.21	2.77E+09	**6.32**	107.6	5.02	131.9	7.28	Cu6Sn5
5	50-110	664.25	114.76	0.32	**114.4**	0.68-2.3	3.04E+09	**5.89**	134.3	8.45	139.1	6.79	Cu6Sn5
6	50-180	610.42	105.47	0.32	**104.2**	0.52-4.80	2.94E+09	**5.15**	116.8	6.67	137.3	6.71	Cu6Sn5
7	40-150	627.25	108.37	0.32	**107.4**	0.58-3.39	3.70E+09	**4.32**	138.4	8.46	121.2	4.27	Cu6Sn5
8	25-200	650.62	112.41	0.32	**111.8**	0.19-6.24	3.20E+09	**5.38**	127.3	7.23	129.4	7.06	Cu6Sn5
11	40-185	642.96	111.09	0.32	**110.4**	0.45-5.26	3.25E+09	**5.18**	129.6	7.85	130.3	6.67	Cu6Sn5
12	30-230	618.45	106.85	0.32	**105.7**	0.26-7.87	2.87E+09	**5.41**	122.3	7.34	137.8	7.03	Cu6Sn5
14	25-170	737.68	127.45	0.32	**128.7**	0.17-4.82	3.60E+09	**6.15**	133.6	6.96	121.4	6.24	Cu6Sn5
15	45-200	668.08	115.43	0.32	**115.2**	0.50-5.88	3.40E+09	**5.34**	123.5	6.92	137.9	6.18	Cu6Sn5
16	25-90	829.56	143.33	0.32	**147.0**	0.19-1.69	3.67E+09	**7.62**	141.3	7.54	128.8	6.54	Ni3Sn4
17	40-155	623.41	107.71	0.32	**106.7**	0.40-3.11	3.72E+09	**4.25**	120.2	5.99	135.5	6.20	Cu6Sn5
19	60-250	637.58	110.12	0.32	**109.3**	0.19-7.18	3.05E+09	**5.41**	82.4	3.49	122.1	6.19	Cu6Sn5
20	35-200	584.46	100.98	0.32	**99.3**	0.34-4.09	3.91E+09	**3.56**	118.5	5.99	98.9	2.34	Cu6Sn5
21	40-150	717.58	123.98	0.32	**124.7**	0.44-3.68	3.70E+09	**5.66**	141.9	7.45	127.9	6.54	Ni3Sn4
22	45-150	696.22	120.29	0.32	**120.6**	0.61-4.44	2.96E+09	**6.66**	145.1	9.59	145.1	6.85	Ni3Sn4
23	30-140	640.34	110.63	0.32	**109.9**	0.10-2.77	2.96E+09	**5.64**	102.8	4.91	140.9	6.42	Cu6Sn5
24	30-140	666.79	115.20	0.32	**114.9**	0.29-3.56	3.01E+09	**6.00**	143.2	8.71	128.8	7.10	Cu6Sn5
26	50-175	608.62	105.15	0.32	**103.9**	0.60-4.50	3.14E+09	**4.80**	130.8	7.23	128.6	6.68	Cu6Sn5
27	30-150	625.49	108.07	0.32	**107.1**	0.25-3.38	3.34E+09	**4.77**	129.9	6.96	136.3	6.37	Cu6Sn5
28	25-150	698.22	120.64	0.32	**121.0**	0.059-3.48	2.87E+09	**6.91**	97.1	4.54	125.6	7.31	Cu6Sn5

29	25-160	624.84	107.96	0.32	**106.9**	0.14-4.06	2.64E+09	**6.01**	144.4	6.42	146.7	7.53	Cu6Sn5
31	25-80	865.98	149.62	0.32	**154.4**	0.20-1.53	3.52E+09	**8.66**	145.5	7.80	129.8	6.48	(Cu,Ni)6Sn5
32	25-115	779.75	134.72	0.32	**137.0**	0.14-1.83	4.90E+09	**5.05**	125.5	4.83	134.8	5.88	Ni3Sn4
33	25-180	739.78	127.82	0.32	**129.1**	0.24-5.48	3.57E+09	**6.24**	156.9	8.75	139.2	6.43	Ni3Sn4
34	50-100	859.29	148.46	0.32	**153.0**	0.08- 1.05	3.28E+09	**9.15**	68.7	2.04	124.7	5.92	(Cu,Ni)6Sn5
35	50-225	243.52	42.07	0.32	**39.2**	0.39- 2.69	1.52E+09	**1.58**	55.4	4.46	57.7	1.30	solder
37	30-155	668.39	115.48	0.32	**115.2**	0.37-4.40	3.03E+09	**6.00**	141.0	8.07	131.3	6.52	Ni3Sn4
38	40-140	597.87	103.30	0.32	**101.9**	0.53-3.88	2.45E+09	**5.93**	143.3	9.81	135.9	6.90	Ni3Sn4
39	30-150	619.25	106.99	0.32	**105.9**	0.28-3.67	3.05E+09	**5.12**	132.0	7.60	135.2	6.66	Cu6Sn5
41	65-170	597.63	103.25	0.32	**101.8**	1.16-3.97	4.06E+09	**3.58**	144.7	8.36	125.6	4.84	Ag3Sn
42	40-150	686.59	118.63	0.32	**118.7**	0.59-5.42	3.05E+09	**6.29**	159.5	10.64	134.6	6.48	Cu6Sn5
43	45-115	728.85	125.93	0.32	**126.9**	0.73- 3.19	3.13E+09	**6.90**	169.4	11.11	136.8	6.64	Ni3Sn4
44	60-170	662.56	114.47	0.32	**114.1**	0.66-4.40	3.22E+09	**5.55**	127.0	6.52	131.1	5.91	Cu6Sn5
46	30-70	886.57	153.18	0.32	**158.6**	0.27-1.11	4.05E+09	**7.90**	159.8	7.51	125.8	5.44	(Cu,Ni)6Sn5
48	50-160	703.55	121.56	0.32	**122.0**	0.61-4.35	3.38E+09	**5.96**	139.9	8.21	127.6	6.29	Ni3Sn4
49	75-170	626.68	108.27	0.32	**107.3**	1.36-4.88	3.27E+09	**4.88**	143.6	8.30	140.5	6.86	Ni3Sn4
54	45-120	521.23	90.06	0.32	**87.7**	0.19-1.87	1.92E+09	**5.76**	78.5	4.01	68.03	1.66	Cu
56	25-105	791.40	136.74	0.32	**139.3**	0.25- 2.39	3.33E+09	**7.65**	159.9	10.20	140.48	6.73	Ni3Sn4
58	115-190	731.87	126.45	0.32	**127.5**	0.62-2.97	3.43E+09	**6.35**	77.4	2.46	113.5	4.91	Ni3Sn4
59	45-145	681.75	117.79	0.32	**117.8**	0.56- 3.88	2.97E+09	**6.36**	132.3	8.04	128.0	5.84	Cu6Sn5
64	50-105	766.74	132.47	0.32	**134.4**	0.33-0.98	7.60E+09	**3.14**	120.1	3.10	131.5	5.17	Ni3Sn4
65	40-100	768.82	132.83	0.32	**134.8**	0.57-2.23	3.44E+09	**7.00**	158.7	9.88	141.7	5.88	Ni3Sn4
66	200-260	697.79	120.56	0.32	**120.9**	0.24-1.16	5.75E+09	**3.44**	37.8	0.38	90.1	3.07	Ni3Sn4
67	35-100	804.03	138.92	0.32	**141.8**	0.28-2.18	2.92E+09	**9.02**	134.5	7.64	142.7	5.68	Ni3Sn4
69	100-170	712.23	123.06	0.32	**123.7**	0.40-2.48	2.89E+09	**7.14**	66.6	2.34	114.3	5.01	Ni3Sn4
71	50-100	929.09	160.53	0.32	**167.5**	0.03-0.17	2.86E+10	**1.22**	72.5	0.42	138.1	3.31	(Cu,Ni)6Sn5

References

[1]. C. C. Chang, C.R.Kao, Dissolution and interfacial reaction between Cu and Sn-Ag-Cu solders in: *International conference on Microsystems, Packaging, Assembly and Circuits Technology*, Taiwan, (2007) 54.

[2]. J. H. L. P. L.Xu, *Thin solid films,* 504 (2006) 362.

[3]. W.Peng, E. Monlevade, M.E. Marques, *Microelectron. Reliab,* 47 (2007) 2161.

[4]. J. W. Yoon, C. B. Lee, S. B. Jung, *J.Electron.Mater,* 32 (2003) 1195.

[5]. P.T.Vianco, A. C. Kilgo, R.Grant, *J.Electron.Mater,* 24 (1995) 1493.

[6]. E.K.Ohriner, *Welding.J.,* (1987) 191.

[7]. V. Belova and G.E. Murch, *Phil. Mag.A,* 82 (2002) 269.

[8]. V. Belova and G.E. Murch, *Phil.Mag.A,* 80 (2000) 2073.

[9]. T. Y. T.Takemoto, *J. JCBRA,* 40 (2001) 309.